Caractérisation et modélisation des effets de surpression en champ proche et du chargement au sol du BLEVE

Roland Eyssette

N°d'ordre NNT : 2018LYSEM020

THESE de DOCTORAT DE L'UNIVERSITE DE LYON

opérée au sein de

MINES Saint-Etienne

délivrée en partenariat international avec Queen's University (Canada)

Ecole Doctorale N° 488
Sciences, Ingénierie, Santé

Spécialité de doctorat : Sciences et Génie de l'Environnement
Discipline : Science de la terre et de l'univers espace

Soutenue publiquement le 16/10/2018, par :

Roland Eyssette

Caractérisation et modélisation du champ de surpression proche et du chargement au sol du BLEVE

Devant le jury composé de :

Reynolds, James	Professeur	Queen's University	Président
Planas, Eulalia	Professeur	Universitat Politècnica de Catalunya	Rapporteur
Ciccarelli, Gaby	Professeur	Queen's University	Rapporteur
Barz, Dominik	Professeur	Queen's University	Examinateur
Hoorelbeke, Pol	Docteur	Total SA	Examinateur
Graillot, Didier	Professeur	Mines Saint-Etienne	Examinateur
Heymes, Frédéric	HDR	IMT Mines Alès	Directeur de thèse
Birk, Michael	Professeur	Queen's University	Co-directeur de thèse
Laboureur, Delphine	Professeur Assistante	Von Karman Institute	Invitée

Spécialités doctorales	Responsables :	Spécialités doctorales	Responsables
SCIENCES ET GENIE DES MATERIAUX	K. Wolski Directeur de recherche	MATHEMATIQUES APPLIQUEES	O. Roustant, Maître-assistant
MECANIQUE ET INGENIERIE	S. Drapier, professeur	INFORMATIQUE	O. Boissier, Professeur
GENIE DES PROCEDES	F. Gruy, Maître de recherche	SCIENCES DES IMAGES ET DES FORMES	JC. Pinoli, Professeur
SCIENCES DE LA TERRE	B. Guy, Directeur de recherche	GENIE INDUSTRIEL	N. Absi, Maitre de recherche
SCIENCES ET GENIE DE L'ENVIRONNEMENT	D. Graillot, Directeur de recherche	MICROELECTRONIQUE	Ph. Lalevée, Professeur

EMSE : Enseignants-chercheurs et chercheurs autorisés à diriger des thèses de doctorat (titulaires d'un doctorat d'État ou d'une HDR)

ABSI	Nabil	MR	Génie industriel	CMP
AUGUSTO	Vincent	CR	Image, Vision, Signal	CIS
AVRIL	Stéphane	PR2	Mécanique et ingénierie	CIS
BADEL	Pierre	MA(MDC)	Mécanique et ingénierie	CIS
BALBO	Flavien	PR2	Informatique	FAYOL
BASSEREAU	Jean-François	PR	Sciences et génie des matériaux	SMS
BATTON-HUBERT	Mireille	PR2	Sciences et génie de l'environnement	FAYOL
BEIGBEDER	Michel	MA(MDC)	Informatique	FAYOL
BLAYAC	Sylvain	MA(MDC)	Microélectronique	CMP
BOISSIER	Olivier	PR1	Informatique	FAYOL
BONNEFOY	Olivier	MA(MDC)	Génie des Procédés	SPIN
BORBELY	Andras	MR(DR2)	Sciences et génie des matériaux	SMS
BOUCHER	Xavier	PR2	Génie Industriel	FAYOL
BRODHAG	Christian	DR	Sciences et génie de l'environnement	FAYOL
BRUCHON	Julien	MA(MDC)	Mécanique et ingénierie	SMS
CAMEIRAO	Ana	MA(MDC)	Génie des Procédés	SPIN
CHRISTIEN	Frédéric	PR	Science et génie des matériaux	SMS
DAUZERE-PERES	Stéphane	PR1	Génie Industriel	CMP
DEBAYLE	Johan	MR	Sciences des Images et des Formes	SPIN
DEGEORGE	Jean-Michel	MA(MDC)	Génie industriel	Fayol
DELAFOSSE	David	PR0	Sciences et génie des matériaux	SMS
DELORME	Xavier	MA(MDC)	Génie industriel	FAYOL
DESRAYAUD	Christophe	PR1	Mécanique et ingénierie	SMS
DJENIZIAN	Thierry	PR	Science et génie des matériaux	CMP
DOUCE	Sandrine	PR2	Sciences de gestion	FAYOL
DRAPIER	Sylvain	PR1	Mécanique et ingénierie	SMS
FAUCHEU	Jenny	MA(MDC)	Sciences et génie des matériaux	SMS
FAVERGEON	Loïc	CR	Génie des Procédés	SPIN
FEILLET	Dominique	PR1	Génie Industriel	CMP
FOREST	Valérie	MA(MDC)	Génie des Procédés	CIS
FRACZKIEWICZ	Anna	DR	Sciences et génie des matériaux	SMS
GARCIA	Daniel	MR(DR2)	Sciences de la Terre	SPIN
GAVET	Yann	MA(MDC)	Sciences des Images et des Formes	SPIN
GERINGER	Jean	MA(MDC)	Sciences et génie des matériaux	CIS
GOEURIOT	Dominique	DR	Sciences et génie des matériaux	SMS
GONDRAN	Natacha	MA(MDC)	Sciences et génie de l'environnement	FAYOL
GONZALEZ FELIU	Jesus	MA(MDC)	Sciences économiques	FAYOL
GRAILLOT	Didier	DR	Sciences et génie de l'environnement	SPIN
GROSSEAU	Philippe	DR	Génie des Procédés	SPIN
GRUY	Frédéric	PR1	Génie des Procédés	SPIN
GUY	Bernard	DR	Sciences de la Terre	SPIN
HAN	Woo-Suck	MR	Mécanique et ingénierie	SMS
HERRI	Jean Michel	PR1	Génie des Procédés	SPIN
KERMOUCHE	Guillaume	PR2	Mécanique et Ingénierie	SMS
KLOCKER	Helmut	DR	Sciences et génie des matériaux	SMS
LAFOREST	Valérie	MR(DR2)	Sciences et génie de l'environnement	FAYOL
LERICHE	Rodolphe	CR	Mécanique et ingénierie	FAYOL
MALLIARAS	Georges	PR1	Microélectronique	CMP
MOLIMARD	Jérôme	PR2	Mécanique et ingénierie	CIS
MOUTTE	Jacques	CR	Génie des Procédés	SPIN
NEUBERT	Gilles			FAYOL
NIKOLOVSKI	Jean-Pierre	Ingénieur de recherche	Mécanique et ingénierie	CMP
NORTIER	Patrice	PR1	Génie des Procédés	SPIN
O CONNOR	Rodney Philip	MA(MDC)	Microélectronique	CMP
OWENS	Rosin	MA(MDC)	Microélectronique	CMP
PERES	Véronique	MR	Génie des Procédés	SPIN
PICARD	Gauthier	MA(MDC)	Informatique	FAYOL
PIJOLAT	Christophe	PR0	Génie des Procédés	SPIN
PINOLI	Jean Charles	PR0	Sciences des Images et des Formes	SPIN
POURCHEZ	Jérémy	MR	Génie des Procédés	CIS
ROUSSY	Agnès	MA(MDC)	Microélectronique	CMP
ROUSTANT	Olivier	MA(MDC)	Mathématiques appliquées	FAYOL
SANAUR	Sébastien	MA(MDC)	Microélectronique	CMP
STOLARZ	Jacques	CR	Sciences et génie des matériaux	SMS
TRIA	Assia	Ingénieur de recherche	Microélectronique	CMP
VALDIVIESO	François	PR2	Sciences et génie des matériaux	SMS
VIRICELLE	Jean Paul	DR	Génie des Procédés	SPIN
WOLSKI	Krzystof	DR	Sciences et génie des matériaux	SMS
XIE	Xiaolan	PR0	Génie industriel	CIS
YUGMA	Gallian	CR	Génie industriel	CMP

Mise à jour : 03/02/2017

Quiet people have the loudest minds

- Stephen Hawking -

Acknowledgements

This PhD project was made possible thanks to a successful cooperation between Mike Birk at Queen's University in Canada and the research team of Physics of the Phenomena at the Institute of Risk Sciences, IMT Mines Alès in France - namely Frédéric Heymes, Laurent Aprin, Pierre Lauret, Christian Lopez and Pierre Slangen. It would have not been possible to reach this level of sophistication in the experiment and the results obtained without the implication of all parts of this cooperation. The expertise and pragmatism of Mike Birk gave very interesting directions to the research, especially when building the experimental apparatus from scratch. The uncountable time and dedication of Frédéric Heymes in planning the experiment and finding a location to make it possible, supported by the experimental skills of the whole French team brought this apparatus and research work to the next level.

This leads me to thank particularly Mike Birk and Frédéric Heymes as co-directors of this PhD work. The guidance, time, opportunities and help they have both offered me during this project were tremendous. I am very grateful for this.

Thank you to the jury, namely James Reynolds, Dominik Barz, Didier Graillot, Pol Hoorelbeke and Delphine Laboureur for making the defense possible. Special thanks to Gaby Ciccarelli and Eulalia Planas for reviewing the thesis with expert eyes to evaluate my work. Everybody complied well to the constraints of video conference as well as the need to satisfy the protocol of both institution, making the defense a very positive experience overall.

I would like to thank the administrative staff - Gabrielle Whan, Jane Davis and Corrine Vincent - for their help in navigating with me through the administrative hustle that was this cotutelle program. Thank you to Jane Paul in helping me through the proof reading process and improving my scientific English.

Thank you to all the lab mates and coworkers I have been sharing time with in France and in Canada – Maverick, Jimmy, David, Giordano, Mohamed, Clément, Frédéric, Pierre, Zac, Laurent, and the whole ISR lab - both for working through interesting scientific progress together and cracking jokes or sharing a beer to when things got too serious. Special thanks to Clément and Maverick, for daring to share an office with me for over two years each and managing to remain sane through this whole experience. And honorable mention to Frédéric, who shared with me his passion for climbing and the mountains. Ice climbing rocks.

Also a big thank you to all the friends and housemates in both countries that made this experience much more than just a PhD – August, Florie, Kas, Alexis, Dan, Fifou, Perrine, Thibault, to name just a

few. The amount of fun times, good talks, life advices, adventures and memories I have shared with all of you through these years is uncountable.

And finally I am grateful to my family – my parents Pascal and Christiane, my siblings and in-law Paul, Delphine and Amandine, and all the others - for supporting my decision to go through this PhD, even though they did not understand much of what I was doing with my explosions, and even if it meant for me to leave for two years 6000 km away from home.

This project was jointly funded by Queen's University, the Natural Sciences and Engineering Council of Canada (NSERC), and IMT Mines Alès.

Table of Contents

List of Figures

List of Tables

List of Abbreviations

BLEVE	Boiling Liquid Expanding Vapor Explosion
C-D nozzle	Converging-Diverging nozzle
CFD	Computational Fluid Dynamics
EoS	Equation of State
FB	Fractional Bias
F-W model	Friedman-Whitham model
GUI	Graphic User Interface
HSI	High Speed Imaging
ISR	Risk Science Institute (Institut des Sciences du Risque)
LFG	Liquid Flammable Gas
LGEI	Laboratory of Industrial Environment Engineering (Laboratoire du Génie de l'Environnement Industriel)
LPG	Liquid Petroleum Gas
NMSE	Normalized Mean Square Error
PILS	Pure In Line Shadowgraph
PLG	Pressure Liquefied Gas
TLOC	Total Loss of Containment
T_{SL}	Superheat Limit Temperature

Chapter 1

Introduction

I - Motivation

Pressurized vessels are commonly used in the industry to store and transport pressure liquefied gas (PLG). Accidents involving these vessels can lead to a specific type of explosion, called a Boiling Liquid Expanding Vapor Explosion (BLEVE). As the acronym indicates, these explosions involve the explosive expansion of the pressurized vapor, and the violent boiling from the liquid suddenly superheated due to the sudden loss of containment. This type of accident is known in the industrial landscape for over six decades now. However, predicting when it will happen, as well as the consequences of such an explosion still remains poorly understood in details.

Emergency responders need to be able to adopt the proper tactics when exposed to a pressurized vessel in hazardous environment, such as fire engulfment. Should they work on cooling down the vessel to avoid explosion or stay at a safe distance to avoid the consequences of the explosion? This question is difficult to answer because of the large number of parameters involved. It is difficult to evaluate the situation when on site: intensity of the fire, pressure inside the vessel, structural strength of the vessel wall, including small defects, rust and other weakening factors of the vessel wall structure.

Industries need to understand better the consequences of BLEVE to place their various vessels at safe distances from critical infrastructures and from each other, in order to avoid domino effects and diminish the severity of an explosion accident.

Finally the transportation industry policy makers need to understand the hazards involved with pressure vessels travelling through roads and railways. What would be the consequences of a BLEVE in a congested urban area, with high rise building? Similarly, what would happen if a road tanker accident lead to a BLEVE on a bridge?

Modeling and experiments have been conducted to improve our understanding of BLEVE. But the current understanding of the detailed physics of the explosion remains poorly understood to answer these questions.

II - Objectives

This project aims at understanding the physics of the compressible flow behavior and the thermodynamics involved in the near field of BLEVE accidents. It will focus on the physics of how the overpressure is generated in the near-field, and its hazardous consequences. One of the main questions it will try to answer is the following: what are the contribution of the vapor expansion and the liquid boiling in the overpressure generation, as well as in other hazards in the vicinity of the vessel?

III - Scope

The scope of this work included experimental research using a novel apparatus designed and constructed for this project. The basic apparatus was designed and constructed in Canada. Preliminary experiments were conducted in Canada using a limited array of instruments. A copy of the apparatus was then fabricated and shipped to France where a much more detailed experimental setup was constructed. The main experiments were conducted in France. Some computational fluid dynamics (CFD) was also conducted using the ANSYS Fluent software. This was done to help understand the observed phenomena. The CFD analysis was started in Canada and continued in France.

This contribution is a challenging experimental work conducted between IMT Mines Ales (France) and Queens' University (Canada). Main experiments were performed in the so called Spark Facility located in France and provided a unique set of experimental data. The main focus of this work was to understand the physics of BLEVE through a small scale experimental setup trying to reproduce realistic cylindrical vessel explosions. The experimental prototype was designed and constructed for the purpose of the project. It consists of a an aluminum tube prepared and machined to burst at various controlled failure pressure, surrounded by blast gages and adequate instruments to capture pressure information, ground loading and other data meaningful to the understanding of the explosion. High speed imaging is set up to capture the explosion under different angles, with help of shadowgraph techniques to visualize the shock propagation. Numerical simulation work is performed to help the interpretation and analysis of the experimental data. The computation work is performed through ANSYS Fluent. It was limited to non-viscous transient compressible flow simulation, to be solved with modest computational capabilities.

This study focuses on the behavior of the fluid as it is depressurized and expands out of the failing vessel. It does not deal with the structural analysis aspect of the vessel failure itself, but it includes the observed deformations leading to its dynamic opening.

IV - Contributions

With the safety engineering orientation of this project in mind, the contributions of the presented work are, in no specific order:

- The presentation of a small scale realistic BLEVE apparatus expanding the set of experimental data and imaging available in the domain of BLEVE research. Scaling in addressed but not fully solved;
- Chronological timelines of the phenomena involved inside and outside the failing vessel during BLEVE, with a graphic user interface developed for the purpose through Matlab;
- A study of the anisotropy of the pressure field out of a cylindrical vessel geometry;
- A discussion on the contribution of both fluid phases in the generation of BLEVE hazards in the near-field;
- A physics based model of the maximum overpressure based on compressible flow assumptions and conservation equations;
- Interpretations of experimental measurements to various flow patterns involved in the complex vessel opening of the BLEVE (side vortices, stationary shock due to critical flow), with help of numerical simulation;
- Experimental evidences and modeling of the ground loading generated by a BLEVE.

Chapter 2

Literature Review

I - Definition of BLEVE

BLEVE (Boiling Liquid Expanding Vapor Explosion) is one of the most feared event in the industry. This accident consists of the failure of a pressurized vessel filled with PLG (Pressure Liquefied Gas), involving expansion of a vapor phase followed by flashing of a liquid phase. BLEVE is known for its powerful overpressure, fire or toxic hazard depending on the type of commodity stored, and the difficulty to predict with accuracy when a damaged vessel will fail. This type of industrial accident is now known for over 50 years. However the definition of BLEVE itself is still controversial. Various authors define "explosion" differently, as well as the influence of speed of the flashing process and its influence on the explosion. In 1979, Reid proposes a definition stating that a BLEVE occurs when the liquid is over its superheat limit at vessel failure (Reid, 1979) leading to homogeneous nucleation and triggering the explosive flashing of the liquid. Theoretically, the homogeneous nucleation induces the strongest explosive phase change possible. However, this state needs a liquid with no suspended particles, a vessel wall that is perfectly smooth with no nucleation sites and no temperature stratification, which never happens in practical case of industrial storage. Following this definition, there has probably never been a BLEVE in an industrial setting.

More recently, in 2007, a more realistic definition focusing on the catastrophic failure of the vessel was proposed by Birk et al. (Birk et al., 2007): "a BLEVE is the explosive release of expanding vapor and boiling liquid when a container holding a PLG fails catastrophically". A BLEVE implies that the vessel will fully open during the failure and leads to a TLOC (Total Loss of Containment). This full opening results in the formation of shock waves that travel out into the surroundings. This late focus on total loss of containment emphasizes the fact that a full opening of the vessel is needed to characterize a BLEVE. Partial opening of the vessel can lead to a strong jet release (Figure 2-1 left), but full opening of the vessel leads to a harmful blast wave and much more violent phase change of the superheated liquid. The flattened remains of the vessel after such accidents are witness of the violence of the explosion (Figure 2-1 right)

Figure 2-1 Vessel failures from experiments (left: partial failure in fish mouth pattern ; right: total failure) (Birk et al., 2006a)

A consequence of the release of LPG or other flammable contents through a BLEVE may lead to fire hazards, such as fireballs, flash fire or vapor cloud explosions. Indeed a fireball is often a very direct consequence of BLEVEs. However it should be clear that fire related consequences are not a necessity for defining a BLEVE. The BLEVE is the mechanical failure of a pressurized vessel, thus BLEVE can happen with non-flammable substances, for example liquid carbon dioxide.

I-1. BLEVE potential hazards

The destructive potential of BLEVE is due to several types of hazards. First, the explosive release of expanding vapor and flashing liquid generates strong overpressure and shock waves propagating into the surroundings. This hazard is of smaller range than fire and projectile hazards. However, it is present for any kind of PLG inside the vessel. Moreover the strength generated by the overpressure can be destructive for nearby structures, such as buildings, tunnels (van den Berg and Weerheijm, 2006), bridges or other vessels likely to trigger a chain reaction. This last scenario happened in the Cosmo Oil accident in Japan 2011 and will be described in Section II - .

Another form of hazard is the projection of vessel fragments. This hazard is much more random, but can be deadly and may be the furthest reaching danger. Hazard ranges for projectiles from rail cars have been observed greater than 1 km. Abbasi (Abbasi and Abbasi, 2007) published a review on the statistics on trajectory, penetrability and other characteristics of this kind of missile.

Finally, if the commodity is flammable, a fireball (Figure 2 2) can be generated. If ignition is not immediate, the flammable gas is dispersed, with risk of a vapor cloud explosion (TNO, 1997). If the gas is toxic (ammonia, chlorine), the explosion is followed by a toxic cloud dispersion.

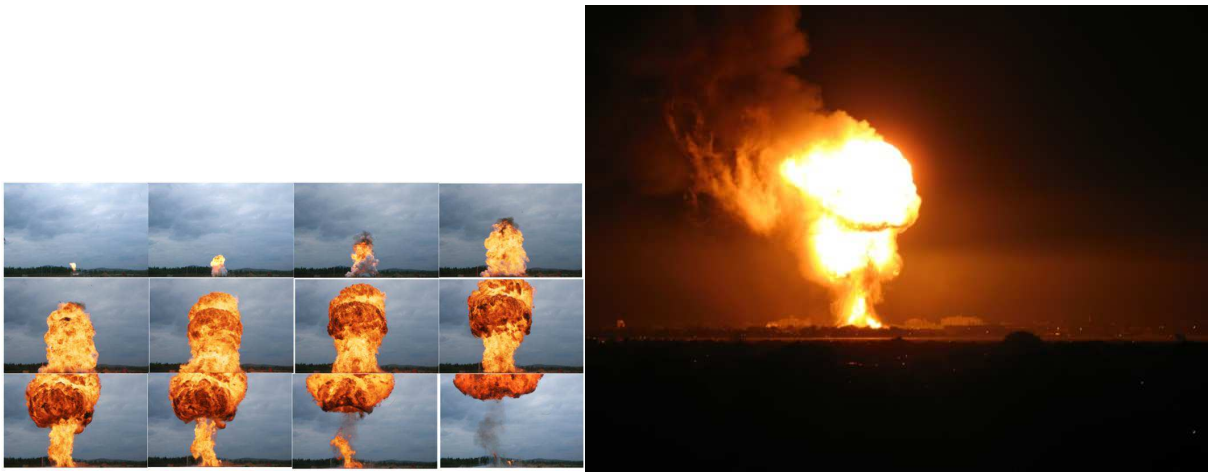

Figure 2-2 Fireballs generated by a vessel rupture containing flammable PLG (left: experimental test from Birk; right: BLEVE accident in Toronto (2008)

This work will focus on the near field overpressure hazard and its consequences. Several physical aspects of this process need to be investigated in more detail to understand the consequences of such an event.

II - Historical cases of major BLEVEs

Abbasi has listed and classified many major accidents depending on their causes and consequences (Abbasi and Abbasi, 2007). Few examples are given here to illustrate the consequences of such accident.

LPG storage farm, Feyzin, France, 1966 (Institution of Chemical Engineers, 1987)**:** Due to a handling issue while draining a 1200 m^3 propane sphere, a leakage led to the generation of a vapor cloud of 1m deep, spreading over 150m. Ignition of the cloud occurred 25min after the leakage start due to a car on an adjoining road. The flash fire came back to the sphere, igniting a pool fire that engulfed the leaking container. After 90min of water spray and firefighters' intervention, the sphere suffered a BLEVE killing 10 firemen, burning severely people up to 140m away, and triggering a domino effect on surrounding spheres due to fragments projection. In the end, 5 spheres and 2 other pressure vessels

Figure 2-3 Aerial view of the refinery after explosions, France, 1966

exploded, killing 18 people, injuring around 80 others and leading to extensive damage to the site. This is the earliest major French BLEVE accident recorded.

Figure 2-4 PEMEX LPG Terminal during the accident, Mexico 1984

PEMEX LPG Terminal, Mexico City, Mexico 1984: This accident is one of the deadliest catastrophes in the history of BLEVE, it resulted in of over 650 deaths and 6400 injuries. The accident was caused by the leakage of flammable LPG through a pipe on an industrial site receiving refinery supply, creating a vapor cloud explosion and a devastating chain reaction of BLEVEs.

Mihama Nuclear Power Reactor, Mihama, Japan 2004: A large pipe of superheated water leaked until pipe rupture. The resulting BLEVE released a strong two-phase flow that killed 11 workers nearby. This is an example of the damages a water BLEVE can lead to.

Figure 2-5 Ruptured pipe of the reactor, Japan 2004

Figure 2-6 Fireball resulting from the propane BLEVE, Toronto 2008

Sunrise Propane, Toronto, Canada 2008: the accident occurred at Sunrise, a company selling propane for commercial purposes. The investigation states that the explosion may have originated from an illegal tank-to-tank transfer. An employee of Sunrise and a firefighter died because of the accident. Consequences like closing a major highway near the explosion, evacuating the surrounding population and cleaning the damage cause by the accident caused $CAD 1.8million. Additionally, law suits led to a $5.3million fine to Sunrise.

Cosmo Oil Company, Chiba, Japan 2011 (Birk et al., 2013): as a consequence of a large magnitude earthquake, this disaster was the largest BLEVE so far, from large propane spheres with a storing capacity of 2000 to 4000m3, generating fireballs of diameters larger than 200m diameter.

Figure 2-7 Cosmo Oil refinery accident, Japan 2011 (left: Storage spheres under fire:; right: fireball resulting from a sphere BLEVE)

III - Mechanisms of failure

III-1. Substances involved in BLEVEs and main causes of failure

Historical surveys state that over 70 BLEVE events happened between 1970 and 2004, 46% of which with LPG (Liquid Petroleum Gas) (Salla et al., 2006), but many other substances have been reported (ethylene oxide for 9.5% of the cases, vinyl chloride for 8%, and sometimes water).

The main causes leading to BLEVE accidents are: train derailments, external fires, load/unloading operations. It is noted that 48% of the cases are classified as transport accidents, where the explosion is mainly due to fire (Salla et al., 2006). A vessel failure can find its origin in many causes: impact on the vessel or between 2 vessels (train derailment), fatigue due to loading/unloading cycles of the vessel, corrosion, poor weld, etc. The most common scenario of failure is a tank engulfed in fire (Table 2-1).

Table 2-1 Main causes of BLEVE (Abbasi and Abbasi, 2007)

Causes of BLEVE	% of occurrence
Fire	36
Mechanical damage	22
Overfilling	20
Runaway reactions	12
Overheating	6
Vapor space contamination	2
Mechanical failure	2

III-2. **Typical fire engulfed vessel failure**

Let us consider the most common scenario from Table 2-1, a vessel containing PLG engulfed in a pool fire (Figure 2-8 a). First, the fire heats up the liquid phase, increasing temperature of the fluid inside the vessel, and consequently the pressure inside the vessel rises. The metallic structure of the vessel is heated up as well. The temperature of the bottom part of the vessel wall remains cool due to the contact with the liquid phase, due to the strong heat transfer coefficient and heat capacity of the liquid. However, the upper part of the tank wall is in contact with the vapor phase. It is exposed to a poor heat exchange due to the low gas thermal properties, and thus heats up dramatically. The high wall temperature weakens the tank structure until its yield strength becomes lower than the hoop stress generated by increasing internal pressure. The vessel deforms until it cracks open to release the high pressure content of the vessel.

When the wall opens, the vapor phase in the vessel (first exposed to the opening in this scenario) starts expanding out, pushing the surrounding atmosphere away (Figure 2-8 b). The pressure drops suddenly in the vessel, putting the liquid phase in a superheat state until sources of instability (nucleation site such as particle in the fluid, wall roughness, etc.) trigger the boiling (Figure 2-8 c). The subsequent boiling is violent because of strong superheat. The whole content is expelled outward, and the vessel wall may be separated into several parts, and propelling some pieces away (Figure 2-8 d).

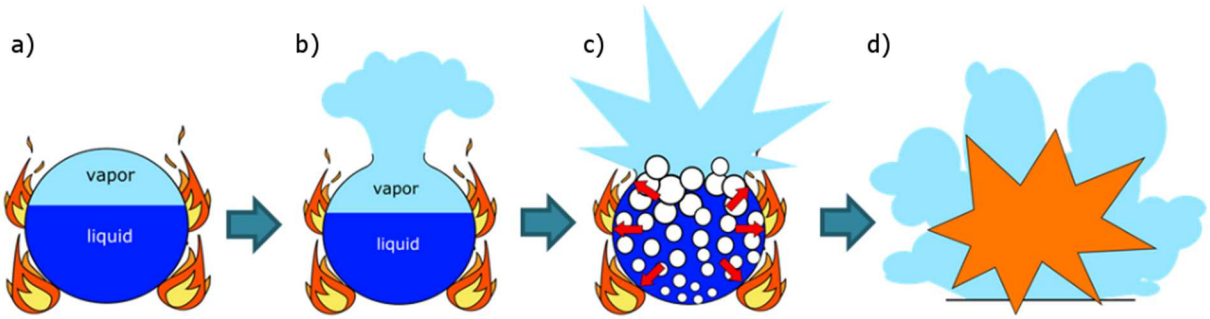

Figure 2-8 Step by step mechanism of a typical BLEVE failure

III-3. **Vessel failure patterns**

To define the rupture patterns of the vessel, one must understand how it weakened first. If the weakened area on the vessel is small, the crack initiated by the opening of the vessel will eventually stop when reaching a stronger part of the wall, leading to a partial failure. The opening will lead to a typical fish-mouth opening pattern (Figure 2-1 left), and the release from this crack will be a two-phase flow jet. This is not a BLEVE.

If the weakened area is larger, the crack may keep propagating along the tank axis until the ends of the vessel. The crack may turn and go circumferential at the ends or it may cut through the ends. A classic failure pattern observed for cylindrical vessels is the following, crack propagates to the cylinder end caps, turn radially where the welds are and end up separating the vessel into 3 pieces: the center body and 2 end caps (Figure 2-1 right; Figure 2-9). The energy of the BLEVE will usually flatten the center part and propel the end caps like missiles.

Figure 2-9 Catastrophic failure of a 1m^3 experimental propane vessel (a) vessel before explosion ; b) explosion and radial propagation of the crack through the ends; c) after explosion, vessel flat on the ground) (Birk et al., 2007)

III-4. **Summary of the potential scenarios**

One typical example of scenario has been described above. Depending on the timing of the different main events leading to a BLEVE (crack propagation, wall weakening, pressure drop and liquid boiling), various scenarios are observed. Figure 2-10 sums up some distinctive scenarios made through literature.

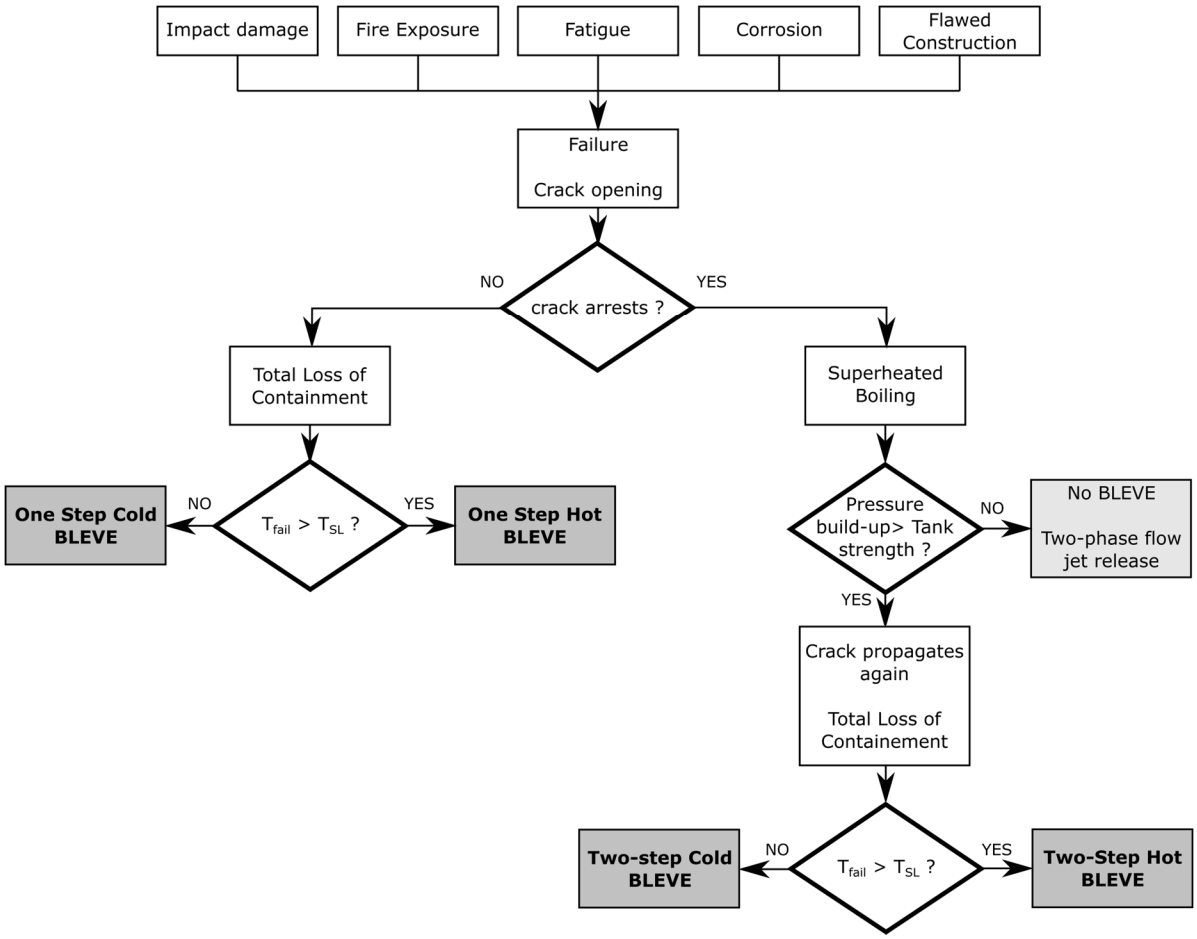

Figure 2-10 Potential failure scenarios of BLEVE

Birk et al. 2007 described the difference between one-step and two-step BLEVE that has been observed in some experiments. These patterns depend on how the crack opening propagates. If the vessel is weak enough, the crack will start and propagate through the whole length of the vessel in a few milliseconds, to then fully open the vessel. This corresponds to one-step BLEVE, the most widely observed BLEVE.

In some cases, the vessel wall is strong enough to stop the crack from propagating after it started. This leads the expansion of the vapor through the opening, and a pressure drop in the vessel. Ultimately, the

liquid phase will boil and a 2-phase flow jet release will take place through the partial opening. This can go until the vessel empties.

However sometimes the boiling is strong enough to cause internal pressure build-up that will trigger the crack to start propagating again, leading to a full BLEVE. This has been called the two-step BLEVE. The observed experimental cases lead to conclude that 2-step BLEVEs seem stronger than 1-step BLEVE. The delay between the crack stopping and propagating again can be up to 2s from experimental observation. The conditions inducing 2-step BLEVEs are an intricate balance of conditions between wall structural strength, weakening conditions, internal pressure build-up and dynamics of the opening.

Another concept presented in the literature is the distinction between hot and cold BLEVE (Birk et al., 1993). Cold BLEVE is when failure is triggered by impact or if vessel fails while liquid is cool and far from the superheat limit temperature (or T_{SL}). Hot BLEVE is when the liquid has been heated to near the T_{SL}. Hot BLEVE tend to be stronger than cold BLEVE. This leads to investigate the thermodynamic concepts behind BLEVE, superheat liquid and violent boiling.

IV - Thermodynamics of BLEVE

Understanding the thermodynamics of the fluid in the vessel helps to evaluate the power and hazards of this accident. Initial definitions of the BLEVE stated that the liquid temperature must be over the Superheat Limit Temperature, to reach homogeneous nucleation and have a BLEVE (Reid, 1979). Since that time experiments from many sources have shown that BLEVEs happen over a range of temperatures (Balke, 1999; Birk et al., 2007, 1993; Johnson and Pritchard, 1991). Superheat is the origin of the violent boiling. This requires us to define the concept of superheated liquid, together with superheat limit temperature.

IV-1. Theoretical superheat limit: homogeneous nucleation

When the vessel fails, the vapor phase expands and the pressure drops inside the vessel. A rapid pressure drop in the liquid phase will result in a non-equilibrium process. However because the pressure drop is very fast, the liquid phase enters a non-saturated equilibrium superheat state. It is a metastable state where the fluid remains liquid while crossing the saturation curve into the vapor region (from B to C Figure 2 12). Ideally, this pressure drop is possible until the fluid reaches the limit of the metastable equilibrium condition (point C Figure 2 12). This condition is defined through stability analysis and must fulfill the following to remain stable (Shamsundar and Lienhard, 1993):

$$\left(\frac{\partial \mathrm{P}}{\partial \mathrm{v}}\right)_{\mathrm{T}} < 0 \qquad (1)$$

When reaching the theoretical conditions ending the stability of the superheat liquid state (point C Figure 2-11), the fluid will start boiling through a phenomenon of homogeneous nucleation. The liquid will boil at the molecular level: the hydrogen bonds break in the body of the liquid phase. This leads to a rapid and violent phase change. The expansion work generated by this phenomenon is understood to be the destructive power of the BLEVE.

Boiling at the molecular level (i.e. homogeneous nucleation) is only possible if no other nucleation sites are available. This is certainly not the case in practical pressure vessels. Therefore achieving this theoretical BLEVE is unlikely.

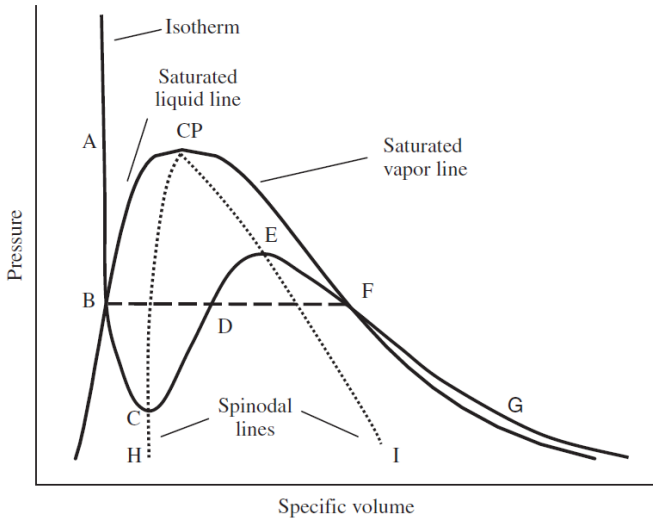

Figure 2-11 P-v diagram describing the various equilibrium state of fluid with rapid changing properties (Salla et al., 2006)

The line describing the theoretical stability limit to superheat state is called spinodal line. (CP-H for liquid and CP-I for vapor on Figure 2-11, dashed line on Figure 2-14). The vertical gap between the saturation line and the spinodal line describes the potential degree of superheat the fluid can reach when going through an ideal isothermal pressure drop. Constant temperature is a common assumption in this case, due to latency of thermal effect compared to pressure changes.

The degree of superheat is determined by this fixed superheat temperature compared to the saturation temperature for the actual liquid pressure (Figure 2-12). The Jakob number is a non-dimensional number to describe the degree of superheat of a fluid. It is defined as follow:

$$Ja = \frac{C_{p_{liq}}(T_{SE} - T_{sat})}{\Delta H_{vap}} \tag{2}$$

Where C_{pliq} is the specific heat of the liquid phase, T_{SE} is the temperature of the superheated liquid after pressure drop, T_{sat} is the saturation temperature of the superheated liquid at this same pressure, and ΔH_{vap} the latent heat of vaporization. Jakob number describes the ratio of excess heat available in the liquid due to superheat state and the heat required for vaporization phase change.

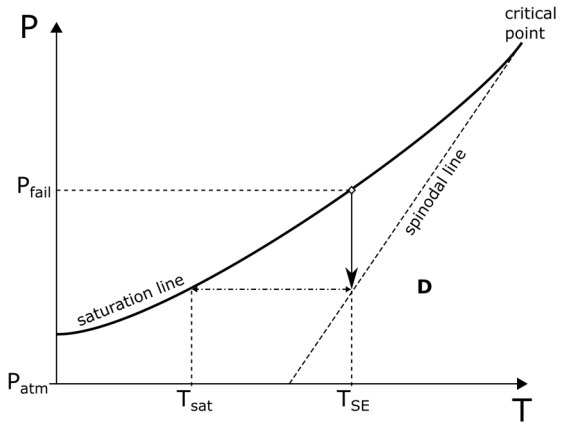

Figure 2-12 Schematic of a P-T diagram describing the saturation and superheat temperature defining the superheat degree

IV-2. **Definitions of the T_{SL}**

The superheat limit criterion brings us to the definition of the atmospheric superheat limit T_{SL}. For a PLG vessel failing in the ambient surroundings the pressure can only drop down to ambient pressure.

Early literature (Reid, 1983) states that the atmospheric superheat limit temperature corresponds to approximately 89% of the critical temperature (in Kelvin), giving 56.2°C for propane.

Then, the definition of T_{SL} was determined through equation of state of the fluid considered and the spinodal stability criterion. Some authors call it thermodynamic superheat limit temperature. However, equations of states are numerous, and their domain of validity depends on the fluid described and its conditions. Two examples of thermodynamic T_{SL} are calculated, for Van der Waals equation and Redlich-Kwong equation, giving $T_{SL-VdW} = 40.5^{o}C$ and $T_{SL-RK} = 59^{o}C$. The disparity of these results show the issue of this definition. Van der Walls equation of state shows a lack of validity for this purpose, as the spinodal line defined from this equation of state go above the saturation curve for propane (Figure 2-13).

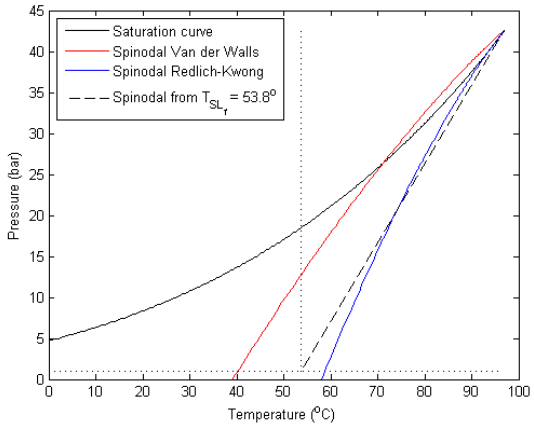

Figure 2-13 Spinodal lines on P-T diagram for propane, based on different equations of state

As a result, some recent studies offer a different approach to superheat. Salla (Salla et al., 2006) proposed a definition not based on thermodynamic stability, but on an energy balance between required vaporization energy of the flashing liquid and available heat in the remaining non-flashing liquid. Based on this method, $T_{SL-f} = 53.8^{o}C$ and corresponds to the maximum energy transfer from the cooling liquid to the vaporizing liquid, leaving the remaining unboiled liquid at the minimum amount of energy possible. The authors of this method proved that their results fit well with classical approaches. Its advantage lies in not depending on equations of state and their domain of validity, relying only the fluid properties instead. This definition is used in prediction model to quantify the energy of the expanding fluid.

Finally, Mengmeng (Mengmeng, 2013) defines a K_{SL}, or kinetic superheat limit. The K_{SL} is defined experimentally, in clean lab conditions. This quantification allows to validate the previous definition of superheat limit. Some experiments are available in the literature, trying to quantify the bubble growth rate in superheat. However, most of these experiments investigated butane superheat properties (Frost, 1988; Shepherd et al., 1982), little results are available to characterize propane experimental superheat limit.

In order to plot spinodal lines on thermodynamic plots with experimental data from this work, the spinodal defined by Redlich-Kwong is chosen for convenience, as the other methods only deliver a single T_{SL} and atmospheric pressure, and not the full spinodal line.

IV-3. Use of the T_{SL} in BLEVE theory

For all these definitions, the T_{SL} corresponds to the temperature on the liquid spinodal corresponding to atmospheric pressure (Figure 2-14). The consequence is that the superheat energy available in the phase change is maximum at the superheat limit temperature T_{SL} and atmospheric pressure. It is visible as

the largest possible drop in pressure between the saturation line and the spinodal line on the P-T diagram (Figure 2-14).

The concept of hot and cold BLEVE (Birk et al., 1993) are based on this definition of T_{SL}. An explosion below superheat limit temperature ($T_{fail} < T_{SL}$) is considered as a cold BLEVE while $T_{fail} \geq T_{SL}$ is considered a hot BLEVE. Cold BLEVEs are limited by atmospheric conditions. Hot BLEVEs are considered stronger due to higher pressure and temperature of failure, and because the liquid can theoretically reach higher degrees of superheat by dropping closer to the spinodal.

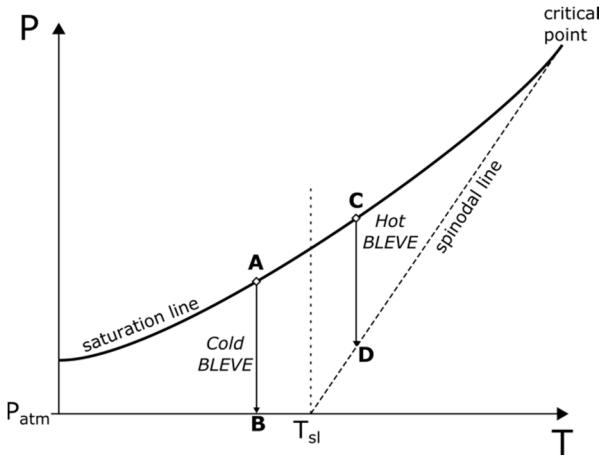

Figure 2-14 P-T diagram of a cold and a hot BLEVE

IV-4. Practical superheat unstability: heterogeneous nucleation

However, the reality of industrial cases and experiments have shown that reaching homogeneous nucleation never happens in practice. Between the saturation line and the spinodal line, the fluid is in a metastable state, waiting for a disturbance to nucleate. If none occurs, it reaches homogeneous nucleation at the theoretical superheat limit. In practical cases such as industrial vessels, wall roughness, dirt or other particles in the fluid provide nucleation site: they are sources of bubbles to grow, triggering a so-called heterogeneous nucleation. The boiling process then starts before reaching the spinodal line.

Because of this practical aspect of superheat, the early definition of BLEVE from (Reid, 1979) seems too restrictive, it considers only explosion above T_{SL} and reaching theoretical superheat. Similarly, the distinction between hot and cold BLEVE is not as sharp as believed in theory. There is no dramatic change in superheat degree in practice before and after the T_{SL}, as shown by some experimental results (Barbone, 1994) (Figure 2-15). In their experiments (in glass tubes) the boiling began before the spinodal was reached. This spreads out the time over which the phase change process occurs and reduces its power.

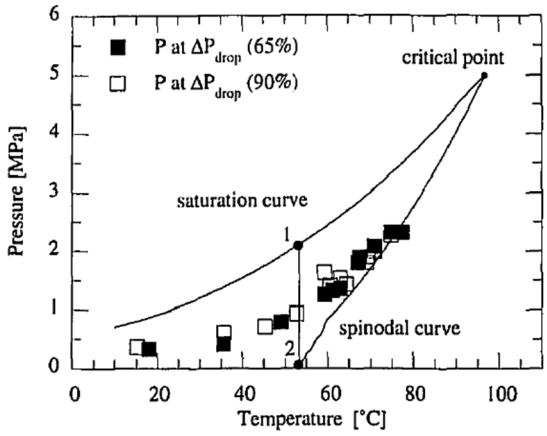

Figure 2-15 P-T diagram of experimental venting of R-22 in steel tubes with different fill level (65 % and 90%), showing the maximum superheat state reached by the liquid (Barbone, 1994)

IV-5. **Experimental studies on superheat boiling**

Experimental studies of superheated liquid boiling have been conducted to define the pressure response in vessels and cylinder.

Barbone (Barbone, 1994) studied the venting of superheated refrigerant R22 from 260mL steel tubes Teflon-coated inside and 75mL glass tubes, through the bursting of a foil diaphragm after reaching equilibrium in the tube. Refrigerant R22 is used because its thermodynamic properties are very similar to propane properties, without the flammable aspect. Pressure in the vessel was measured at the bottom and top. The study was run by varying the following parameters: vessel pressure before diaphragm burst, liquid fill fraction, vent cross section area at exit of the tube, wall surface conditions (Teflon or glass) and level of pre-nucleation. First, he shows that superheat boiling of R-22 through a limited cross section area will lead to a pressure rise after a limited drop, while a fluid not superheated like water will drop down to atmospheric pressure (Figure 2-16). The pressure drop defines the level of superheat reached by the fluid.

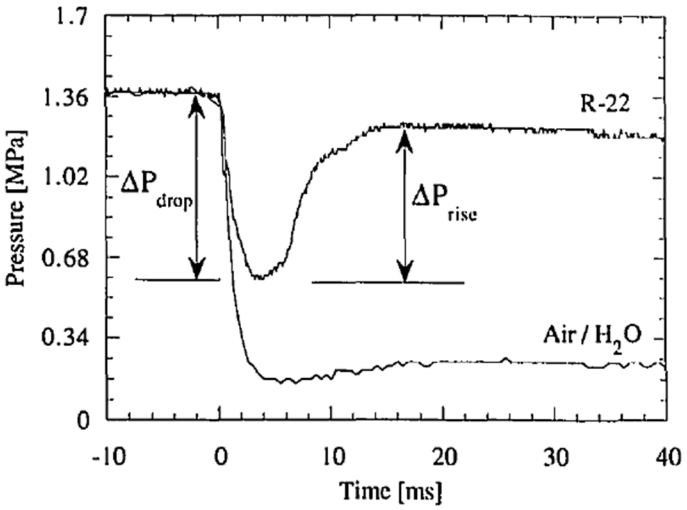

Figure 2-16 Evidence of a pressure rise due superheated venting in a tube after a limited drop

His results with the steel vessel confirm that heterogeneous nucleation starts before reaching the theoretical thermodynamic stability criterion (or spinodal) (Figure 2-15). It also shows that the pressure rise from the violent boiling is proportional to the pressure drop, and thus to the superheat degree reached by the liquid (Figure 2-17).

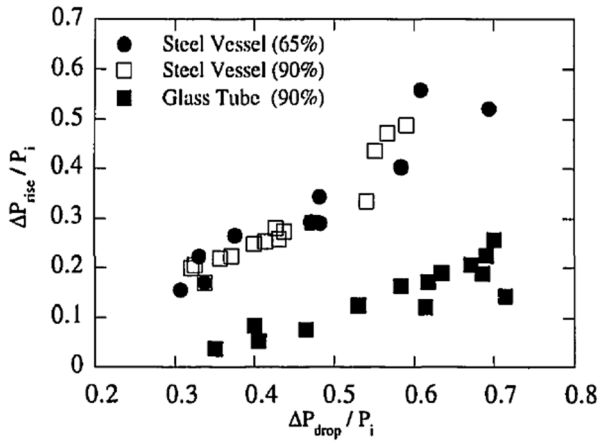

Figure 2-17 Superheat venting of R-22 test tubes (left: P-T diagram of the steel vessels, with thermodynamic state before pressure rise; right: relation between pressure rise and pressure drop) (Barbone, 1994)

Chen (Chen et al., 2008) performed a boiling experiment with water in a larger squared section tube (160mm x 160mm x 880mm – 22.5L) with a rupture disk to reach superheated state. He measured transient pressure at the bottom and top of the tube following the boiling, while recording high speed imaging of the phase change inside the cylinder. The imaging show two different regimes of boiling (Figure 2-18 left A) to a fully two-phase flow mixture (Figure 2-18 left C). The corresponding pressure

signal shows a strong pressure peak (4bar at 34ms Figure 2-18 right) when the whole fluid is fully boiling, showing experimental correlation between violent boiling and pressure wave in a contained volume.

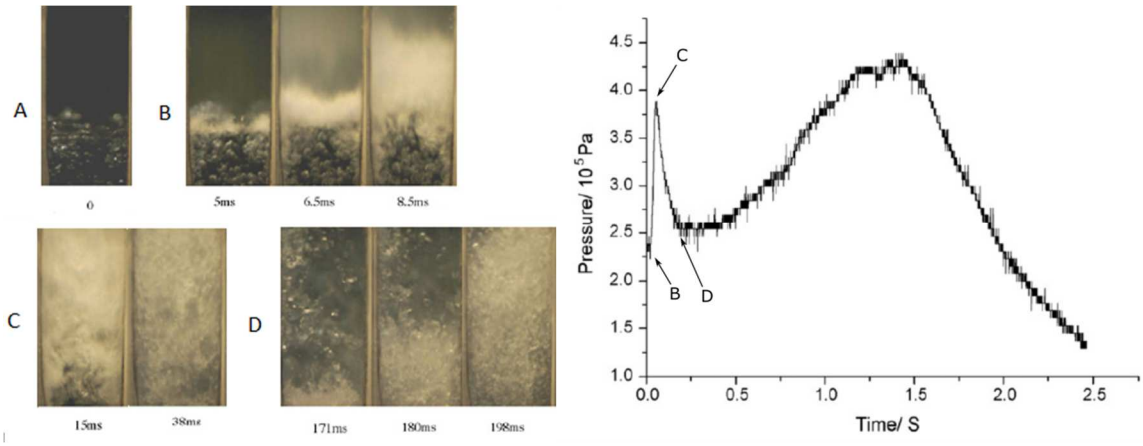

Figure 2-18 Results from experimental superheat boiling inside an open-ended cylinder (left: imaging inside the cylinder ; right: pressure signal at the top of the cylinder) (Chen et al., 2008)

Similar experiments are also conducted with CO2, with studies both inside (Ciccarelli et al., 2015) and outside the tube (Hansen, 2018). These experiments also showed that liquid boiling from superheat state add a significant increase in pressure inside the tube of restricted section. Various flow patterns, similar to Mach diamonds from a choked jet flow, are visible and simulated outside the tube.

These experiments showed interesting characteristics of the consequence of superheat. However, they are all conducted in cylinders failing at one end along the cylinder axis. Thus the opening cross section area is more restrictive than vessel failure observed in BLEVEs. This restriction leads to longer venting time, thus larger and steadier pressure rise conditions, that the dynamic opening of BLEVE make harder to observe.

V - Experimental research in BLEVE

From the statements made so far, BLEVE seems to be a complex combination of variables: external conditions acting toward vessel failure, wall vessel structure, internal pressure, superheat response of the liquid etc. Experiments have tried to isolate some of these variables (example with the superheat experiments previously discussed). In order to have a more global picture of the phenomenon, more realistic experiments of vessel failure have been conducted. From small lab tests to real size vessel explosions, an interesting range of experiments already exists to characterize and understand better the BLEVE. The variety of the scales covered by experiments in the literature covers an interesting range over critical variables such as failure pressure, vessel size, measurement distance from the vessel.

V-1. Small scale BLEVE experiments

Small scales experiments are mostly set for their convenience to set up (cheap, most likely indoor in lab conditions) as well as the potential to do many experiments, for parametric analysis and repeatability. However, dimensional analysis is needed when scaling back to real size problems.

V-1.1. Davison 2008

Experiments on commercial gas cylinders used for portable cooking as in camping. The canisters contain 440g of liquefied gas, in a proportion of 70% propane 30% butane. Some tests were performed for the potential BLEVE effects of such containers exposed to a heat source.

BLEVEs were observed in a repeatable way, and difference is made between the rupture patterns of BLEVE and hydrostatic rupture. But no overpressure data is available through these experiments.

V-1.2. Laboureur 2012

The experiments of Laboureur (Laboureur, 2012) cover supercritical failure of small scale propane vessel. Her experiments are the smallest vessels observed in literature so far, with containers of 41g (95mL) for propane experiments and around 6g (13mL) for butane, but by far burst at the strongest pressures (from 50 to 450bar). They consist of a small cartridge filled with PLG, machined notch on top and heated until failure by an electrical resistor. Overpressure data and high speed imaging is available for these experiments.

The main outcome of this work is the distinction of two regimes of supercritical failure, vapor-like or liquid-like, depending on which side of the saturation dome the rupture conditions are located. Distinctive cloud shapes are visible according to the case observed, varying from a spiky irregular cloud structure for liquid-like (Figure 2-19 left) to a smooth dome for vapor-like expansion (Figure 2-19 right).

Figure 2-19 Visualization of supercritical propane explosions (left: liquid-like expansion ; right: vapor-like expansion)(Laboureur, 2012)

Shock wave visualization has also been set up on this experiment, with a few images presenting an initial shock ahead of the cloud (Figure 2-20). The shock is captured with retro-reflective shadowgraph, with a Phantom V7.1 at 14kHz, with a 128x128 resolution. These images allow measuring the shock and cloud velocity. The order of magnitude of the velocities measured is over 400m/s for the shock and 200 to 300m/s for the cloud. These are the first experiments showing shadowgraphs of shock wave ahead of a supercritical fluid explosion. However, due to the supercritical nature of the explosion, the question of the contribution of each phase as in real BLEVE accident is unresolved.

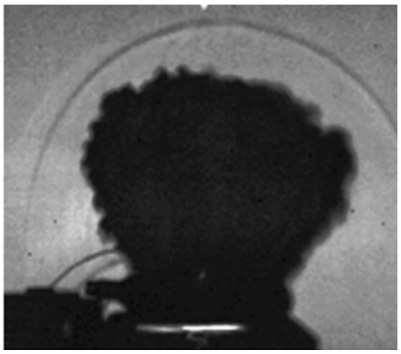

Figure 2-20 Shadowgraph of the vessel burst, capturing the shock propagation (Laboureur, 2012)

Another contribution of this work to the literature on pressure vessel burst characterization is the measurement of overpressure on top and sides of the cylindrical vessel.

V-2. **Mid-scale BLEVE experiments**

V-2.1. Giesbrecht 1981

Giesbrecht experiments (Giesbrecht et al., 1981) used small to medium scale model vessels, from 0.125kg (0.226L) to 452kg (1m3). The test fluid was propylene. The vessels were 100% full of liquid phase before controlled failure with puncture mechanism, between 40 to 70 bar. His work focused on the consequences of the flammable cloud ignition, one of his conclusions being that the shock generated by pressure expansion work is significant close to vessel but decays quickly compared to potential vapor cloud explosion hazards.

It is a significant work defining superheated liquid boiling overpressure generation from a vessel. Unfortunately, overpressure data with time from mechanical burst are not presented, thus it is hard to deduce the actual impact of liquid on shock wave generation.

V-2.2. Birk 1994 - 2007

Birk tested propane BLEVE on cylindrical vessels of 400L and 2000L with a various range of liquid propane filling (Birk et al., 2007, 2006b, 2006a, 1993; Birk and Cunningham, 1994). The failing pressures were between 20 to 26 bar, with pressure relief valves. These experiments have shown several interesting aspects of the BLEVE. A first conclusion is that the setting of pressure relief valves at 25 bar prevents a stronger build-up of pressure, but only delays the failure in the fire. Moreover, 25 bar is close to the superheat limit of propane, bringing the risk of superheat energy in the liquid to its strongest. It also emphasizes the effect of thermal stratification in the vessel, reducing the total energy in the reservoir before failure. Finally, these tests are the origin of the definition of two-step BLEVE described previously (paragraph III-4), as some have been observed through this work. Hot and Cold BLEVE also came from this work. In one test the 400L vessel was weakened by machining a groove along the top of the vessel. The vessel failed very rapidly while the liquid was still near ambient temperature. The result was a single step rapid BLEVE with very weak overpressures and no significant projectiles.

Some blast pressure traces taken in the far field were the bases of hypotheses made on the contribution of the vapor phase and the liquid phase in the overpressure. Figure 2-21 shows the overpressure trace measured 20m away from the side of a 2000L tank. It presents two first peaks separated by a negative pressure, characteristic of a vapor explosion (Kinney and Graham, 1985), and a third overpressure peak that is not really a shock. Its origin is assumed to be coming from the liquid boiling repressurization, but validation of this hypothesis is still pending.

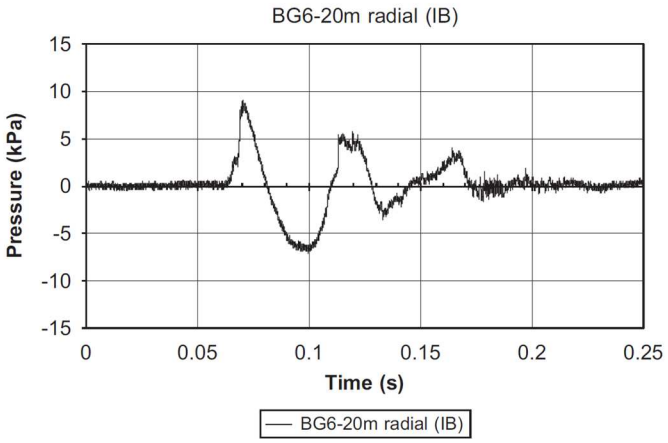

Figure 2-21 Overpressure at 20m from the side of a 2000L tank (Birk et al., 2007)

V-3. **Large scale BLEVE experiments**

V-3.1. Johnson et al. 1991

Seven BLEVE tests were performed by British Gas (Johnson and Pritchard, 1991). The tested vessels were mostly 5.6m3 filled with butane at around 80%. The failure was executed by a controlled linear shaped explosive charge on top of the vessels, after heating the containment up to 15 bar. Overpressures were measured at several distances (25, 50, and 75, 100 and 150 m).

According to the author, the overpressures measured are lower than the energy prediction model for BLEVE overpressure, which may be due to a liquid temperature at failure, being too low for homogeneous nucleation. These tests where done when it was still believed a BLEVE could only happen with the liquid temperature at the T_{SL}.

V-3.2. Balke et al. 1999

The BAM performed one large scale BLEVE test (Balke, 1999) on a 45m^3 vessel, filled with 5.1 tons of liquid propane (22% of liquid volume). This is the largest BLEVE test with blast measurements available in the literature. The vessel was engulfed in a pool fire until rupture at 25bar. Overpressures are reported at 3 distances from the vessel (100 -150 -200m).

V-3.3. RAX 201 by RPI-AAR 1975

The largest BLEVE experiment performed so far was done in a cooperative program between the Railway Progress Institute and the American Association of Railways (Manda, 1975). Two tests were performed on DOT-112A and DOT-114A railroad tank cars of 131,000L. Through those tests, the

pressure vessel was fully engulfed in fire and heated until rupture. A pressure relieve valve was present on the vessel, preventing the pressure to rise higher than 24 bar. The rupture was initiated by thermal stress on the unwetted top half of the vessel wall, leading to a failure at around 23bar with a pressure vessel approximately half full of liquid.

The main objectives of the tests were to characterize the thermal response of the pressure vessels to fire engulfment of different characteristics. These led to different test durations before failure. Unfortunately, these tests did not record any overpressure blast measurements.

V-4. **Summary of the experiments and results obtained**

Literature offers an interesting range of failure conditions at various scales. The data from Birk exposes a wide range of BLEVE at saturation from cold to hot BLEVE. The large scale data also show one cold BLEVE (Johnson and Pritchard, 1991) and one hot BLEVE (Balke, 1999). The data from Laboureur (Laboureur, 2012) is not presented on this graph due to very high burst pressure (> 100 bar), which is out of the scope of this study.

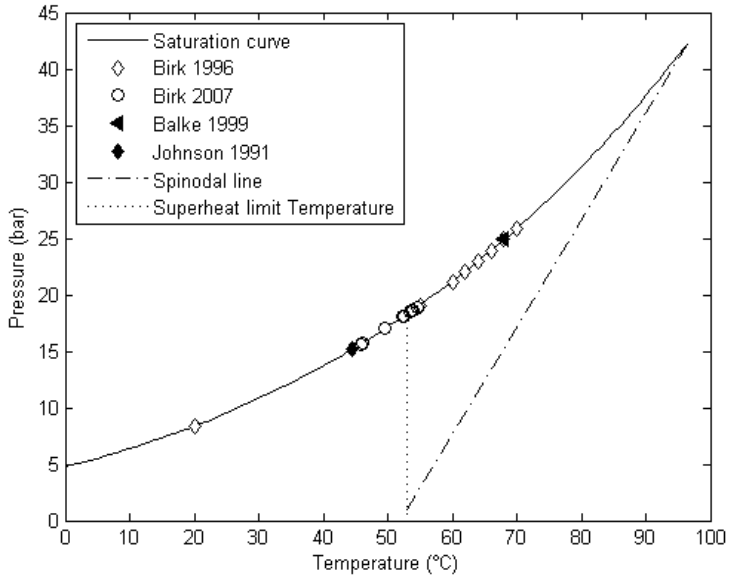

Figure 2-22 Summary of experimental BLEVE with propane on P-T diagram

Overpressure from these literature references are extracted and presented Table 2-2. Measurements are available on the sides of the vessels (radial direction) and ends of the vessel (along the axis of the vessel). The distinction is made in the table beside the distance of the measurement with the index ‘s’ and ‘e’, respectively for ‘side’ and ‘end’. They will be used in a future chapter for modeling purpose.

Table 2-2 Experimental overpressure from literature

Reference	Fluid	Tank volume (m3)	Mass (kg)	Failure pressure (bar)	Liquid filling (%)	Distance (m)	Overpressure (kPa)
Birk (1993)	Propane	0.4	145	15.0	61%	10s/10e	5.2/6.9
	Propane	0.4	121	24.5	52%	10s/10e/20s/20e	12.4/14.3/3.2/8.5
	Propane	0.4	171	21.2	66%	10s/10e/20s/20e	2.1/3.2/1.3/1.6
	Propane	0.4	100	26.8	41%	10s/10e/20s/20e	14.5/9.0/4.8/5.2
	Propane	0.4	122	21.1	51%	10s/10e/20s/20e	13.1/7.6/3.6/3.4
	Propane	0.4	99	21.7	39%	10s/10e/20s/20e	15.0/10.1/3.6/4.8
	Propane	0.4	177	23.8	68%	10s/10e/20s/20e	1.2/1.3/0.5/0.5
	Propane	0.4	145	14.9	60%	10s/10e/20s/20e	9.9/8.9/3.9/3.9
	Propane	0.4	153	20.0	68%	10s/10e/20s/20e	10.3/7.4/6.3/4.1
	Propane	0.4	165	19.5	73%	10s/10e/20s/20e	5.4/5.0/3.5/2.7
Birk (2007)	Propane	2	150	18.6	8%	10s/20s/30s/30e/40s/40e	6.7/3.5/4.2/3.1/2.7/2.1
	Propane	2	309	18.5	28%	10s/20s/30s/40s/40e	4.0/3.8/2.3/2.1/1.5
	Propane	2	116	17.0	5%	10s/20s/40s/40e	5.3/2.8/1.8/1.7
	Propane	2	184	18.9	12%	10s/40s	5.0/1.7
	Propane	2	109	15.7	5%	10s/20s/30s/40s	4.1/2.6/1.6/1.3
	Propane	2	453	18.0	46%	10s/20s/30s/30e/40s/40e	13.1/9.0/6.0/3.0/4.1/3.4
	Propane	2	475	15.6	48%	10s/20s/30s/40s	4.6/3.4/1.9/1.6
	Propane	2	470	18.1	48%	10s/20s/30s/30e/40s/40e	4.2/3.0/2.3/3.0/0.6/0.6
	Propane	2	538	18.6	57%	10s/20s/30s/40s	5.4/5.1/3.6/2.7
Balke et al (1999)	Propane	45.36	6234	25.0	22%	100s/150s/200s	2.5/1.4/1.2
Johnson (1991)	Butane	5.66	2000	14.6	73%	25s/100s/150s	6.2/1.3/1.1
	Butane	5.66	2000	15.1	73%	25s/50s/100s/150s	6.3/3.9/0.9/0.6
	Butane	5.66	1000	15.2	32%	25s/50s/100s/150s	5.0/2.8/1.2/0.8
	Butane	5.66	2000	7.7	67%	25s/50s/100s/150s	1.0/0.5/0.2/0.2
	Butane	10.77	2000	15.1	34%	25s/50s/100s/150s	8.2/3.4/1.4/0.7
	Propane	5.66	2000	15.2	75%	25s/50s/100s/150s	2.3/1.2/0.3/0.3
	Butane	5.66	2000	15.2	73%	25s/50s/100s	7.0/3.4/1.3

VI - Modeling of the overpressure hazard

VI-1. Damage analysis from explosion overpressure

Several characteristics of pressure waves have an impact on surrounding structures and casualties. A classic overpressure signal from point source high explosive is characterized by the following:

- An initial steep first peak that has a strong destructive power, due to its suddenness.
- A lasting positive pressure phase (Figure 2-24 B) that has 2 effects: the impulse of this overpressure has a longer lasting effect on structures than the sudden shock. Moreover, this phase is also characterized by a blast wind, adding a dynamic load to the target.
- A negative overpressure, triggering the opposite loading (static and dynamic) than of the previous phases (Figure 2-24 C). Depending on the source strength, volume and shape, it can be followed by a second smaller pressure peak and similar behaviors until energy of the source is dissipated. In a BLEVE the negative phase and overexpansion triggers the liquid to change phase. Thus the negative phase is certainly changed by the presence of the liquid.

Some cases in literature expose the formation of a second blast wave after the negative pressure phase. The origin of this second shock is not clear in the literature. More attention on this phenomenon is given in Chapter 3 when trying to understand the fluid mechanics behind this process.

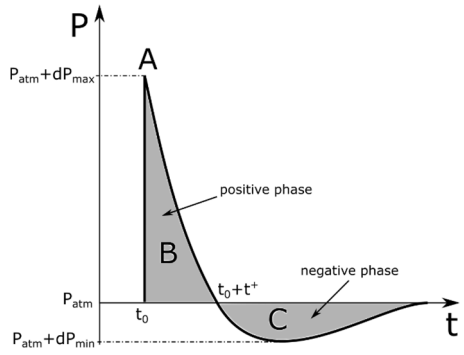

Figure 2-23 Schematic representation of the different phases of a pressure wave

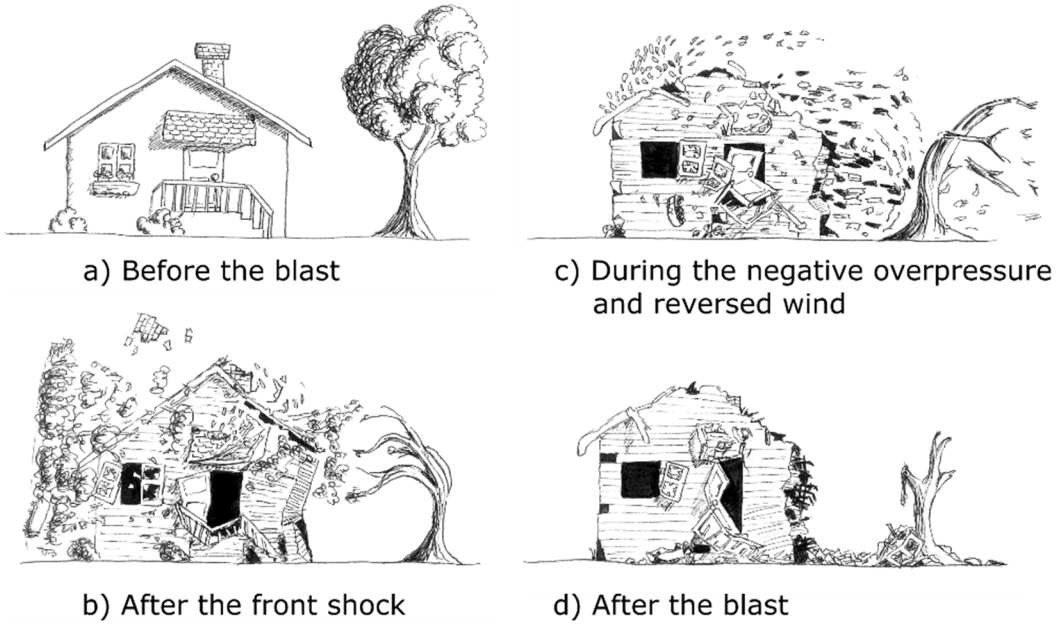

Figure 2-24 Artistic representation of the damages induced by a blast wave

Literature on BLEVE focuses mainly on characterizing the first maximum overpressure. Damage criteria are available from several institutions (example is given with the French ministry of environment Table 2-3 (INERIS, 2005)), for risk evaluation of explosion hazards and design of structures to withstand such hazards. According to this organization, the acceptable thresholds of maximum overpressure for design and risk prevention are 20 mbar if human casualty is involved and 50 mbar if considering only structural damage (excluding bursting windows). These thresholds are determined from experiments and feedback from real accidents.

Table 2-3 Overpressure thresholds from French legislation (INERIS, 2005)

Threshold (France)	**Effect on structures**	**Effect on humans**
20 mbar	Destruction of glass windows	Damage by glass projection from windows
50 mbar	Light damage to structures	Significant irreversible damage to human
140 mbar	Heavy damage to structure	Lethal damage to human
200 mbar	Initiation of domino effects	
300 mbar	Very heavy damage to structures	

These thresholds are the starting points for safety evaluation of potential accidents. However the determination of overpressure is not a straight-forward process. Experimental studies mentioned section V - give results for certain configurations. In order to evaluate overpressure generated by potential PLG storage explosion accident ahead of time, prediction models are established.

VI-2. Overpressure prediction models

A range of prediction models have been developed in the literature, based on the experiments mentioned above for validation. They can be classified in two groups: the global approach models, based on thermodynamic principles and energy consideration; and the models describing the propagation of the blast wave through the Navier-Stokes equations and Computational Fluid Dynamic (CFD).

VI-2.1. Energy-based models

VI-2.1.1 General Method

This category of models is developed based upon thermodynamic principle of energy transfer from the compressed fluid to the atmosphere. The general method for each of these models can be summed up in three steps:

Calculation of the expansion energy E*:*

The first step consists in calculating how much energy is released in the expansion from the compressed state at failure conditions to final state at ambient conditions. The calculation is based on general thermodynamic principles, each model having its hypotheses guiding how to calculate the expansion energy.

Conversion from expansion energy to scaled distance:

Scaling laws are of prime interest in blast estimation in order to predict properties of shocks and explosions at large scales based on smaller scale tests. The most used scaling is the “cubic-root” scaling law, also known as Hopkinson scaling law, from the person who formulated it (Hopkinson, 1915). The law states that “self-similar blast waves are produced at identical scaled-distance when two explosive charges of similar geometry and of the same explosive, but different in sizes, are detonated in the same atmosphere”. (Strehlow and Baker, 1976). The scaling implications are presented Figure 2-25. Based on this scaling law, scaled distance is usually applied for blast similarities in the form of $\bar{R} = \frac{R}{W^{1/3}}$ where $\bar{R}$ is the scaled distance in $\frac{m}{kg^{1/3}}$, R is the distance from the center of the explosive, and W is the total energy of the explosive. It should be noticed that the scaled distance has a dimension for this type of scaling.

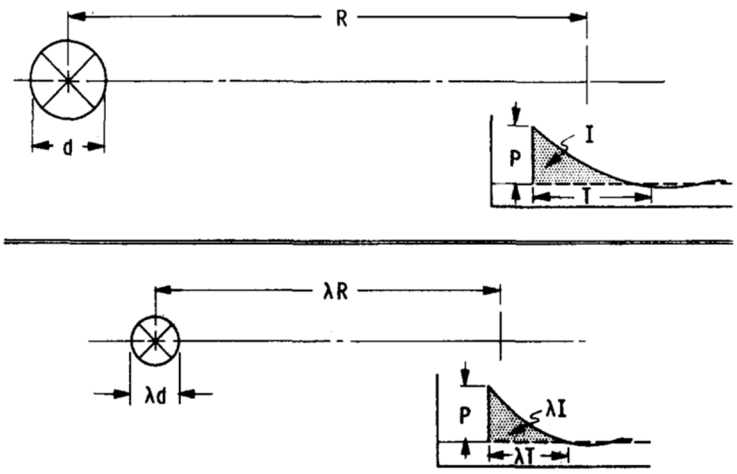

Figure 2-25 Hopkinson blast wave scaling law (Strehlow and Baker, 1976)

From the scaling law, various references exist to link scaled distance to equivalent overpressure:

- TNT equivalent mass:

$$\overline{R_{TNT}} = \frac{R}{m_{TNT}^{1/3}} \tag{3}$$

Where $\overline{R_{TNT}}$ is the TNT scaled distance, R the distance to the source m_{TNT} the TNT equivalent mass, calculated as follow:

$$m_{TNT} = \frac{E}{W_{TNT}} \tag{4}$$

Where W_{TNT} is the TNT heat of combustion ($W_{TNT} = 4680\ kJ/kg$) and E the expansion energy calculated in the first step of the method.

- Sachs scaling:

$$\overline{R_{sachs}} = R * \left(\frac{P_{atm}}{2E}\right)^{\frac{1}{3}} \tag{5}$$

Where $\overline{R_{Sachs}}$ is the scaled distance proposed by Sachs, R the distance to the source P_{atm} the atmospheric pressure and E the energy released in the explosion.

Conversion from scaled distance to overpressure:

Once the energy is converted to scaled distance, the evaluation of the overpressure is made graphically from curves available in literature (Figure 2-26). Plenty of experiments have been conducted from 1947 to 1973 with various sources (TNT, pentolite, atomic, point source, real gas, etc) to create these characteristic curves. They brought a wide variability between them, depending on the substance used and

the configuration (Baker et al., 1983). These two curves are the most commonly used nowadays when it comes to overpressure scaling of vessel burst.

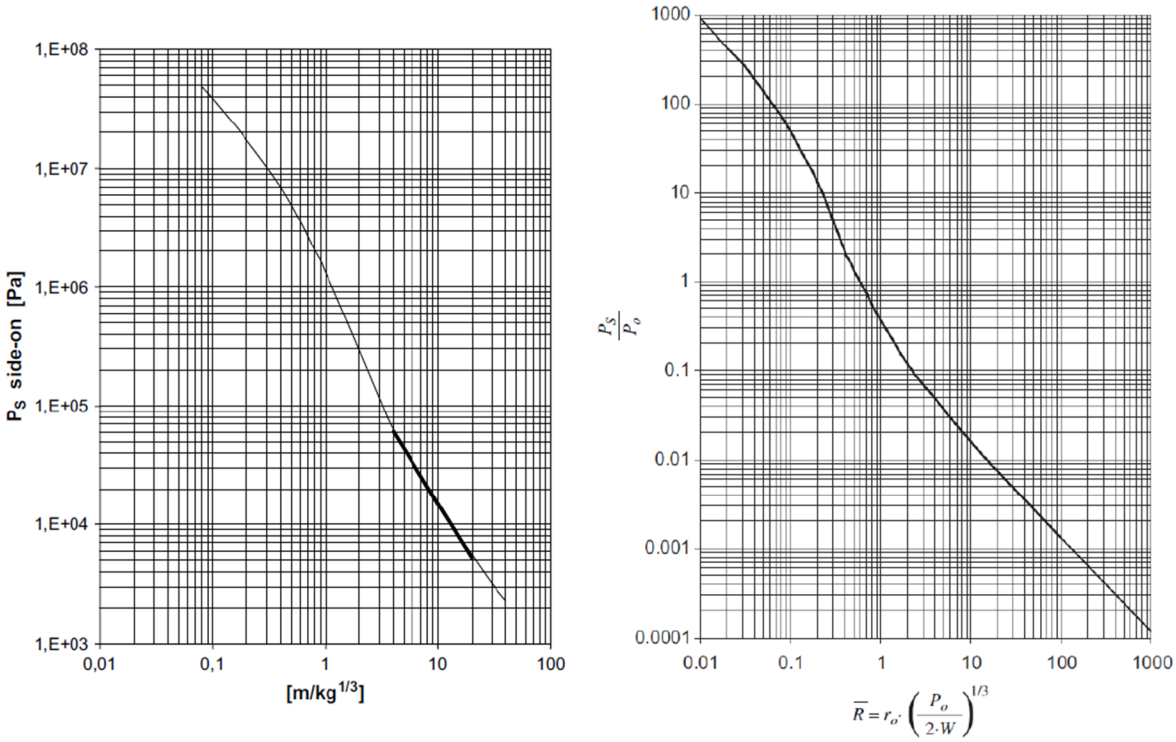

Figure 2-26 Curves of overpressure versus scaled distance (Left: TNT scaling ; Right: Sachs Scaling) (Laboureur, 2012)

The scaling choice defines which curve to use for data extrapolation. Those data were made through experimental overpressure measurements of TNT explosions. Depending on the curve used, the user ends up directly with an overpressure (P_s on Figure 2-26 left) or a dimensionless overpressure ($\frac{P_S}{P_0}$ on Figure 2-26 right, with P_0 ambient pressure near the source of explosion).

Historically, the TNT scaling is obtained from TNT explosion tests, and design to scale side-on overpressure from explosion at ground level, thus hemispherical propagation. Meanwhile the Sachs scaling is design to model spherical explosion above ground level, even at high altitudes (example: ballistic missiles), introducing the use of P_0 in the dimensioning.

To make Sachs scaling fit with ground level hemispherical blast propagation, a factor 2 is added with the expansion in the scaled distance expression. This factor is ideal and does not take into account potential friction loss or energy loss in crater formation, assuming that the ground is a perfectly reflective surface (Sachs, 1944). The results given by both models converge to a similar solution. The use of each

scaling can be considered equivalent from this statement. Because of the non-dimensional scaled distance of Sachs and the wider range of its curve, results will be presented using this scaling for this work.

Finally, these curves have been developed based on side-on overpressure measurements. This must be taken into account when considering realistic vessel measurements.

These condensed explosives are closer to instantaneous point sources than BLEVEs. This is not the same as a BLEVE that has a much lower starting pressure at the source. For this reason these curves can only be used for the far field of a BLEVE overpressure. They are not to be used in the near field.

VI-2.1.2 Expansion energy calculation

A range of models exists in the literature to estimate the expansion energy available through the explosion. Once quantified, this expansion energy will help define the scaled distance and thus, model the overpressure thanks to initial conditions of the vessel. Final condition is usually defined by equilibrium at atmospheric pressure. A few theoretical bases can be expressed before presenting the model.

i. Thermodynamic definition of expansion energy

For most models, the expansion energy will be described by the variation of internal energy from the initial compressed state to the final state at atmospheric pressure. From the first principle of thermodynamics:

$$dU + dE_c + dE_p = W + Q \tag{6}$$

where dU is the change of internal energy, dE_c the variation of kinetic energy of the fluid (usually neglected, considering initial and final state at rest), dE_p the change of potential energy of the fluid (neglected for this application), W the work done on the fluid, and Q the heat transfer to the fluid. Most of the models consider adiabatic process, because the timescale of the expansion phenomenon is usually much faster than timescales involved in heat transfer, thus $Q = 0$. From this basic assumption, the difference between models will be in their assumptions (reversible process or not) and on which part of the fluid to consider for this energy change (vapor phase, liquid phase, or both)

ii. Flash fraction

Boiling, or vaporization, requires heat input to occur. Thus, the superheat boiling of the BLEVE will continue as long as it has energy to drive the phase change. The heat is taken from the liquid phase, which means the liquid phase drops in temperature while mass is converted from a liquid to a vapor state. Based on this, the energy conservation equation can be written as:

$$M_l C_l dT = \Delta H_{vap} dM_l \quad (7)$$

where M_l is the mass of liquid (kg), C_l the specific heat of the liquid (kJ/kg/K), ΔH_{vap} the latent heat of evaporation (kJ/kg), dT the temperature drop (K) and dM_l the liquid mass that evaporates, due to evaporation (kg).

The end condition of the superheat boiling process is when the liquid reaches its boiling temperature at ambient pressure (-42ºC for propane). By integrating equation (7) from initial state to boiling temperature, one can obtain the quantity of liquid that boiled, also called flash fraction f:

$$f = \int_{T_{fail}}^{T_{boil}} \frac{dM_l}{M_l} = 1 - e^{-\frac{C_l(T_{fail} - T_{boil})}{\Delta H_{vap}}} \quad (8)$$

This flash fraction is used in some models to specify the part of the energy to consider in the modeling, or as an ending condition to the modeling.

iii. Calculation models

The expansion models available in the literature are summed up in Table 2-4. The initial available energy as well as the way it is transmitted to the atmosphere are the difference between the models. The details of the calculation process of these models are exposed Appendix A.

Table 2-4 Overpressure prediction models based expansion energy calculation

Reference	Assumptions	Energy calculation	Correction factors
(Brode, 1959)	Isentropic expansion Ideal gas Vapor only Constant volume energy addition	Pressurized gas expansion from thermodynamic first principle: $E_{Brode} = \frac{(P_{fail} - P_{atm}).V_v}{\gamma_1 - 1}$	
(Prugh, 1991)	Isentropic expansion Ideal gas	Expansion from the vapor volume and flash fraction from the liquid phase: $E_{Prugh} = \left(\frac{P_{fail}.V^*}{\gamma - 1}\right)\left(1 - \frac{P_{atm}}{P_{fail}}\right)^{\frac{\gamma-1}{\gamma}}$	
(Planas-Cuchi et al., 2004)	Adiabatic irreversible expansion Real gas	Similar calculation than (Prugh, 1991), with less ideal hypotheses: $E_{planas} = \beta * \Delta U$ $with\ \Delta U = -P_0 \Delta V$ (graphical or analytical solving available in appendix or in the paper)	Fraction of energy remaining from losses in ductile mechanical rupture of the vessel: $\beta = 0.4$
(Casal and Salla, 2006)	Isentropic expansion OR Adiabatic irreversible expansion	Calculation of superheat energy based on energy-based superheat limit (Salla et al., 2006): $E_{casal} = \beta * m_l * SE$ With $SE = h_l(T_{fail}) - h_l(T_0)$	Fraction of superheat energy contributing to the overpressure generation based on maximum from experimental fit $\beta = 0.14$ (isentropic hypothesis) $\beta = 0.07$ (adiabatic irreversible hypothesis)
(Genova et al., 2008)	Adiabatic process	Calculation of excess heat available in the superheated liquid: $E_{Genova} = \chi.m_l.C_p(T_{fail} - T_{boil})$ With $C_p = \frac{C_p(T_{fail}) + C_p(T_{boil})}{2}$	From experimental data fit: $\chi = 0.07$

(TNO, 1997)	Isentropic expansion	Variation of internal energy from table data: $E_{TNO} = m_l \left(u_{l\,fail} - u_{l\,atm}\right) + m_v(u_{v\,fail} - u_{v\,atm})$	$\overline{R_{sach}} < 2$: near-field
(Birk et al., 2007)	Isentropic expansion	Similar to (TNO, 1997) but with vapor only: $E_{birk} = m_v(u_{v\,fail} - u_{v\,atm})$	

In addition to these energy calculations, a couple of empirical factors are set by (CCPS - American Institute of Chemical Engineers, 1994) to characterize some conditions of isotropy of the flow, depending on the model assumptions:

Ground Effect[1]	Multiply energy by 2 for all $\bar{R}$
Ground Reflection[2]	Multiply overpressure by 1.1 for $\bar{R} > 1$
Cylindrical Tank[3]	Multiply overpressure by 1.6 (for $1.6 < \bar{R} < 3.5$) Multiply overpressure by 1.4 (for $\bar{R} > 3.5$)
1: hemispherical propagation: already taken into account in the scaling of $\overline{R_{sach}}$ and $\overline{R_{Hop}}$ *2:Mach stem overpressure* *3: anisotropy effect*	

These factors correct the assumption of point source explosions implied in the TNT approach. This bring a first argument in defining the near-field. The near-field in term of isotropy of the pressure field can be defined as the limit between spherical pressure field (far-field) and anisotropic pressure field (near-field). However beside the factors mentioned above, little data is available to characterize the limit of the near-field.

The model from TNO (1997) states that the TNT curve is not valid for BLEVE overpressure prediction below $\bar{R} < 2$, setting a value for a near-field in term of modeling. This value is dependent on the way the expansion energy is calculated, but gives another definition for near-field.

VI-2.1.3 Error calculation for model comparison

In order to get a sense of how models compare to each other, some error calculation tools were investigated for this work. The purpose of these models is to predict reality. Reality means feedback from accidents. In this work, “reality” was experimental results, with the error they induce. There is thus a combination of errors between the experiment and the model trying to predict it. In order to have a good prediction, we need an accurate modeling with respect to experiments, meaning:

- True: the prediction is the correct value compared with experiments. To gage this characteristic, systematic error is calculated;
- Precise: the dispersion of the values predicted compared to experimental values is small. Random error calculation allow to gage this characteristic of a model. The random error usually comes experimental data.

Figure 2-27 represents schematic parity plots of models with (a) high precision but poor trueness, (b) poor precision but high trueness, (c) poor precision and trueness, (d) high precision and trueness.

To gage these characteristics, two types of error are investigated in this work (Chang and Hanna, 2004):

- Fractional Bias (FB):

$$FB = 2\frac{\overline{X_{expe} - X_{model}}}{\overline{X_{expe}} * \overline{X_{model}}} \tag{9}$$

This value quantifies the systematic error. The FB of a true prediction tends toward zero. A negative FB describes an over-predicting model, while a positive FB means the model is under-predicting.

- Normalized Mean Square Error (NMSE):

$$NMSE = \frac{\overline{\left(X_{expe} - X_{model}\right)^2}}{\overline{X_{expe}} * \overline{X_{model}}} \tag{10}$$

This value calculates the total error between model and experiments, meaning a composition of systematic error and random error. The NMSE of an accurate prediction tends toward 0, considering the ideal case that the experiments are perfect.

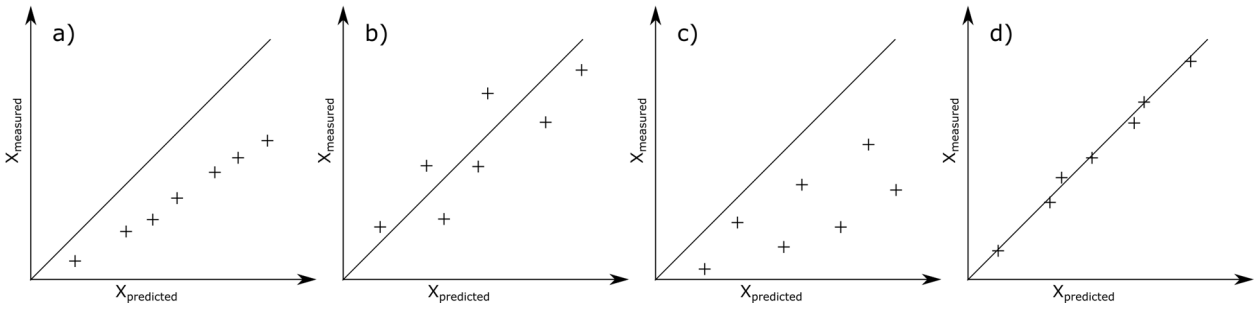

Figure 2-27 Schematic of the different types of errors: a) high systematic error; b) high random error ; c) high systematic and random error ; d) low systematic and random error (inspired from (Asch, 2010)*)*

These two factors were used to compare existing and new models to the experimental data this work proposed. The interpretation of model accuracy should not rely solely on one of these values, but on the combination of them and critical thinking toward the equations involved in the models compared to the physics observed in experiments.

In the case of BLEVE overpressure prediction, reducing the error is important for an accurate modeling of the blast. But safety applications require conservative predictions, which is not fully quantify by these factors. It is another criterion of validity used in this work.

VI-2.1.4 Comparison of models with experimental data in the literature

A comparison between previously presented overpressure from literature (medium scale Birk experiments and large scale experiments) is made through different sources in the literature (Hemmatian, 2016; Laboureur et al., 2014). In conclusion to these comparative analysis, two types of models seem to arise from the ones mentioned above:

- The conservative models, leading to a larger error but safer approach (examples are Brode and Prugh models)
- More accurate models (smaller error between model and experiment), with potential underprediction for some experimental cases (examples are the irreversible models from Planas and Casal)

One must understand the purpose of modeling before choosing one or the other. A balance between safety factor and financial costs of prevention measures generally guides this choice.

From these references, models from Genova and Casal are the most accurate in term of error calculation. However it is noticed that all of them used correction coefficients calculated by fitting the experimental data available to the model. Thus the agreement with experiments is good because the construction of the models, not the physics involved. These models do not really predict, but reflect the experiments they were fitted with.

The question of the contribution from different phase (liquid and vapor) on shock generation brings another distinction between available models:

- models considering only vapor in the expansion energy calculation (Brode, Birk);
- models considering a fraction of liquid as expansion energy (all others).

Some references state that the lead shock is only generated by the vapor phase (Baker et al., 1983; Birk et al., 2007; Laboureur et al., 2015). This question is a source of division in the BLEVE modeling. This work tries to verify this assumption and bring light on the validity of the concepts used by these various models.

VI-2.2. Phase change modeling with use of CFD

Phase change models are available in the literature to describe a more detailed view of the BLEVE phenomenon. They are solved through CFD because they describe the flow into more details. CFD

computational cost makes it more challenging to implement and test, particularly for complex geometries such as a vessel opening at failure. They are however interesting in the insight they bring.

Van den Berg (2004-2008)

Van den Berg presents a model to calculate the blast generated by the evaporation of the superheated liquid (van den Berg et al., 2004). The source of this blast is the evaporation rate of the liquid dM_l/M_l determined through the energy balance described equation (7). The model is expansion limited. It assumes the phase change is not the limiting factor. The gas dynamic of the surrounding is, and will give the evaporation rate.

The author takes conservative assumptions concerning the evaporation rate:

- The intrinsic evaporation of the liquid occurs infinitely fast. This means the source strength of the blast is guided only by the liquid boiling rate and the gas dynamic inertia.
- The liquid release rate is also infinitely fast. This corresponds to a vessel failing instantaneously and releasing all the liquid at once.

With these two assumptions, the evaporation rate is limited by the gas dynamic of the vapor expanding and pushing the surrounding atmosphere away. This model is called expansion-controlled evaporation. The gas dynamic itself is governed by the Euler equations, for compressible inviscid perfect gas, with the vapor pressure of the superheated liquid set as a pressure inlet boundary condition on the surface of the source. This vapor pressure coupled with the gas dynamic equations determine the mass flow rate from the source and the consequent blast. By conservation, this mass flow is then regulated into a liquid mass loss and temperature loss, updating the vapor pressure of the superheated liquid, until reaching equilibrium boiling conditions.

Based on this model, 3 types of 1 dimensional meshes are treated:

- Hemispherical mesh to model a BLEVE in free space at ground surface
- Cylindrical mesh to model a BLEVE between two parallel rigid planes
- Planar mesh to model a BLEVE in a tube or tunnel

Van den Berg presents blasts charts for the most common pressure liquefied gas present in industrial cases and scenarios of BLEVE, such as ammonia, butane, CO_2 and propane (Van den Berg, 2008).

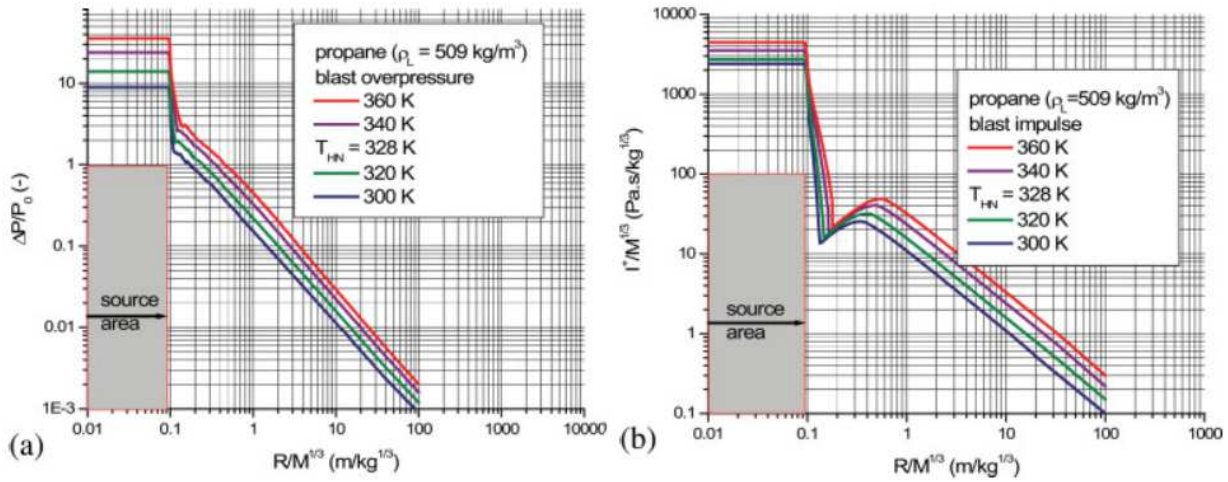

Figure 2-28 Blast chart for propane liquid explosion from Van den Berg simulation work (Van den Berg, 2008)

Finally, the use of an acoustic volume source model emphasizes the impact of the second hypothesis of instant liquid release, by showing how dramatically the overpressure drops if liquid is released over a defined span of time. This is an interesting argument when considering real liquid boiling, for example, in non-ideal case, will the liquid boil fast enough to generate overpressure and a shock?

Pinhasi (2007)

Pinhasi (Pinhasi et al., 2007) proposes a 1D CFD model of the expansion process of the BLEVE. The vapor expansion is modeled with isentropic compressible flow equations, except for the shock wave treated separately. The liquid boiling is governed by three different stages, distinguished by the void fraction in each stage, governed by the surface area of transfer from liquid to vapor, considering bubble growth or droplet size.

The author validates his work of water BLEVE simulation with energy models presented before, reversible expansion (Prugh, 1991) and irreversible expansion (Planas-Cuchi et al., 2004), stating that reversible model overestimates the numerical results, while irreversible model is more accurate in the prediction. Finally, the author shows that weak initial conditions ($\frac{T_0}{T_c} = 0.70$ where T_0 is initial temperature and T_c is critical temperature) lead to pressure build-up from the boiling, but not sufficient to generate a shock wave. At stronger initial conditions $\left(\frac{T_0}{T_c} = 0.95\right)$, the build-up becomes powerful enough to form a shock from the liquid boiling only. The ability for liquid boiling to generate a shock depends on the degree of superheat reached for with this numerical model. However simulations were performed with

a fully liquid initial pressurized chamber, thus ignoring the time a vapor piston would add to the expansion process.

Hansen et al. (2016)

A CFD approach of the BLEVE blast is made based on this principle of liquid energy converted before expansion to compressed vapor. Hansen et al.(Hansen and Kjellander, 2016) computed 3D vessels based on experiments in the literature. The initial state considers the compressed vapor phase with the energy of the compressed vapor, added to a flash fraction equivalent energy of the liquid boiling. The choice of the flash fraction is empirical, based on experimental curve fit of the overpressures, bringing similar physics as the one approached in isentropic flash fraction expansion (Prugh, 1991).

Yakush (2016)

Yakush (Yakush, 2016) generated another numerical model, based on ideal gas for the vapor phase modeling and equilibrium boiling for the liquid evaporation. The purpose of this study is to show what overpressure is generated due to an equilibrium boiling wave, and if the boiling is fast enough to generate a shock. A comparison of the CFD work with TNT model prediction show that BLEVE overpressure from propane explosions tend to be lower than prediction from TNT-curve, thus high explosive overpressures (Figure 2-29).

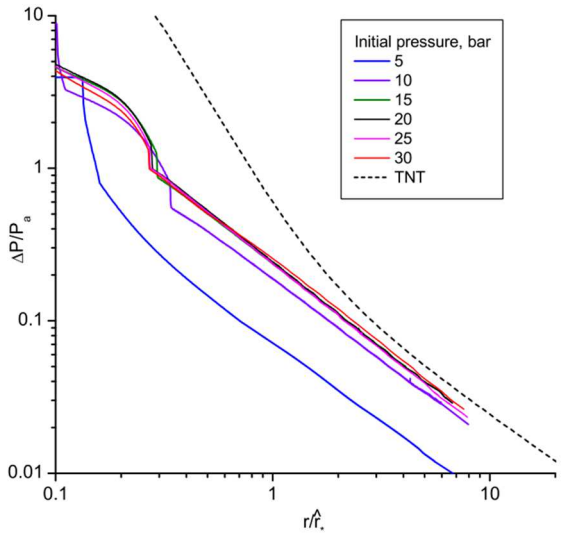

Figure 2-29 Scaled overpressure-distance curves for liquefied propane explosion from CFD, in comparison with TNT curve (Yakush, 2016)

VII - Conclusion

The purpose of this chapter was to introduce to the phenomenon of BLEVE, exposing the different scenarios of failure, the physical phenomena involved in the explosion and the hazards generated by such an event. The focus is on overpressure hazard; due to lack of information on how such an event would impact urban congested areas and urban structures such as tunnels and bridges. Moreover, emergency responders are often located in the vicinity of vessels when working on fire hazard mitigation before BLEVEs occur.

A range of experimental data is available, from small to large scale, recording overpressure at various distances from vessels. However, little data is available on what happens near the vessel when exploding in terms of overpressure and imaging. It would help understanding the effect of the opening dynamic on the pressure field.

Literature also shows a wide range of studies and models proposed to predict overpressure of the BLEVE. Most of them are can predict BLEVE overpressure far from the source, based on energetic approach and high explosive charts. However, little of them give conclusive results in the near-field, due to the complex physics involved. A model has been initiated to take into account the dynamics of opening of the vessel and the shock generation, but lacks experimental data to validate. Research on BLEVE is lacking understanding on what happens in the near-field of a PLG vessel rupture.

The current problem is: how to characterize and model the BLEVE overpressure effects in the near-field? Several questions are proposed to help decompose this problem:

- What is the contribution of each phase (liquid and vapor) in the overpressure generation?
- How the overpressure is initially generated regarding the opening dynamic of a pressure vessel?
- Can CFD help modeling the near field blast from a BLEVE, with accessible engineering CFD code such as ANSYS FLUENT?

The present work will introduce a new experimental apparatus to produce small scale BLEVEs failing along realistic failure patterns, adding overpressure, imaging and load data to the existing data available on BLEVE characterization. Analysis of the results obtained, combined with CFD, will help understand the physics of the BLEVE in the near-field and its consequence on direct surrounding structures. A model based on fluid conservation equations will be presented as a non-energetic approach to the BLEVE

overpressure prediction. Finally, data on load generated downward by the BLEVE is analysed to bring a first model of this hazard.

Chapter 3

Compressible flow theory and key variables

Understanding the physics of the explosion involves a better understanding of the fluid behavior. The aim of this chapter is to present the key equations and concepts from compressible flow theory useful for this study.

I - Euler equations of gas dynamics

To approach the various problems of compressible flow needed to understand the BLEVE problem such as the shock tube, critical flow through converging-diverging nozzle, a range of simplifying hypotheses is commonly used. In the scope of this work, it will be assumed that the flow is non-viscous, is one dimensional and can be considered as a perfect gas. This leads to the 1D Euler equations (White, 2008)

$$\frac{\partial}{\partial t}\begin{pmatrix}\rho\\ \rho u\\ E\end{pmatrix}+\frac{\partial}{\partial x}\begin{pmatrix}\rho u\\ \rho u^2+p\\ (E+p)u\end{pmatrix}=0 \tag{11}$$

with E being the total energy of the gas:

$$E=\frac{p}{\gamma-1}+\frac{\rho}{2}u^2 \tag{12}$$

The perfect gas assumption is usually used in classic compressible flow problems, leading to the following equation of state

$$p=\rho RT \tag{13}$$

The validity of these hypotheses will be discussed when examining the more complex problem of BLEVE phenomena.

II - Isentropic flows

An isentropic process is one with no heat transfer and no irreversibilities. When a compressed gas is expanded with no heat transfer and no losses (no shocks) then that is called an isentropic process. A liquid can also undergo an isentropic expansion process including phase change.

The process equation for isentropic process with an ideal gas is:

$$\frac{P}{\rho^{\gamma}} = constant \tag{14}$$

III - Normal shock

III-1. Shock formation

A shock is a strong pressure wave, characterized by the fact that it induces a discontinuity in the flow properties. A controlled way to generate a shock is by pushing a piston regularly, creating a succession of compression waves. Each successive compression wave propagates upstream in a medium that becomes more compressed with each push, thus temperature and speed of sound are higher (Figure 3-1 left). The upstream compression waves catch up to each other, coalesce and generate a pressure wave strong and steep enough to be considered as a shock (Figure 3-1 right).

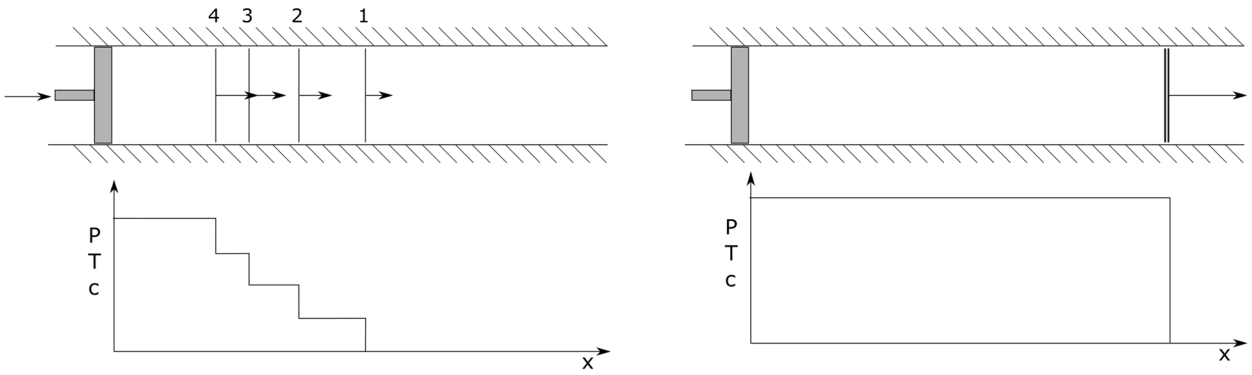

Figure 3-1 Schematic of the shock formation process by piston effect

Examples of shockwaves in everyday life are the ones generated by planes at supersonic speed, creating a loud noise when flying above us.

The Mach number is an essential non-dimensional number when discussing compressible flow and shocks. This is the ratio of the velocity of the flow element considered (object in the flow, pressure wave such as shocks, or the flow velocity itself) over the speed of sound of the flow considered.

$$M = \frac{u}{c} \tag{15}$$

If the Mach number is less than one, the flow is subsonic, meaning the acoustic pressure information travels faster than the flow itself. If Mach number is greater than 1, the flow is supersonic. The flow travels faster than the pressure information, creating discontinuities such as a shock wave.

III-2. **Stationary shock**

The jump of the flow properties through a shock can be predicted using the conservation equations of classic fluid mechanics, mass, momentum and energy conservation:

$$\rho_1 u_1 = \rho_2 u_2 \tag{16}$$

$$P_1 + \rho_1 u_1^2 = \rho_2 u_2^2 \tag{17}$$

$$\frac{1}{2C_p} u_1^2 + T_1 = \frac{1}{2C_p} u_2^2 + T_2 \tag{18}$$

The subscript 1 refers to the supersonic side of the shock, while the subscript 2 refers to the subsonic side of the shock. By knowing the conditions of the flow upstream of the stationary shock, one can easily find the flow properties downstream. It must be mentioned that a shock can only be a compression shock. An expansion shock would violate the second law of thermodynamics, making it not physically possible. Through a compression normal steady shock, the flow moves from supersonic to subsonic.

Rankine-Hugoniot equations are used to relate both sides of the shock properties with the shock Mach number (Hirsch, 2007):

$$\frac{p_2}{p_1} = \frac{2\gamma}{\gamma + 1} M_1^2 - \frac{\gamma - 1}{\gamma + 1} \tag{19}$$

$$\frac{\rho_2}{\rho_1} = \frac{2}{\gamma + 1} M_1^2 - \frac{\gamma - 1}{\gamma + 1} \tag{20}$$

$$u_2 = \frac{2}{\gamma + 1} \left(M_1 - \frac{1}{M_1} \right) \tag{21}$$

III-3. **Moving shock**

The energy equation (18) used above is valid when considering a steady shock because it is gaging the conservation of stagnation properties. To calculate moving shock properties, one must change from steady reference frame (where the shock is moving Figure 3-2 a) to a reference frame moving with the shock (where the shock is steady Figure 3-2 b). The resulting flow velocities can used in the energy equation.

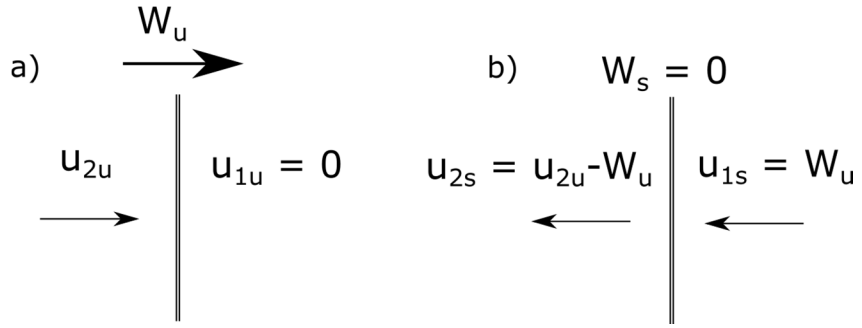

Figure 3-2 Shock and flow velocity depending on the reference frame (a) Steady frame, unsteady shock of velocity V_u, analog to traveling blast wave; b) Moving frame, steady shock)

III-3.1. Moving shock model applied to BLEVE

A moving shock model adapted to vessel explosion is expressed based on conservation equation of compressible flow and isentropic expansion theory (Laboureur et al., 2015). This model describes the formation of a shock due to the cloud expansion from the vessel. It involves several steps in order to calculate the pressure evolution:

- State 0: rest state, at failure conditions in the vessel. Velocity of the flow is assumed negligible.
- State 1: Propane vapor isentropically expanded from state 0 to 1. Its work on the surrounding is defined by conservation of stagnation enthalpy.

$$\frac{u_1^2}{2} = h_0 - h_1 \tag{22}$$

- State 2: ideal air is compressed from the edge of the propane cloud at state 1 to the initiation of the shock at state 2. Euler equations are used here.
- State 3: The jump in pressure through a normal moving shock is defined by assuming $P_3 = P_{atm}$.

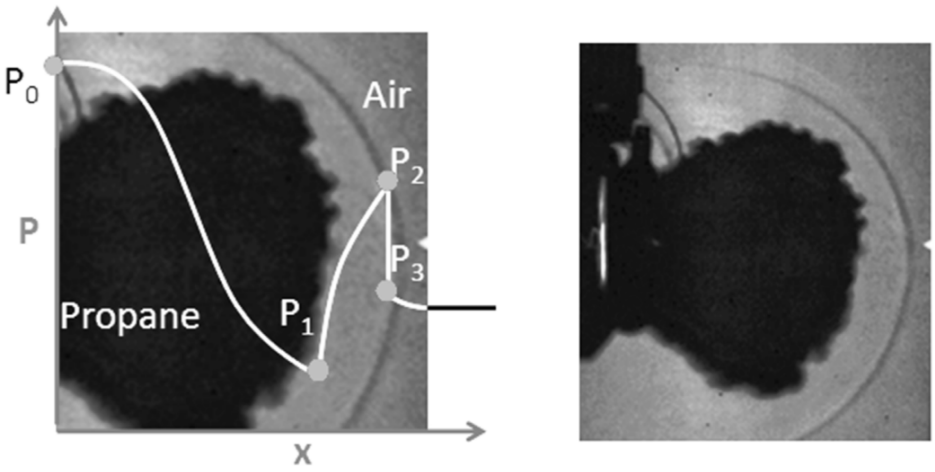

Figure 3-3 Pressure evolution hypothesis and moving shock, observed by Laboureur (Laboureur et al., 2015)

IV - **Shock tube**

A shock tube is a tube composed of a high pressure chamber (driver section) and a low pressure chamber (driven section, usually at atmospheric pressure) separated by a membrane (or diaphragm) (Figure 3-4). The chambers may each contain the same gas or different gases. The main purpose of the device is to burst the membrane and observe the normal shock generation and propagation in the driven section. It is a well-known and widely used instrument to study characteristics of compressible flows and shock propagation. Thus, the flow can be described with one-dimensional non-viscous conservation equations. The shock tube is also a commonly used to test the robustness and ability of CFD numerical solvers to describe highly compressible flows.

Figure 3-4 Shock tube apparatus available in the laboratory of ISR

IV-1. Shock tube wave structures

At initial time $t = 0$, the rupture disk bursts, leading to a discontinuity in the flow properties (Figure 3-5). Due to the pressure difference, the high pressure gas will propagate in the low pressure side 1. The propagation of the high pressure gas works like a piston and generates a shock wave. This shock travels at the speed W. It is generated by the high pressure gas set in motion behind it. A series of rarefaction waves propagates in the opposite direction through the high pressure chamber. Unlike compression shock, rarefaction waves spread away from each other throughout their propagation, leading to a continuous range of pressure waves in the fluid. At the time scales considered in pressure wave propagation in the shock tube, diffusion is neglected, thus the two gases do not mix. The contact discontinuity travels with the fluid at a velocity $u_c = u_2$ (Figure 3-6).

At this stage, different zones appear in the shock tube:

1. Driven section: Not yet reached by the shock wave, the gas has the properties of the initial driven section (low pressure and no velocity).

2. Region of the initial driven section affected by the shock passing through it. The gas is driven at a velocity u_2 to the right of the tube shown Figure 3-5. The pressure rises through the compression shock, as does the density and the temperature.

3. Expanded part of the driver section: between the rarefaction waves traveling left to the driver section and the contact surface (initially rupture disk) traveling right at velocity u_2, this section is similar in pressure and velocity to section 2, but has a different gas, density and temperature.

4. Driver section: Not yet affected by the rarefaction waves, this section has the properties of the initial driver section, that is high pressure and no velocity.

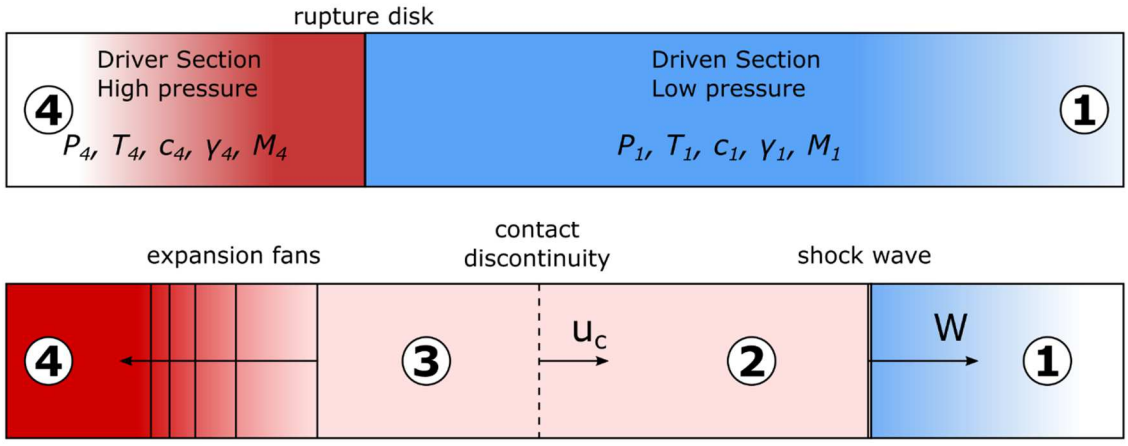

Figure 3-5 Shock tube wave structure (top: before membrane rupture, bottom: after membrane rupture)

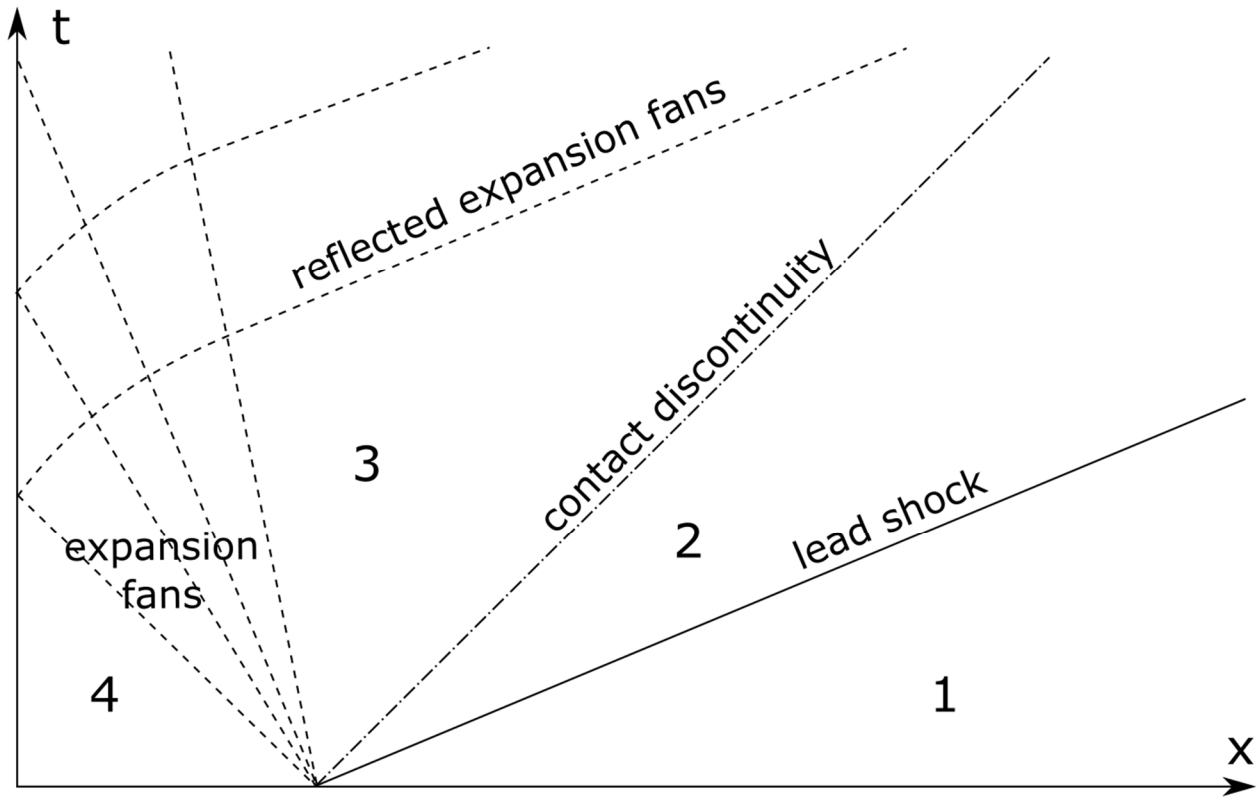

Figure 3-6 x-t characteristics plot of wave structures emerging from a shock tube

IV-2. **Analytical solution**

The shock tube device permits the study of a classic compressible flow problem. Conservation equations applied to the three shock tube interfaces allow solution of the problem and the prediction of the flow variables in the four sections of the tube. From the compressible flow equations noted earlier, the shock tube problem can be solved.

Between section 1 and section 2, the Rankine-Hugoniot equations applied to the moving shock are applied.

The contact interface between section 2 and section 3 is a separation of gases, such as a virtual wall moving at the flow velocity. Thus:

$$u_{3u} = u_{2u} \tag{23}$$

$$P_3 = P_2 \tag{24}$$

Finally, flow states in section 3 and section 4 are separated by continuous isentropic expansion fans,

$$u_3 + \frac{2}{\gamma_4 - 1} c_3 = u_4 + \frac{2}{\gamma_4 - 1} c_4 \tag{25}$$

After working through the equations, one ends up with a relation between the initial conditions of the shock tube $\frac{p_4}{p1}$ and $\frac{c_4}{c_1}$ and the Mach number M_1 of the shock expanding through the driven gas. More detailed information on shock waves may be found in (Bauer et al., 2015).

$$\frac{p_4}{p_1} = \frac{2\gamma_1 M_1^2 - (\gamma_1 - 1)}{\gamma_1 + 1} \frac{1}{\left(1 - \frac{\gamma_4 - 1}{\gamma_1 + 1}\frac{c_1}{c_4}\left(M_1 - \frac{1}{M_1}\right)\right)^{\frac{2\gamma_4}{\gamma_4 - 1}}} \tag{26}$$

The contact discontinuity velocity can also be extracted from the conservation equations used previously, giving the following:

$$u_2 = \frac{2}{\gamma_1 + 1} c_1 \left(M_1 - \frac{1}{M_1}\right) \tag{27}$$

From the Mach number of the shock, it is possible to find all the characteristic data of a shock tube simulation, such as driver gas pressure p_4 (equation (26), example Figure 3-7 left), shock overpressure $p_2 - p_1$ (equation (19), example Figure 3-7 right), shock velocity U_s (from the definition of the Mach number equation (15)) and the contact discontinuity velocity u_2 ,(equation (27)).

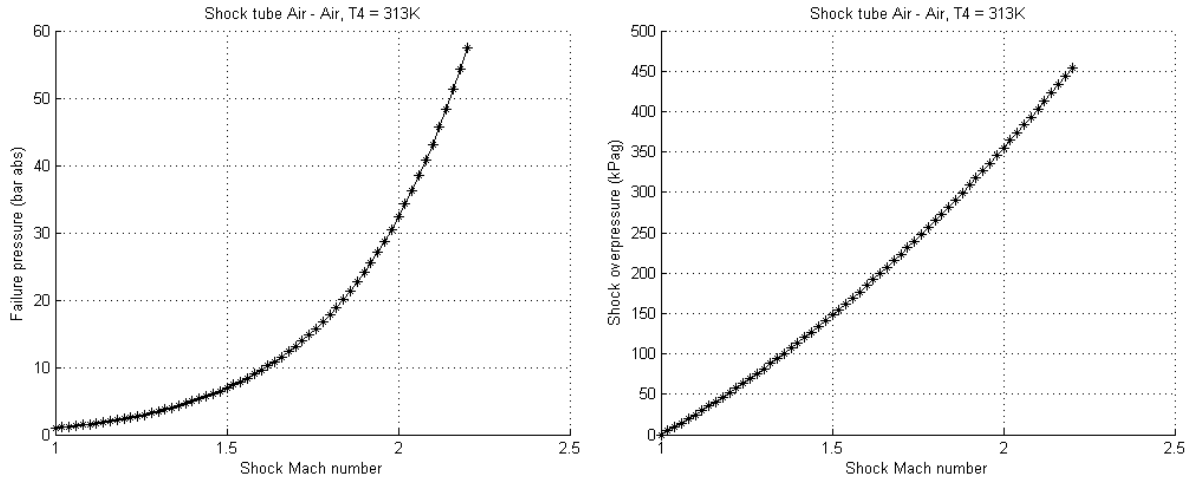

Figure 3-7 Calculation of shock tube characteristics from shock Mach number and conservation equations for a case involving air (left: failure pressure p_4; right: shock overpressure, $p_2 - p_1$)

From this data relating Mach number, failure pressure p_4 and shock overpressure $(p_2 - p_1)$, polynomial curve fits are used to obtain $p_2 - p_1$ as a function of failure pressure p_4 (example Figure 3-8). This will be used later in this work to model initial conditions of some explosions.

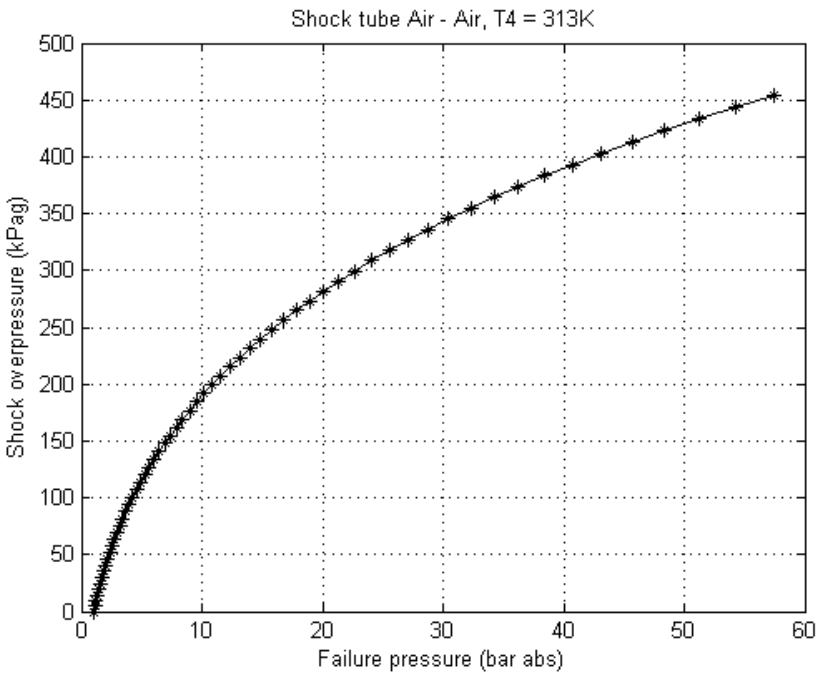

Figure 3-8 Shock overpressure from failure pressure of an Air-Air shock tube case

V - C-D nozzle and under-expanded jet

The Converging-Diverging nozzle (or C-D nozzle) is a particular channel shape widely used in aerospace engineering for its properties to accelerate flows and generate thrust. Its shape influences the characteristics of the flow traveling through it. The analogy with C-D nozzle flow can be made at specific times of the explosion, particularly at the early stage of the opening of the vessel, when the flow propagating out of the fish-mouth crack opening chokes due to limited opening area. In order to better understand these early flow patterns, the theory behind the C-D nozzle is explained briefly.

CD nozzle flow is similar to the flow that occurs as the vessel fails. The flow accelerates out of the vapor space and becomes sonic at the minimum flow section. The flow is sonic and choked at this minimum section. Beyond this section the flow accelerates to supersonic. This overexpansion results in a shock standing near the exit to bring the flow back to subsonic conditions. As the pressure decays in the vessel this shock moves back into the vessel and reduces in strength. When the pressure in the vessel drops below the critical pressure the shock disappears and the flow becomes subsonic everywhere.

If the vessel bursts fully open during this process it is not clear what happens to this shock. Does it fly away or does it collapse back into the vessel? We plan to determine during the testing whether it propagates outward or collapses back into the vessel.

V-1. **Isentropic solution and choked flow**

The first step in studying the analytical solution of the Converging-Diverging nozzle is to linearize the continuity equation through a 1D channel of varying cross section area:

$$\frac{d\rho}{\rho} + \frac{dA}{A} + \frac{du}{u} = 0 \tag{28}$$

where ρ is the fluid density, A is the cross section area of the duct and u is the fluid velocity. In nozzle flow, the fluid velocity is driven by a pressure gradient between the inlet and the outlet. When the pressure decreases, the flow accelerates. Through changes in cross section areas, one is able to accelerate the flow in various ways.

By replacing density using the continuity Euler equation and by assuming isentropic flow, one can obtain the following:

$$\frac{du}{u} = \frac{1}{M^2 - 1}\frac{dA}{A} = \frac{dP}{\rho u^2} \tag{29}$$

From this equation, one can understand the relation between flow velocity and variation on the cross section area of a duct, depending on its sonic regime. For example, a subsonic isentropic flow through a diverging nozzle (also called diffuser) will decelerate, resulting in an increase in pressure and density. For the supersonic case, the opposite occurs: the flow accelerates and its pressure and density decrease. The behaviors of these variables are summarized for all 4 cases in Table 3-1.

Table 3-1 Behavior of isentropic flow through converging and diverging nozzles

	M < 1			M > 1		
	du	dP	dρ	du	dP	dρ
Divergent: dA+	-	+	+	+	-	-
Convergent: dA -	+	-	-	-	+	+

An interesting property of equation (29) is observed when designing a complete Converging-Diverging nozzle, particularly when defining the transition from one to the other. This equation states that there is no sonic solution possible (M=1) except if $\frac{dA}{A} = 0$. It implies that the transition from Convergent to Divergent must be smooth, and that the sonic condition will be located at this transition. To bring a flow from subsonic to supersonic, it is first accelerated through a Convergent section at M < 1, reaches M=1 at the nozzle throat and keeps accelerating through the Divergent section at M > 1. Although the

Divergent-Convergent nozzle is conceptually possible, such a nozzle decelerates the flow and consumes thrust power rather than generating it, thus it has no relevant application here.

When flow reaches M = 1 at the nozzle throat, it is called "choked". The mass flow rate through a choked nozzle depends only on the stagnation pressure P_0 and stagnation temperature, T_0 upstream of the convergent section, and no longer on the back pressure P_b at the exit of the diffuser. The pressure at the throat, P^* reaches a characteristic ratio of $\frac{P^*}{P_0} = 0.5283$.

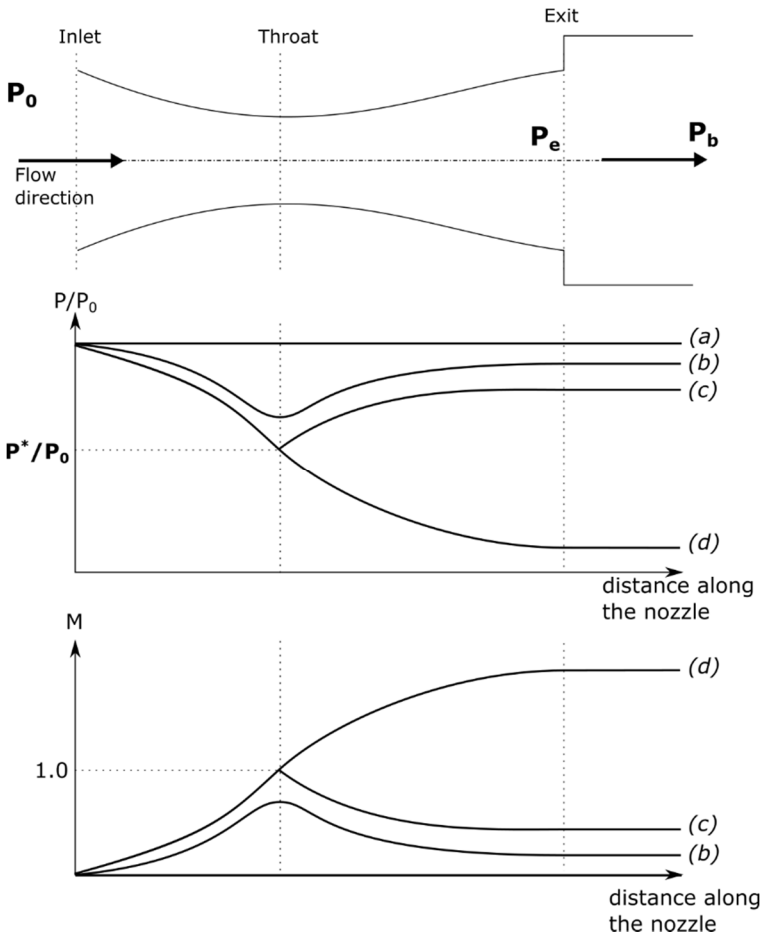

Figure 3-9 Pressure and Mach number along isentropic flows through a C-D nozzle

To generate flow through the nozzle, the back pressure P_b is decreased until flow change is observed. Figure 3-9 illustrates this process. At case (a), $P_b = P_0$, the flow is at rest. At case (b), P_b has decreased below P_0, thus drawing slowly some flow through the nozzle. Static pressure drops in the convergent section, reaches a minimum at the throat, and increases in the diffuser. Velocity behavior is opposite to that of the pressure as seen Table 3-1. The flow remains subsonic. The stronger the decrease of P_b, the larger the minimum pressure at the nozzle throat and the greater the acceleration of the flow, until case (c).

At case (c), the back pressure drops enough to reach the sonic condition at the throat. The flow is choked, leading to a maximum mass flow and a critical pressure ratio. When the sonic condition is reached, two isentropic solutions are available: a subsonic solution (c), and a supersonic one (d). For P_b as in case (c), the flow will decelerate in the diffuser and remain subsonic. For P_b as in case (d), also known as design pressure of the nozzle, the flow will accelerate in the supersonic range and remain lossless. The mass flow will not increase, but the velocity of flow, thus the thrust of the nozzle, will dramatically increase.

However, if the back pressure is between (c) and (d) or bellow (d), there is no isentropic solution. The pressure of the flow will adjust through a shock, located inside or outside the diffuser.

V-2. **Shock formation in the nozzle**

Figure 3-10 presents the different configurations possible in a C-D nozzle when the back pressure does not meet the requirements to keep the flow isentropic through the nozzle. Starting from the subsonic isentropic solution (Figure 3-10 a), the back pressure drops to point (b). At this point, the flow accelerates isentropically from the throat to somewhere in the diffuser at supersonic velocity where a normal shock suddenly appears. A transition from supersonic to subsonic flow occurs at the shock. Beyond the shock, the flow proceeds to the exit exhibiting subsonic isentropic behavior. The back pressure will determine the position at which the normal shock appears in the diffuser. As the back pressure drops, the shock will move toward the exit, until reaching configuration (c), where the normal shock occurs at the exit. Point (e) has been presented previously as the supersonic isentropic solution, or design pressure. If the back pressure is between the conditions of (c) and (e), the flow in the nozzle will remain undisturbed. However it will adjust outside of the nozzle, with a succession of oblique shocks and complex flow patterns. This flow is over-expanded. When the back pressure is below the design pressure, the flow will adjust outside the nozzle with a succession of expansion waves and reflected shocks. This flow is under-expanded.

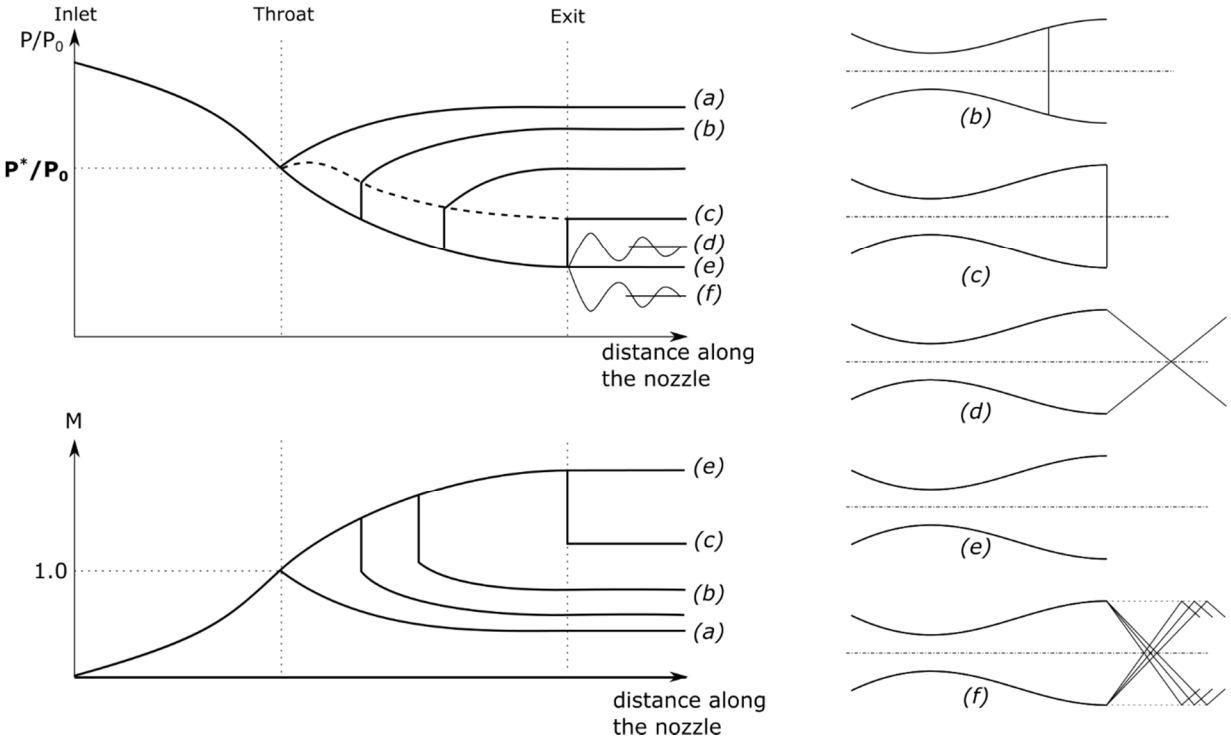

Figure 3-10 Pressure and Mach number along non-isentropic flows in a C-D nozzle

V-3. **Under-expanded jet**

Under-expanded jets are of interest in their structure because similar phenomena occur when the vapor and liquid of a failing vessel expand through the crack while opening. These jets are usually encountered in the context of a jet engine. Strongly under-expanded jets follow a repeating pattern, sometimes called Shock diamond or Mach diamond, due to their shape (Figure 3-11).

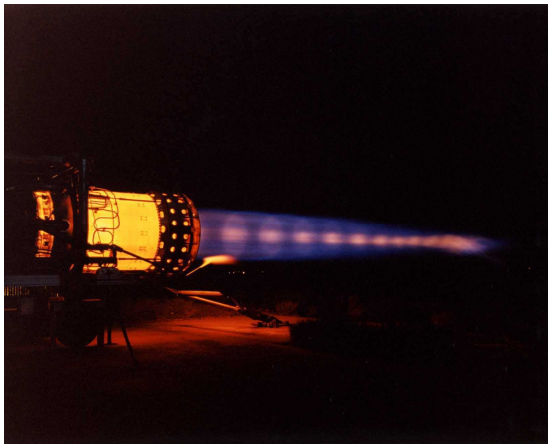

Figure 3-11 Mach diamonds behind a statically mounted Pratt & Whitney J58 engine on full afterburner while disposing of the last of the SR-71 fuel prior to program termination. (By NASA [Public domain], via Wikimedia Commons)

Their structure is detailed Figure 3-12. One interesting characteristic of the jet flow is the Mach disk observed at a certain distance from the nozzle exit, because of the analogy that can be made with similar shock present in explosion flows.

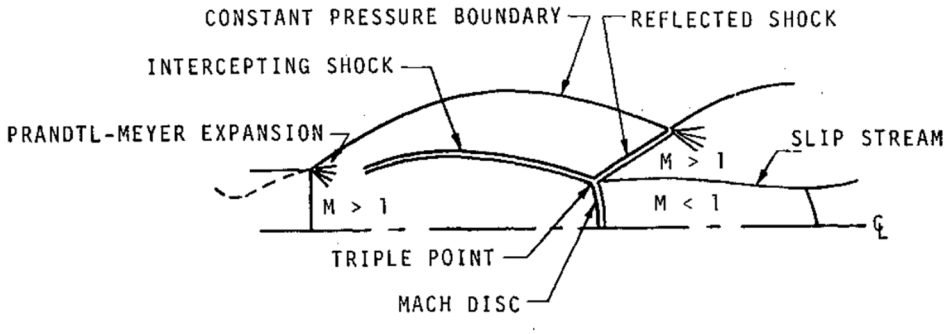

Figure 3-12 Schematic describing the topology of under-expanded jet (Abbett, 1971)

V-4. **Stationary shock model applied to BLEVE**

The transient start of supersonic jet flows is thoroughly studied in the literature (Radulescu and Law, 2007). This type of flow presents a structure similar to that of the under-expanded jet of CD-nozzle flow, with the presence of the Mach shock at the exit of the jet (Figure 3-13).

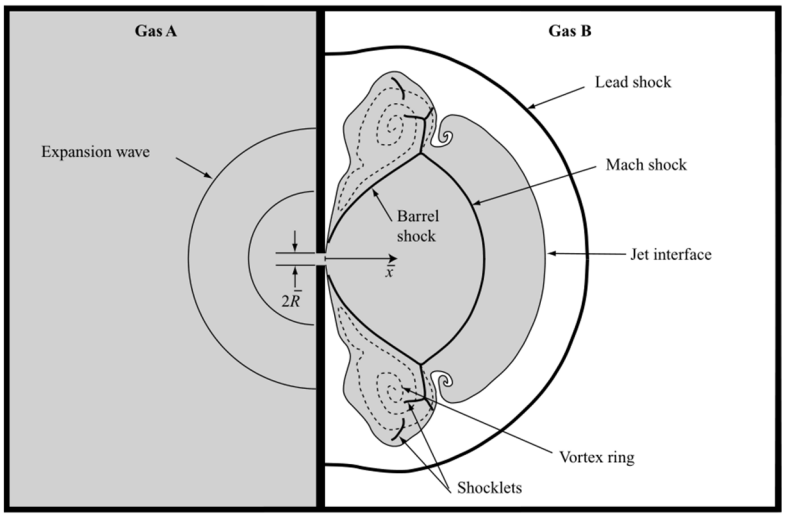

Figure 3-13 Schematic of the flow patterns involved in the transient start of a supersonic jet (Radulescu and Law, 2007)

This phenomenon is also of interest in the study of BLEVE overpressure as it has been observed and studied in recent work on BLEVE.

A model (Laboureur et al., 2015) tries to predict the jet flow at the exit of the vessel, at the first step of a 2-step BLEVE (Figure 3-14). It is assumed that the fish-mouth opening of the vessel creates a vena-contracta. The model involves the following steps in the flow:

- State 0: fluid at rest, at the conditions before failure;
- State 1: represents the exit from the vessel. The fluid expands isentropically until reaching sonic conditions at this point. P_1 is determined by iterating until the Mach number equals one, or $U_1 = a_1$.
- State 2: the flow expands isentropically until over-expanded;
- State 3: a discontinuity brings the flow back to an isentropic solution fitting the final flow state behind the lead shock.

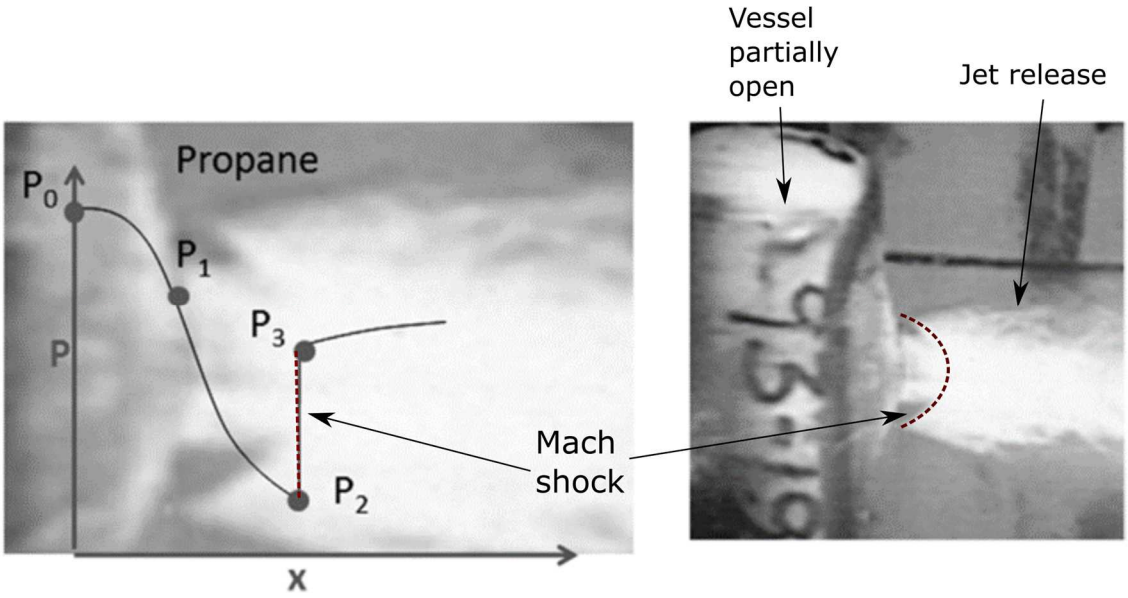

Figure 3-14 Pressure evolution and stationary shock, during first step of BLEVE observed by Birk (left: pressure profile prediction; right: evidence of Mach shock at exit of a vessel) (Laboureur et al., 2015)

Evidences of stationary shock formation and collapse from critical flow is provided by CFD simulation of BLEVE with liquid only in the vessel before failure (Yakush, 2016). Figure 3-15 describes these steps as follow:

1. Immediately following the beginning of the expansion, the lead shock forms and expands outward ($t = 0 \rightarrow 5ms$);

2. Upstream the lead shock, the flow is over-expanded. It drops below atmospheric pressure and a reversed shock forms. The shock progresses to a certain distance from the center of explosion before stabilizing ($t = 5 \rightarrow 15ms$);
3. As the fluid expands from the initial sphere, the flow upstream of the reversed shock slows, leading to the collapse of this shock toward the center of the sphere ($t = 15 \rightarrow 23ms$);
4. Due to the spherical symmetry of the geometry, the shock reflects at the center of the sphere to propagate outward ($t = 24 \rightarrow 35ms$). It forms the 2nd shock observed in classic spherical explosion.

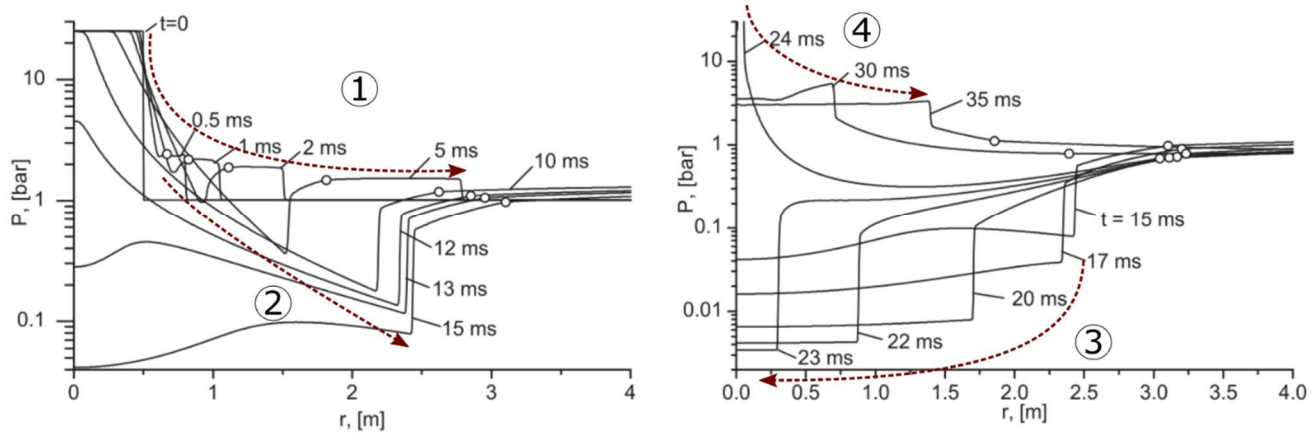

Figure 3-15 Pressure profile in expanding propane cloud, circles denote the contact surface, for $P_{fail} = 25bar$ *(Yakush, 2016)*

This overexpansion process repeats itself with an elastic behavior, until the energy contained in the initial compressed volume is dissipated. With a sphere full of superheated liquid exploding at 25bar, the author observes three pressure peaks in the vicinity of the sphere (Figure 3-16). A vapor spherical explosion would most likely show only two shocks, due to the smaller amount of energy that the vapor can release over time.

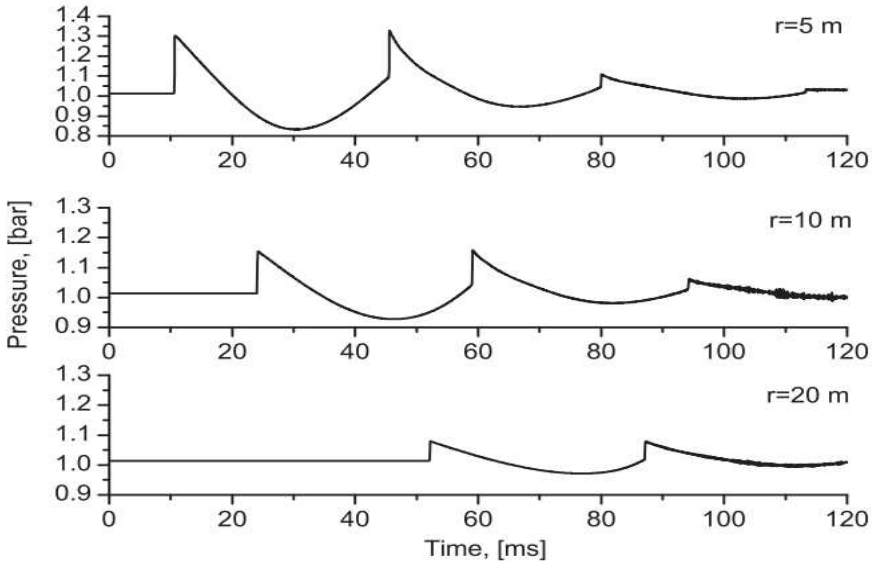

Figure 3-16 Time profiles of pressure at different distances from the center, $P_0 = 25bar$ (Yakush, 2016)

Previous reference (Kornegay, 1965) on experimental work of vapor explosion from sphere mentions the presence of a secondary shock in the pressure history of the explosion (Figure 3-17), where state 1 is the undisturbed low pressure surrounding gas, 4 is the undisturbed high pressure source gas, 2 is the compressed surrounding gas after the lead shock has travelled through, 3 is the expanded source gas travelling outward, and 5 is the overexpanded source gas between expansion fans travelling toward the center and the secondary shock. Its path in time is very similar to the one observed on the BLEVE CFD simulation. It must be noted that it is observed with vapor. This shock is not the second blast perceived in the far-field. It travels to a certain distance away from the center of explosion. Once the flow has expanded enough inside the sphere (Figure 3-17 line between 4 and 5), the secondary shock travels back toward the center.

The author compares the spherical explosion with one-dimensional explosion, and states that the secondary shock is a specificity encountered in spherical bursts only. He does not mention what happens to this shock once it reaches the center of the sphere. But the results of Yakush presented above show that it reflects outward, thus generating the second blast sometimes measured in the far-field.

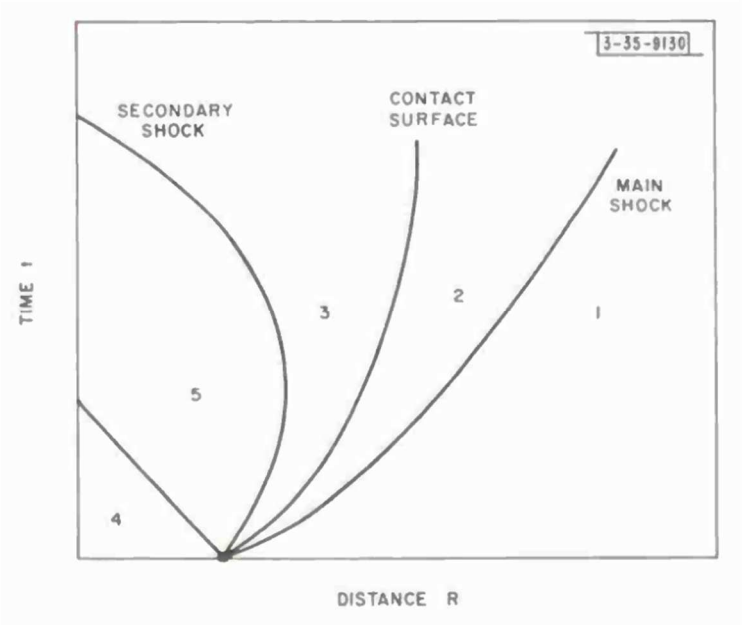

Figure 3-17 Distance versus Time for spherical flow field (Kornegay, 1965)

This argument shows that the second blast appearing in the far-field comes from a secondary shock formed in the near-field up to a certain distance from the center of explosion. Once the expansion is sufficiently advanced inside the spherical source, the secondary shock travels back inward, to finally reflect at the center and to generate a blast wave traveling out in the far-field.

V-5. **Spherical shock propagation**

From the equations of motion described previously, Friedman and Whitham (Kornegay, 1965) presented an analytical solution to spherical shock propagation from an initial pressurized sphere of vapor of radius R_0(Kornegay, 1965)(Kornegay, 1965)(Kornegay, 1965)(Kornegay, 1965). It is refered as the F-W model through this work. To do so, the linear form of the momentum conservation equation was used again:

$$dP + \rho a.du = -\rho \frac{a^2 u}{u+a} \frac{dA}{A} \tag{30}$$

By substituting Rankine Hugoniot equations into this equation of motion, and identifying the change in area of the channel $\frac{dA}{A}$ as the spherical shock surface, a differential equation relating the shock Mach number to the shock radius was obtained:

$$-\frac{dR}{R} = \frac{MdM}{(M^2-1).K(M)} \tag{31}$$

$$with\ K(M) = \frac{2}{\left(1+\frac{2}{\gamma+1}\frac{1-x^2}{x}\right)\left(2x+1+\frac{1}{M^2}\right)}$$

$$with\ x^2 = \frac{(\gamma-1)M^2+2}{2\gamma M^2-\gamma+1}$$

where M is the Mach number of the shock, and γ is the ratio of specific heat of the ambient medium in which the shock propagates (in most cases, ambient air). This differential equation is integrated to give the following explicit formula:

$$\left(\frac{R}{R_0}\right)^2.\frac{Y-Z}{M}\left[\sqrt{\gamma-1}.Y+\sqrt{2\gamma}.Z\right]^{\sqrt{\frac{2\gamma}{\gamma-1}}}.Y^{\frac{2}{\gamma}}.exp\left\{\frac{1}{\sqrt{2\gamma-2}}.\sin^{-1}\left[\frac{2Y^2-(\gamma-1).Z^2}{(\gamma+1)^2.M^2}\right]\right\} = C \tag{32}$$

$$with\begin{cases} Y^2 = 2\gamma M^2-\gamma+1 \\ Z^2 = (\gamma-1)M^2+2 \end{cases}$$

where R is the distance to the center of the sphere, R_0 is the radius of the initial bursting sphere, and C is the constant of integration. The constant of integration is obtained through the initial conditions at the radius R_0, where the 1D shock tube theory is applied for an initial Mach number (equation (26)). Using the Rankine-Hugoniot equations again at the distance R (equation (19)), one can relate the overpressure of the shock and the distance to the source.

VI - Critical boiling flow modeling

The purpose of critical boiling flow modeling is to estimate critical flow with two-phase flow from conservation equations. Consider a boiling wave traveling through a liquid phase at saturation under rupture conditions, leaving behind a diphasic flow of quality x_2. The real case indicates that the boiling wave travels downward through the liquid phase at velocity U_{boil}, producing two-phase flow upward at velocity U_2 due to expansion of the fluid (Figure 3-18 A). In order to apply steady conservation equations to this case, the reference frame is changed to a steady boiling wave, traveling through liquid at velocity U_{boil} and diphasic flow generated at velocity $U_{boil}+U_2$ (Figure 3-18 B).

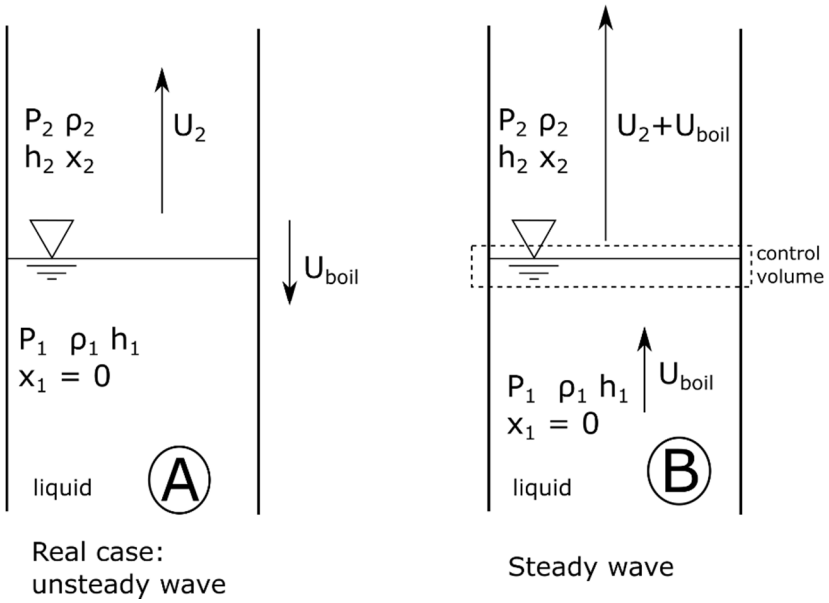

Figure 3-18 Descriptive schemes of the definition of the control volume for conservation equations through boiling wave

Based on the steady reference frame (B), conservation equations are applied:

Mass conservation: $$\rho_2 * (U_2 + U_{boil}) = \rho_1 * U_{boil} = \dot{m_{steady}} \quad (33)$$

Momentum conservation: $$P_2 + \rho_2 * (U_2 + U_{boil})^2 = P_1 + \rho_1 * U_{boil}^2 \quad (34)$$

Energy conservation: $$h_2 * \frac{(U_2 + U_{boil})^2}{2} = h_1 * \frac{U_{boil}^2}{2} \quad (35)$$

where $\dot{m_{steady}}$ is the mass flow from liquid to vapor in the steady boiling wave reference frame (B). Pressures are defined according to the problem solved, and densities are defined according the properties of the fluid at the designed pressure. The conservation equations are used to solve for the velocities of the flow in the vapor space and of the boiling wave. These equations assume homogeneous diphasic flow (temperature is homogeneous through phase 2) and equilibrium flow (both phases are saturated).

The objective of this problem is to define the critical flow through a given liquid-vapor interface, thus defining the conditions at which the mass flow from liquid to vapor is maximum. To do so, pressure P_1 in the liquid is set to the failure pressure of the comparison case. P_2 is increased from atmospheric pressure to P_1. The real case involves calculating transient mass flow through the moving boiling wave:

$$\dot{m_{real}} = U_2 * \rho_2 \quad (36)$$

Its evolution is tracked with pressure ratio. Its maximum defines the choked conditions for a particular failure pressure. For example, with 21 bar in the vessel, the critical maximum mass flow obtained is $\dot{m}^* =$

$8300kg.m^{-2}.s^{-1}$ for a pressure ratio of 0.55, leading to a boiling wave velocity of $25m.s^{-1}$. This theoretical approach based on conservation equations provides a quick estimate of the velocity of the boiling wave in critical flow.

Chapter 4

Experimental setup

I - Introduction and objectives of the experiment

A small scale experimental BLEVE apparatus was designed in the scope of this PhD work. The apparatus was designed with the following ideas in mind:

- We wanted a realistic rupture of a horizontal cylindrical vessel;
- We wanted a range of controlled failure pressures and failure lengths;
- The apparatus should be small enough to conduct tests indoors under controlled conditions;
- The explosions should be small enough to not damage close in instruments and cameras;
- The volume of the vessel should be small enough such that propane release in the Spark facility leads to no risk of vapor cloud explosion.

The objectives of the experimental setup designed were multiple:

- Understanding the contribution of several factors for rupture on the consequences of BLEVE: failure pressure, liquid fill level, and longitudinal failure length.
- Measuring a complete overpressure field around the BLEVE: near-field, far-field and in all directions (sides, ends and top).
- Evaluating the ground loading generated by a BLEVE
- Observing the shock at the vessel exit to understand the mechanisms of shock formation.

The aim of this chapter is to describe the design process of the experimental apparatus. First a quick study of the main parameters involved in the study of BLEVE is presented, in order to guide the choices made in the design of the experimental setup. Then the apparatus is presented here. The initial design of the apparatus and its evolutions are presented in Appendix B. The instrumentation setup is detailed, from monitoring instruments to high speed transducers. The high speed imaging tools used are described, together with the optical techniques used for shock detection. From the apparatus presentation, a summary of the main variables studied is made. The chapter ends with a discussion of the experimental protocol used for each test during the last testing series, and the safety aspects involved with the experiment.

II - Key parameters involved in the study of BLEVE

II-1. Hazard key variables and their independent parameters

From a study of the literature and of the theory involved in the BLEVE, the relation between key parameters is examined in order to design the experiment. The main hazards characteristics of interest in the near-field of a BLEVE are the following:

- Overpressure characteristics: maximum static overpressure dP, positive impulse I_{dP}^{+}, 2nd peak overpressure, delay between 1st and 2nd peak, dynamic overpressure, etc;
- Ground loading characteristics: maximum load F_{max}, positive impulse I_{F}^{+}, duration of positive impulse t_{F}^{+};
- Internal transient pressure characteristics: pressure drop P_{drop}, repressurization in the vessel P_{rise}, emptying duration;
- Dynamic of opening: speed of crack propagation, size of vessel opening, speed of flattening of the vessel;

This work focuses on maximum overpressure dP, and maximum ground load F_{max} and presents some secondary flow pattern behaviors.

These hazard dependent variables are function of the following parameters:

$$dP = f(P_{fail}, \Phi_{liq}, r_{vessel}, l_{vessel}, R, \theta, opening\ characteristics, substance\ properties, boiling\ properties)$$

where:

- P_{fail} is the failure pressure. One of the main parameters to control, P_{fail} is one of the variables that defines the overpressure generated by vapor explosion in shock tube theory. It was varied from 11 to 32 bar in the experiments;
- Φ_{liq} is the liquid volume fraction. It defines the amount of mass, thus compressed energy in the vessel. It also defines the ratio between liquid and vapor present in the vessel. It was varied from 0 to 100% liquid by varying the mass of propane in the vessel before explosion;
- r_{vessel} is the radius of the vessel, l_{vessel} the length of the vessel. These were fixed at 5cm and 30cm respectively, by choosing a small scale experimental setup. Studies involving larger values of these variables are available in the literature.

- R and θ are the distance angles from the vessel at which measurements are taken. Distance was varied from 15cm to 3m from the vessel, measuring near-field and far-field data. Angle was varied to measure data from the sides of the vessel, similar to studies in the literature, but also to measure data above the vessel and at a 45° angle to the vertical. These additional data measurement provided insight on the anisotropy of the pressure field for a cylindrical vessel;

Similarly, the process can be done with F_{max}:

$$F_{max} = f(P_{fail}, \Phi_{liq}, r_{vessel}, l_{vessel}, L_w, T_{SL}, T_{fail})$$

Dimensional analysis on these parameters will lead to ratios such as:

$$\frac{F_{max}}{P_{fail} r_{vessel} l_{vessel}} = f(\Phi_{liq}, \frac{L_w}{r_{vessel}}, \frac{l_{vessel}}{r_{vessel}}, \frac{T_{fail}}{T_{sl}})$$

This type of dimensional analysis will be used for the ground loading characterization.

II-2. **Opening characteristics:**

Opening characteristics examined included mainly the speed of opening, and the size and the shape of the opening. They depend on the following:

$$opening\ characteristics = f(P_{fail}, r_{vessel}, l_{vessel}, L_w, \sigma_{yield}, \rho_{metal})$$

where:

- L_w is the weakened length on the top of the vessel: it was varied from 50 to 150mm as a result of the machining process.
- σ_{yield} is the yield strength of the vessel material. It was set to 96 MPa by choosing aluminum 6061 and annealing it for machining constraints. It was not varied;
- ρ_{metal} is the density of the vessel material: it was set to 2720 kg/m^3 by choosing aluminum 6061 and was not varied;
- P_{fail}, r_{vessel} and l_{vessel} have been discussed above;

The material characteristics are different for real size pressure vessels as they are made of steel rather than aluminum. The choice of a weaker material like aluminum was made to compensate the large ratio wall thickness over diameter of the small scale tube, in order to have failure pressure within a reasonable range. Opening characteristics may vary with the material. It is assumed that events tend to occur more slowly with steel since the material is heavier and more resistant.

II-3. **Fluid properties**

Fluid properties involve characteristics such as k (specific heat ratio), c (speed of sound in the fluid), C_p (specific heat capacity), ΔH_{vap} (latent heat of vaporization), γ (surface tension), etc. This study focuses on propane since this is the fluid involved in most BLEVE accidents. For safety reasons, water was used initially as a non-flammable fluid in the first steps of the experiment but no analysis was done on the variation of fluid properties.

II-4. **Boiling characteristics**

Boiling characteristics include variables such as P_{drop} (pressure drop before repressurization) and P_{rise} (pressure rise in the vessel), emptying time of the vessel, superheat degree or J_a Jakob number. These parameters depend on the following independent parameters (non-exhaustive list):

- Superheat limit of the fluid and spinodal: this is set by the fluid choice: propane.
- Surface roughness as potential nucleation site: The aluminum tubes were fairly smooth. However the impact of its roughness on the study was not investigated because it was not perceived as fundamental to the questions asked;
- Suspended particle properties as potential nucleation site: these include particle diameter, density of particle per volume area, etc. The fluids used were either tap water or commercial pure propane. The suspended particle properties of these fluids were not measured, thus the influence of this parameter on the boiling properties is not known.
- Bubble diameter and growth rate: these have not been considered. This study does not focus on the influence of micro-scale events. We assume that thermodynamics consideration is sufficient to address the questions asked so far.

Some boiling characteristic variables are measured (P_{drop}, P_{rise}, J_a), but they have not been related to the independent variables at the microscopic scale mentioned above. Boiling characteristics will be indicators for the phase change behavior and its potential impact on the hazardous variables (dP, F_{max}, I^+, etc.) but were not varied with control.

III - **Apparatus design**

The apparatus was custom designed and made in the Machine shop in the Department of Mechanical and Materials Engineering, Queen's University. It consisted of aluminum tubes (diameter: 50.8mm = 2 inches, length: 300mm) made of the alloy 6061 T6, sealed by Swagelok fitting for the pressure and closed

by steel nuts and end caps designed in the lab to accommodate piping and instruments passing through while remaining sealed.

The cap on one end of the tube had airtight fittings for instrumentation (thermocouples and high-speed pressure transducer) and holes designed for filling and venting the tube. On the other end, two different caps were available: a solid closed cap or one with a window to permit visualization inside the tube (Figure 4-1). All steel caps are reusable between the tests.

The tubes were supported at the ends on cradles to hold the tube in place. Below the tube was a blast plate to absorb the downward force of the BLEVE. This blast place was supported on load cells to measure the transient force generated by the BLEVE.

The entire apparatus was set at height of 1m meter above ground on concrete blocks to permit better access to the instrumentation, in particular for the optical axes necessary for high speed imaging (Figure 4-2).

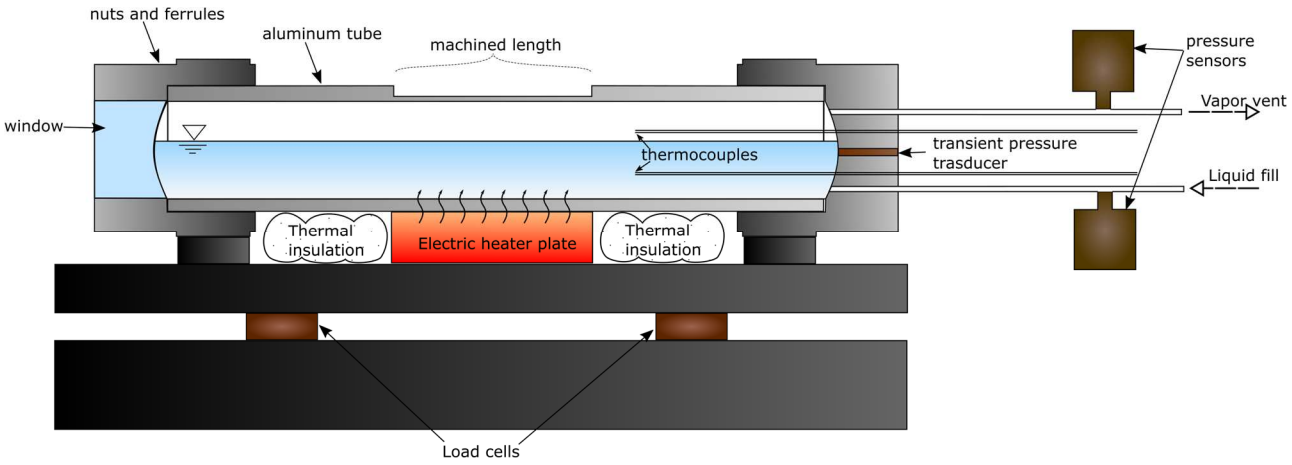

Figure 4-1 Schematic of the tube apparatus

Figure 4-2 Photo of the experimental tube (left: close-up view before experiment; right: view on concrete stand, after burst)

The ends were sealed with Swagelok ferrules. These were fastened on the aluminum tube with a swaging machine from Swagelok. When mounting the end cap and the nut on the tube, the sealing was completed using 2 zones of contact between the ferrules, the nuts and the end cap (Figure 4-3). The sealing process required applying a specific grease on these zones of contact, as well as on the thread between the end cap and the nut. The grease was supplied by Swagelok along with the ferrules. The ferrules are not reusable and need to be changed for each test.

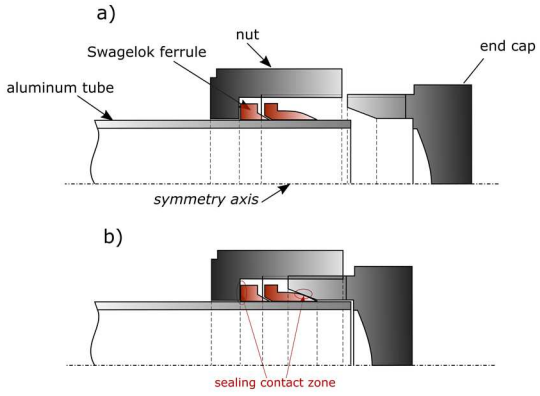

Figure 4-3 Design of the seal with steel nut, end cap and Swagelok ferrules (a) open ; b) closed and sealed)

The tube itself was treated and machined to fail at control pressures ranging from 15 to 30 bars. The annealing and machining process are explained in the next paragraph. The filling and venting of the tube was monitored remotely with solenoid valves (Figure 4-4). The fluid used for this set of experiments was pure propane.

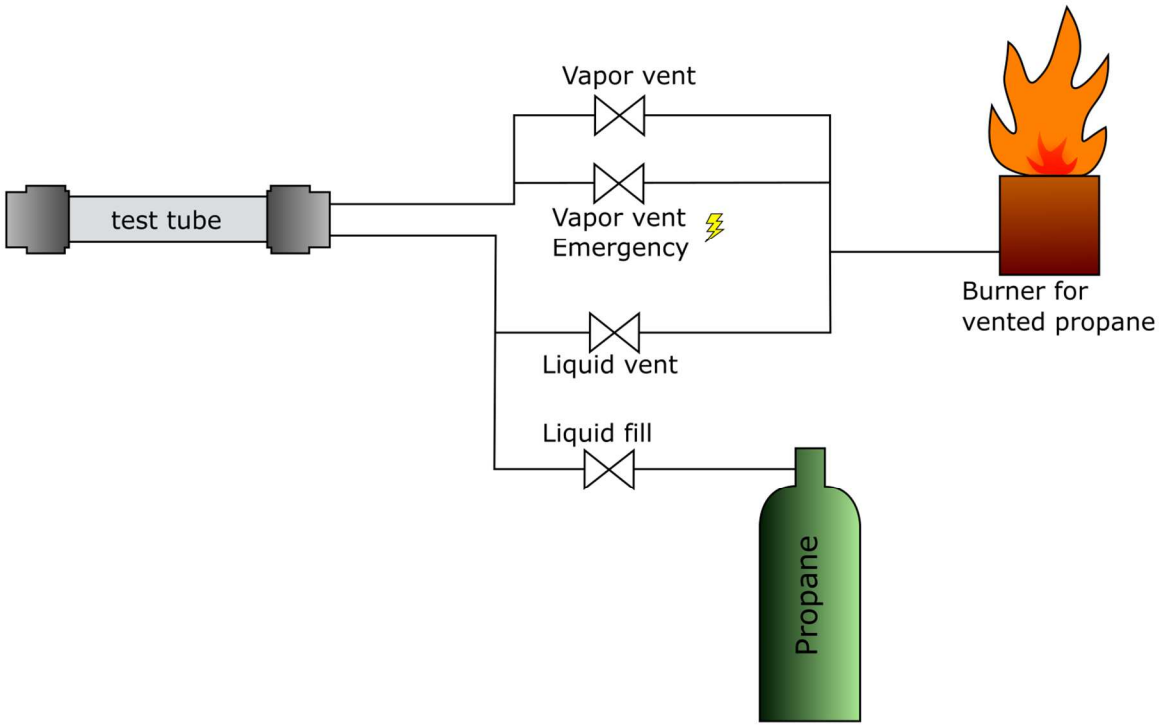

Figure 4-4 Schematic of the piping circuit mounted for remote control of the filling and venting

An electric heater attached to a steel plate that fit the shape of the tube was used (Figure 4-5). It allowed complete remote control of the heating which was very steady and posed less risk of ignition.

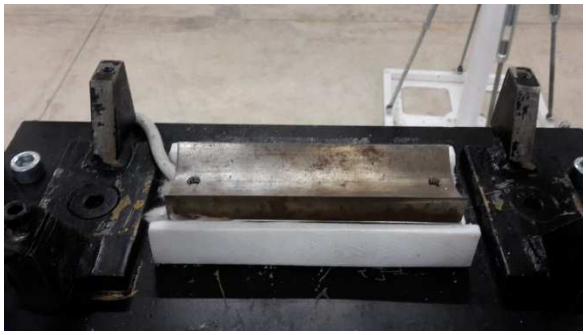

Figure 4-5 Electric heater plate, machined to match the shape of the tube

III-1. Machining process for failure prediction

In order to gain control over the failure pressure of the aluminum tube used in the experiments, an annealing and machining process was developed to weaken the tube and have a satisfying range of failure pressure.

The machining consisted of a flat milling along the length of the tube with 2 characteristic lengths: the longitudinal length and the depth of machining (or remaining wall thickness). The burst pressure was controlled with the latter (wall thickness) and the aluminum yield strength. The relations linking these two parameters to known parameters are the following:

$$\sigma_h * h = P_{fail} \cdot \frac{d_{in}}{2} - P_{atm} \cdot \frac{d_{out}}{2} \quad (37)$$

$$0.866 * \sigma_{h\,VM} = YS \quad (38)$$

Equation (37) gives the relation between hoop stress σ_h and the geometry of the tube, d_{in} the inner diameter, and d_{out} the outer diameter. The machining process changes the wall remaining thickness h. Equation (38) states the failure condition, based on Von Mises criterion for cylinders and slow rupture (Yield Strength involved rather than Ultimate Tensile Strength).

The dimensioning challenge was finding a combination (yield strength; wall thickness) that gives the desired failure pressure within a feasible range for the machining process. On one hand, the tube wall cannot be milled under 0.2mm thickness, due to machining constraints such as the accuracy of the tube dimensions and tools used for machining, the variations on the initial wall thickness due to the tube provider, and the ductility of the aluminum that breaks open when machined at very small wall thicknesses.

On the other hand, the aluminum yield strength depends directly on the heat treatment applied to it and the aging of the material. It is not possible to machine the tube to extremely small thickness because of the soft properties of aluminum and the irregularities in the tube diameter. To weaken the tube further, the following annealing process has been adopted:

- Heat the tube for 2h at 413°C
- Cool at a rate of 28°C/h until tube is at a temperature of 260°C
- Finish the cooling under ambient air conditions
- When cooled, freeze the tube to prevent aging until it used for an experiment.

The final alloy is estimated to be an aluminum 6061-O with yield strength of 96 MPa and ultimate strength of 151 MPa. From these material values and the expected failure pressures, the remaining thickness h_{min} is calculated. To characterize the machining process (Figure 4-6), the flat width is calculated:

$$w = 2 * \sqrt{d_o^2 - (d_o - h_{max} + h_{min})^2} \tag{39}$$

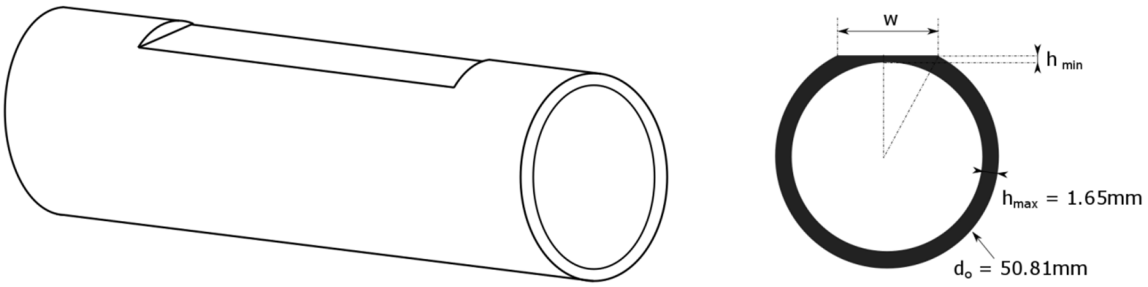

Figure 4-6 Characteristics of the machining process on the tube

III-2. Failure pressure prediction: comparison with experimental failures

This section compares the predictions made for vessel failure pressure when annealing and machining the vessels with the actual failure obtained. For the last test campaign, failure pressure was predicted as a function of the depth of the flat machining. The results are compared in Figure 4-7. Overall, the tubes failed earlier than expected. The main assumption made to explain this behavior is that predictions were made based on yield strength of the aluminum. The experimental failure pressures fall within a 10% range of error for pressures of 20 bar and above. Tubes designed for lower failure pressures tended to fail at a higher pressure than expected. This can be attributed to the uncertainty in the machining for the very thin walls.

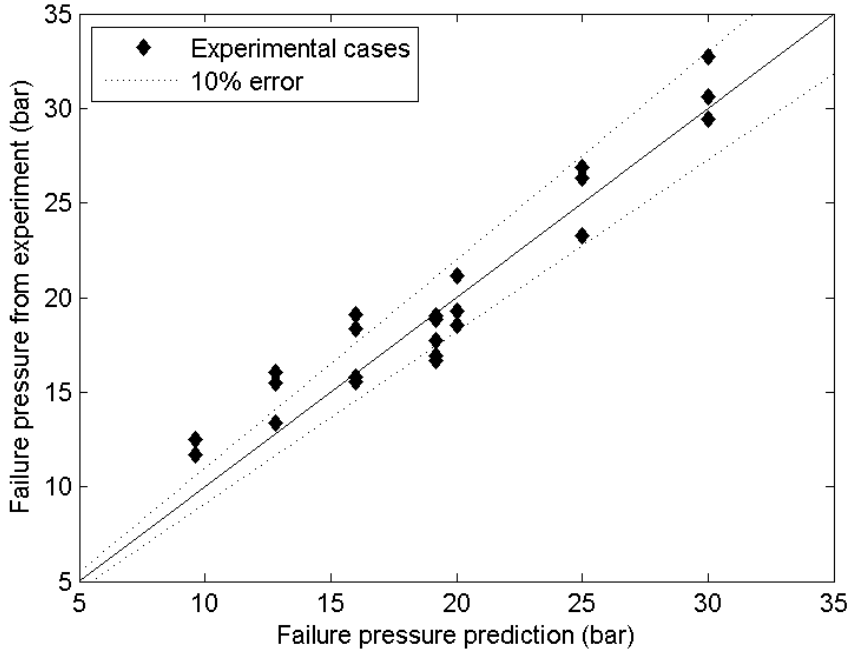

Figure 4-7 Failure pressure for test campaign 2017, predicted versus actual

IV - **Instrumentation**

A wide range of instruments was used to fulfill all the needs of the experiment.

IV-1. **Low speed: Initial condition and monitoring of the test before BLEVE**

To monitor the evolution of the fluid properties in the tube, two pressure sensors TCDirect 716-072 (full scale 0-40barg, accuracy -/+0.3% of reading, response time 0.5s, output 4-20 mA) were set on the fill and vent pipe. These measured the pressure in the vessel for all of the steps preceding explosion: filling and pressuring of the vessel.

Type K thermocouples were positioned at various locations to monitor temperature. The most important thermocouples in terms of results were the two inside the tube which were meant to measure liquid and vapor temperature for most test cases. However, with low or high liquid fill level (below 20% or above 80%), they may actually measure only one phase. In this case, they accounted for potential stratification in the height of the tube. More thermocouples were positioned on the tube wall, at the heater plate and at other locations. These did not provide useful results for the analysis but were necessary for the experimental control and safety

IV-2. **High speed: Consequences of the explosion**

The purpose of the experiment was to capture the explosion properties, such as overpressure, ground loading and pressure discharge in the tube.

Blast gages (PCB piezoelectric sensors model 137A23) were placed around the tube to measure overpressure. They were mounted perpendicular to the flow on a steel pencil shaped structure to collect static pressure with as little disturbance in the shock path as possible. The maximum pressure they can measure is 3.447 bar, with a sensitivity of around 13.5mV/kPa and a response time of 4µs. The non-linearity of the response is estimated to be 0.2% of the full scale, leading to errors of up to 7mbar. Twelve blast gages were placed around the tube at various orientations (vertical, inclined and horizontal) as well as at different distances, to capture near-field and far-field overpressure (Figure 4-8, Figure 4-9):

- dP1 – dP2 – dP3 – dP4 – dP14: above the tube, respectively at 15 – 20 – 30 – 40 – 300cm from the top wall above;
- dP5 – dP6 – dP7 – dP8: at 45^{o} angle around the tube, all at 30cm from the top wall of the tube;
- dP9 – dP10 – dP11: at tube height on its horizontal plan, respectively at 30cm and 30cm on sides, and 60cm on one end;
- dP12 – dP13 – dP20 – dP21: at tube height on its horizontal plan, respectively at 290 – 290 – 320 – 320cm.

The blast gages are design to disturb the flow as little as possible. However, the presence of numerous blast gages potentially some influence on the flow itself. This influence was not measured, but requires some tests with fewer probes to do so.

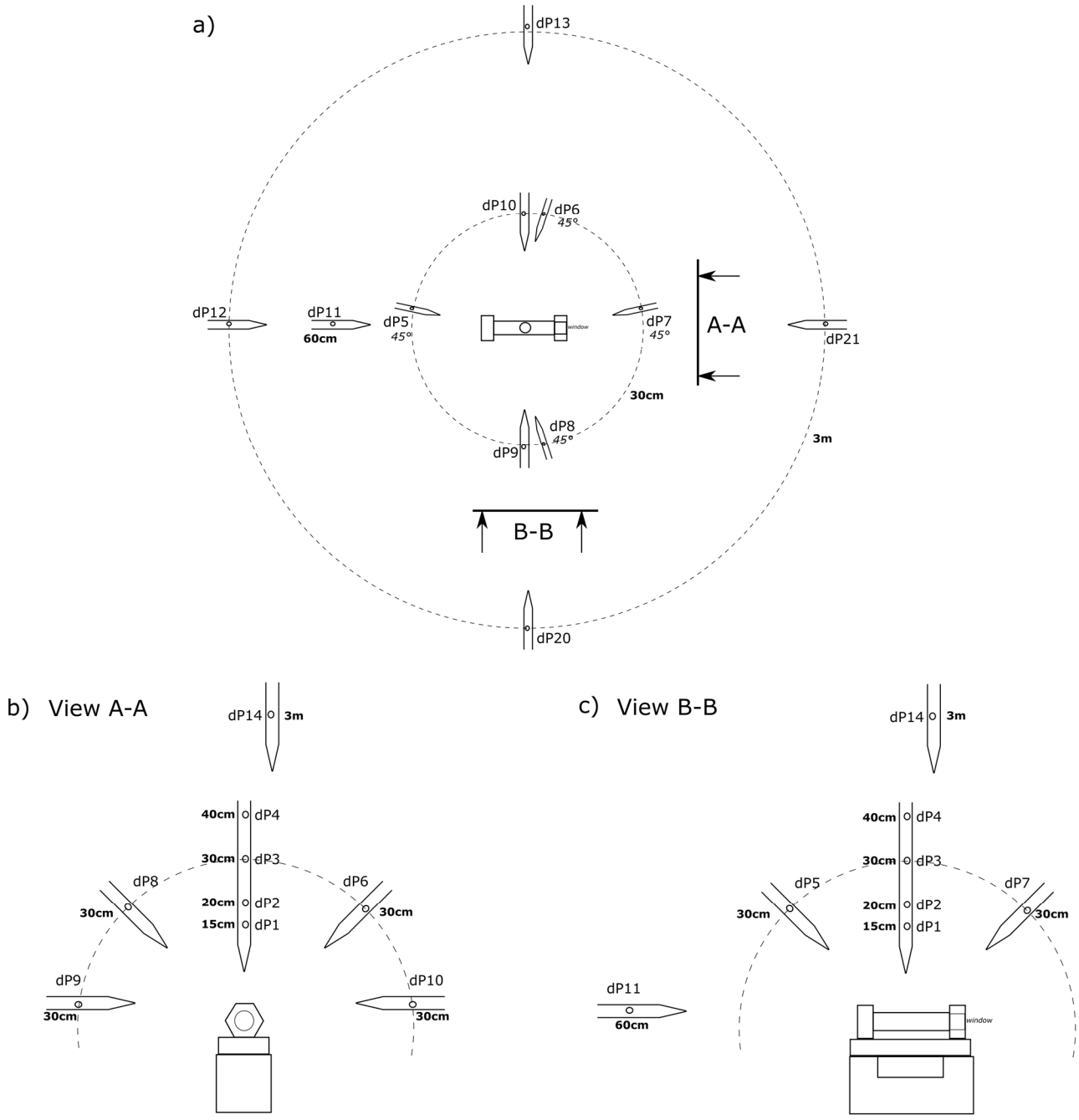

Figure 4-8 Blast gage positions and angles (a) top view; b) longitudinal view c) radial view)

Figure 4-9 Photo of the blast gages setup

A four-probe blast gage was designed by ISR based on the characteristics and shape of the PCB blast gages. Four PCB piezoelectric sensors model 113B28 (max pressure measured: 3.447 bar, sensitivity: 15mV/kPa, rise time: 1µs) were screwed onto a longer steel pencil shaped structure (Figure 4-10). To avoid overheating of the sensors a cooling system was designed in the structure of the gage. The gage was positioned above the tube as close as possible to the tube wall to capture the overpressure decay in the near-field of the tube (Figure 4-8 b and c).

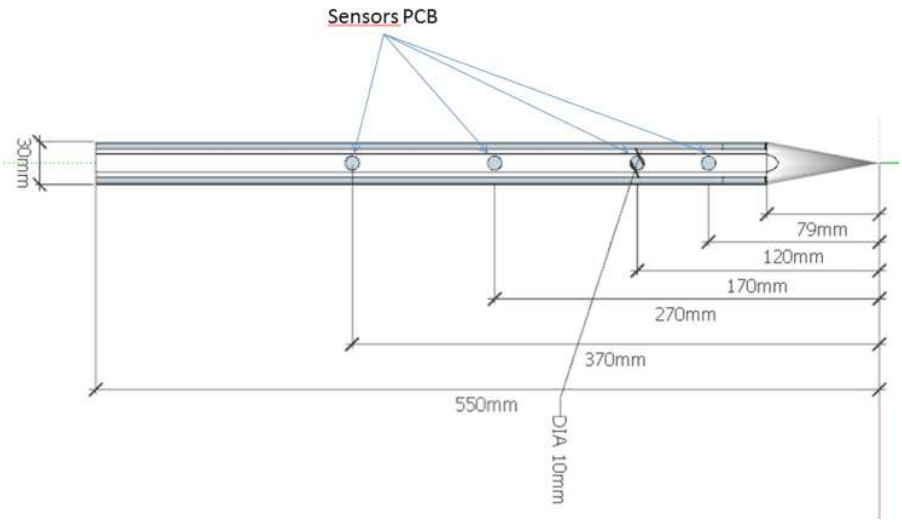

Figure 4-10 Schematic of the four-sensor blast gage

Four load cells were placed under the base plate of the apparatus (one on each corner of the plate) in order to measure the ground force generated by the BLEVE. Each of these PCB piezoelectric sensors (model M202B) can measure up to 44.48kN, with a sensitivity of 112.4mV/kN (+-15%), with a max frequency of event captured at 60 kHz. It must be noted that a steel plate of 8kg is mounted on top of the load transducers, increasing the mass of the system, thus reducing the maximum response frequency of the system. The total load will be the sum of the four signals. Due to the constraints of assembly, they were mounted to measure compression only; the values of negative signals will not be relevant when measured.

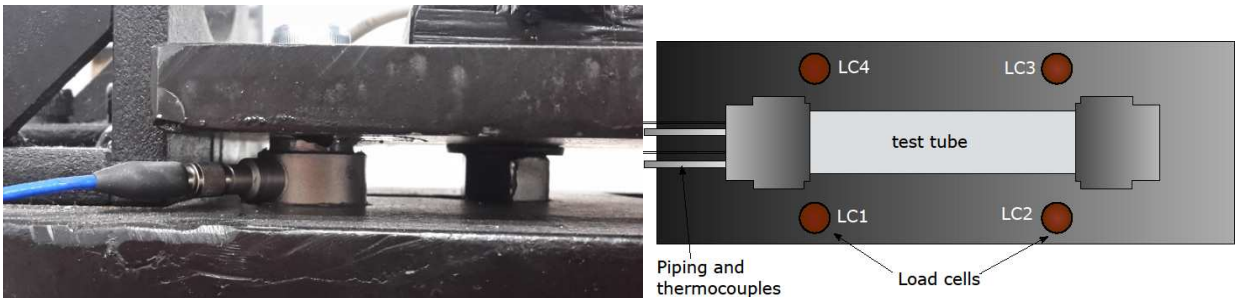

Figure 4-11 Load cell mounting (left: photo of one load cell mounting under the base plate; right: descriptive scheme of the 4 load cells with regards to the tube

One high speed pressure transducer with thermocouples and piping was placed inside the vessel at the end of the tube in the center of the end cap. It was a PCB piezoelectric sensor model M101A02 calibrated to measure a max pressure of 34.5 bar, with a sensitivity of 6760 kPa/V and a rise time of 1.5µs. Its purpose was to measure the pressure behavior in the vessel when rupture occurs.

Table 4-1 Sensor characteristics

Sensor use	***Designation***	***Range***	***Response time***	***Sensitivity***	***Uncertainty***
Static pressure in the vessel	TCDirect 716-072	0-40 bar	0.5s	0.4mA/bar	+/-0.3% of measurement
Blast around the vessel	PCB 137A23	3.45 bar	4 µs	14.5mV/kPa	0.2% Full scale (7mbar)
4-sensor blast gage above the vessel	PCB 137B28	3.45 bar	1µs	14.5mV/kPa	< 0.2% Full scale (7mbar)
Transient pressure drop in the vessel	M101A02	34.5 bar	1.5µs	0.15mV/kPa	< 0.4% Full scale (138 mbar)
Ground loading	PCB M202B	44.5 kN	60Hz max frequency	112.4mV/kN	< 0.2% Full scale (0.01 kN)
Temperature in the vessel	Thermocouple Type K (1mm diameter)	-270 to 1260°C	Low speed*		Greatest of +/- 2.2°C or +/- 0.75%

** response time small enough for the low speed heating monitoring, but not guaranteed for explosion phenomena*

V - Data acquisition and Control

V-1. Low speed data acquisition chain

Low speed pressure transducer data was collected through a current input module National Instruments NI-9103 (maximum sample rate 200kS/s, 16bits, -20mA to 20mA). Thermocouples were plugged into a temperature input module National Instruments NI-9211 (maximum sample rate 14S/s, accuracy 0.92°C, 4 input channels). Data was gathered on a computer through a Labview home-made program at a sample rate ranging from 1 to 100Hz depending on the tests.

V-2. High speed data acquisition chain

The high speed data from the piezoelectric transducers (blast, transient pressure and ground load) was collected by signal conditioners (PCB 483C50) and sent to a transient recorder DAQ HBM Genesis GEN7t (transfer rate 400MB/s), mounted with 2 acquisition cards GN815 (8 analog channels, input range +-10mV to +-50V, sample rate 2MS/s) and one acquisition card GN610B (6 analog channels, input range +-10mV to +-1000V, sample rate 2MS/s). The data was collected and processed with Perception, proprietary software from HBM. The acquisition sample rate was set at 200kS/s. The trigger was set on the blast gage dP5 (Figure 4-8). It was set at a 45^{o} angle to avoid a false trigger from potential drift due to the heating just below for the vertical 4-probe sensor. A manual trigger through the graphic user interface was set as a back-up, but has never been necessary.

VI - High Speed Imaging tools and techniques

VI-1. Optical material available and optical axes

Coupled with the high speed data acquisition system, high speed imaging allowed a clear visualization of the phenomenon for quick interpretation, and qualitative conclusions as well as quantitative input of shock detection. The optical techniques used were direct visualization and shadowgraph.

The instruments available at the lab are 4 high speed cameras (Phantom V711, Phantom V2512, Phantom VEO710 and Photron SA3). These cameras are based on CMOS sensors coupled to rolling buffer memory, leading to very large rapid memory capacity (8 to 288GB depending on the model), thus high speed acquisition at full frame. Rolling buffer memory is FIFO memory giving the possibility to effectively trigger the recording images sequence before and after the triggering event (live image change, external signal, etc) . More details on the camera technology is given by (P. Slangen et al., 2016; Pierre

Slangen et al., 2016). In the early stage of the experiment, some high speed imaging has been done with a Photron SA5. However poor lighting did not allow to use this camera to its best capacity. The main characteristics of the cameras are summed up Table 4-2.

Table 4-2 Camera characteristics

Camera	Max frame rate at full resolution	Full frame (pixels)	Min exposure time (µs)
Phantom V2512	26 kfps	1280 x 800	1 (0.265 with FAST option)
Phantom V711	7 kfps	1280*800	1 (0.3 with FAST option)
Phantom VEO710	7.4 kfps	1280 x 800	1 (0.3 with FAST option)
Photron SA3	2 kfps	1024 x 1024	2
Photron SA5	7 kfps	1024 x 1024	1

Further information on each camera is available on the constructors' websites (Table 4-3).

Table 4-3 Link to camera datasheets

Camera	Link to data sheet
Phantom V2512	https://www.phantomhighspeed.com/products/cameras/ultrahighspeed/v2512
Phantom V711	https://www.phantomhighspeed.com/products/cameras/vseries/v711
Phantom VEO710	https://www.phantomhighspeed.com/products/cameras/veo/veo710
Photron SA3	https://photron.com/wp-content/uploads/2014/07/FASTCAM_SA3.pdf
Photron SA5	https://photron.com/wp-content/uploads/2014/07/FASTCAM_SA5.pdf

The camera were used in various configurations for the last stage of the experiments (2017):

- Direct visualization from the side of the vessel was set to observe the opening mechanism. The Photron SA3 was installed for this purpose, with a lens Tamron 70-300mm capturing the event at 10000fps. The lighting used for this optical axis was an Veritas Constellation 120 (20000 lm).
- Direct visualization from the end of the vessel was set to observe the internal boiling through the end window. The Phantom V711 was positioned for this purpose capturing the event at 21000fps. Superlum LED lamps 18lm were mounted and directed inside the vessel.

- Shadowgraph from the side of the tube captured the shock propagation out of the tube at the opening. The phantom V2512 was set for this purpose. A Z-type 2-mirror shadowgraph system was installed, with 2 parabolic mirrors of 30cm diameter and 2.54m of focal distance. A high power Hg(Xe) arc-lamp was used for this application (Newport 66142 500W). The light beam was focused to a point source placed at the focal point of the parabolic mirror. The camera speed was between 20000fps to 37400fps depending on the tests. A Tamron 70-300mm zoom lens was used for the optics.

  During some of the testing, a Z-type 2-mirror shadowgraph was installed along the longitudinal axis of the tube with the Phantom V711, with similar mirrors and a single Superlum LED 18lm light source. The purpose of this system was to capture the shock along another axis in order to better understand its 3 dimensional behavior, as well as to validate the technique with 2 simultaneous captures.

- A system for the direct visualization of the top of the tube was installed in order to observe and measure in more detail the crack opening phenomenon. The Phantom VEO710 was used for this purpose. A LTM cinepar 575W HMI projector was used for the lighting of this optical axis.

More characteristics about the lighting devices are available on the constructors' data sheet (Table 4-4)

Table 4-4 Link to lighting device datasheets

Device reference	Link to data sheet
Veritas Constellation 120	https://veritaslight.com/constellation-120/
Hg(Xe) arc-lamp Newport 66142 500W	https://www.newport.com/medias/sys_master/images/images/hfb/hdf/8797196451870/Light-Sources.pdf
Superlum LED 3.8lm	https://www.superbrightleds.com/moreinfo/through-hole/5mm-white-led-30-degree-viewing-angle-18000-mcd/256/1183/

LTM Cinepar 575W HMI Projector

LAMP SPECIFICATIONS

Watts	Color Temp	Item #	Price
575	5600°K	GBHS575HR	209.95

PHOTOMETRICS

MEDIUM FLOOD LENS

Distance	Beam Diameter	Footcandles	Lux	F-Stop*
15' (4.6m)	7.4' (2.3m)	815	8,770	16.5
20' (6.1m)	9.9' (3.0m)	458	4,928	16
25' (7.6m)	12.3' (3.7m)	293	3,153	11
30' (9.1m)	14.8' (4.5m)	204	2,195	8.5

NARROW SPOT LENS

Distance	Beam Diameter	Footcandles	Lux	F-Stop*
15' (4.6m)	2.4' (0.7m)	6,000	64,560	45.8
20' (6.1m)	3.2' (1.0m)	3,375	36,315	45
25' (7.6m)	4.0' (1.2m)	2,160	2,3241	36.5
30' (9.1m)	4.8' (1.5m)	1,500	16,140	22.5

*1 foot candle = 10.76 lux. F-stops provided as a general guide only. *With ISO 100 film @ 1/8 sec.*

The optical data configuration is summarized in Table 4-5

Table 4-5 Summary of high speed optical axes and properties

Axis of view	Camera		Frame rate (fps)	Resolution	Exposure (µs)	Aperture	Magnifigcation (mm/pixel)
Direct radial	Photron SA3	DIR 1	10000	256 x 512	100	f/5.6	0.852
Direct axial	V711	DIR 2*	21000	600 x 512	1 - 6	f/2.8	0.256
Shadowgraph radial	V2512	SDW 1	25000 - 37400	800 x 1200 - 896 x 720	1 - 5.938	f/5.6	0.235-0.256
Shadowgraph axial	V711	SDW 2*	22400 - 26000	640 x 480 - 512 - 480	2	f/2.8	0.581-0.620
Direct top	VEO710	DIR 3	19000 - 22000	640 x 512 - 640 x 448	10 - 3	f/5.6	0.408

The positions of the cameras are presented in Figure 4-12. The direct axial view DIR 2 (through the window) and the shadowgraph axial view SDW 2 were done using the same camera (V711), hence both views are not available on the same test. Thirteen tests were done with axial shadowgraph and 6 with direct view through the window.

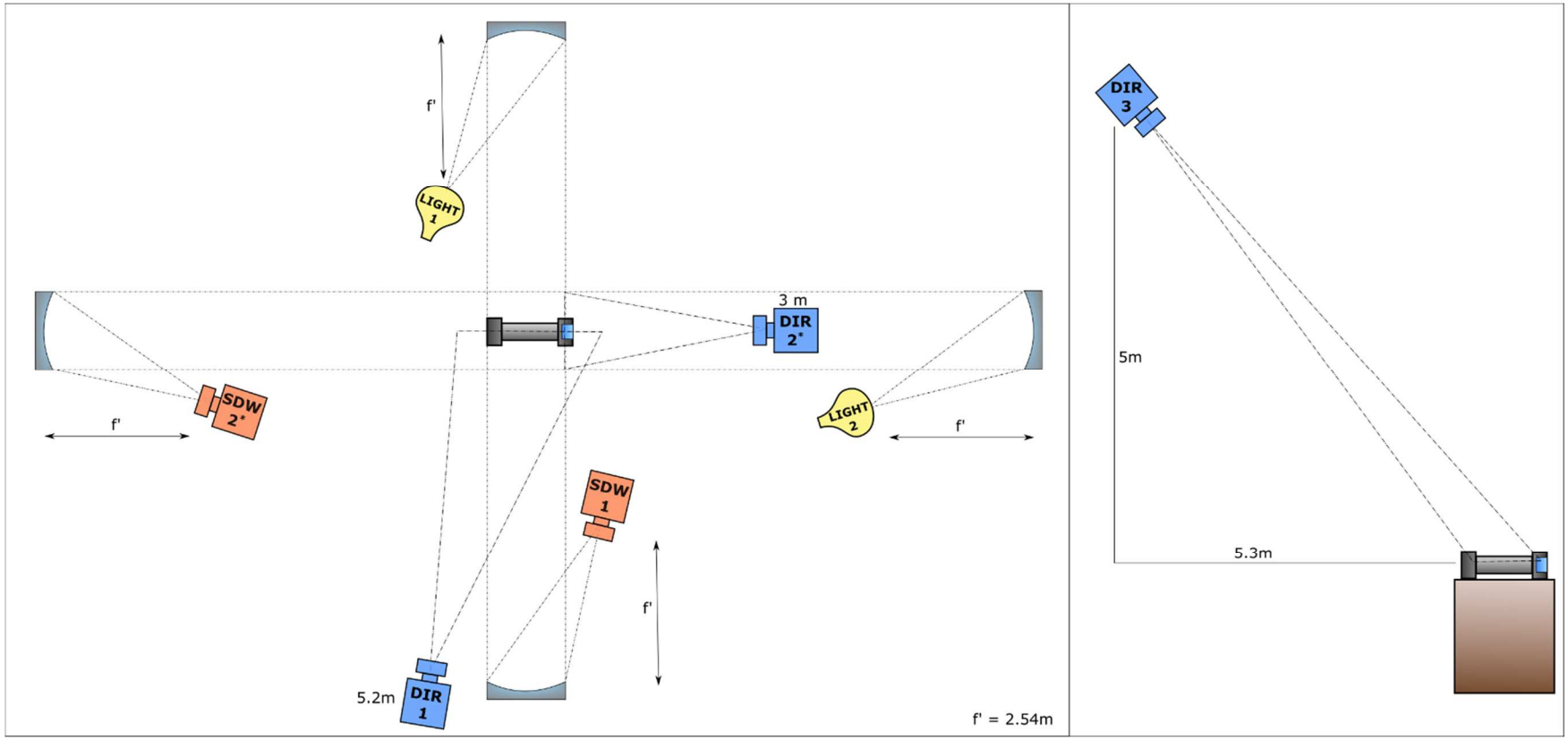

Figure 4-12 Optical axes of measurement

VI-2. **Shadowgraph optical technique**

In order to understand the images seen through shadowgraph, an introduction to this optical technique is presented. Shadowgraph is an optical technic which allows observation of density gradients in transparent media such as air or water. The principle is to observe the shadow of a phenomenon that refracts light due to the gradient in the index of refraction. It is similar to observing the shadow of the waves at the bottom of a swimming pool from the sun (Figure 4-13 left), or the shadow of convection from a heater by a window under strong sunlight. In the scientific community, it is used in many supersonic applications as a way to detect shockwaves for applications such as supersonic projectiles (rifle bullet in Figure 4-13 right) or explosions.

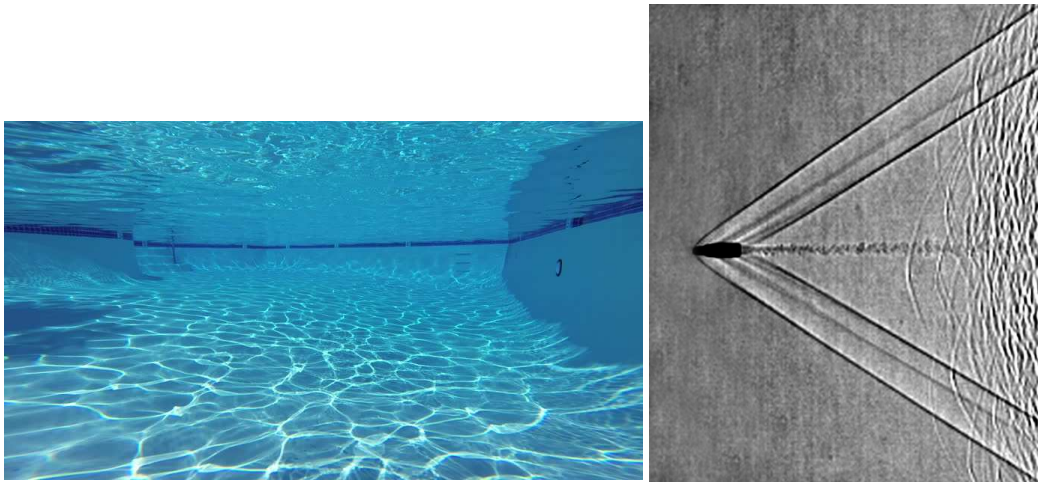

Figure 4-13 Examples of shadowgraph visualization (left: pool bottom projection of the waves at the surface; right: shocks generated by a rifle bullet ((Settles, 2001)*, CC BY-SA 3.0)*

The base principle of shadowgraphy is to use the variation of refractive index with fluid density. This variation is set by the Gladstone-Dale relation:

$$n - 1 = k\rho \tag{40}$$

Where n is the refractive index, k is a Gladstone-Dale constant and ρ is the density of the fluid. Shadowgraphy consist in capturing the deviation of the light ray induced by this change of refraction index. The density gradient is observed through the second derivative of the refraction index for shadowgraph. It allows the observation of sharp changes in density field, such as those that occur in shocks.

One parameter of the optical technique is its sensitivity: it is defined by the size of the smallest variation than can be observed. Parameters such as camera resolution, choice of the technique and proper optical setting have a strong influence on the sensitivity.

More sensitive techniques exist, like schlieren. They capture smaller changes in density, like weaker compression waves and expansion waves, temperature changes, etc. More details on these different techniques is available in the literature (Merzkirch, 1987; Settles, 2001).

VI-2.1. Z-type 2-Mirrors shadowgraph system

By having a point source light placed at the focal distance of one parabolic mirror, a parallel light beam is generated from the mirror. The object of study is placed in this parallel light beam. Any change of refraction index that happens in this light beam will be captured. The parallel light is then focused through another parabolic mirror. A camera is placed at the focal point of the mirror to capture the deviation of the optical light ray, thus the second derivative of the refraction index. (Figure 4-14). The camera can be focused on the object of study, for sharper contours. However, a common practice is to focus further away from the object, to increase the sensitivity of the shadowgraph on the density changes happening in the test section.

The main drawback of the Z-type shadowgraph system is that the size of the field of view is limited to the size of the parabolic mirrors. They are an expensive and fragile component of the optical setup, particularly when considering that an explosion will occur in the test section. So the distance between mirrors and "explosion" must be increased. This leads to integrate more optical path in the set up and so noise coming from other sources (heating, fanning) than the phenomenon under study.

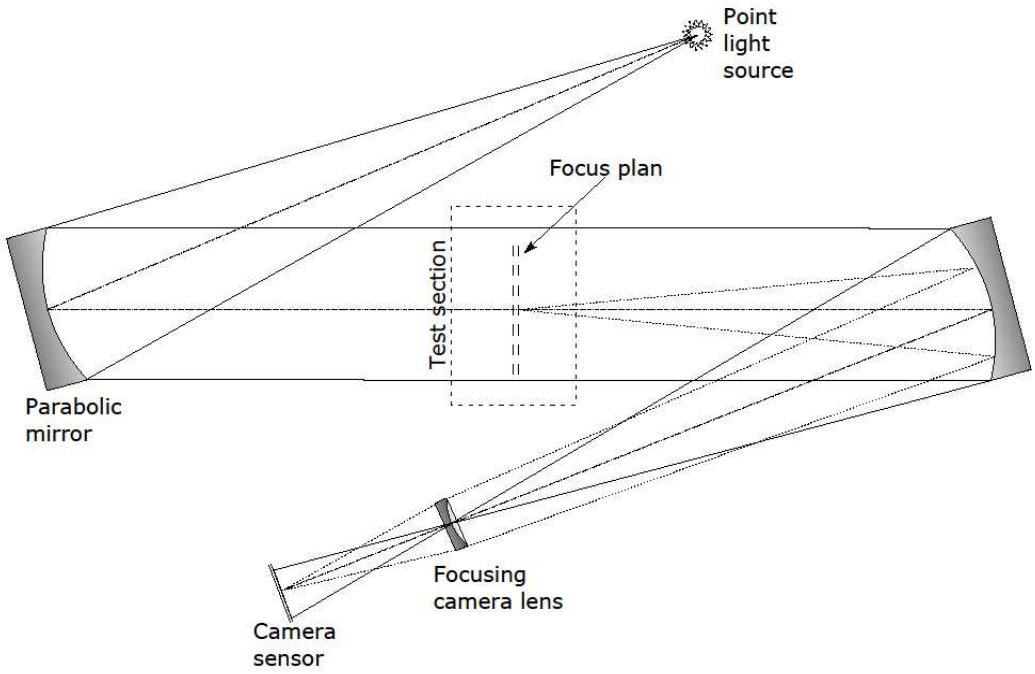

Figure 4-14 Scheme of Z-type shadowgraph configuration used in the testing

VII - Choice of experimental key parameters

The purpose of the experiment was to understand the behavior of a few hazard key parameters: dP_{max} maximum overpressure, F_{max} maximum ground loading, and some secondary flow patterns.

The experimental setup and the parameter choices bring constraints over some independent variables: fluid properties, vessel material properties, vessel dimensions. The main independent variables chosen to be varied with control are summarized in Table 4-6.

Table 4-6 Key independent parameters varied with control over the small scale experiments.

Variables	P_{fail}	Φ_{fill}	L_w	R	θ
Designation	Failure pressure	Liquid volume fraction	Weakened length	Distance of blast measurement to tube opening	Angle of blast measurement from horizontal
Range	11→ 32 bar	0 → 100%	50 →150 mm	0.15-0.2-0.3-0.4-3m	90° (vertical)– 45° – 0° (Horizontal)

VIII - **Experimental Procedure**

The experimental protocol was composed of the following steps:

- Sealing of the tube: Swagelok fittings placed on each end of the tube using a MS-MHSU-O-E Swagelok swaging machine. These are manually tightened using a tightening control gage. The tube is then set up on the base plate by locking it, screwing the fill and vent pipes, and plugging the transient pressure sensor and thermocouples.
- Purge of the tube: 3 successive fills and vents of the tube with vapor propane, to replace the air in the tube by propane.
- Filling the tube to the wanted mass of liquid propane. Initial pressure in the tube is then between 6 to 8 bars, depending on its temperature when in the tube.
- Heating of the tube with the electric heater plate to increase the pressure inside until rupture. The rate of heating ranged from 0.5 to 1 bar/min.
- Acquisition of the data at rupture with automated trigger.
- Venting of the test facility to eliminate residual propane and avoid VCE risks.
- Taking pictures of the results of the explosion; saving the data; removing broken tube in preparation for a new test.

IX - **Safety**

To remove overpressure hazards for the persons present on the testing site, all experiments could be controlled remotely from the control room. No one was permitted to be in the experimental room when the tube was under pressure.

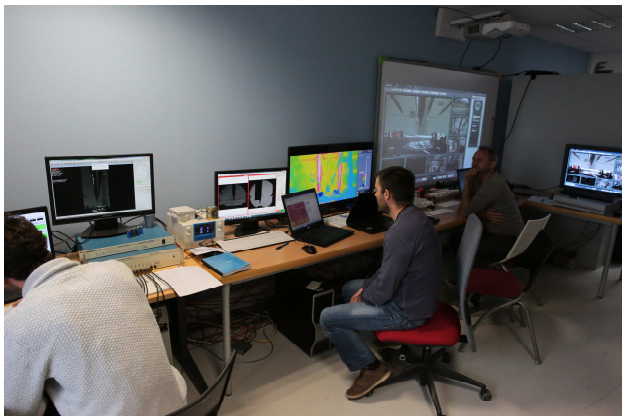

Figure 4-15 Spark control room

It has to be noted that experimental BLEVE occurred in the closed testing facility (in a 150 m^2 space), releasing propane in the room. Using propane introduces the risk of ignition, fire and explosion. As far as possible ignition sources were removed or protected in pressurized shelter. In particular, the burner for heating the tube was replaced by an electric heater. Moreover, 3 FID Mocon Baseline Series 9000 (2 at Full-scale 1 - 20,000ppm (Methane) and one at Full-scale 0.01 - 100% (Methane)) were set to detect the flammability threshold of the propane concentration after release, in order to gage when it was safe to return into the experimental room after venting. The detection sites were placed at 3 different heights near the test tube, (ground level, 1.5m and 3m).

A thermal camera FLIR GF320 was used to detect propane leaks during the test, allowing to stop a test if the leak was considered too large.

In case of emergency or technical issue, the propane was released by an emergency valve and pipe to a flare located outside the building.

Chapter 5

Experimental results

I - Summary of the test campaigns

Twenty-four propane explosions and one air vessel burst were performed during the final series of testing of the small scale apparatus. The control parameters for failure were failure pressure P_{fail}, liquid volume fraction Φ_{liq}, and the machined weakened length on top of the tube L_w. Failure pressure ranged from 11.6 bar to 32.7 bar. The liquid volume fraction ranged from 0 to 100%, with three main intervals of data: approximately 20%, 60% and 90%. Finally, 4 different cut lengths were tested: 50mm, 75mm, 100mm and 150mm. Twenty tests out of 25 were conducted with a 150mm cut, and the 5 remaining tests with the other lengths. Figure 5-1 summarizes all the tests based on these 3 parameters.

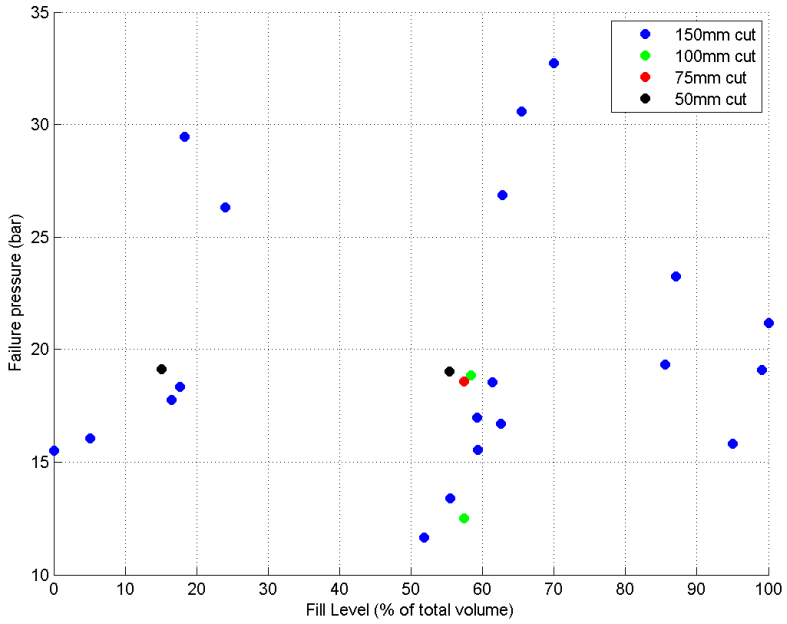

Figure 5-1 Failure control parameters of all tests on a Liquid Fill - Failure Pressure scatter plot

Due to slow heating, convection in the liquid resulted in uniform liquid temperature such that almost all tests were on the propane saturation line at failure (Figure 5-2). This meant that no temperature stratification was present in the liquid phase, so the liquid superheat state was the strongest possible at failure. Three exceptions are visible on the P-T diagram: two tests gave results above the saturation line,

and one test gave results below. The test yielding results below corresponded to a vapor test, with no liquid. The vapor was superheated in this case, leading to a pressure vessel burst with vapor propane. The test result closest above saturation corresponded to the air case. The saturation line of propane is not relevant for this case. The case is kept on Figure 5-2 for comparison purposes. It shows that burst occurred at a pressure equivalent to the propane vapor case. Finally, the test result well above the saturation line in the compressed liquid region corresponded to a test overfilled with liquid. It was a hydraulic failure due to liquid dilation during the heating of the vessel. Thus, as noticed in the results, the energy in the liquid was much weaker than near saturation. These three cases with test results not on the saturation line are not considered as BLEVE due to lack of superheated liquid.

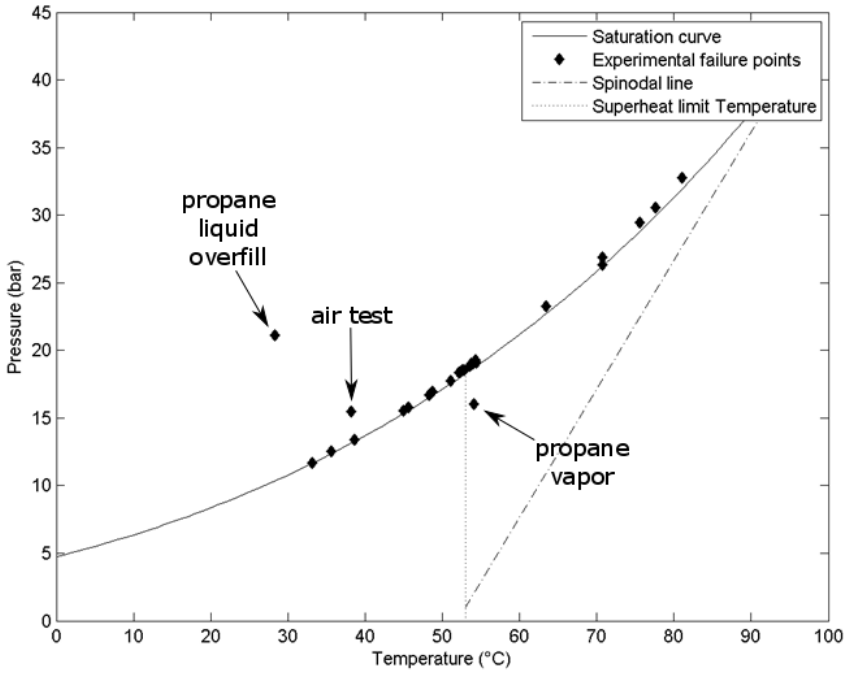

Figure 5-2 P-T diagram with failure condition of all plots with propane saturation curve

I-1. Earlier test campaign summaries

Previous test campaigns are also plotted on a P-T diagram with their corresponding saturation curve. Substances used for these tests were water (Figure 5-3 left) and commercial propane (Figure 5-3 right).

Some low failure pressure tests with water led to partial failure only. This was partly due to the weakening process caused by a flame heating the top of the wall. The control over this process was very limited and led sometimes to partial failure with jet flow through the opening. Moreover, the water was not always at saturation before failure. The process of heating was much faster with flames than with the

electric heater, leading to potential stratification in the vessel. Similar observations were made for the commercial propane tests (Figure 5-3 right).

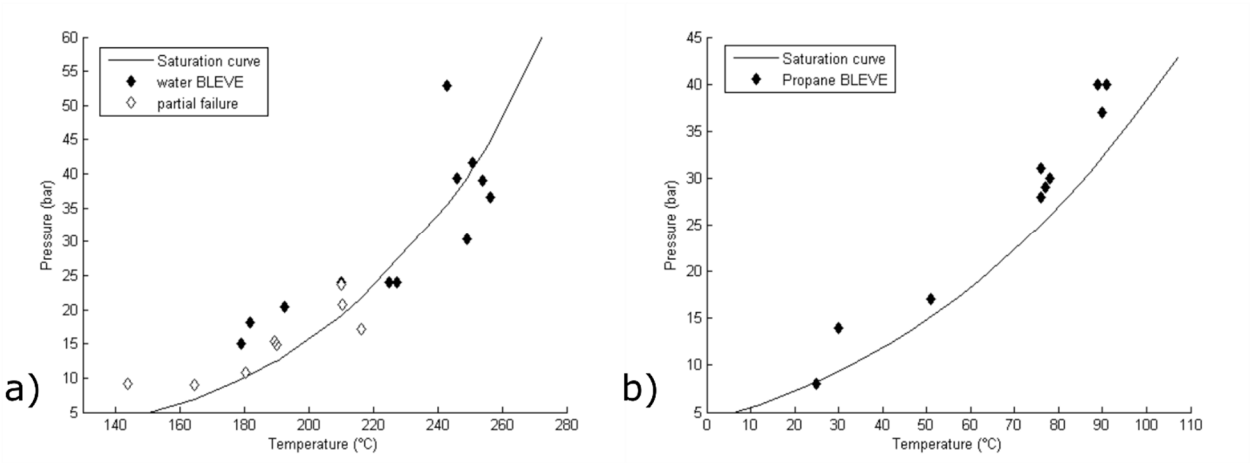

Figure 5-3 P-T diagram with failure conditions for water BLEVE test campaign (2014 and 2015) (a) and commercial propane (2015) (b)

II - Rupture patterns

Various types of failure patterns were observed during the experimental campaigns depending on the experimental conditions. The main patterns noticed in the first campaign were either a partial vessel opening in a fish-mouth pattern (Figure 5-4) or a complete opening, with the vessel flattened on the base plate and even tears up the vessel sides, resulting in three separated pieces after the burst (Figure 5-5). These patterns were very comparable to actual vessel failure.

Figure 5-4 Partial failure with fish-mouth type of opening ($P_{fail} = 15bar$, $\Phi_{liq} = 60\%$, wall thickness = 0.9mm)

Figure 5-5 Full opening: catastrophic failure with flattening of the tube and separation into 3 pieces ($P_{fail} = 20bar,\ \Phi_{liq} = 60\%$, wall thickness = 0.9mm)

The conditions under which these patterns occur is shown Figure 5-6, where each failure was plotted against its failure pressure and the longitudinal length of the rupture. For the water BLEVE of 2014, the weakening of the tube was done with a burner on top of the vessel at different distances in order to vary the weakened area on top of the tube. This was the most realistic of the weakening processes used in this experiment. It mimicked real engulfing fires. However it was difficult to have complete control over this parameter independently from the others parameters.

Data showed that all partial failures had a failure length smaller than the tube diameter, while all of the catastrophic failures led to failure lengths from 1.3 to 2.1 tube diameter. Moreover, catastrophic failures were associated with significantly larger failure pressure than partial failures. This was particularly noticeable for thick walled tubes.

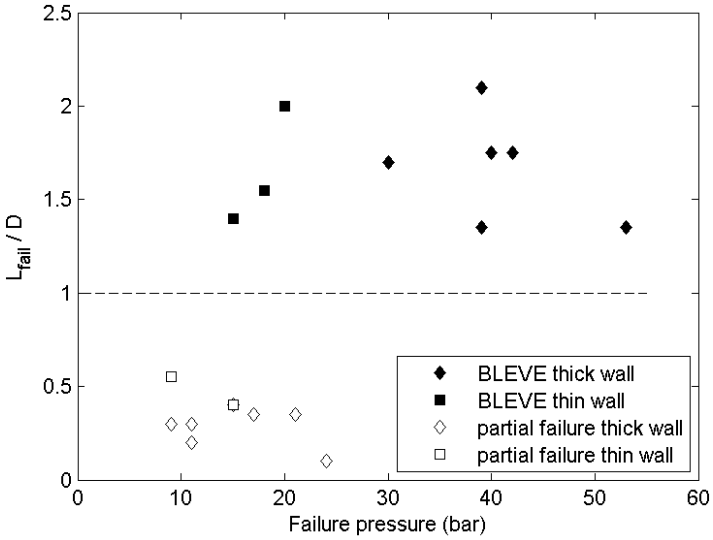

Figure 5-6 Mapping of failure types with failure pressure and failure length (water BLEVEs 2014)

During the next test campaign, fewer partial failures were studied as they were not interesting for the pressure field characterization. To force the vessel into catastrophic failure, the weakened lengths chosen when machining the tube were always equal to or above one diameter (50mm and above).

The machining process was less realistic when compared to fire weakening, but much more controllable. The presence of the electric heater plate below the tube limited the propagation of the crack around the full diameter of the vessel, impacting the realism of the catastrophic failure. Catastrophic failures of the latest BLEVE from 2017 were characterized by a tube flattened on the base plate, molding to the shape of the heater beneath the tube and remaining in one single piece, as seen Figure 5-7. This was still considered to be a full opening.

Figure 5-7 Full opening: catastrophic failure with flattening of the tube ($P_{fail} = 18.3bar,\ \Phi_{liq} = 18\%,\ L_w = 150mm$)

The complete flattening of the tube was still a strong characteristic differentiating BLEVE from non-BLEVE. One vessel burst was made with air only, leading to a large opening but the tube was not fully flattened (Figure 5-8). As recognized in the literature, the superheat boiling of the BLEVE certainly has a noticeable impact on the destruction of the vessel.

Figure 5-8 Full vessel opening from air burst ($P_{fail} = 15.5bar,\ Air, L_w = 150mm$)

Finally, due to the different cut lengths, we observed one-sided opening (Figure 5-9). This pattern was due to the limited surface of tube wall available for the boiling fluid to exert pressure and tear the vessel. It was also due to low failure pressure. This failure pattern was an intermediate between the partial failure, where the work from the pressurized fluid did not have the ability to tear the vessel wall radially, and the catastrophic failure, where the expansion work from boiling flattened the vessel wall fully.

Figure 5-9 One-sided openings (left: $P_{fail} = 19.0bar,\ \Phi_{liq} = 56\%, L_w = 50mm$; right: $P_{fail} = 12.5bar,\ \Phi_{liq} = 59\%, L_w = 100mm$)

All rupture patterns from 2015 and 2017 are summed up in I - .

III - Physical measurements of BLEVE experiments

III-1. Heating monitoring: pressure and temperature in the tube

The evolution of the heating process was monitored by measuring pressure and temperature in the tube before failure.

As seen in the experimental setup section, two pressure sensors were used to measure the pressure in the filling pipe and the pressure in the venting pipe. The two phases were at equilibrium during heating. The pressure was the same in the entire tube during this phase. It was verified by having very similar signal between the 2 pressure sensors (difference < 4%).

The configuration of the thermocouples was similar to the pressure sensor-configuration (top vapor and bottom liquid, depending on the fill level of the test). However, unlike pressure, the system did not have to have a uniform temperature distribution in the vessel: It could be stratified. This would induce a hot layer of liquid at the liquid-vapor interface, which set the saturation pressure. In this case, the average state of the liquid was subcooled due to a core temperature lower than the temperature corresponding to the saturation condition.

To verify if the liquid was at saturation, pressure and temperature of the liquid (or temperature from the bottom thermocouple when there was a low liquid level) were plotted on the saturation curve of propane for each test. For most of the tests, the data matched the saturation conditions very well during the entire heating process, thus validating that the heating was slow enough with respect to the thermal inertia of the tube to have no stratification (Figure 5-10). The liquid had the maximum thermodynamic energy before failure. The data on the P-T diagram after the burst must be considered very carefully for two reasons:

- The sampling rate of this pressure and temperature were only up to 100Hz which was too slow to notice the full behavior of the pressure variations in the tube;
- The thermocouples were quickly pushed out of the tube during the explosion, thus the temperature measured does not correspond to the exact temperature in the tube after the drop (Figure 5-7).

As mentioned above, one test did not explode at saturation conditions due to overfill. It led to a hydraulic burst of the vessel induced by the thermal expansion of the propane (Figure 5-11). The energy in the liquid at failure was lower than saturation conditions: it did not generate a shock wave, and it did not fully flatten the tube.

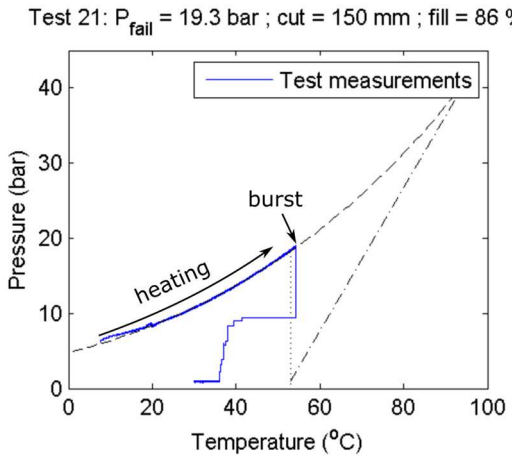

Figure 5-10 Evolution of the heating process of a test with respect to the propane saturation curve on a P-T diagram

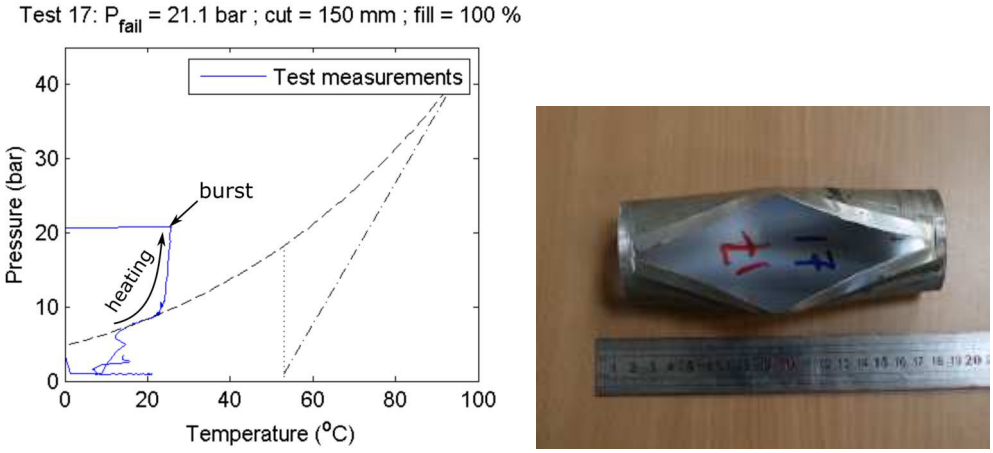

Figure 5-11 Liquid overfilled test (left P-T diagram ; right: tube not fully open after burst)

III-2. **Explosion measurements**

The following measurements present the consequences of the explosion measured at higher acquisition speed than the previous monitoring results. They allowed to build a more accurate account of the explosion.

III-2.1. Blast overpressure

One main measurement needed to characterize a blast wave is the overpressure measurement from the blast gages. As seen in the experimental setup, blast gages were placed at various distances and angles around the vessel. Four main zones in the space around the cylinder were explored.

The first zone was the vertical near-field above the vessel. The measurements from the 4-sensor blast gage provided information on the decay of the blast in this zone. It was noticed in several cases that the

maximum overpressure between the first and the second sensor were almost equal (Figure 5-12). This implied that the blast was still developing at the second sensor. The decay was then clearly visible for the third and fourth sensor. After the first peak overpressure, some cases presented a strong consistent negative (relative) pressure before leading to a second peak. This behavior was observed mostly on the first two sensors. In some cases, the pressure drop corresponded to the cloud arrival on the sensors. As the sensors were not thermally insulated, it is not clear for these cases whether the signal drop corresponded to an actual pressure drop or a temperature increase from the hot cloud touching the sensors.

It was known that for the burst of a gas sphere the shock does not fully develop until some distance away from the interface (Glass, 1974). We expected to see this in these tests. This result is discuss in the following chapter.

A comparison of the measurement made by the fourth sensor of the 4-probes sensor and a classic PCB blast sensor is made Appendix D.

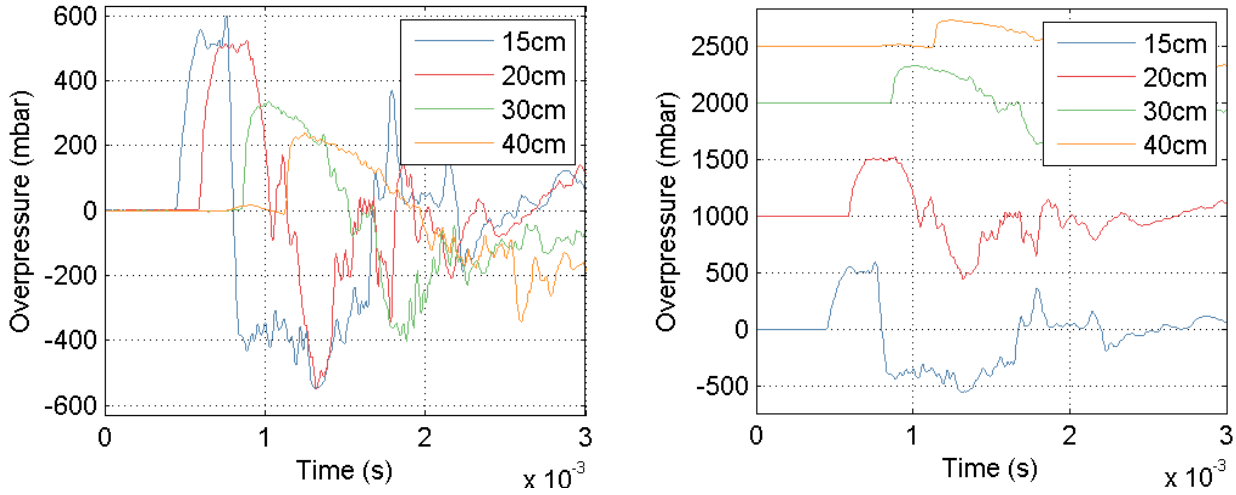

Figure 5-12 Measurements from the 4-sensor blast gage above the vessel ($P_{fail} = 17.7bar, \Phi_{liq} = 17\%, L_w = 150mm$) (left: pressure signals with same origin of pressure; right: same pressure signals shifted vertically for readability)

The near-field at a 45° angle above the vessel was measured by four sensors. The superposition of these signals showed that the maximum overpressure was the same for all directions around the vessel (Figure 5-13 left). However a major drop in pressure was measured on the sides, but not on the ends. This behavior was again observed during several tests. A hypothesis to be verified was the following: this drop in pressure revealed the presence of strong vortices on the sides, due to the sheer involved with the jet flow out the tube during the dynamic opening.

The horizontal near-field plane was measured giving maximum overpressure on the sides and end (Figure 5-13 right).

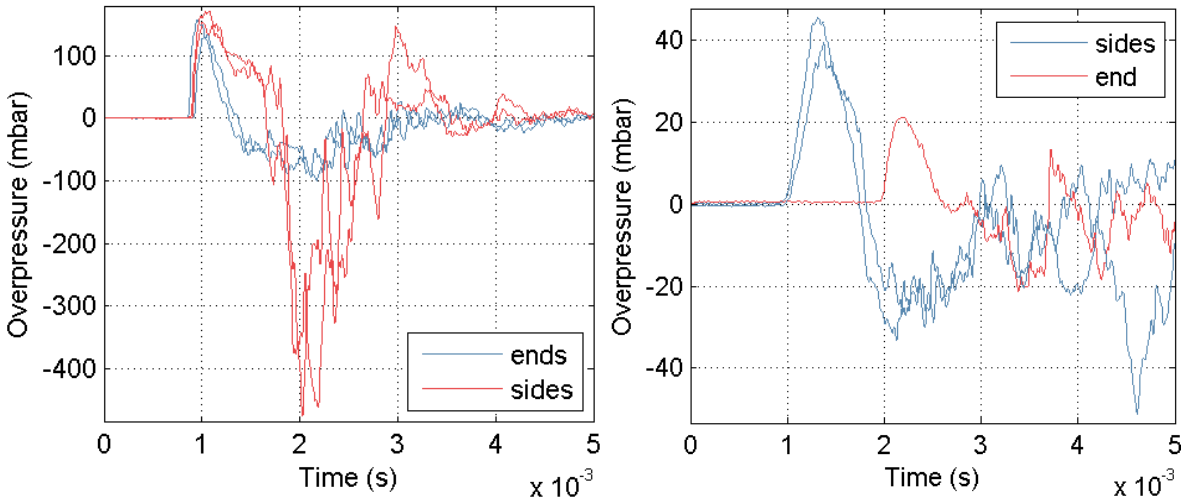

Figure 5-13 Measurements from the near-field blast gages surrounding the vessel: left: 45° angle; right: horizontal plan ($P_{fail} = 17.7bar, \Phi_{liq} = 17\%, L_w = 150mm$)

Blast gages measuring the far-field, both horizontally and above the vessel, showed that little difference existed between the side and end direction at 3m distance of the vessel on the horizontal plan (Figure 5-14). The overpressure above the vessel however showed a clear larger maximum. Moreover, the shock appeared much sharper (near vertical slope of pressure rise) on the pressure signal from the top of the vessel.

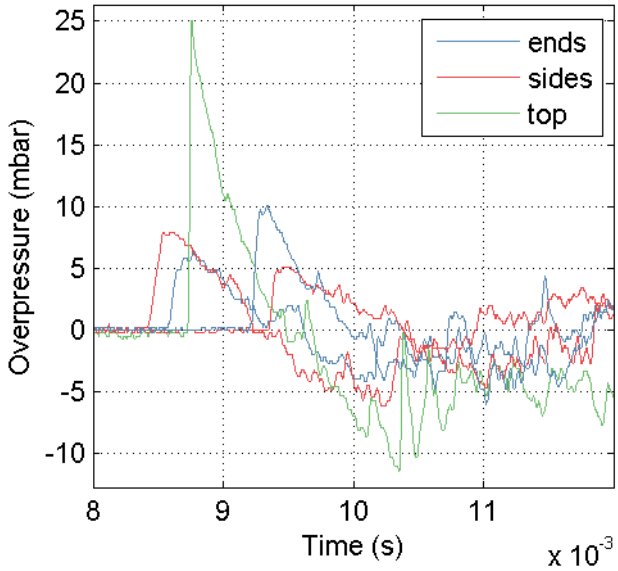

Figure 5-14 Measurements from the far-field blast gages surrounding the vessel ($P_{fail} = 17.7bar, \Phi_{liq} = 17\%, L_w = 150mm$)

III-2.2. Ground loading

As shown in the experimental program, the ground loading measurement was done through four load cells, one placed at each corner of the plate. By summing the signals of all four load cells, the total load exerted by the tube BLEVE on the plate was obtained. On Figure 5-15 left, the load profile was similar for all load cells, because this case corresponded to a fully open symmetrical failure, similar to that shown Figure 5-7. On Figure 5-15 right, the load signal obtained for a non-symmetric opening such as Figure 5-9 presented different profiles for each load cells, based on their position on the plate.

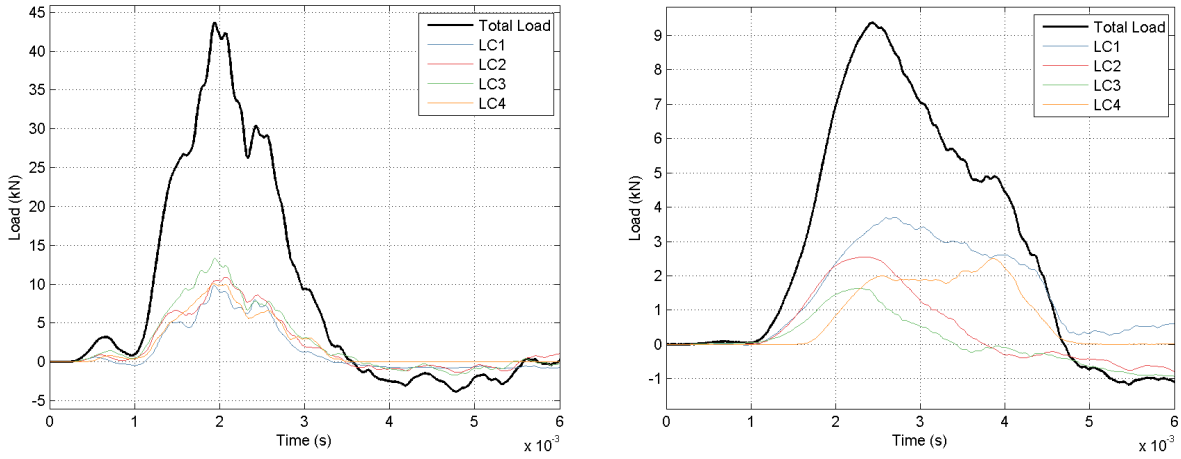

Figure 5-15 Ground loading measurement, load cells individually and total sum (left: $P_{fail} = 26.9bar - \Phi_{liq} = 61\% - L_w = 150m$; right: $P_{fail} = 19bar - \Phi_{liq} = 56\% - L_w = 50m$)

Two major aspects of the ground loading data were of interest:

- it gave a first estimate of the actual force exerted by a small BLEVE on the ground;
- comparison of its timing with transient pressure in the vessel and other measurements led to significant conclusions in term of contribution of liquid and vapor phase on the hazards.

Scaling this data to larger industry cases is introduced in Chapter 9.

III-2.3. Transient internal pressure

Transient pressure was measured at the instrumented end of the tube, at the center of the cross section. Depending on the initial conditions, several behaviors were observed. In some cases, the pressure dropped continuously from failure pressure to atmospheric pressure (Figure 5-16 (a)). Some profiles presented a slow and late pressure increase after a large drop ($> 50\%$ of P_{fail}) (Figure 5-16 (b)). One case showed a

rapid early pressure peak (Figure 5-16 (c)). Finally, an early large pressure increase occurred in some cases, after a very short pressure drop (Figure 5-16 (d)).

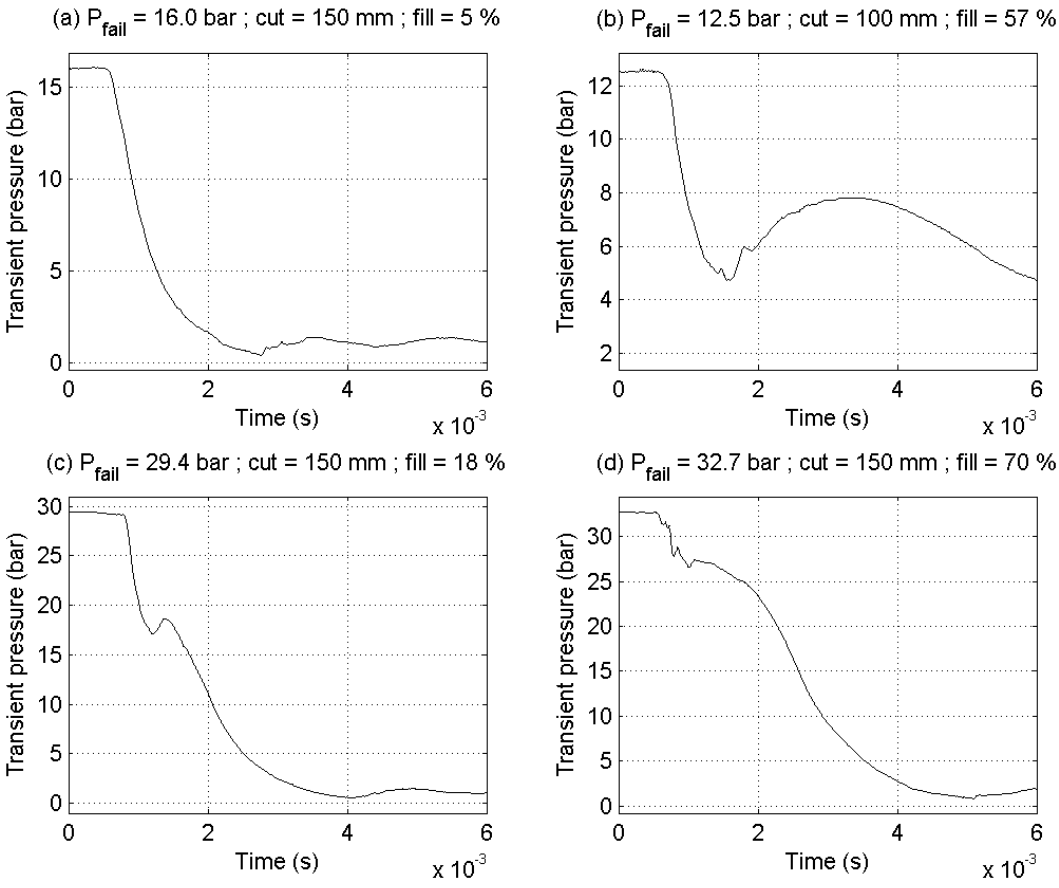

Figure 5-16 Various transient pressure profiles measured inside the tube

Characterization of the signal obtained with this sensor was analyzed in more detail in Chapter 8 .

The data introduced above is presented for all tests in Appendix E.

IV - **High speed imaging data**

High speed imaging was used to visually capture the mechanisms involved in the explosion. Different stages of the experiment under various angles are presented in the following section. The high speed imaging was intended to show:

- the tube opening process
- the lead shock formation and speed
- the flow pattern in the initial jet

- the vapor cloud formation and cloud speed
- the flashing of the liquid in the tube

IV-1. Direct imaging

IV-1.1. Side - Radial view for water BLEVE (2014)

The first test campaign provided a radial view of the explosion generated with water BLEVEs (Figure 5-17). This imaging result showed all of the stages of a realistic failure: fish-mouth opening with initial jet beginning, the crack propagating toward the ends, tube opening on the sides, and flaps of the tube flattening on the base plate below. This imaging confirmed that the small scale apparatus was able to produce realistic vessel failure.

An interesting feature observed was the evolution of the shape of the cloud with time. The initial jet became a light cloud as the crack propagated toward the ends of the tube. When the tube was sufficiently open, a second cloud that was thicker than the first seemed to emerge from the container. Due to the timing of these events, the hypothesis was proposed that the first cloud would be linked to the condensation of vapor phase expansion, while the second cloud would represent the boiling of the liquid phase.

IV-1.2. Side - Radial view for propane BLEVE (2017)

For all tests, the tube opening was observed from the side, radial to the tube, through direct imaging. Similar to the water BLEVE imaging, this axis of imaging showed various stages of the opening process. The initial crack opened longitudinally until it reached the ends of the machined section (Figure 5-18 a) and b)). The crack then turned radially resulting in a full opening, as seen section I-1. When the tube opened, a cloud appeared with various noticeable patterns. First, a thin cloud appeared, with a transparent dome inside the boundaries of the cloud (Figure 5-18 b) to d)). This cloud propagated in a V shape out of the opening. When the tube was sufficiently open and the boiling process advanced enough, a second cloud grew from inside the tube, thicker and larger than the first (Figure 5-18 f) to j)). Through observation of various cases, the two successive clouds phenomenon was repeatable. It is hypothesized that the first cloud was due to the vapor phase expanding and condensing, while the second cloud, coming later (between 0.8ms and 1ms Figure 5-18) was due to superheated liquid boiling.

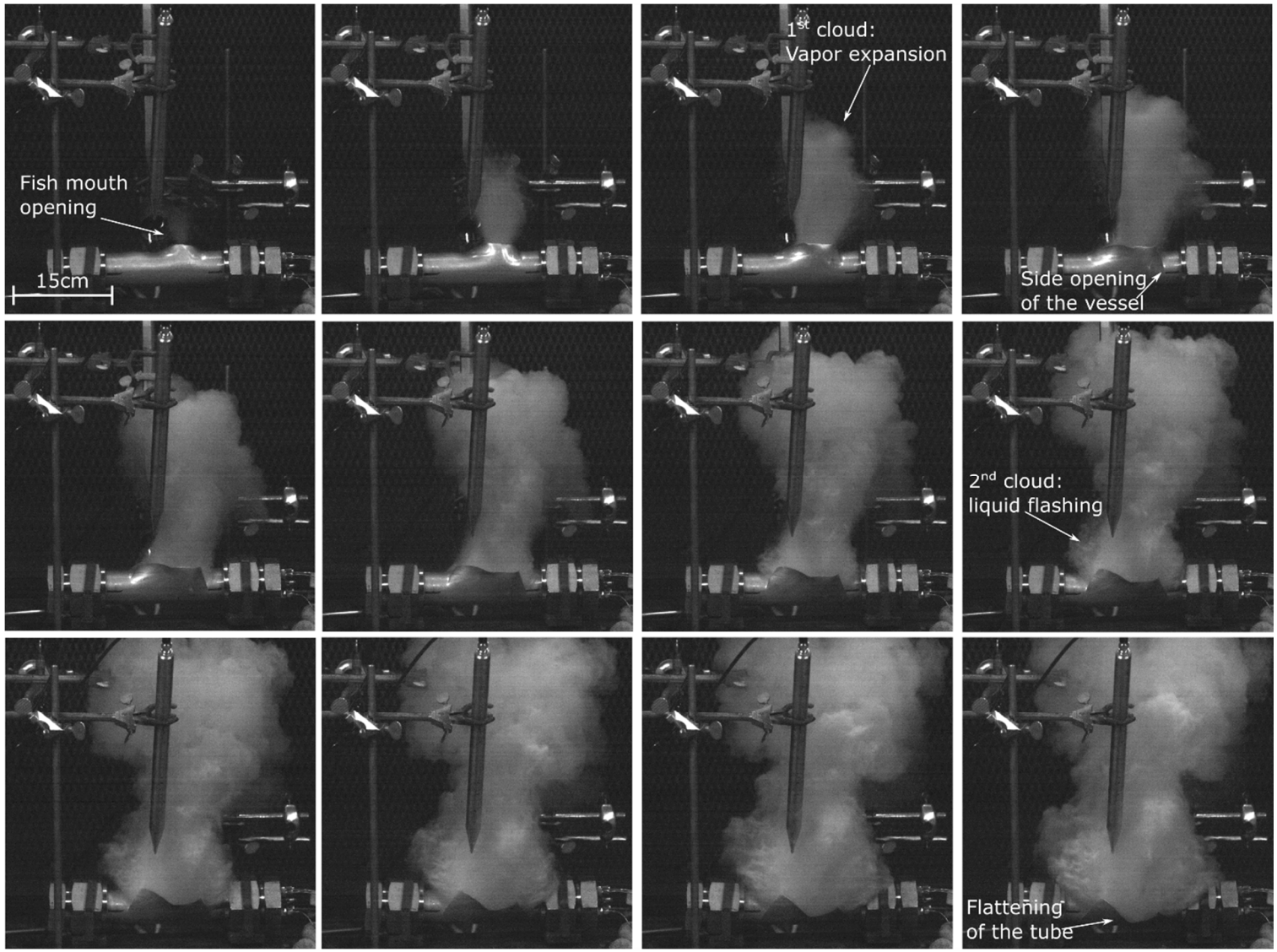

Figure 5-17 Side view with direct high speed imaging (camera Photron SA5, $\Delta t = 142\mu s$, $P_{fail} = 20\ bar, \Phi_{liq} = 60\%\ water, no\ weakening$)

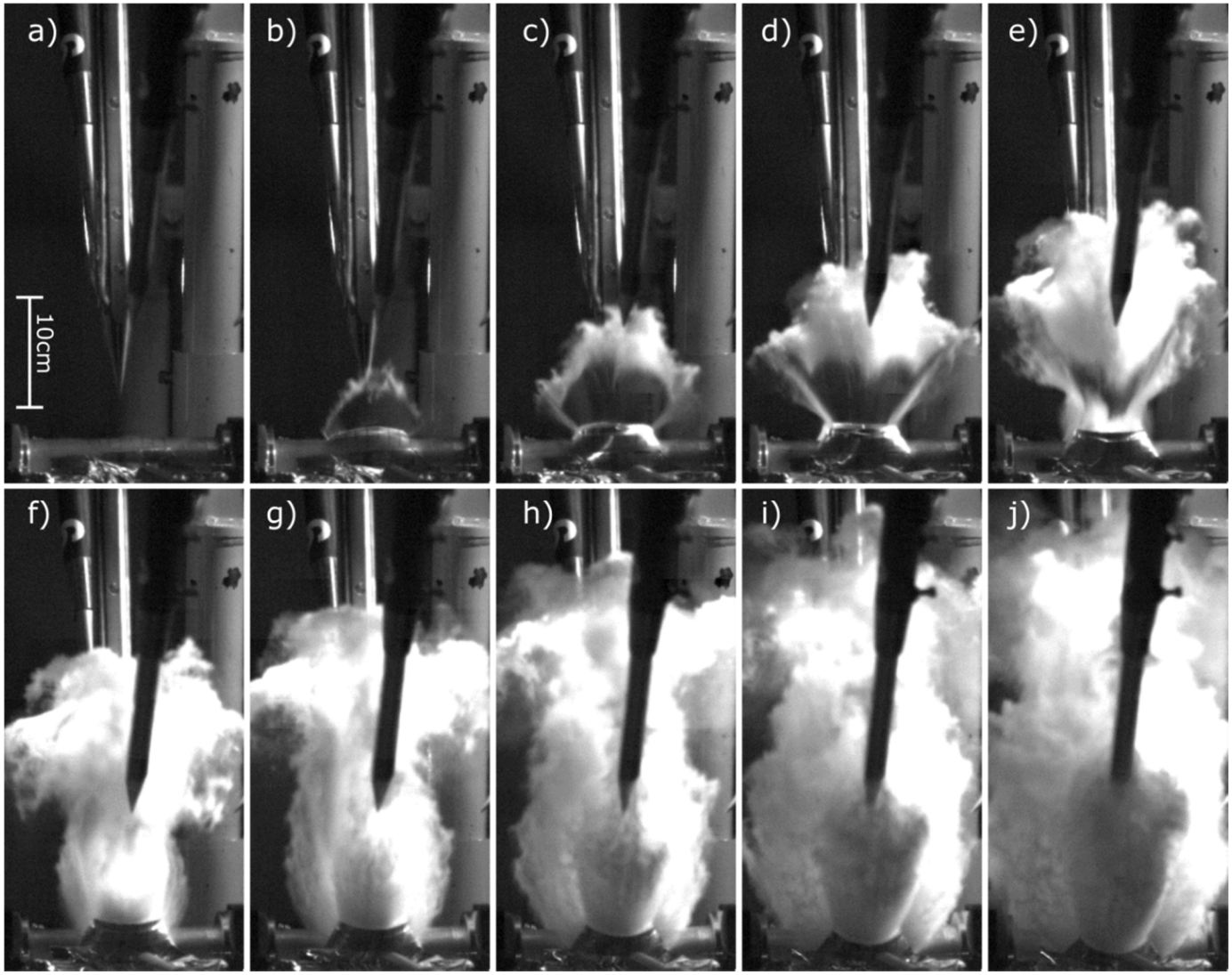

Figure 5-18 Side view with direct high speed imaging (camera Photron SA3, $\Delta t = 200\mu s$, $P_{fail} = 18.6\ bar, \Phi_{liq} = 56\%, L_w = 75mm$)

IV-1.3. Top view

Visualization from the top of the vessel allowed observation of the crack opening and propagation in the longitudinal direction. The case presented Figure 5-19 showed step by step the fish mouth opening. The duration of the longitudinal opening process was extracted from this camera view by detecting when the crack reached the end of the machined length to propagate radially (Figure 5-19 g)). $t_{open} = 0.312ms$ for the presented case, leading to a crack velocity of 240m/s in the aluminum. The image showed the liquid doing little or nothing while the vapor escaped to produce the lead shock. The liquid flashing followed after the sequence shown Figure 5-20.

IV-1.1. Axial - Window view

Direct imaging of the axial view presented two main interests: showing the shape of the escaping cloud in the axial direction, completing the radial view (Figure 5-20 a) to e)); and seeing the boiling process inside the tube due to imaging through the end window (Figure 5-20 f) to j)).

A better visualization of the liquid-vapor interface and its boiling front was made in 2015 (Figure 5-21), showing a clear vessel opening with no change inside the vessel up to $t = 0.28ms$. A blurry boiling front seems to appeared after in the background of the window, while the cloud outside the vessel grew significantly in size ($t = 0.52 - 0.84ms$). Finally, a clear whitening of the liquid-vapor interface at the window was visible at $t = 0.96ms$ and thicken with time.

Unfortunately, no window imaging has given such a clear result in 2017, for which the synchronization of all data was made possible.

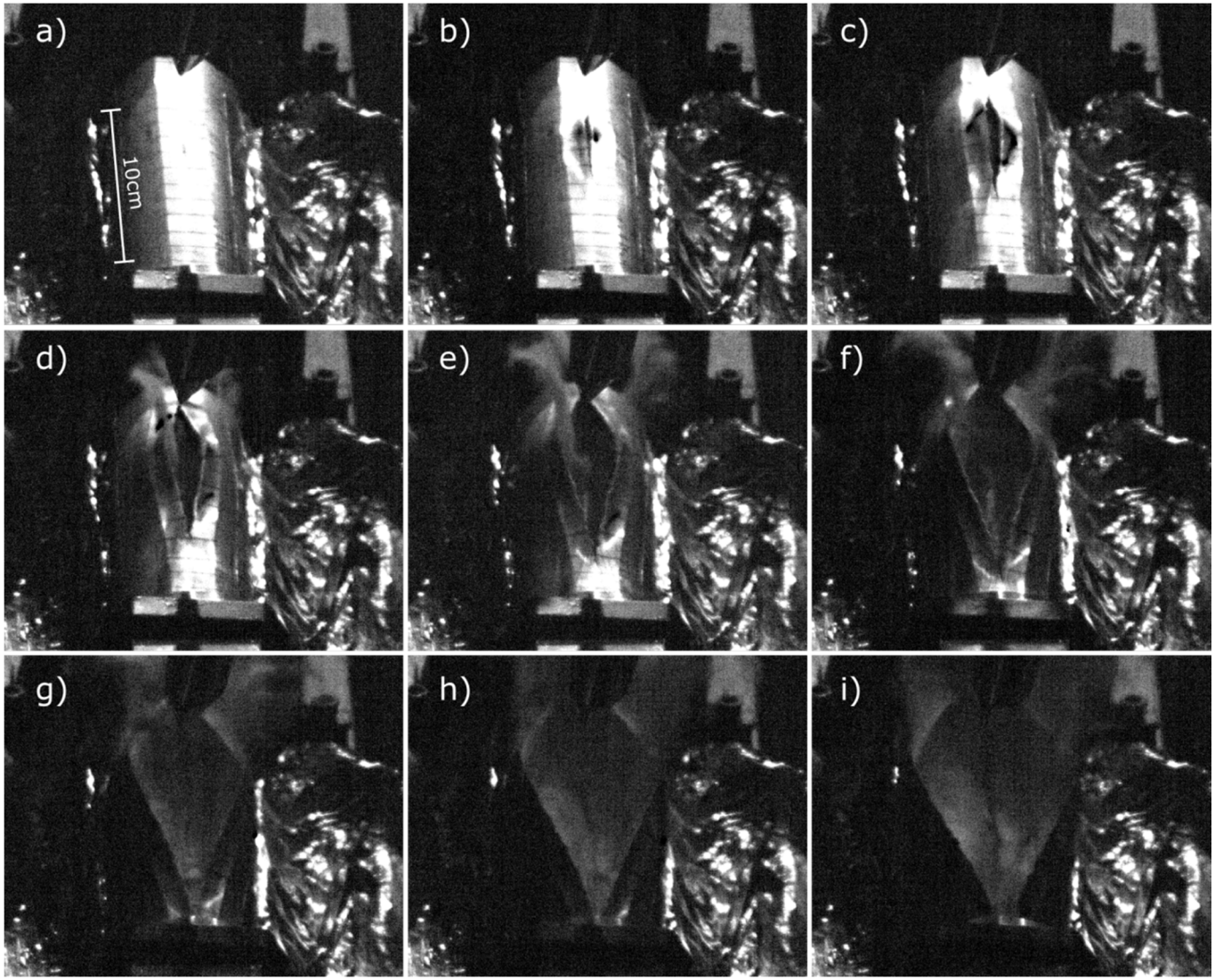

Figure 5-19 Top view with direct high speed imaging (Camera Phantom VEO710, $\Delta t = 52\mu s$, $P_{fail} = 19.3\ bar, \Phi_{liq} = 84\%, L_w = 150mm$)

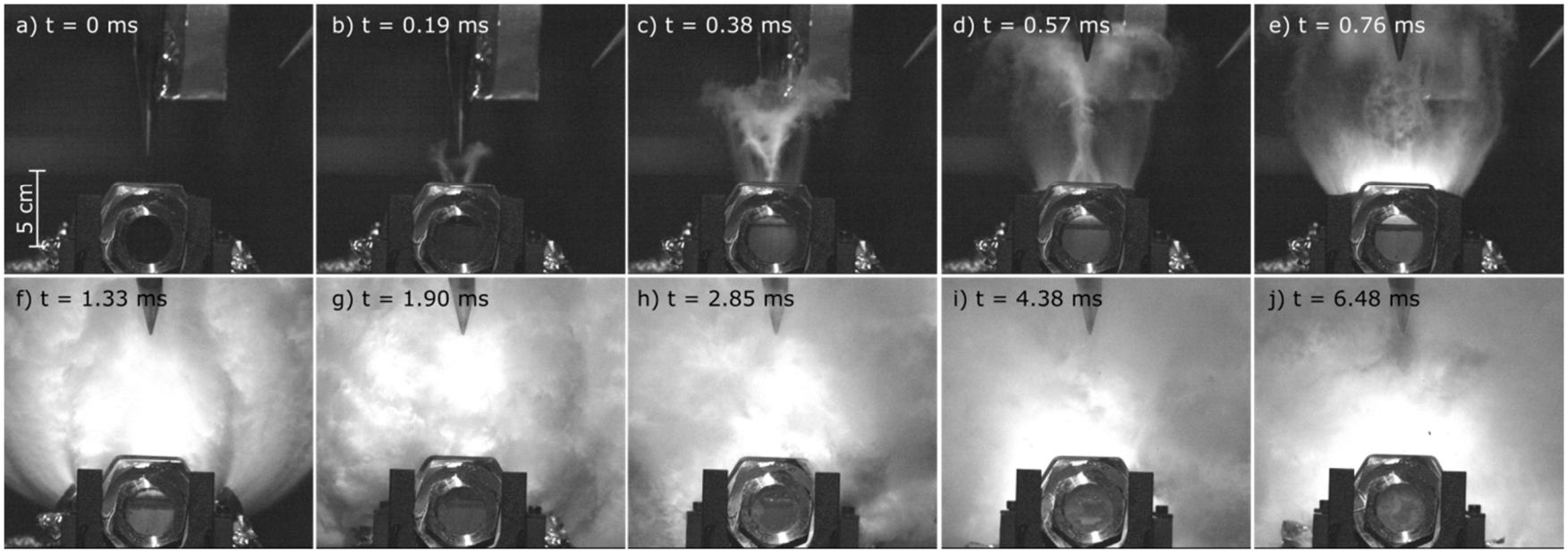

Figure 5-20 Axial view with direct high speed imaging (Camera Phantom V711, $\Delta t = 190\mu s$, $P_{fail} = 19.3\ bar$, $\Phi_{liq} = 83\%, L_w = 150mm$)

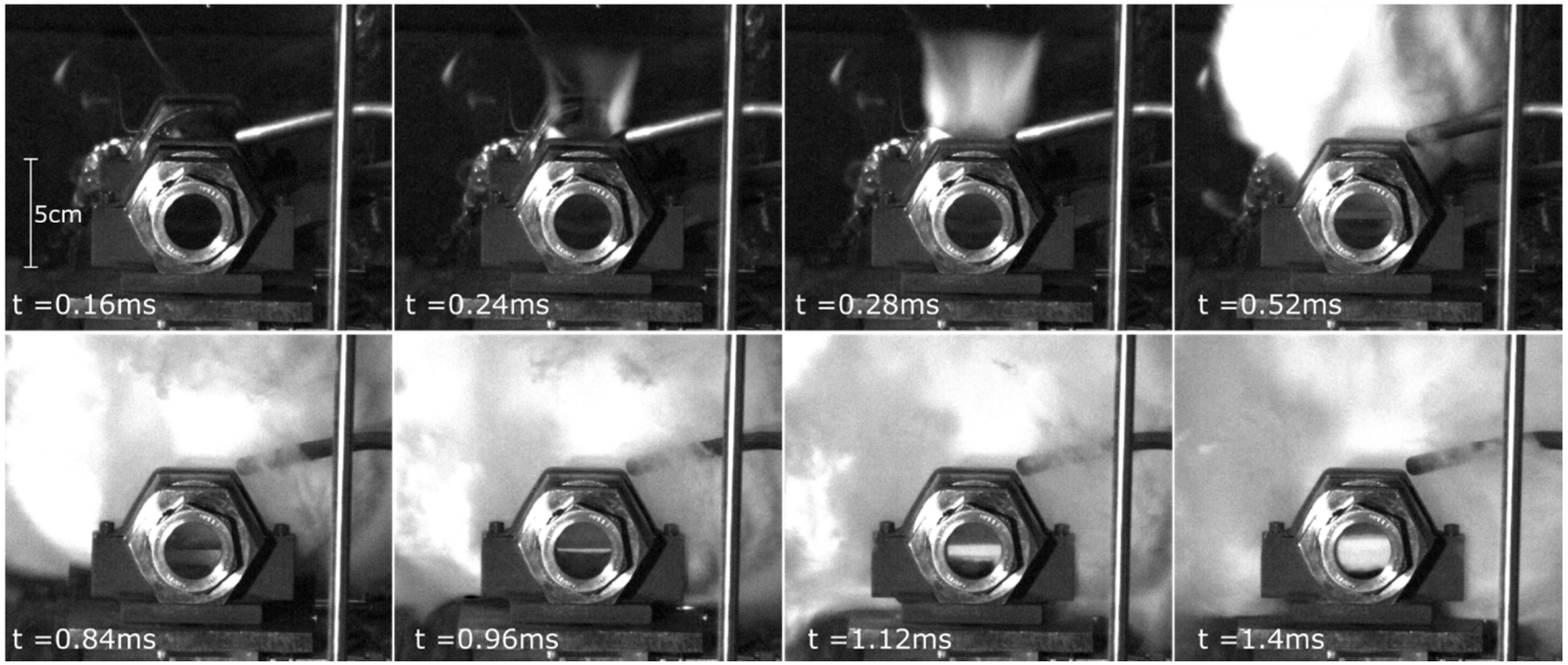

Figure 5-21 Axial view with direct high speed imaging made in 2015 (Camera Phantom V711, $P_{fail} = 28\ bar, \Phi_{liq} = 56\%, L_w = 75mm$)

IV-2. Shadowgraph

The Shadowgraph optical technique was set up to capture the shock formation and propagation at the exit of the tube. Depending on the configuration, one or two optical axes were available with shadowgraph: radial and axial views. From previous configuration of the experiment (2015), a large view of the explosion was set up through retro-reflective shadowgraph.

IV-2.1. Side -Radial view

For all tests, the radial (side) view of the tube was available through shadowgraph. The fastest camera available was used for this application (Phantom V2512), giving images at frame rates from 25 to 37.4 kfps.

Figure 5-22 shows results along the radial axis. The frame rate for this test was 25kfps, but the figure shows only one in three frames, resulting in $\Delta t = 120\mu s$ between the images shown. At the center of each image, the 4-sensor probe was visible. The 2 first sensors (dP1 and dP2) were visible in the field of view.

The imaging data from this axis gave the origin of the timeline analysis. The origin t = 0 was chosen to be the time at which the vessel starts to open. This axis of view was most suited to evaluate this reference time for several reasons:

- it clearly showed the location of the start of the opening due to the appearance of the propane cloud;
- it was available for all tests of the last test series;
- it was the fastest acquisition rate of all the high speed imaging views, thus reducing the error induced by the time between frames.

This view also showed an interesting phenomenon: the progressive formation of the shock wave. The lead shock first became visible in frame c) and strengthened in the following frames. This phenomenon of progressive shock formation was analog to the piston effect described Chapter 3 .

IV-2.2. Axial view

An axial view of the shadowgraph was also available for some tests. Figure 5-23 shows an axial shadowgraph of the tube. It was taken at 26kfps, and one in three frames are presented, resulting in $\Delta t = 115\mu s$ between the images shown. This view provided insight on the 3D aspect of the blast wave and the

cloud. In the center of the image was the 4-sensor probe. On its left was a protection case for the sensor cables facing the blast wave and the strong wind from the explosion. This view did not offer a direct view on the tube top as the sealing nut was in the way. It needed to be synchronized with other views in order to define the exact start of the explosion.

Its corresponding radial shadowgraph is presented Figure 5-24. It was taken at 37.4kfps, and one in four frames are presented, resulting in $\Delta t = 107 \mu s$ between the images shown. Horizontal lines are visible in the background of this shadowgraph. This was an aberration due to the poor quality of planar mirrors, necessary to solve space issue during the setting up of the experiment. This problem was solved for later tests, as seen Figure 5-22, but did not affect the visibility of the shock or the cloud.

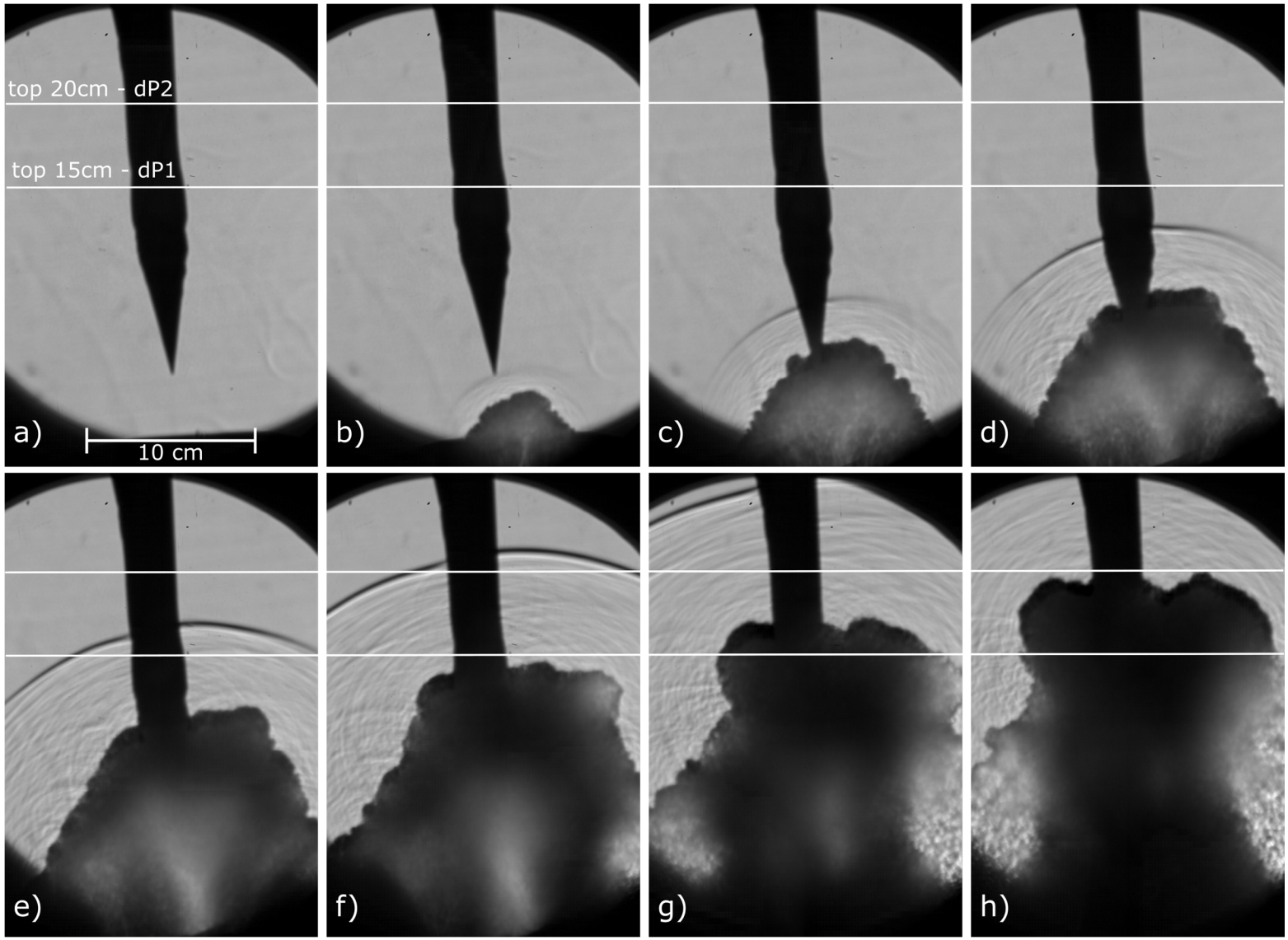

Figure 5-22 Radial view with shadowgraph high speed imaging (Camera Phantom V2512, $\Delta t = 120\mu s$, $P_{fail} = 19.3\ bar, \Phi_{liq} = 86\%, L_w = 150mm$)

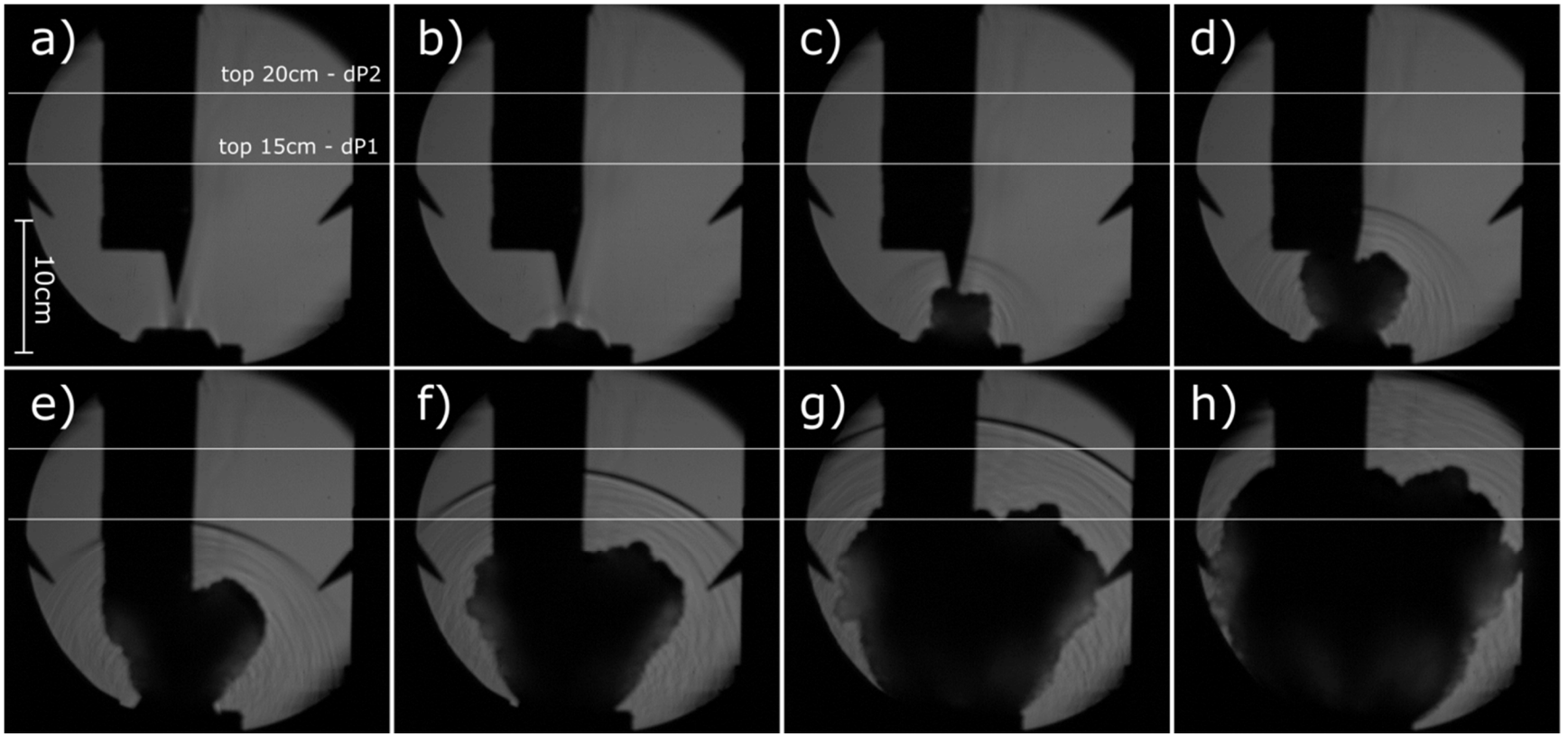

Figure 5-23 Axial view with shadowgraph high speed imaging (Camera Phantom V711, $\Delta t = 115\mu s$, $P_{fail} = 18.3\ bar, \Phi_{liq} = 18\%, L_w = 150mm$)

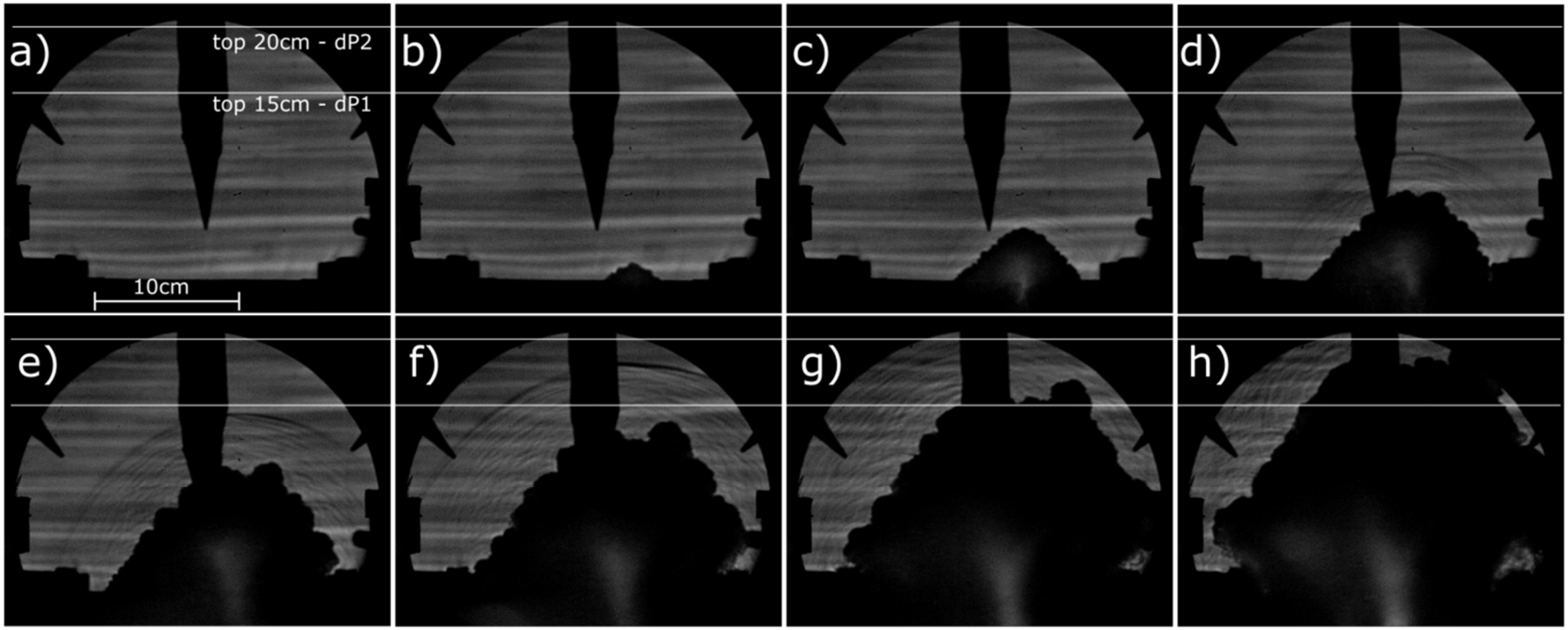

Figure 5-24 Radial view with shadowgraph high speed imaging (Camera Phantom V2512, $\Delta t = 107\mu s$, $P_{fail} = 18.3\ bar, \Phi_{liq} = 18\%, L_w = 150mm$)

V - Chronology of a BLEVE: example case

One test was presented using chronological analysis because of the completeness of the results available for this specific case, as well as the range of phenomena observed. Figure 5-25 presents the timeline of this test, with transient pressure, ground loading, overpressure signal of the two first vertical probes, and some characteristic frames of high speed imaging. The time origin t = 0s was chosen to be the time at which the vessel starts to open.

The chronological study was made possible by designing a graphic user interface through Matlab. The details of this interface are presented Appendix F.

V-1. **Chronology inside the vessel**

At t = 0.27ms (Figure 5-25 A), the crack reached both sides of the machined length and its propagation velocity was estimated to be 137m/s. An error of 20m/s was estimated due to a frame of uncertainty, as the crack seemed to be well open on the frame considered.

The pressure remained constant at the pressure sensor in the tube until time t = 0.68ms, at which time it started to drop. The calculated time for the expansion wave to reach the sensor from the opening was 0.41ms. The calculated time was smaller, but was of similar order of magnitude. A small increase in ground loading was visible from this point, marking the start of a slow rise.

The initial load rise stabilized around 2kN. It corresponded to the main pressure drop in the tube, 11bar from t = 0.68ms to t = 1.54ms, where inner pressure reached a local minimum.

Inner pressure then oscillated and hit a maximum of 9.5 bar at t = 2.37ms, which was closely related to the load maximum of 20.4 kN, 0.02ms later.

The tube was fully open at t = 2.4ms (Figure 5-25 G). This corresponded to the plateau of maximum load. It also corresponded to the maximum flat surface area of tube wall available for the fluid to exert a downward pressure while expanding.

V-2. **Chronology outside the vessel**

Through the shadowgraph pictures, the formation of the lead shock was visible (Figure 5-25 B2 - C - D). It can be seen on these frames that the shock appeared stronger with time over these shadowgraphs. It was not clear whether this was due to shock being built-up by piston effect and/or if it was a geometrical

effect due to the radius of the shock getting larger. For this reason it was difficult to say when the shock was fully formed.

At the early stage of tube opening, it can be seen that the shock started forming while the liquid in the vessel remains undisturbed (Figure 5-25 B2 and B3). Thus, the liquid phase was still undisturbed when the shock was already propagating outward. This observation supported the idea that the lead shock strength was only dependent on the compressed vapor phase characteristics. This was investigated further Chapter 6 . The passage of the shock over the sensors as shown on the shadowgraph pictures corresponded, as expected, to the pressure rise on the blast signals (Figure 5-25 C: Top 15cm; D: Top 20cm).

A transparent dome was visible inside the cloud of the two-phase flow expanding from the crack (Figure 5-25 B1). However it did not appear transparent on the corresponding shadowgraph image (Figure 5-25 B2). The cloud was a two-phase flow, most likely vapor propane condensing during its expansion. The dome illustrated a manifestation of a choked flow through the opening, creating a shock similar to the so called Mach disk in under-expanded jets. Due to three dimensional expansion of the vapor cloud, the top edge of the dome remained visible for only a few frames. By extrapolating its position just before it fully disappeared, it arrives at the sensor dP1 around t = 0.85ms (Figure 5-25 E1), corresponding to a pressure drop on the signal 'Top 15cm'. This was in agreement with the physics of a Mach shock passing over the sensor. This phenomenon was investigated Chapter 7 .

Another phenomenon was noticed starting at t = 0.85ms. The radial and axial direct imaging both showed the start of a second white cloud rising from the tube (Figure 5-25 E1 and E2). It also corresponded to the slow initial rise in ground loading. This second cloud grew larger and thicker than the first white release (Figure 5-25 F), together with a strong rise in the ground loading. This phenomenon was noticed on most of the BLEVE experiments having high speed imaging of the radial view.

The following hypothesis was made based on observations: the first white cloud corresponded to condensation from the compressed vapor expanding, while the second cloud corresponded to the boiling of the superheated liquid. The liquid boiling was a slower process, but the quantity of energy available in the liquid leads to a major contribution in the ground loading to various processes: vertical thrust of the flow through the opening starting on the top of the vessel; kinetic energy of the vessel walls hitting the base plate; dynamic pressure of the boiling liquid on the flattened tube.

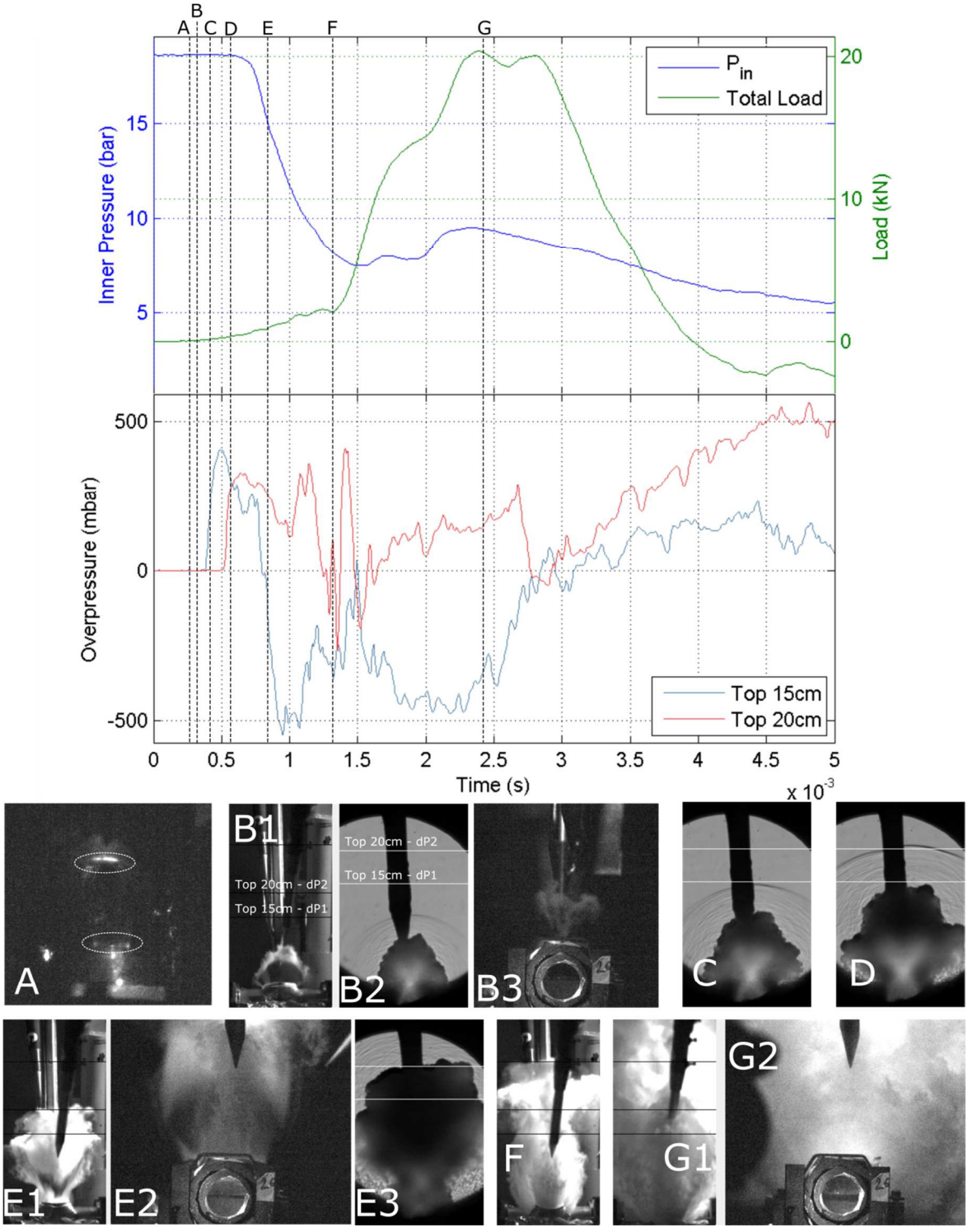

Figure 5-25 Chronology of a BLEVE through physical measurements and high speed imaging ($P_{fail} = 18.6bar, \Phi_{liq} = 52.61\%, L_w = 75mm$)

V-3. **Main conclusions from timeline analysis**

First it should be noted that compared to other scenarios presented in the literature, the BLEVE presented here was a One-Step BLEVE. Once the crack started, it propagated to its full length with no interruption. All of the experiments presented in this work led to similar BLEVE. No Two-Step BLEVE was observed.

From this first timeline of the BLEVE, the following assumptions were made:

- The lead shock properties (strength, velocity) are mostly governed by the vapor phase expansion;
- The boiling liquid is a slower process, it happens some time after the initial opening. It does not appear to contribute to the lead shock, but is a major contribution to the ground loading and repressurization inside the vessel, possible projectile effects and near field drag loading of objects.

The contribution of the boiling liquid to the overpressure field surrounding the exploding vessel needs further investigation to quantify its hazardous consequences.

Chapter 6

Lead shock and maximum overpressure characteristics

When talking about BLEVE overpressure, the hazard most studied, understood and modeled is the maximum overpressure. Many models exist for BLEVE overpressure and most predict well its behavior in the far-field. However most models predict it based on the liquid energy.

This chapter presents the results concerning the maximum overpressure measured in the case of the small scale BLEVE experiments. An overview of the far-field data was given, to compare with known work. The novelty of this work was in its near-field data, particularly in understanding the behavior of the lead shock at early times of the explosion.

This chapter first presents symmetry and isotropy of the pressure field. The anisotropy of the explosion due to the cylindrical geometry of the vessel, adding some accuracy to the existing vessel shape factors for blast correction. Then the formation mechanism of the lead shock was studied. Imaging showed some evidence of a progressive build-up of the lead shock depending on the opening velocity of the vessel. Finally, modeling of this overpressure was presented. It was done from existing literature models first, but the physics of these models did not satisfy the physics of the contribution of the vapor to the shock overpressure. Thus, a new model was presented based on assumptions that the experiment confirmed. Finally the new model predictions were applied to larger scale BLEVEs (scale up 2000L in volume) and the approach was validated.

I - Anisotropy of the pressure-field

The small scale experiments conducted in the present work provided a range of measurements in all directions. A study of the anisotropy of the pressure field was conducted to fill in some of the gaps mentioned above.

I-1. Symmetry of the opening and consequent blasts

Before studying the anisotropy of the pressure field, it was useful to look at the symmetry of the pressure field using the probes placed symmetrically with respect to the vessel. Because of their symmetrical position around the vessel and the symmetry of the vessel shape before, during and after the opening, some symmetries in the pressure field were expected: one plane of symmetry along the vertical axial plane crossing the cylindrical vessel, and one plane along the radial plane crossing the tube in its

middle. This involved the blast gages placed at a 45° angle, (sides dP6-dP8 and ends dP5-dP7), the probes for the near-field side-on overpressure (dP9-dP10), and the probes in the far-field again (sides dP13-dP20 and ends dP12-dP21). Configuration of the blast gages is available in Chapter 4 .

The symmetry of these measurements was verified Figure 6-1.

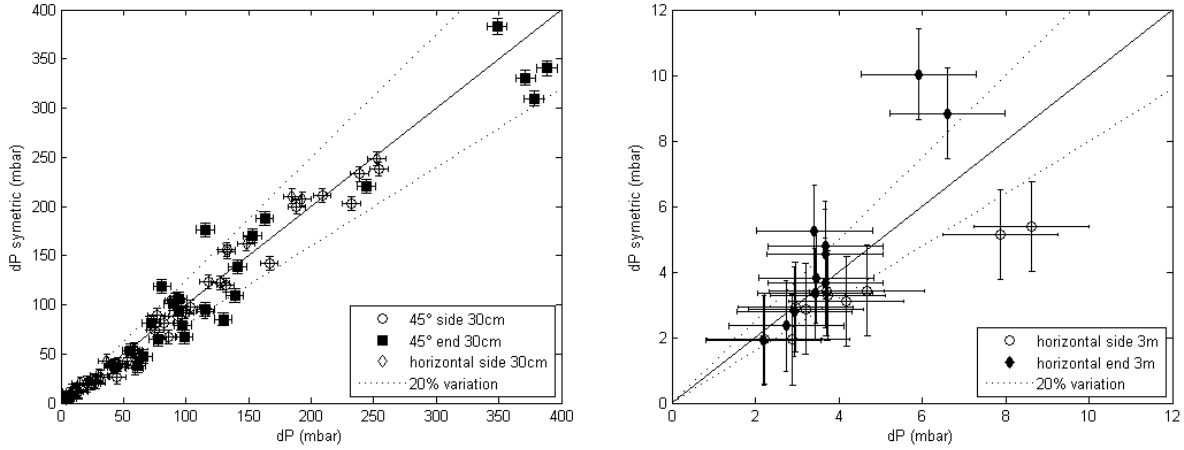

Figure 6-1 Overpressure ratios of gages with symmetric positions (left: at 30cm; right: at 3m)

The near-field overpressure showed a reasonable symmetric behavior (with 20% variation).

Asymmetry was observed in the far-field. These measurements were made on an experimental setup focused on detecting near-field data. Many probes and structures were located between the far-field blast sensors and the source of explosion. Moreover, the values obtained in the horizontal far-field were mostly within the uncertainty range. It was thus difficult to draw conclusions from horizontal far-field overpressures.

I-2. Pressure ratios for the different directions

Overpressures were compared over the different available directions to draw conclusions based on literature data and ideas on cylindrical anisotropy of the pressure field.

I-2.1. Horizontal plan: side – end comparison

Most of the experimental data available on the anisotropy of the pressure field from BLEVE concerned the comparison of overpressure measured on the side of vessels (radial direction of the cylinder) and on the ends of the vessel (axial direction of the cylinder). CCPS (CCPS - American Institute of Chemical Engineers, 1994) advised a 1.4 ratio between side and end in the far field. Some authors

presented a scaling based on the cylinder shape to balance the difference of pressure between side and end.

Ratios were measured between gages dP13 with dP12 and dP20 with dP21 (Figure 6-2). The small scale experiment did not validate the ratios expressed in the literature (Figure 6-3). Different behaviors came from this distinction. The first ratio $\frac{dP_{13}}{dP_{12}}$ showed a behavior close to the ratio mentioned in the literature. It was however generally smaller, between 1 and 1.4. The second ratio $\frac{dP_{20}}{dP_{21}}$ varied from 0.6 to 1.2, but was mostly bellow 1. It showed that side-on measurements were smaller than on the ends.

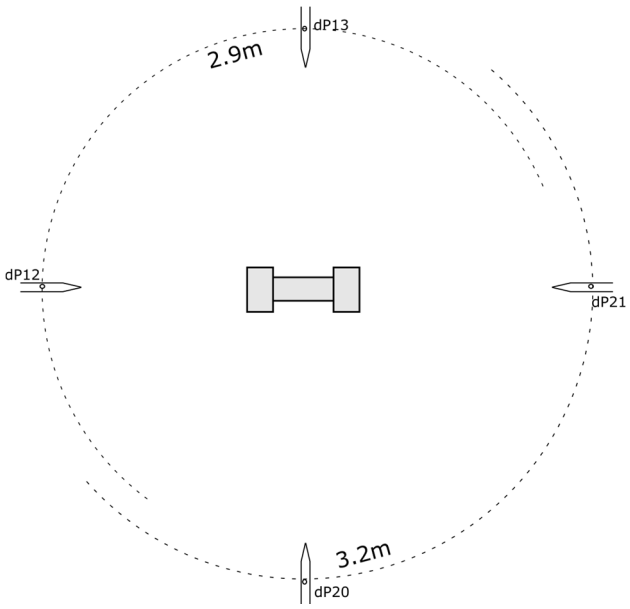

Figure 6-2 Position of the far-field horizontal blast transducers around the tube

The distance from the tube differed slightly between each ratio. However each pair of transducers were consistent in distances to the tube (dP12 and dP13 at 2.9m from the tube, dP20 and dP21 at 3.2m from the tube). Thus this did not explain such a difference in behavior. This difference could be explained be the presence of multiple probes and tools on the way between near-field and far-field, altering the signal captured by the probes in the far-field.

The conclusion on the far-field was ambiguous because the setup was focused on measuring near-field data, not far-field. It showed that when far enough, the behavior of the pressure field tended to become more isotropic, and became sensitive to the topology of the vessel surrounding.

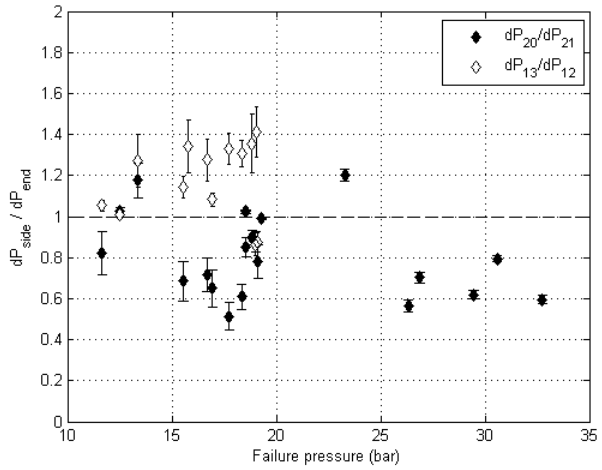

Figure 6-3 Ratio of overpressures side / end overpressure at 3m from the vessel

I-2.2. 45° – vertical comparison (near-field)

The main contribution of this small scale experiment in terms of overpressure measurement was in measurements made close to the vessel. A variety of probes were located at the same distance of 30cm and from the tube in various directions.

The 45° angle probe measurements were compared to the top probe Figure 6-4. Side measurements are larger than end measurements, giving ratios ranging from 0.4 to 0.7 on sides, and 0.2 to 0.45 on the ends. This was consistent with the literature. Because of the geometry of the vessel, and particularly the geometry of the opening as sensors were located slightly above the tube, the pressure field was stronger on the sides. These ratios also indicate that the pressure above the vessel was stronger by factor of 2.5 than at 45° angle on the sides, and stronger up to a factor 5 than at 45° angle on the ends.

The behavior of the liquid overfill case was different, as no shock was generated and the overpressures were very low. Thus the isotropy of the pressure field was less significant for this case.

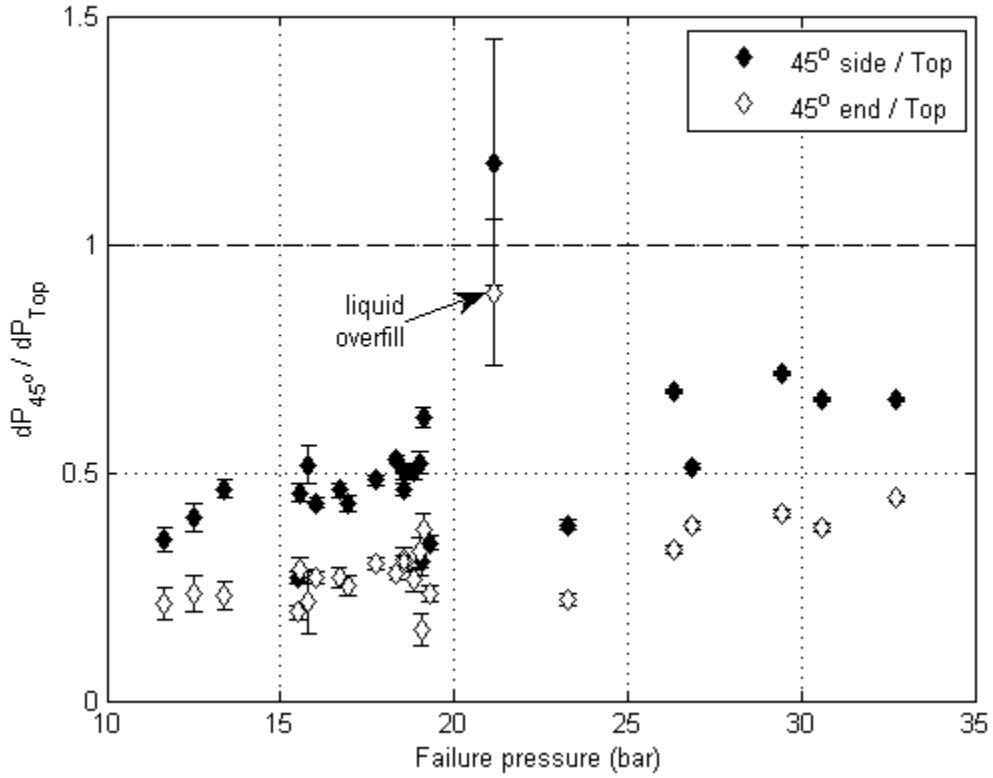

Figure 6-4 Ratio between maximum overpressure measured at 30cm from above the vessel and 45° angle

I-2.3. Horizontal side – vertical overpressure comparison: near and far-field

Ratios on the horizontal side overpressure compared to top overpressure measurements ranged from 0.05 to 0.3 in the near-field, and 0.2 to 0.55 in the far-field (Figure 6-6). Near-field showed a very strong blast on the top compared to the side. This anisotropy was smaller in the far-field, but still being very present. This showed evidence of the directional pressure field tending toward a spherical shape while propagating outward.

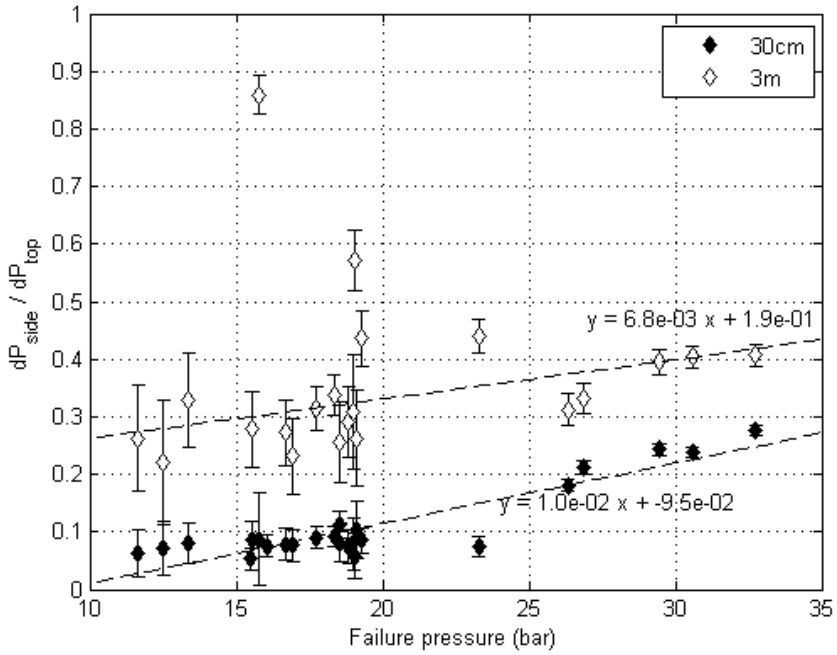

Figure 6-5 Ratio between top and side-on overpressure in the near-field (30cm), compared with the far-field (3m)

The anisotropy diminished with increasing failure pressure. To explain this, a parallel was made with the velocity of opening of the tube, evaluated with high speed imaging (Figure 6-5). The tube opened more rapidly with larger failure pressure. With a faster opening, the tube walls did not influence the pressure field isotropy on the sides as much as if they opened slowly, reducing the difference of maximum overpressure between the side, end, and top measurements.

An odd behaving point was noticed with a pressure ratio of 0.85 in the far-field (Figure 6-5). It corresponded to a case with the following failure conditions: $P_{fail} = 15.8bar, \Phi_{liq} = 94\%, L_w = 150mm$. Although the high liquid content of this case may help to explain this behavior, it was not fully understood as many factors induced in the realistic explosion may influence that behavior.

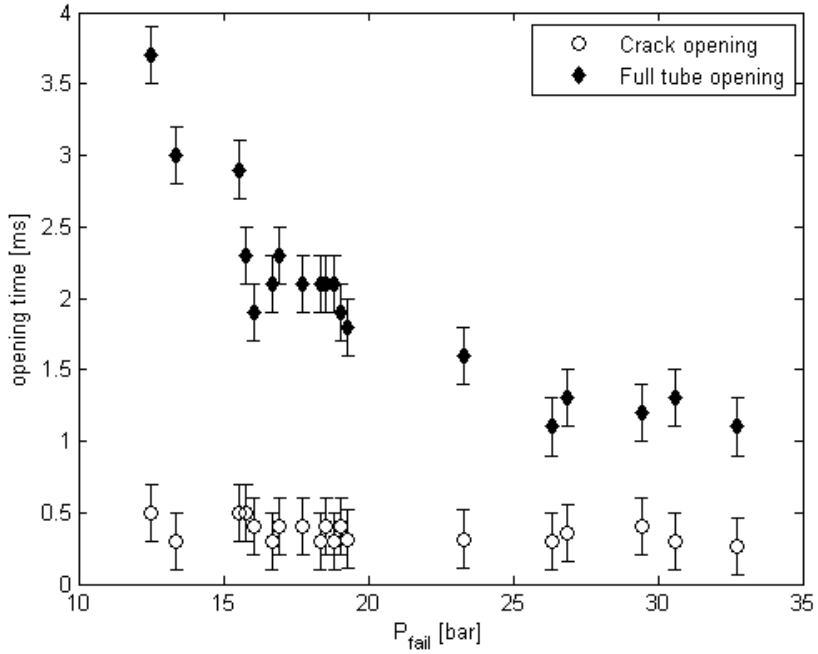

Figure 6-6 Opening time of the tube against failure pressure

II - Shock formation: observations

Understanding the propagation and impact of the lead shock in the near-field required to make sense of its formation process as well as the way it propagated after being formed. To understand the latter, the former was important.

As exposed in Chapter 3 , one way the shock formed was through piston effect: successive compression waves generated by a forward moving piston, coalescing to become a shock. This piston effect has been observed in the literature for high pressure bursting capacity (spheres, shock tubes, etc) (Glass, 1974; Rothkopf and Low, 1976). Experiments also showed that this phenomenon was the case of the cylindrical vessel burst.

Shadowgraph images showed a non-existent shock in the early stage of opening (Figure 6-7 a). However, a train of compression waves were visible (Figure 6-7 b). These compression waves were generated by the high pressure vapor inside the vessel expanding outward, acting as pistons pushing on the surrounding atmosphere. The dynamic opening of the vessel led to an increasing surface area for the vapor piston to push on the surrounding air, leading to a piston increasing size while the opening got bigger. Thus more compression waves were sent out, until they piled up sufficiently to form a sharp distinguishable shock (Figure 6-7 c).

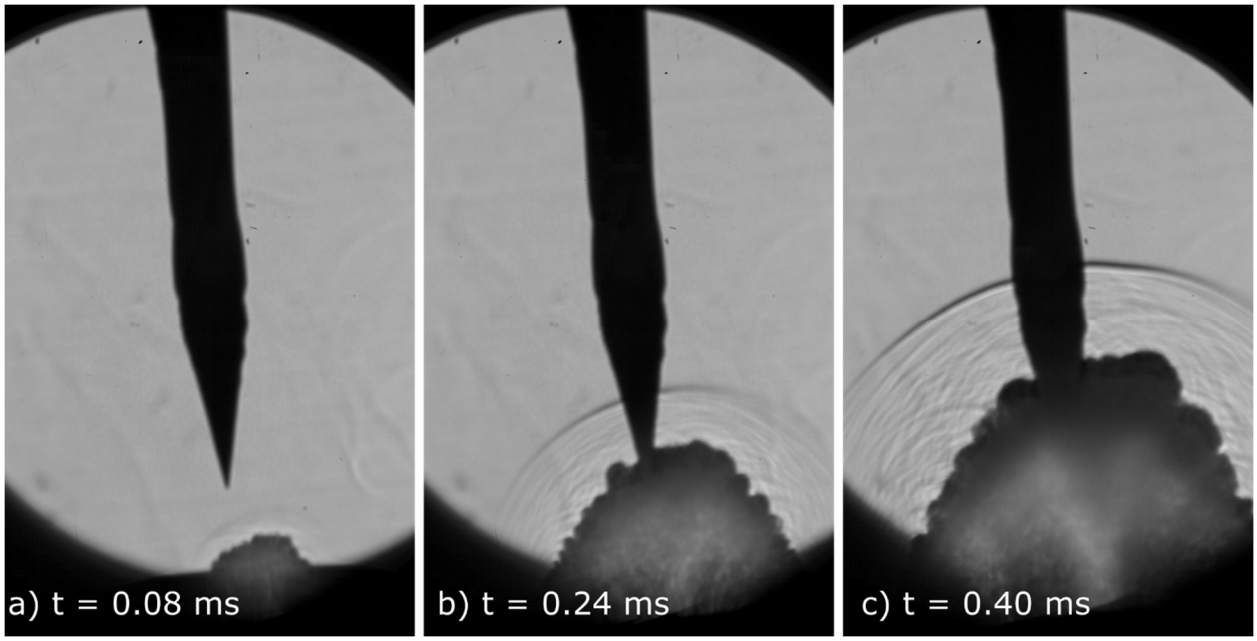

Figure 6-7 Different stages of shock formation through shadowgraph ($P_{fail} = 19.3bar$, $\Phi_{liq} = 85\%$, $L_w = 150mm$)

Defining the exact moment at which the shock was fully formed is difficult. Several arguments were explored. One argument stated that when the shock was fully formed, it was at its strongest: it was the transition state between the formation process and the start of the decay due to three dimensional spherical expansion effects. Thus, defining the position and time at which the shock was fully formed required us to detect when it is strongest. Shadowgraph measurements only shows the second derivative of the pressure field, thus shows only how strong is the inflection of the show. A stronger inflection is correlated to a stronger shock, but shadowgraph did not allow to quantify the actual shock strength from the imaging. Schlieren would be necessary to quantify this.

In some cases, the overpressure signals measured on the vertical probe above the vessel showed no decay and sometimes even a pressure increase between the first and the second sensor, respectively at 15 and 20cm from the top of the vessel (dP1 and dP2) (Figure 6-8). It was worth noticing that the decay was then visible for further sensors, at 30 and 40cm from the vessel top (dP3 and dP4). This presented further evidence that for some tests, the shock did not start to decay before reaching the first sensor 15cm above the tube opening. It gave a range for the distance of formation, although without exact value. For such cases, the maximum strength of the lead overpressure was most likely between dP1 and dP2, and potentially right after dP2.

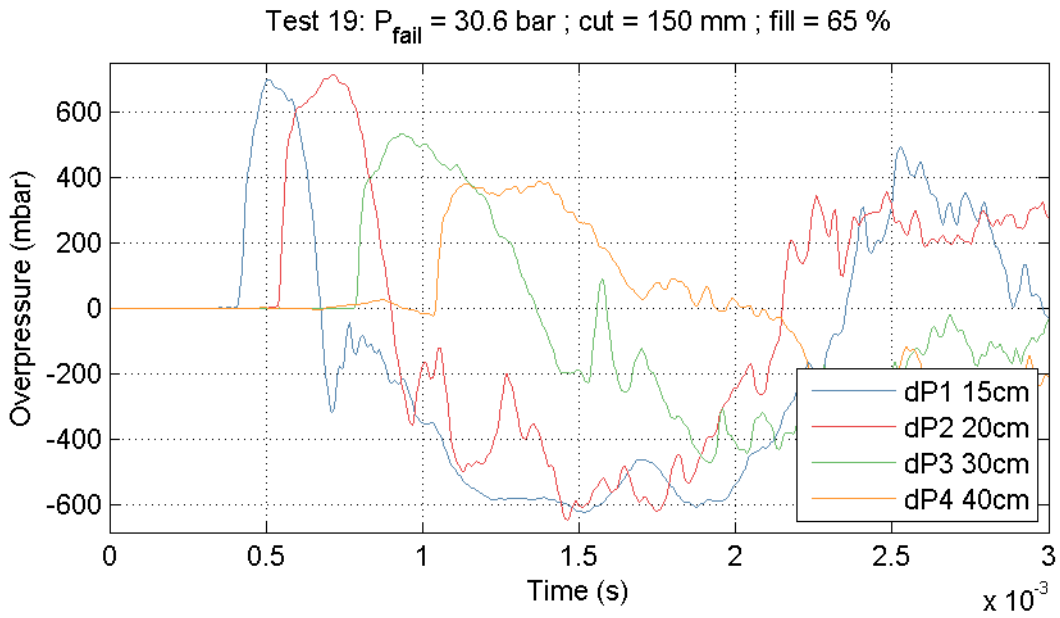

Figure 6-8 Overpressure signals from blast gages above the tube ($P_{fail} = 30.6bar$, $\Phi_{liq} = 65\%, L_w = 150mm$)

III - **Parametric analysis with failure variables**

The evolution of the overpressure from the lead shock was studied with regards to the failure parameters. To do so, the maximum overpressure measured on the five sensors above the vessel was extracted and correlated to the variations in failure parameters: failure pressure, liquid fill level and cut length. Results are summed Table 6-1. The correlation coefficients used for these comparison are Person correlation coefficient.

Table 6-1 Correlation table between failure parameters and maximum overpressure above the vessel

	P_{fail}	Φ_{liq}	L_w
dP1 (15cm)	0.79	-0.31	0.44
dP2 (20cm)	0.81	-0.31	0.49
dP3 (30cm)	0.86	-0.24	0.46
dP4 (40cm)	0.87	-0.19	0.45
dP14 (3m)	0.90	-0.26	0.40

To comment and validate these correlation coefficients, maximum overpressure variation with respect to each parameter was plotted for cases with similar conditions over the other parameters.

III-1. **Maximum overpressure correlation to failure pressure**

A first obvious but clear statement was made by comparing the variation of the overpressure variation with respect to the failure pressure: overpressure was strongly correlated to failure pressure. This came as

no surprise as it was exposed in vapor vessel burst theory such as shock tube theory. The correlation coefficient between failure pressure and overpressures on top of the vessel were close to 1. Overpressures for cases of similar fill level (≈ 60%) and cut length (150mm) were plotted with respect to failure pressure Figure 6-9. The increasing trend was clearly visible on these graphs, confirming similarity to basic theories such as shock tube theory.

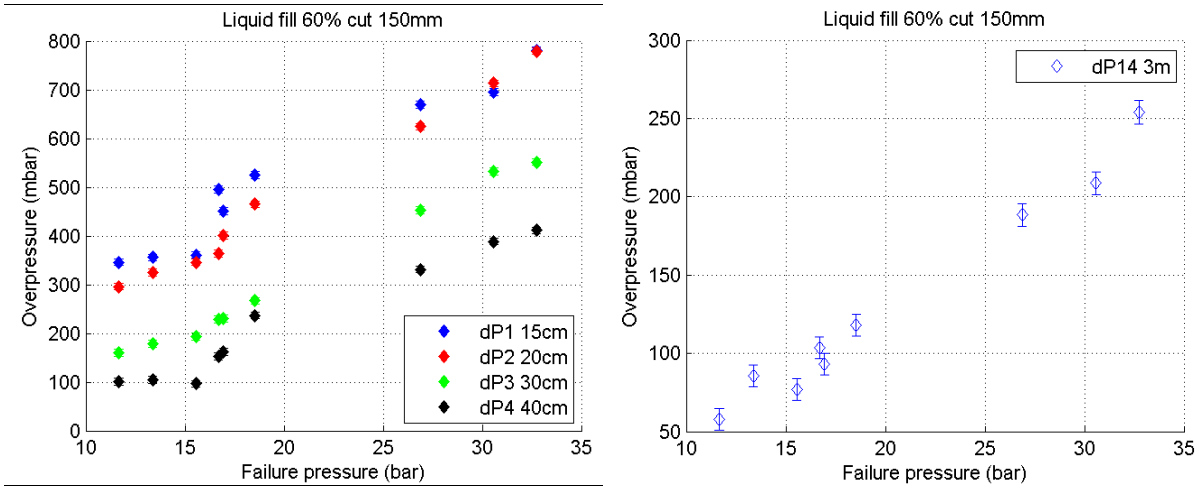

Figure 6-9 Overpressure evolution above the vessel with failure pressure, for cases with 60% liquid and 150mm cut length (left: near-field; right: far-field)

III-2. **Maximum overpressure correlation to liquid volume fill level**

The correlation between overpressure and liquid volume fill level brought an interesting statement: the overpressure tended to decrease when the liquid fill level increased. The correlation coefficients were negative and Figure 6-10 validated this statement for failure pressures around 17 to 19 bar. Inversely, this statement was expressed as such: overpressure increased with vapor volume fraction available in the vessel before rupture. The more vapor space, the stronger the overpressure. This was a strong statement linking directly the overpressure generation of the first lead shock to the vapor space when questioning the contribution of each phase. The more vapor fraction in the vessel before failure, the more volume of compressed vapor piston available, thus the stronger compression waves generated. Analogy can be made with the driver length of a shock tube: a longer driver length leads to a longer train of compression waves coalescing.

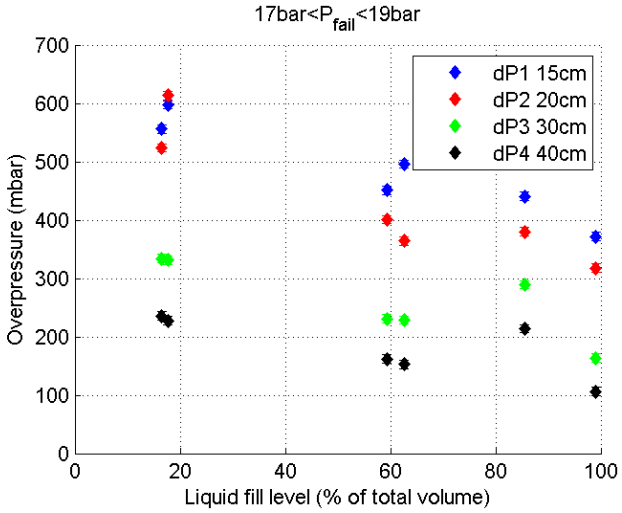

Figure 6-10 Overpressure evolution above the vessel with liquid fill level, for cases of failure pressure between 17 to 19 bar, and 150mm cut length

III-3. **Maximum overpressure correlation to cut length**

Comparison of overpressure and cut length was positive. The available cases showing the variability through cut length at similar fill level and failure pressure confirmed this positive correlation (Figure 6-11). Overpressure increased with cut length. Physically, this was interpreted as such: a larger cut length resulted in a larger piston of compressed vapor pushing through the surrounding air, leading in a stronger piston generating compression waves, ending up in a stronger shock.

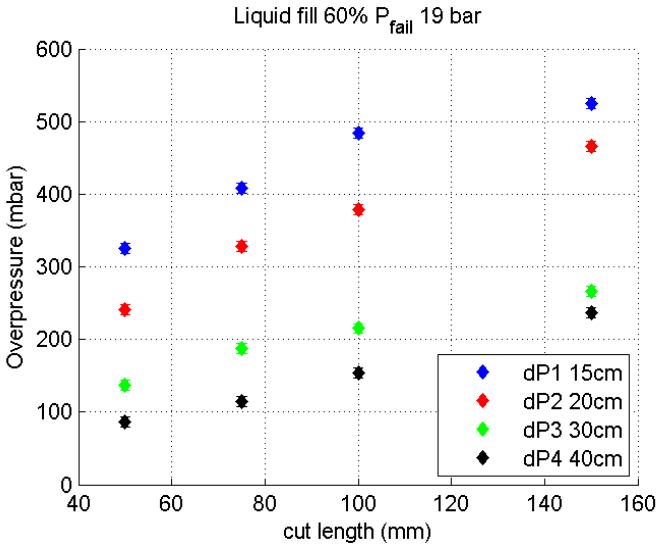

Figure 6-11 Overpressure evolution above the vessel with cut length, for cases with 60% liquid and 19 bar failure pressure

III-4. **Contribution of vapor and liquid phase in the generation of the lead shock**

The previous paragraphs argued three different points coming down to one main argument: the maximum overpressure of the small scale BLEVE behaved similarly to simple theories about high pressure vapor bursting vessel, such as shock tube theory and piston shock formation. This suggested that the liquid did not play a major role in generating the first lead overpressure. Some references have stated for a while that the lead shock was mainly induced by the vapor space (Baker et al., 1983; Birk et al., 2007).

An experimental case leading to hydraulic failure emphasized this argument. Figure 6-12 showed that little overpressure was generated ahead of the cloud of propane escaping through the opening. This overpressure was not significant enough to create a steep shock as observed on pressure signals of other superheated failure. But this was not a saturated liquid and we would not expect a shock. It was neither enough to generate pressure waves significant enough to be visible through the shadowgraph, even though pressure waves were ahead of the cloud according to the pressure signal. However this argument must be taken carefully: the liquid was not superheated, which did not lead to violent boiling.

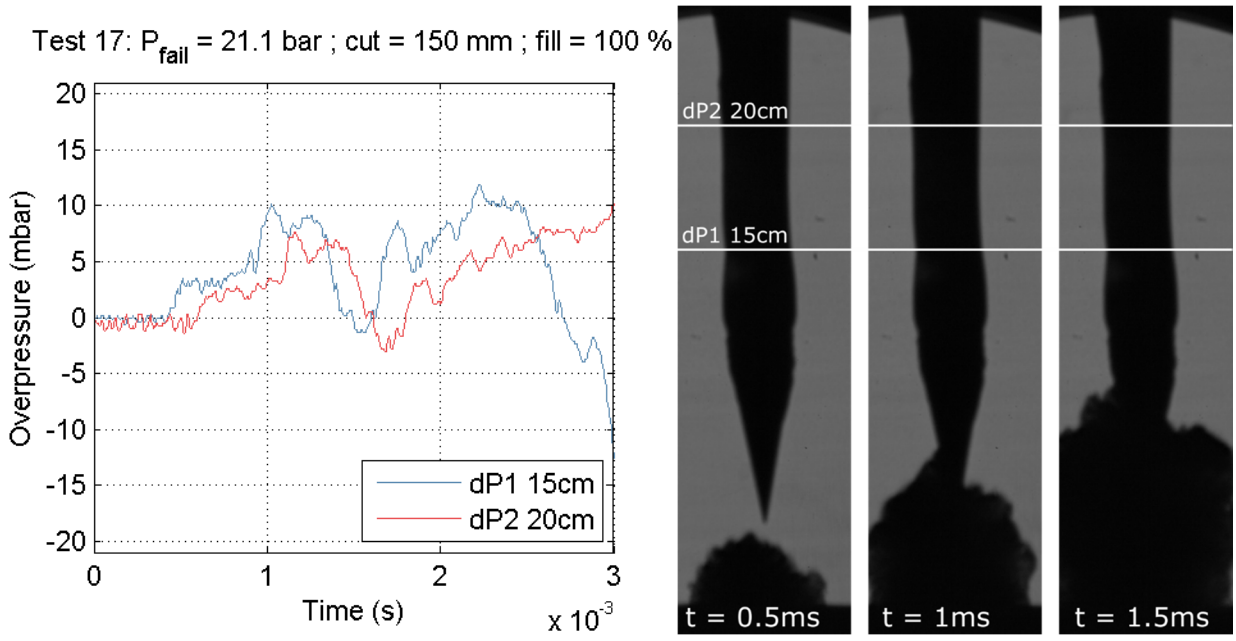

Figure 6-12 Pressure waves generated through a test resulting in hydraulic failure (left: pressure signals from gages above the tube; right: shadowgraph)

Another case almost full of liquid before failure presented the following overpressure profile (Figure 6-13 left). Unlike the previous case mentioned, the fluid inside the vessel was at saturation conditions

before failure and would have been superheated upon vessel failure. The liquid reached some superheat degree before boiling. But when comparing with a mostly vapor case of similar failure conditions (Figure 6-13 right), the slope of the initial pressure increase was more gentle when it came to the liquid case. Consequently, the maximum overpressure reached for the liquid case was almost half of the overpressure generated by the vapor case. This can be related to the driver length analogy, as mentioned above.

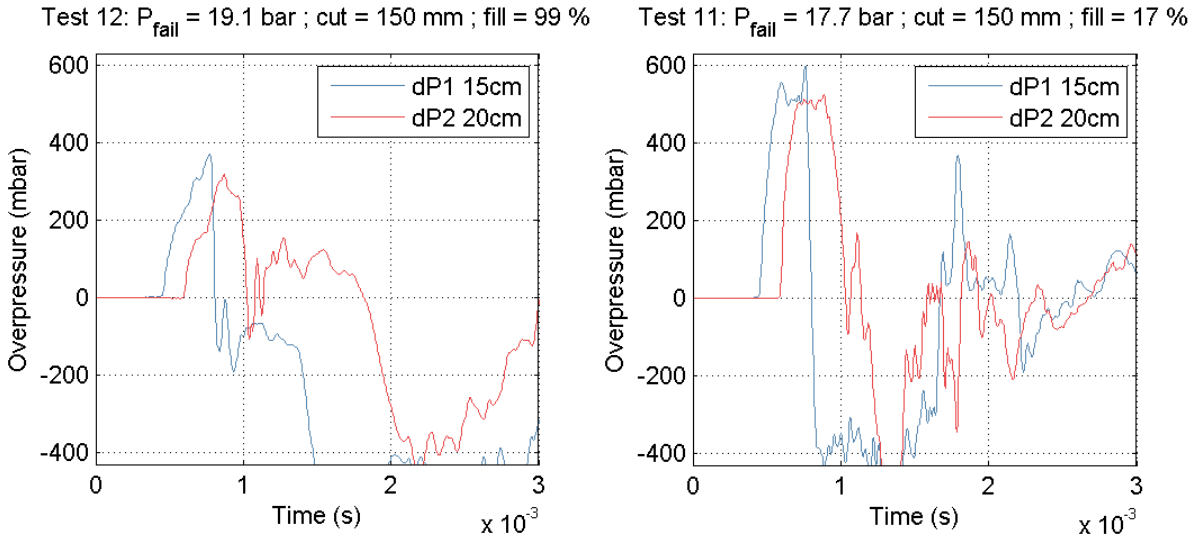

Figure 6-13 Overpressure signals above the vessel for cases of similar failure pressure but different liquid fill level (left: high liquid content; right: high vapor content)

The shadowgraph images confirmed the trend observed with pressure signals. Figure 6-14 showed the shock formation for the two cases presented above. A lead pressure wave was visible for both cases. However, the case with high vapor content had a sharper density change than the case with high liquid content.

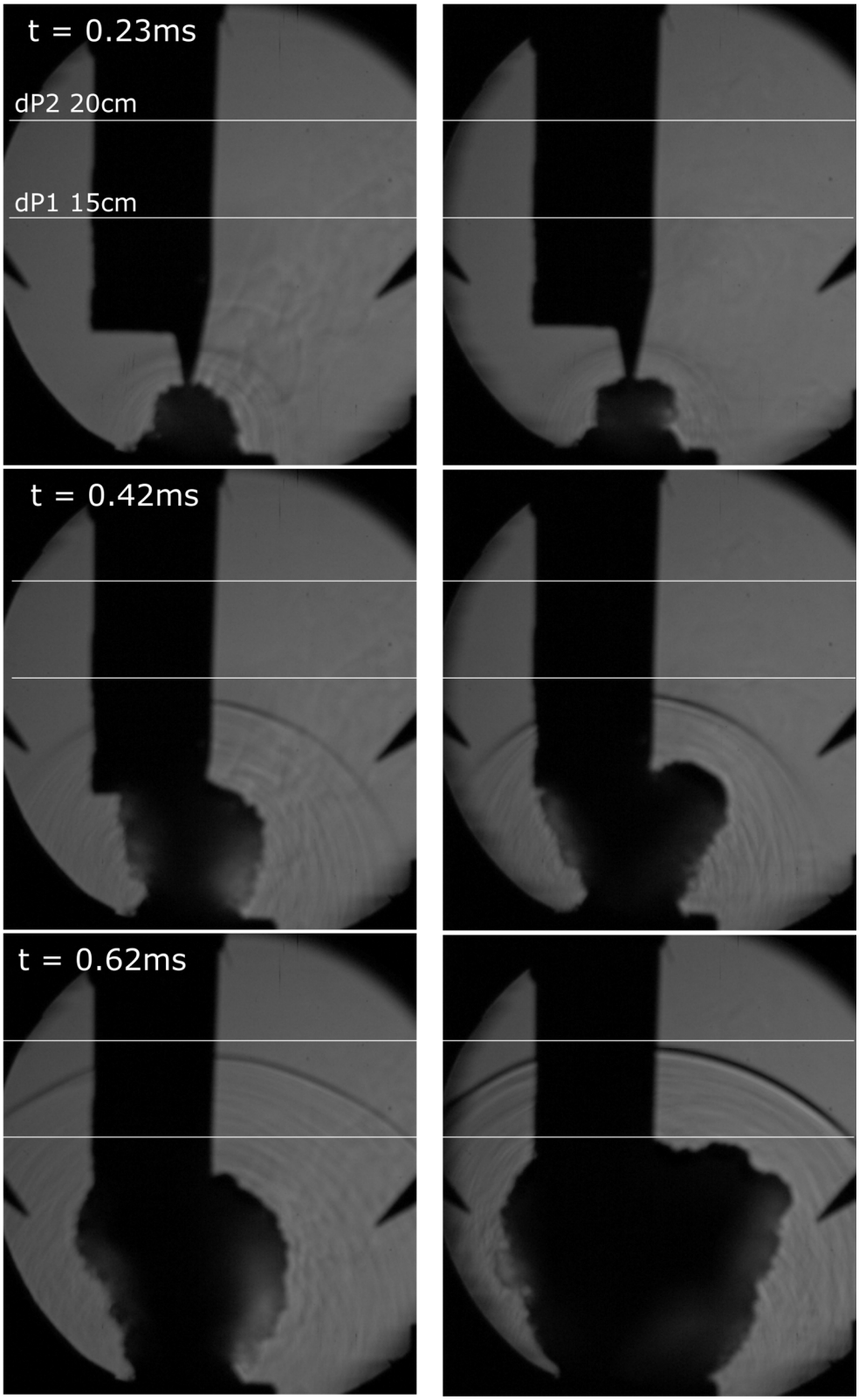

Figure 6-14 Axial shadowgraph showing the shock formation process for a high liquid content (left) and high vapor content (right). Tests conditions exposed Figure 6-13

This led to have a critical look at studies from experiments in the literature measuring overpressures from fully liquid filled vessels before a BLEVE. Some of the first experimental work on BLEVE was done with 100% liquid vessel (Giesbrecht et al., 1981). Maximum overpressure data are given through this work. However no pressure signal was shown in his results. This work did not present how steep these overpressure were. Considering the superheated liquid overpressure obtained with Figure 6-13 left, these experiments may not present steep shocks but only strong near field overpressures.

Similarly, what was the relevance of using liquid properties in calculating the lead shock overpressure? A wide range of models based on expansion energy is available in the literature (Casal and Salla, 2006; Planas-Cuchi et al., 2004; Prugh, 1991). These models use liquid properties such as flash fraction or superheat energy to quantify the expansion energy contributing to the shock. It was argued so far that taking into account these characteristics is irrelevant to such estimation. They were also based upon far-field experimental data. It was expected in this work that some of these models are not correct for vessels with low fill levels (large vapor volumes) and near field data.

IV - Modeling

Predicting the overpressure hazard in the near field with more accuracy has been one major concern with BLEVE accidents. A wide range of models has been developed through the years for the far-field.

IV-1. Expansion energy models

The overpressure experimental data was compared to the modeling prediction from the expansion energy models presented in Chapter 2 . Two models were chosen for the comparison: a conservative model (Prugh, 1991) ; and an accurate model (Casal and Salla, 2006) irreversible. The conservative and accurate terminology was used in a recent work comparing all these models (Hemmatian, 2016).

All overpressure measurement data were plotted for 2015 and 2017 experimental campaign for propane tests (Figure 6-15 and Figure 6-16). Distinction was made between measurements from the top, the sides and the gages at 45^{o} angle.

The scaled distance and overpressure ranges were summarized for each test campaign and models Table 6-2, as well as the error made between the model and the experiment through FB and NMSE presented Chapter 2 for each direction of measurement (vertical, 45^{o} and horizontal). The distance range covered by the last test campaign was larger because blast gages were placed as close as possible to the vessel wall (15cm) as well as much further (3m). The overpressure range scaled consequently.

The first set of data confirmed the approach of each model (Figure 6-15): conservative for Prugh isentropic expansion with flash fraction, more accurate for Casal irreversible superheat energy. The horizontal gage measurements (or side-on overpressures) were predicted very conservatively for the first and closer to the curve, but still below for the latter. 45° angle measurements were closer to the curve but still well predicted. However some measurements from the top were not predicted conservatively. This was most certainly due to anisotropy presented earlier. The models have been validated or fitted with side-on overpressure measurements, they were not designed to predict overpressure from the top of a cylindrical burst.

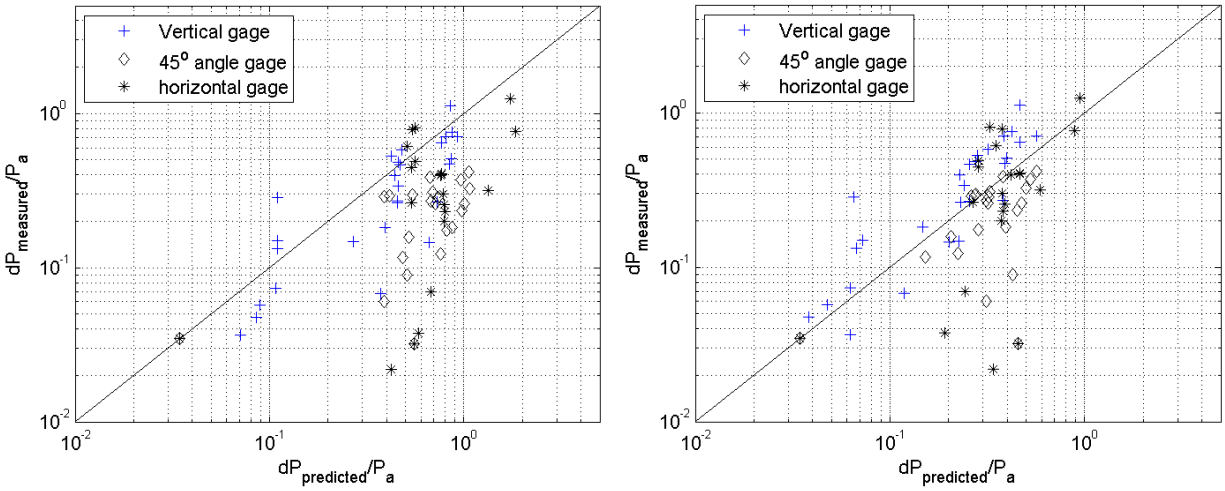

Figure 6-15 Comparison between energy models and experimental data from small scale BLEVE 2015 (left: Prugh 1991; right: Casal 2006 irreversible)

Similarly side-on overpressure was still well predicted by Prugh (1991) for the data from 2017. The overall accuracy of the irreversible model was better, but some side-on overpressure was under-predicted. Measurements above the vessel and at 45° angle brought similar conclusions with data from 2017 and 2015. Correction factors accounting for anisotropy could be added on the overpressure to make it predictable with these energy models.

It was also noticed that a lot of experimental overpressure fell well under the prediction curve. This was because of the non-ideal type of explosion that are BLEVEs. The overpressure depended on a wide range of parameters that were difficult to take into account in the modeling, particularly when considering the dynamic of opening and the vessel structure.

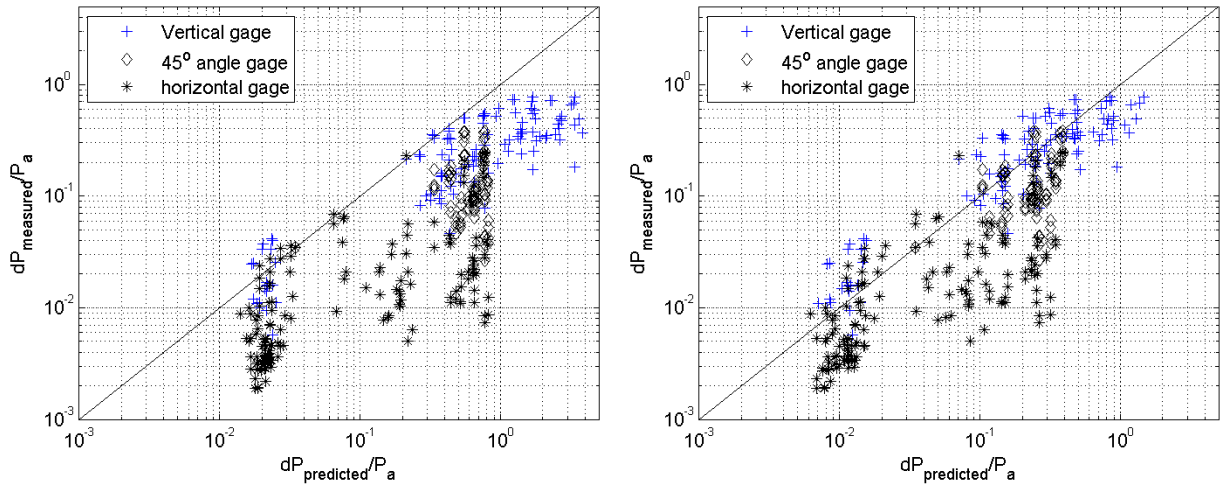

Figure 6-16 Comparison between energy models and experimental data from small scale BLEVE 2017 (left: Prugh 1991; right: Casal 2006 irreversible)

Table 6-2 Scaled distance, overpressure range and error of experimental test campaigns through expansion energy modeling

		Prugh (1991)	Casal (2006) irreversible
2015			
Scaled distance range		$0.5 < \bar{R} < 3$	$0.8 < \bar{R} < 5$
Scaled overpressure range		$0.02 < \frac{dP}{P_a} < 1$	
Horizontal	FB	-1.01	-0.44
	NMSE	1.46	0.28
45°	FB	-1.00	-0.40
	NMSE	1.56	0.34
Vertical	FB	-0.25	0.39
	NMSE	0.26	0.44
2017			
Scaled distance range		$0.3 < \bar{R} < 10$	$0.5 < \bar{R} < 25$
Scaled overpressure range		$0.002 < \frac{dP}{P_a} < 0.8$	
Horizontal	FB	-1.56	-1.06
	NMSE	16.2	4.62
45°	FB	-1.29	-0.56

	NMSE	3.15	0.60
Vertical	FB	-1.11	-0.19
	NMSE	4.27	0.57

However, rather than improving these models by adding constants from experimental curve fit, the relevance of the physics behind the models needed to be questioned. Both models used above consider energy coming from the boiling liquid to predict the lead shock overpressure, either through flashing fraction or through superheat energy. It was discussed previously in this work that, because of the timing of the succession of events, the lead shock should be generated mostly from the expansion of the vapor phase. Thus, even though fitting coefficients made the prediction models accurate (particularly with Casal irreversible model and the use of $\beta = 0.07$ based on experimental fit), the physics behind the model does not match the physical reality exposed above.

IV-2. **Expansion-controlled propane charts** (Van den Berg, 2008)

The expansion-controlled model presented by Van den Berg (van den Berg et al., 2004) presents another physical approach.

Experimental data has been compared with this approach. To do so, the charts created by the authors required the use of a mass as source of energy for the expansion. The model was based on vessels full with 100% liquid. As seen previously, this was rarely the case for our experiments, as well as for real cases of BLEVE. The full mass of propane from experiments was considered for the scaled distance.

The charts exposes different curves for different failure temperature (Figure 2-28). Based on the failure temperature of the experiment, the curve chosen was the nearest temperature above the failure temperature (example: if $T_{fail} = 332K$, we chose to compare it to the curve based on $T = 340K$).

Comparison between some cases and different curves of the expansion-controlled chart showed the choice of using the whole mass of propane was conservative (Figure 6-17). This model was not limited to model side-on overpressure measurement because of the hemispherical CFD domain. The points that were significant in defining the conservative aspect of this model were the overpressure measurements from the above the vessel. The focus was placed on those for the comparison.

Comparison through a parity plot between experiment and expansion-controlled prediction confirmed the conservative aspect of this model (Figure 6-18). Based on the way the model was implemented to the small scale BLEVE data, it led to a strictly conservative model. Error values were compared together with other model in the next section.

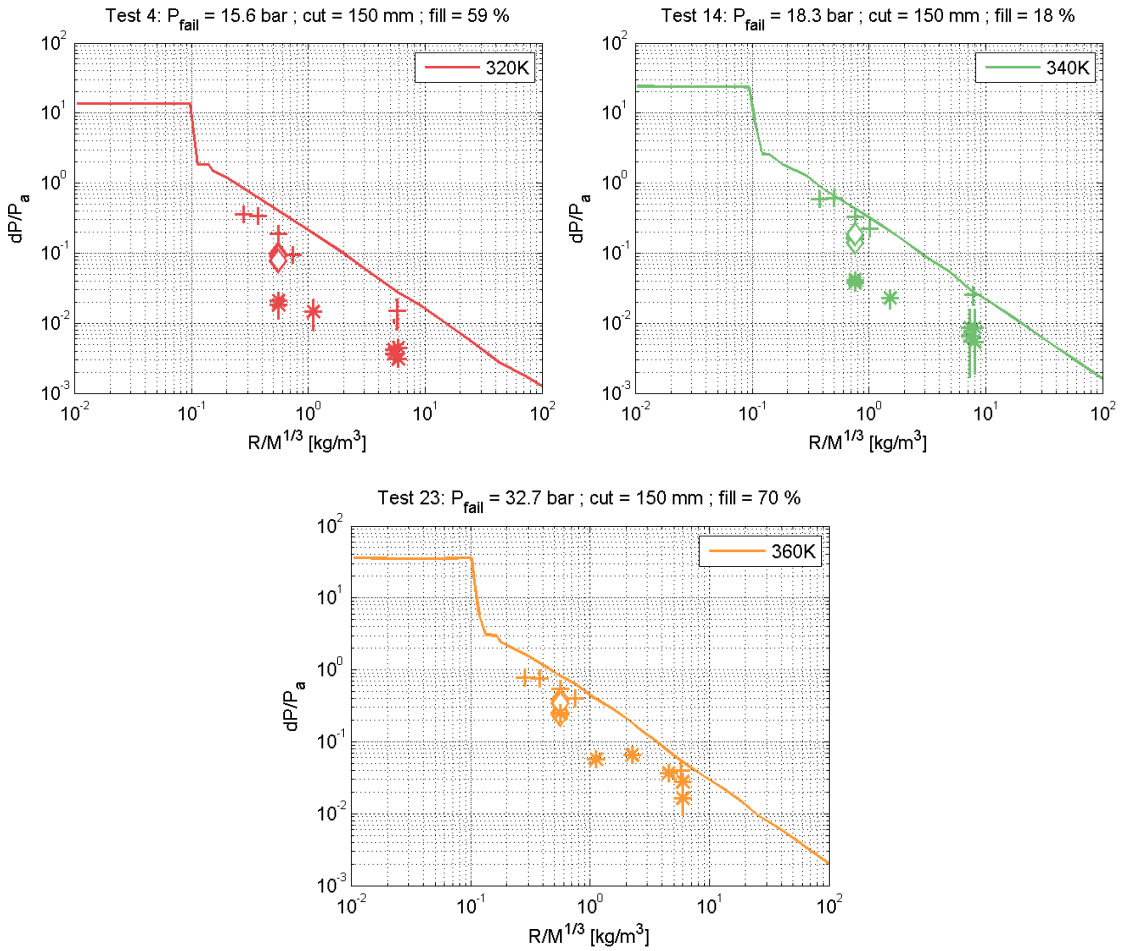

Figure 6-17 Comparison of experimental data for three experimental cases with the corresponding expansion-controlled curve from (Van den Berg, 2008)

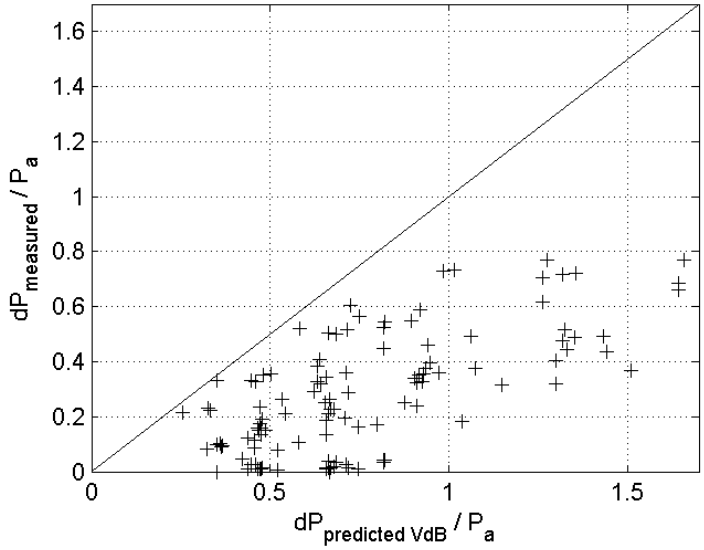

Figure 6-18 Prediction from expansion controlled model versus experimental results

Modeling the lead shock overpressure based on the evaporation rate of liquid boiling is again not in line with our findings of shock generated by the vapor phase expansion.

The next part of this work propose a prediction model based on first principle of compressible flow and thermodynamics, to model the maximum lead shock overpressure based solely on the vapor expansion of the BLEVE.

IV-3. Overpressure prediction through hemispherical shock propagation model

IV-3.1. Theory reminder

A new approach was investigated through this work to predict maximum overpressure with no need to consider expansion energy and properties from the liquid phase. To do so, the method developed by Friedman and Whitham (also called F-W through this work) (Kornegay, 1965) was used and implemented to the cylindrical vessel burst. This method was detailed in Chapter 3 **.** The method consists in calculating the analytical spherical decay of a shock, based on initial conditions at the burst interface calculated from shock tube theory (reminded here equation (26)). The interest of this method was that it uses only properties from the vapor space.

$$\frac{p_4}{p_1} = \frac{2\gamma_1 M_1^2 - (\gamma_1 - 1)}{\gamma_1 + 1} \frac{1}{\left(1 - \frac{\gamma_4 - 1}{\gamma_1 + 1}\frac{c_1}{c_4}\left(M_1 - \frac{1}{M_1}\right)\right)^{\frac{2\gamma_4}{\gamma_4 - 1}}} \tag{26}$$

Initial conditions were independent of the geometry, and based solely on the failure conditions (failure pressure p_4 and temperature) and fluid properties γ_4 and c_4. This model assumed ideal gas for the propane vapor to work as a piston. This assumption is not valid when the temperature drops far enough after expansion of the vapor, but remains valid for the formation of the shock and the first steps of its propagation.

To make an analogy between this theory and the BLEVE experiment required to set assumptions on the spherical aspect of the experimental shock. The tube was set 1m above the ground. Thus, far-field measurements can be considered as measuring spherical shock. However in the near-field, the tube shape and the base plate were in the way of the downward propagation of the shock. Hemispherical behavior seemed closer to this part of the flow. The purpose of this work being modeling the near-field blast in a safety conservative perspective, hemispherical behavior was chosen.

The spherical propagation equation from Friedman and Whitham was developed by transforming equation (41) into equation (42) by formulating the shock area A in term of the radius of its spherical shape R.

$$-\frac{dA}{A} = \frac{2MdM}{(M^2-1)K(M)} \tag{41}$$

$$-\frac{dR}{R} = \frac{MdM}{(M^2-1)K(M)} \tag{42}$$

Where A is the shock surface area, R is the radius of the spherical shock, M the Mach number of this shock, and K(M) a function of M (see (Kornegay, 1965) for more details).

The transformation from equation (41) to equation (42) is the same if the shock shape considered is a sphere or a hemisphere (equation (43)).

$$\frac{dR}{R} = 2 * \frac{dA}{A} \tag{43}$$

Friedman and Whitham integrated equation (42) to get the equation characterizing the radius of the spherical shock based on its Mach number and initial radius (equation (44)). Based on the equation (43), the propagation equation (44) can be used both for a sphere and a hemisphere.

$$\left(\frac{R}{R_0}\right)^2 * \frac{Y-Z}{M}\left[\sqrt{\gamma-1}*Y+\sqrt{2\gamma}*Z\right]^{\sqrt{\frac{2\gamma}{\gamma-1}}} * Y^{\frac{2}{\gamma}} * e\left\{\frac{1}{\sqrt{2\gamma-2}} * \sin^{-1}\left[\frac{2Y^2-(\gamma-1)*Z^2}{(\gamma+1)^2*M^2}\right]\right\} = C \tag{44}$$

$$with \begin{cases} Y^2 = 2\gamma M^2 - \gamma + 1 \\ Z^2 = (\gamma-1)M^2 + 2 \end{cases}$$

The decay calculation was based on an initial reference radius R_0. As the model was thought for spherical burst, some adjustments were needed to be made to apply it to the vessel geometry. As a first estimation, the reference radius R_0 was chosen to be the equivalent sphere radius to the vapor space volume at failure. Thus, the more vapor, the larger radius and the stronger piston to push the shock away.

Then, because assumption of hemispherical shock was used, the conversion was made to consider the radius of an equivalent hemisphere.

$$R_{0\ hemisphere} = 2^{1/3} * R_{0\ sphere} \tag{45}$$

IV-3.2. First experimental estimation

The overpressure based on this first estimation was calculated and compared with experimental overpressure measurements. The experimental data points taken for comparison were the measurements above the vessel, near-field (dP1 to dP4: 15cm to 40cm) and far-field (dP14: 3m). Most experimental data points were predicted by the model in a conservative way (Figure 6-19 left). One case was under-predicted (Figure 6-19 right). This under-predicted case was full of liquid, the volume of the vapor phase was very limited. Thus it reached a limit of the model: if the vapor volume is close to null, the shock decays very fast and result in a weak shock at the transducers position.

It was observed that the overpressure from experimental data decayed faster than the prediction for a hemispherical propagation of the shock: F-W model predicted a decay of the form $\frac{dP}{P_a} \propto \frac{R}{R_0}^{-n}$ with $n = 0.9$ while a least square linear curve fit on the experimental points lead to $1.03 < n < 1.23$ depending on the cases.

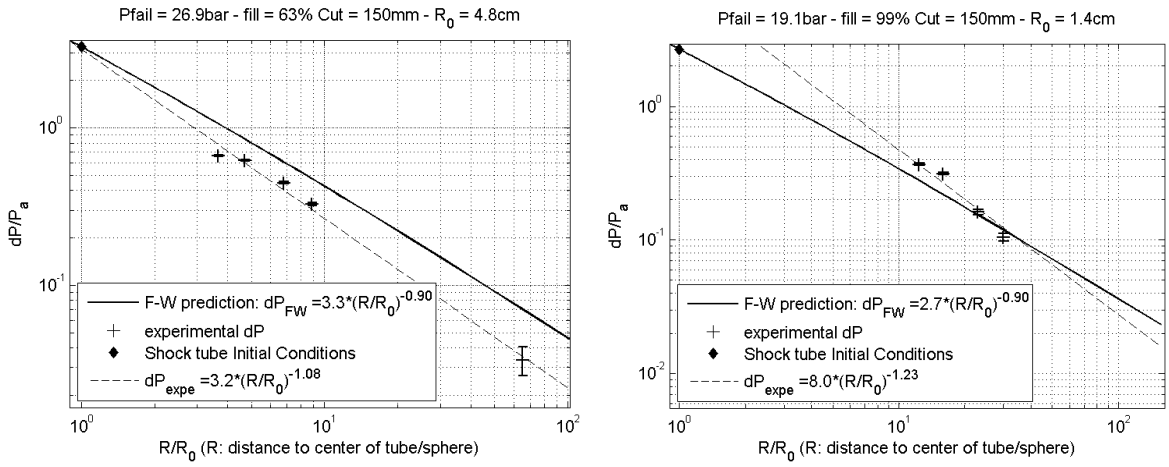

Figure 6-19 Comparison of experimental overpressure measurements with Friedman Whitam prediction for one test case of small scale BLEVE 2017 (left: conservative prediction for most tests; right:underpredicted case, mostly liquid)

The results of the prediction were summarized and compared with experiment on the parity plot Figure 6-20. Unlike the expansion controlled model, a few experimental points were under-predicted. However, comparison of the NMSE between prediction and experiments for F-W model and the models previously presented showed that F-W model was conservative, but also as accurate as Casal superheat energy model at predicting the blast overpressure above the vessel (Table 6-3), which was proven to be not conservative enough when predicting vertical blast measurements from 2015 and 2017 (positive FB Table 6-2).

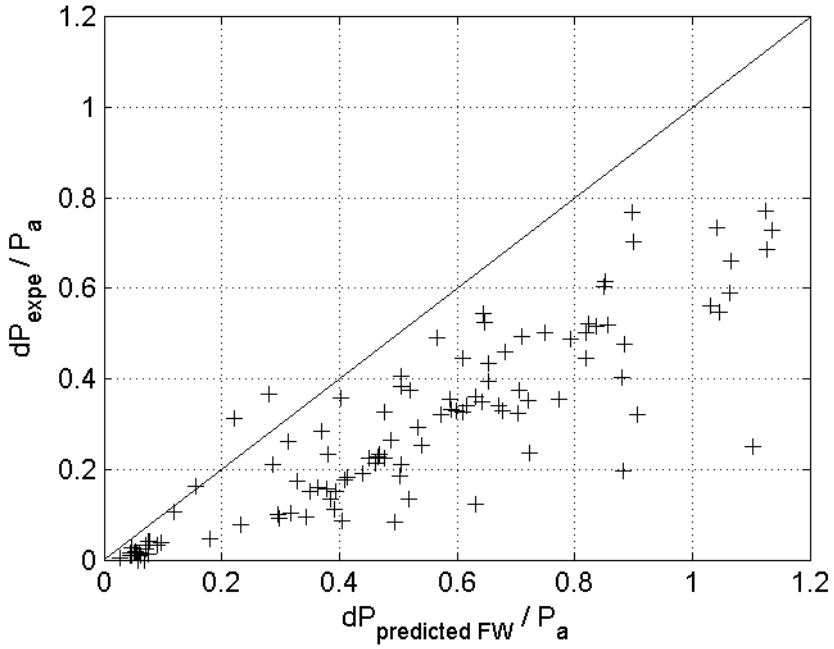

Figure 6-20 Prediction from Friedman-Whitham model versus experimental results

Table 6-3 Comparison between prediction models: errors between predicted and measured overpressure

Model	Prugh (1991) Isentropic	Casal (2006) Irreversible	Van den Berg (2004) Expansion controlled	Friedman Whitham Hemispherical vapor burst
Fractional Bias	-1.11	-0.19	-0.74	-0.57
Normal Mean Square Error	4.27	0.57	1.11	0.55

IV-3.3. Adjustment of the modeling: effective vapor volume fraction

A small over-prediction is the safe approach used when modeling for risk analysis and emergency responders. However it was decided to investigate in making these prediction more accurate, to understand the underlying mechanism behind shock generation with BLEVE.

To get an accurate prediction of the overpressure for each experimental case, the initial radius R_0 was adjusted until one of the over-predicted experimental data points get an exact prediction from theory (Figure 6-21). This criterion has been chosen to stay conservative.

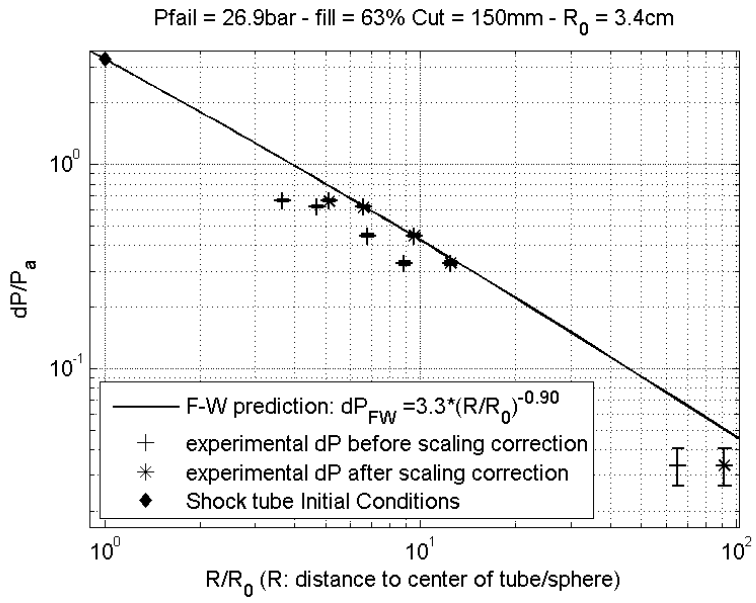

Figure 6-21 Comparison of experimental overpressure measurements with Friedman Whitham prediction before and after radius adjustment

From the adjusted initial radius, the volume of the equivalent hemisphere of radius $R_{0\,adjusted}$ was calculated. By comparison with the real volume of vapor phase before failure, it resulted in an effective fraction of vapor volume involved with production of the shock. In other words we are suggesting that depending on the details of how the vessel opens up, not all of the vapor was involved in the production of the shock. We expected that for rapid opening (i.e. high failure pressure) most if not all the vapor was generating the shock. This was called the effective vapor volume. This was the volume of vapor that effectively contributes to the generation of the shock.

In the case presented above (Figure 6-21), the radius reduced from 4.8 cm to 3.4 cm, leading to an effective vapor volume fraction of 43%. Only 43% of the vapor space contributed to the piston generating the lead shock wave. It can be explained in considering the dynamics of the opening of the vessel: a longer opening vessel lead to a smaller fraction of the vapor actually pushing for the initial shock to propagate in the atmosphere. Low failure pressure lead to lower lead shock overpressure for two reasons: equivalent shock tube overpressure was smaller, and opening velocity of the vessel was slower (as seen Figure 6-6).

Most cases were overestimated by the F-W method, requiring an effective vapor fraction below 1 (Figure 6-22). For one case, the experimental measurements were under-predicted by the spherical propagation model. A safe conservative criterion was applied to calculate the excess vapor playing a role in the lead shock overpressure. This excess vapor was converted in liquid volume fraction to get an idea

of how much liquid would be required to balance the modeling in a conservative way. The equivalent volume fraction of liquid was calculated with the liquid and vapor density ratio:

$$x_{liq} = x_{vap} * \frac{\rho_{vap}}{\rho_{liq}} \tag{46}$$

The amount of liquid necessary to balance the model conservatively was 0.2% of the full liquid volume. It was small compared to the contributing flash fractions expressed in the literature (50% of the liquid volume for propane failing at $T_{fail} = 53^{o}C$ (van den Berg et al., 2004)).

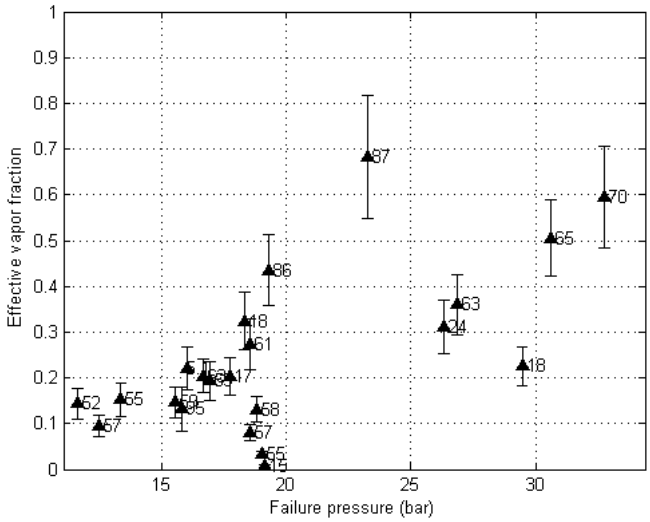

Figure 6-22 Effective vapor fraction based on Friedman-Whitham theory compared with small scale BLEVE experiments, with liquid fill value at each point ($\gamma_4 = 1.13$)

IV-3.4. Scaling up to larger scale experiments

After formalizing this compressible flow model with small scale experimental data, it needed to be verified with larger scale. To do so, experiments of 400L (Birk et al., 1993), 2000L (Birk et al., 2006b) and 5000L (Johnson and Pritchard, 1991) BLEVEs were used. The method previously used was applied to these cases. For conservative purpose, only the cases giving the strongest overpressure for each experiment was investigated.

Based on initial conditions, the shock tube overpressure and the initial vapor sphere are determined. From F-W equations, the spherical decay was calculated. Finally, by fitting the model to the experiments, a vapor fraction was calculated (Figure 6-23).

The prediction gave a reasonable vapor fraction, in good agreement with the behavior observed with small scale experiments (Figure 6-24).

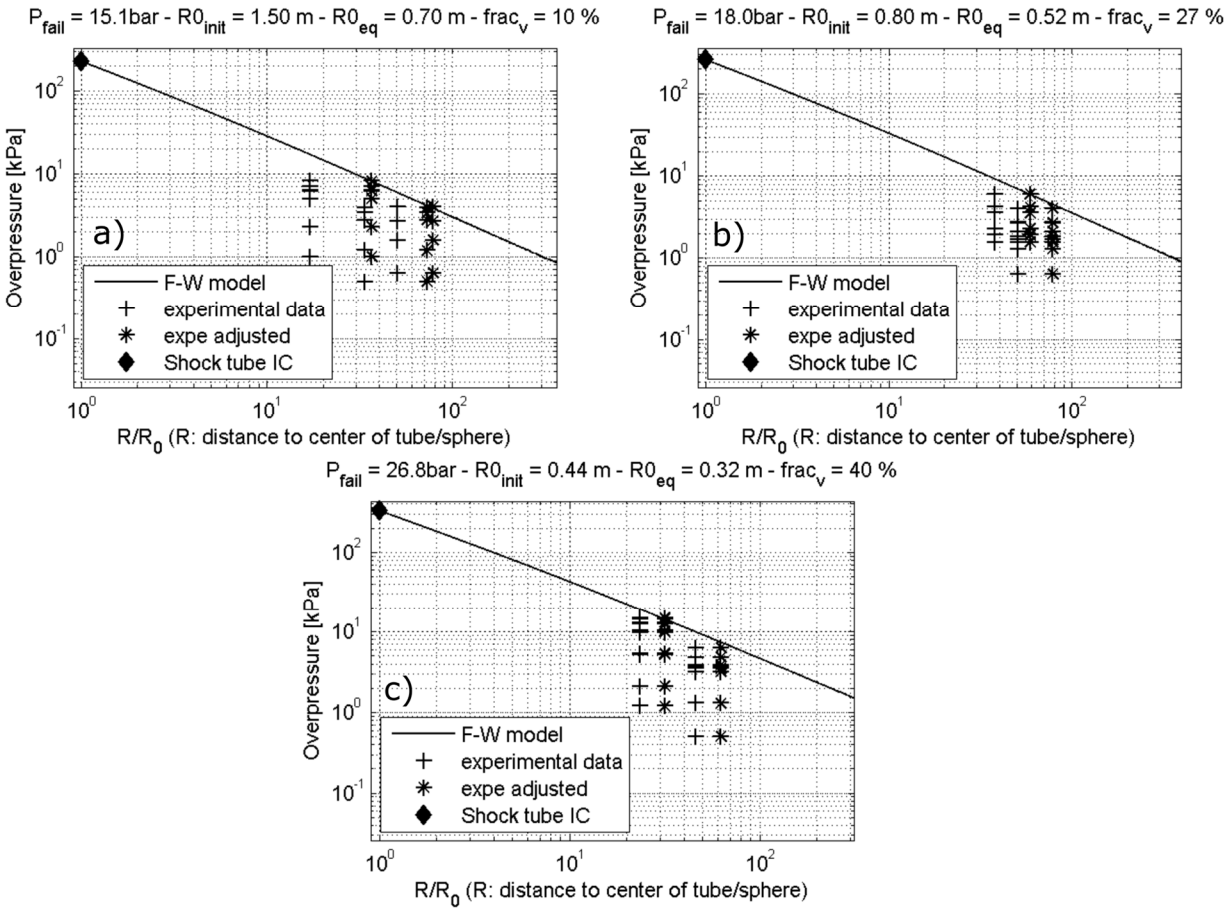

Figure 6-23 Prediction of large scale experiments from literature with F-W model: a) 400L, b) 2000L, c) 5000L

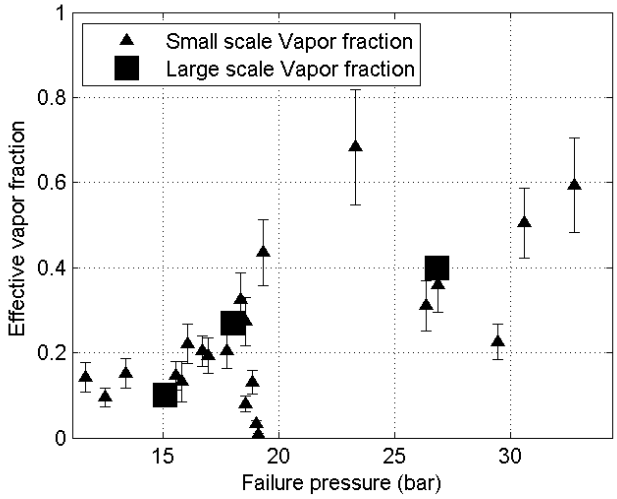

Figure 6-24 Effective vapor fraction based on Friedman-Whitham theory compared with small scale BLEVE experiments and large scale experiments from literature ($\gamma_4 = 1.13$)

This suggested that the approach scales well to larger vessels. It also showed that higher burst pressures produce stronger shocks because of the higher shock tube overpressure, and the faster opening allowed more of the vapor content to be involved with production of the shock.

It was noticed however that the experimental data decayed too fast compared to the F-W hemispherical prediction. This induced a significant systematic error. Perspective of improvement of the model need to implement a dissipative term in the propagation equation in order to fit with experiment.

V - Conclusion on lead shock characterization

This chapter presented several aspects of the maximum overpressure generated by a BLEVE through the experimental setup:

- Anisotropy of the pressure field from cylindrical burst gave strong differences between the overpressure above the vessel and on the sides. Difference was noticed between side and end measurements in the near-field too. However, far-field measurements showed that the blast was more isotropic for side-end measurement comparison, while the pressure above the vessel was still significantly larger.
- The maximum overpressure seemed to be directly correlated to the amount of vapor volume in the vessel before failure. This showed a strong dependency between lead shock strength and the vapor phase. This statement worked in favor of the argument that vapor was the main contributor to the lead shock overpressure.
- Energy models from the literature gave decent agreement with experimental results. These models were based on the liquid energy. The physics they use is against the statements made above about the contribution of the vapor to the lead shock overpressure. They used a fair amount of liquid flash fraction or superheat energy. This was the reason why a new model based on compressible flow conservation equations was developed.
- The hemispherical vapor burst approach consisted in applying shock tube conditions on an initial sphere of volume equivalent to the vapor space, and propagate the shock formed based on spherical propagation equations. Because the BLEVE was a non-ideal and non-spherical explosion, adjustment was required to match experimental results. To do so, the initial hemisphere radius was adapted (reduced most of the time, increased for one case).
- To calculate conservative BLEVE overpressure based on F-W model, one must assume 100% of the vapor is involved in the shock formation with its ideal gas properties as initial guess. Refining

this guess requires to quantify the amount of vapor fraction based on failure parameters (failure pressure, opening length, etc.).

- The prediction in term of contributing vapor fraction made decent physical sense with the small scale experimental BLEVE presented in this work, as well as with larger scale experiments from literature. This was encouraging, considering the many strong assumptions made to come up with this prediction: hemispherical propagation, ideal gas propane expanding, etc.

Chapter 7

Secondary flow patterns

Ⅰ - Purpose of the chapter

In the previous chapter, we discussed the origin of maximum overpressure of the first pressure peak, debated the relevance of the energy models based on liquid flash fraction and proposed a model based on the vapor phase characteristics only. This chapter focuses on the later peaks and features of the pressure field, in order to understand better its origins, source of diverging opinions in the literature. This leads to a clear picture of the flow patterns in the near-field. It introduces some explanation for the source of the 2nd shock and potential 3rd shock.

Ⅱ - Second shock formation process

Literature showed that BLEVE strong enough usually lead to more than one overpressure peak. It was common to have two successive overpressure peaks, and some cases showed a third one, even though it was not always considered as a shock (Figure 2-21).

Literature also showed that for spherical geometry, the second shock comes from overexpansion of the flow behind the lead shock, creating a semi-stationary shock sustained by critical outward flow from the explosion. This shock can be assimilated to a Mach shock. When the flow cannot sustain the shock anymore, the flow turns inward, the shock collapses toward the center of the sphere. Its reflection at the center of the sphere generate another shock propagating outward (Figure 3-15). The characteristic plot for spherical wave propagation presented in the literature can be extended to Figure 7-1.

The purpose of this section was to use this explanation for the second shock formation to interpret data collected with the small scale BLEVE apparatus. Some CFD work of transient start of jet supersonic jet helped the comprehension of the data observed.

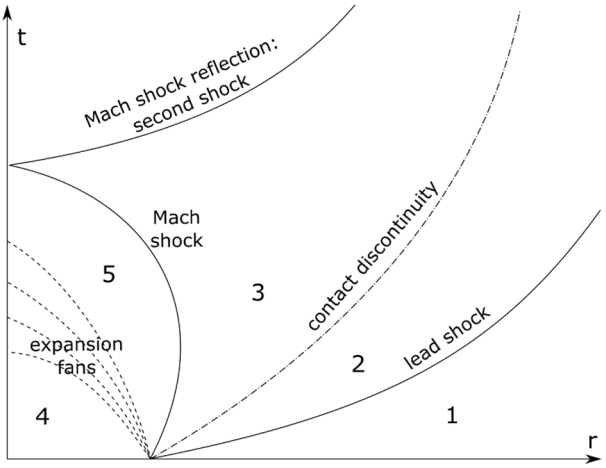

Figure 7-1 Time versus distance for spherical flow field propagation with Mach shock reflection

II-1. Understanding of the Mach shock behavior through transient jet CFD

II-1.1. Analogy of the transient jet start with Mach disk and second shock formation from literature

CFD of transient supersonic jet start and collapse was performed to observe the behavior of the flow leaving the tube at opening. The simulation of the cylinder geometry presented in the experimental setup was initiated, but did not

Time constraints did not allow to complete simulations on the geometry of the cylinder as presented in the experimental setup. However, the study of another prototype available at the laboratory of IMT Mines Alès through CFD allowed to emphasize some flow patterns useful for the understanding of the phenomena with the cylinder burst. The design of the tube was based on an experimental prototype. Experiments have not been run with this apparatus yet. Thus the simulation was used to find analogy between literature and small scale BLEVE experiments. More details on the simulation geometry and numerical scheme is given in Appendix G.

The open-ended shock tube simulation was ran with compressed air, failure at 20bar, to have similar failure pressure than the most common BLEVE cases from experiment.

The flow after burst showed the general behavior presented Figure 7-2. Contour plot of the pressure field showed an initial lead shock, behavior expected and understood from Chapter 6 . Upstream of the lead shock, it showed a reversed shock, moving up to a certain distance away from the tube (x = 0.37). Finally, coincidently with sufficient pressure drop in the tube, the shock collapses toward the tube exit, showing complex vortex patterns.

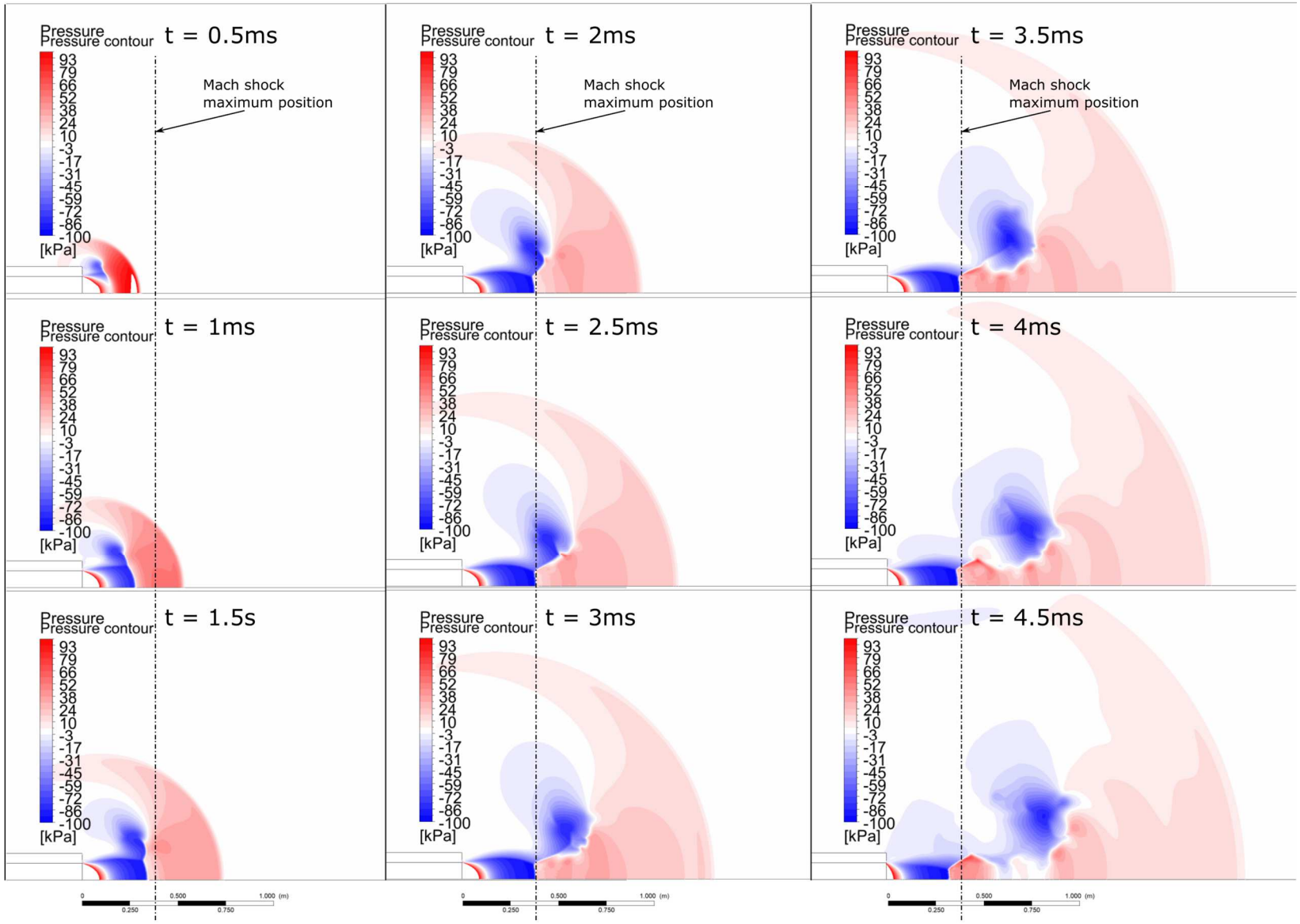

Figure 7-2 Contour plots of the pressure evolution after burst of the compressed air chamber

Stationary CD-nozzle theory explained the presence of this shock with the critical choked flow upstream, following isentropic expansion through the nozzle geometry and requiring under-expanded shock structure to fit the flow conditions outside the nozzle. The structure of the simulated shock were very similar to the topology of under-expanded shock from literature (Figure 7-3).

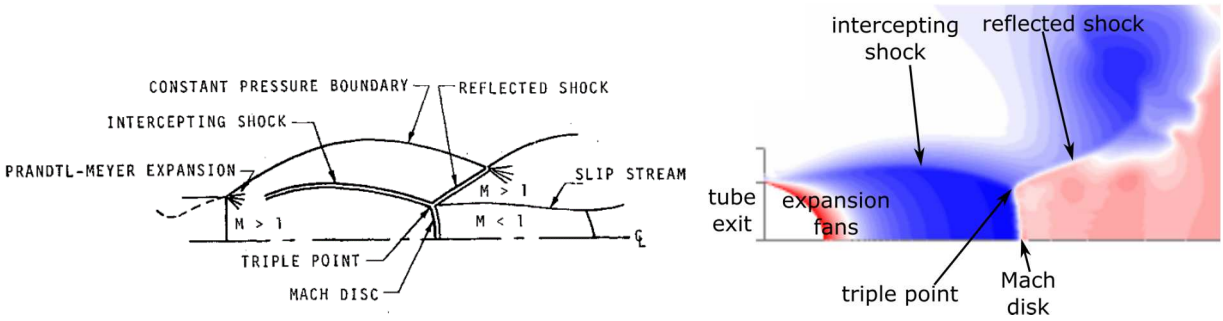

Figure 7-3 Structure of the under-expanded shock (left: schematic at nozzle exit ((Abbett, 1971)*); right: CFD of transient jet start, at t=2ms)*

Spherical burst BLEVE simulation showed a similar reversed shock (Yakush, 2016). This phenomenon was the origin of 2nd shock when it collapsed. The analogy between spherical burst and this OEST simulation was made by comparing pressure profiles along the axis at different time steps (Figure 7-4). The Mach disk progression visible Figure 7-2 up to x=0.37m was observable Figure 7-4 as the steep pressure discontinuity from negative gage pressure to positive gage pressure, also reaching a maximum position of x=0.37m (Figure 7-4 left) before collapsing toward the x-coordinate x=0m, exit of the tube (Figure 7-4right).

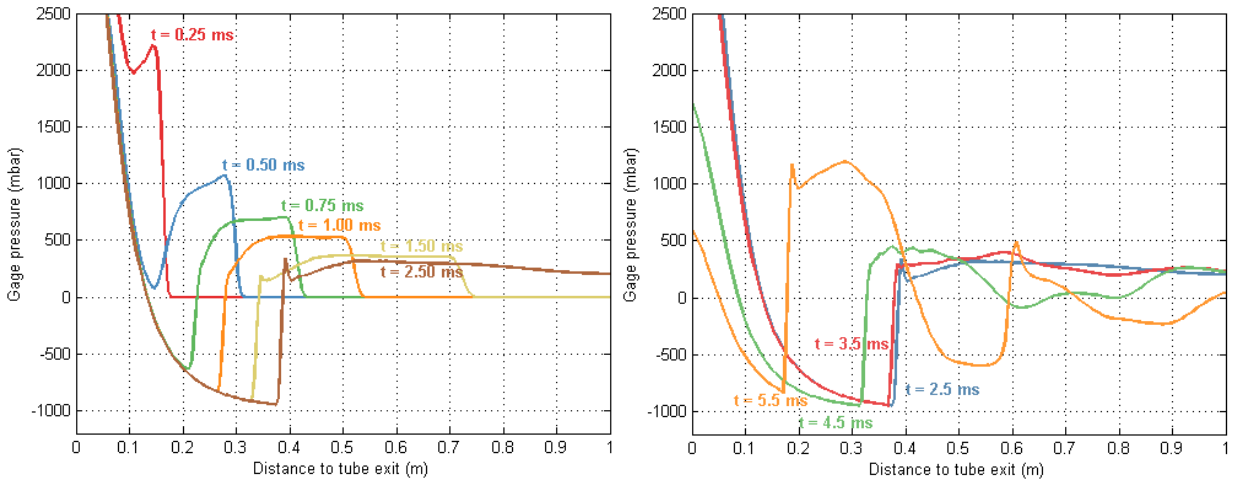

Figure 7-4 P-x plot after burst at the tube exit for various time steps (x=0: tube exit)

II-1.2. Analogy between transient jet and BLEVE experimental overpressure

In order to relate the literature and CFD statements with experimental results, one need to comprehend the link between P-x plots available with numerical simulations and P-t plots available with experiments. This was made possible thanks to the CFD of the transient jet. For the purpose of the analogy, pressure monitors were placed along the axis of tube, simulating blast gages. When observing the pressure monitors at the locations surrounding the Mach disk maximum distance away from the tube (x=0.2 - 0.3 - 0.4), the profiles presented Figure 7-5 were obtained. By combining Figure 7-4 and Figure 7-5, one can understand the behavior of the pressure at the monitors, equivalent to the sensors in experiments, with the formation and collapse of Mach shock. The following steps were recognized:

- lead shock formation: visible successively through x=0.2m, 0.3m, 0.4m at t=0.25, 0.5 0.75ms, with decaying maximum overpressure as seen in the previous chapter;
- Mach disk formation: visible with a pressure drop into negative gage pressure through x=0.2m, then x=0.3m. No steep pressure drop was visible on x=0.4m. As seen Figure 7-2 and Figure 7-4, the Mach shock did not reach this location;
- Mach disk collapse: visible through a strong pressure rise back into positive overpressure, first on x=0.3, then x=0.2. The order was important to notice, as it showed the progression of the phenomenon from downstream toward upstream.

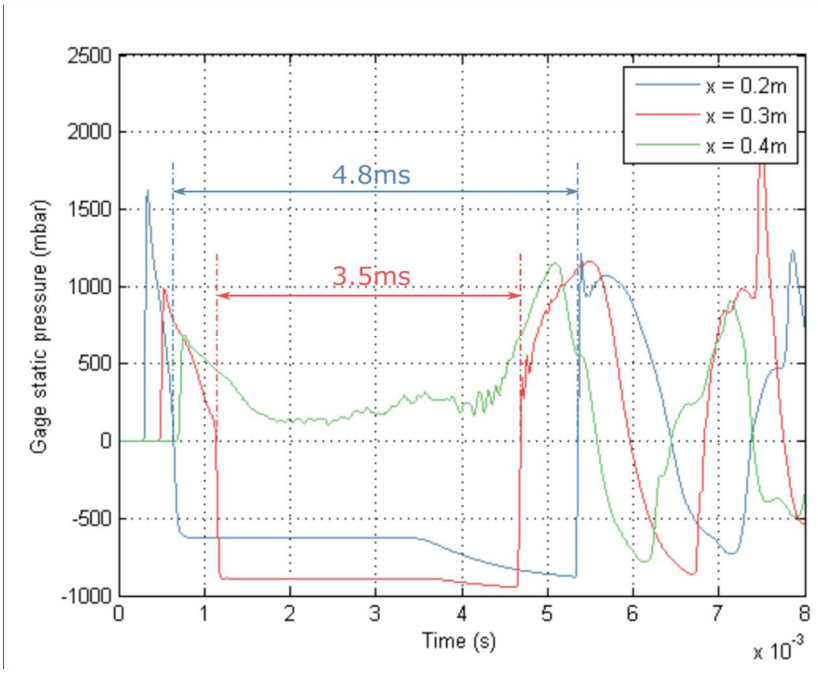

Figure 7-5 Pressure profile against time at different locations around the Mach disk maximum reach based on transient jet CFD

For small scale BLEVE experiments, pressure measurement along the whole axis above the tube or cylinder was practically not possible to set up. Only punctual blast gages were placed at discrete locations above the vessel. Pressure profiles for one case is presented Figure 7-6. The patterns observed previously on transient jet start were found again for the first milliseconds after opening of the cylindrical vessel:

- A pressure rise successively on each sensor decaying with distance, which corresponded to the lead shock propagation;
- A pressure drop successively on dP1 (t = 0.7ms) and dP2 (t = 1ms). A short lasting pressure drop was visible on dP3 (t=1.4ms).
- A pressure rise, first on dP2 (t = 2.3ms), then on dP1 (t = 2.5ms). The pressure signal of dP3 did not show a large continuous drop, only a short one.

A possible interpretation of this observation is the following: a Mach shock has formed at the exit of the vessel, reaching a maximum height between dP2 and dP3 (20 and 30 cm) above the tube. It collapsed back in the tube when pressure in the vessel and restriction from tube opening were too weak. This type of pressure profile was visible on 8 BLEVEs over the 24 cases obtained with propane.

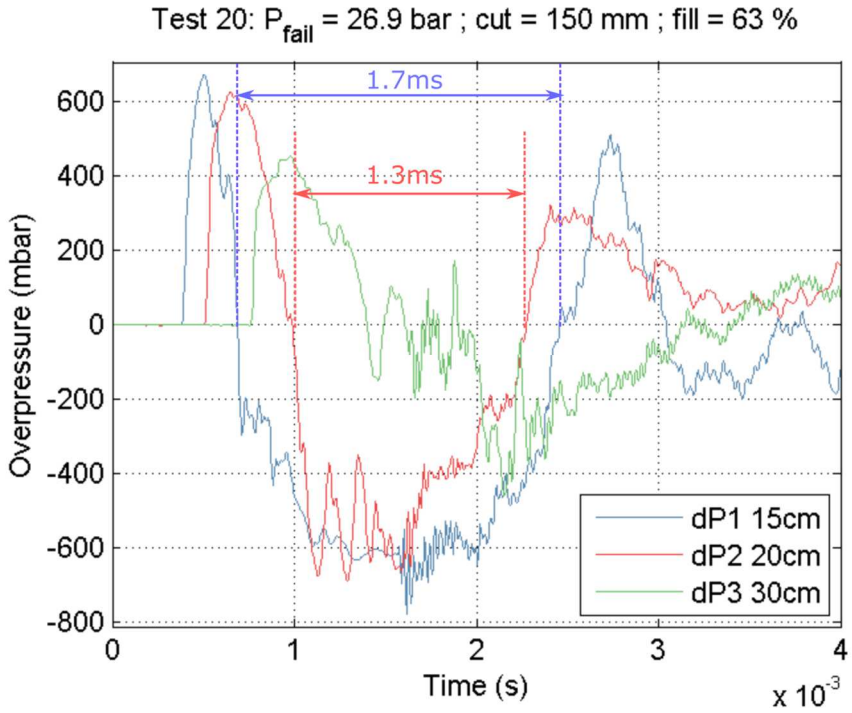

Figure 7-6 Overpressure measurements above the vessel for small scale BLEVE experiments ($P_{fail} = 26.9bar, \Phi_{liq} = 63\%, L_w = 150mm$)

Attention is brought to distinguish the Mach shock and the second blast observed in literature in the far-field. If a fluid is expanding fast enough, it will eventually over-expand and generate a Mach shock while reaching critical mass flow conditions. The collapse of this Mach shock brings an overpressure on the blast gages on its path (dP1 and dP2 for some small scale BLEVE cases). However this overpressure is not the second blast propagating outward noticed in the literature for explosions. The second blast is the reflection of this Mach dome on the center (in case of spherical explosion) or on a surface allowing proper reflection.

In the case of the small scale BLEVE experiment, the second blast was not visible on blast gages. This may be due to poor reflection on the bottom surface of the tube, because of the complex geometry of the tube when the Mach shock collapses. As seen in the CFD transient jet example, if the geometry of the source is too complex or restricted, the Mach dome collapse only generates complex vortices and flow patterns, but no clear second blast.

II-1.3. Mach shock imaging evidence

For all case, after the opening of the vessel, a white opaque cloud was visible above the vessel. Because of the assumption that vapor on the top of the vessel expands first, it was assumed that this cloud corresponded to condensation of the expanding vapor. Two cases exhibited a transparent dome inside this cloud (Figure 7-7).

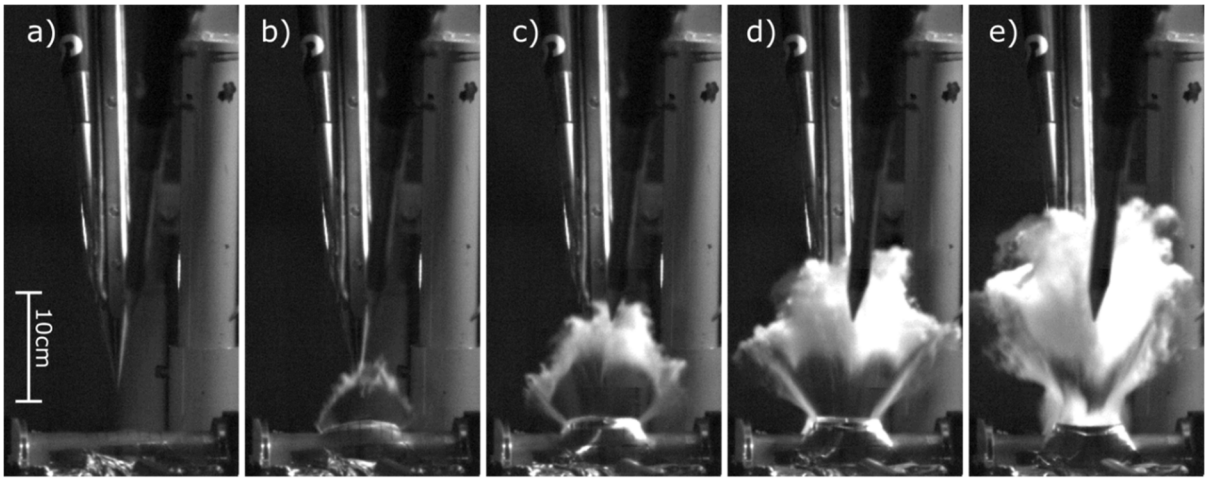

Figure 7-7 Formation of a condensation cloud above the Mach shock above the vessel ($\Delta t = 200\mu s$, $P_{fail} = 18.6\ bar,\ \Phi_{liq} = 56\%,\ L_w = 75mm$)

Based on the phenomenon presented previously, the interpretation of this phenomenon was the following:

- Vapor inside the vessel expanded through a restricted opening. The restriction acted like a converging-diverging nozzle (or vena contracta). It was assumed that the flow accelerated isentropically and became supersonic in the transparent dome. The pressure and temperature of the vapor dropped (state 5 Figure 7-8)
- Similarly to converging-diverging nozzle and supersonic transient jet, the flow over-expanded. To get back to the compressed state of the ambient air (after lead shock propagation), a reversed shock was formed, the so called Mach shock for transient jet. With the cylindrical vessel geometry, the Mach shock has a dome shape. The expanding vapor traveled through this shock, leading to strong pressure and temperature increase, leading to condensation downstream of the Mach dome (state 3 Figure 7-8).

Such analogy between BLEVE and stationary shock from jet flow was made in the literature (Figure 3-14) (Laboureur et al., 2015). Similar analogy was used here, with to the transient jet flow topology (Figure 7-8).

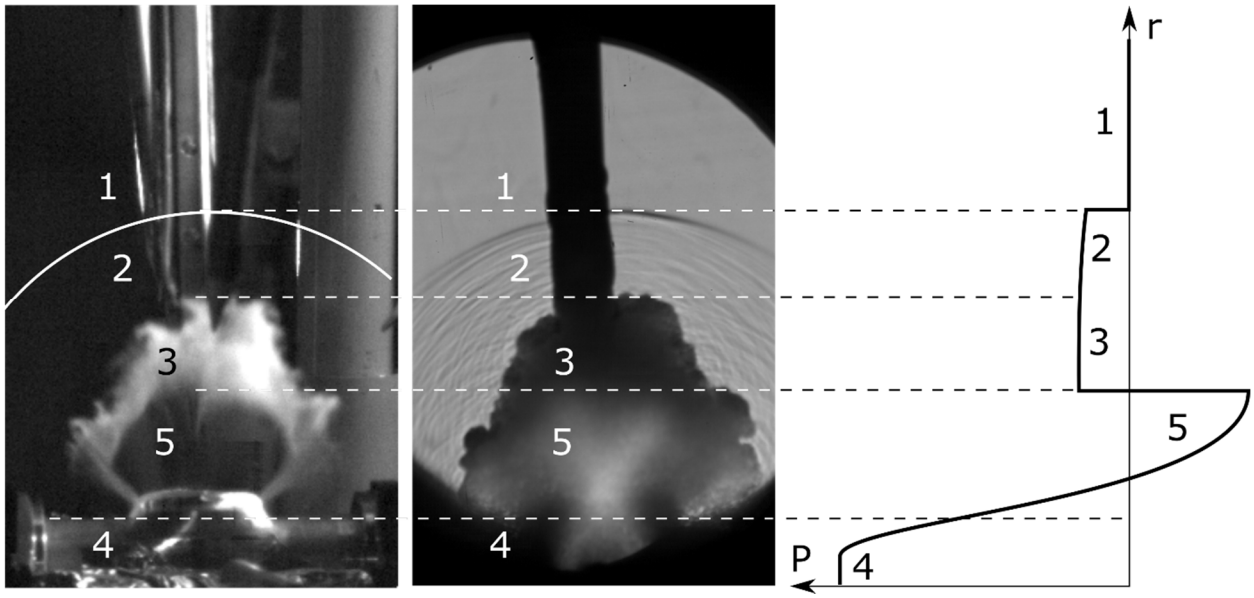

Figure 7-8 Pressure evolution through the flow features at the early steps of a BLEVE ($P_{fail} = 18.6\ bar$, $\Phi_{liq} = 56\%, L_w = 75mm$)

Pressure drop interpreted as the passage of the Mach shock was observed on eight cases. The Mach dome was visible on two cases. The other cases did not show evidence of this behavior. Two conclusions can be taken for these cases:

- The conditions of energy release and transient opening necessary to create the Mach shock were not met for all these cases. This could be due to a too weak failure pressure, or a too fast vessel opening that did not to allow constricted flow through the crack.
- Another argument could be that the conditions necessary for Mach shock formation and collapse were met, but the Mach shock did not expand further than 15cm were the first blast transducer is located. Thus, no experimental evidence allow to capture the phenomenon for other cases.

II-2. **Influence of liquid fill content on the Mach shock process**

It was stated in the literature that the second shock for BLEVE pressure profile comes from vapor space, and that a third pressure peak, although not a shock, may come from liquid energy. The objective of this paragraph is to link the Mach shock structure behavior to the liquid fill level, or the initial mass of propane in the vessel. It has been stated that the collapse of this shock is the source of the second blast shock propagating outward. Understanding the behavior of the former helped understand the latter.

For this purpose, overpressure from cases with similar failure pressure, cut length but varying liquid fill level are plotted Figure 7-9. From this graph, it was determined the following:

- As shown in Chapter 6 , the maximum overpressure of the lead shock decreased with increasing liquid fill level, for similar failure pressure. This was a reminder of Figure 6-10, relating the maximum overpressure to vapor phase volume.
- The lead shocks were not steep shocks. They turned less sharp with increasing liquid content. As exposed in the previous chapter, the formation of the shock through piston effect was visible with shadowgraph imaging. It was also visible on the pressure signals. For some cases, the shock appeared not fully formed and sharp at 15cm above the opening. Another argument was that BLEVE are non-ideal explosion, with a non-ideal opening and release of energy. Thus the blast generated were not as sharp shock as blasts from high explosives and detonations.
- The main point of this plot concerned the Mach shock phenomenon, particularly the duration of the negative gage pressure drop. With increasing liquid fill level, the duration of this drop increased (Figure 7-9 right). This meant that the Mach shock was sustained longer with larger amount of liquid. If liquid content delays its collapse, it is also linked to the delay of the second shock expelled outward. It should be noted that the slow pressure rise of the tests with large liquid fill level are not shocks such as the Mach disk, but serve a similar role in this flow.

This last argument agreed with one made through the work of numerical simulation of BLEVE from full liquid (Yakush, 2016): the second blast propagating outward from an explosion was not necessarily

due to the vapor only, but to a combination of liquid and vapor generating a Mach shock while over-expanding. Although some explosion of compressed vapor have enough energy to generate this phenomenon, when liquid boiling is involved in the explosion, it does play a role in delaying this second blast.

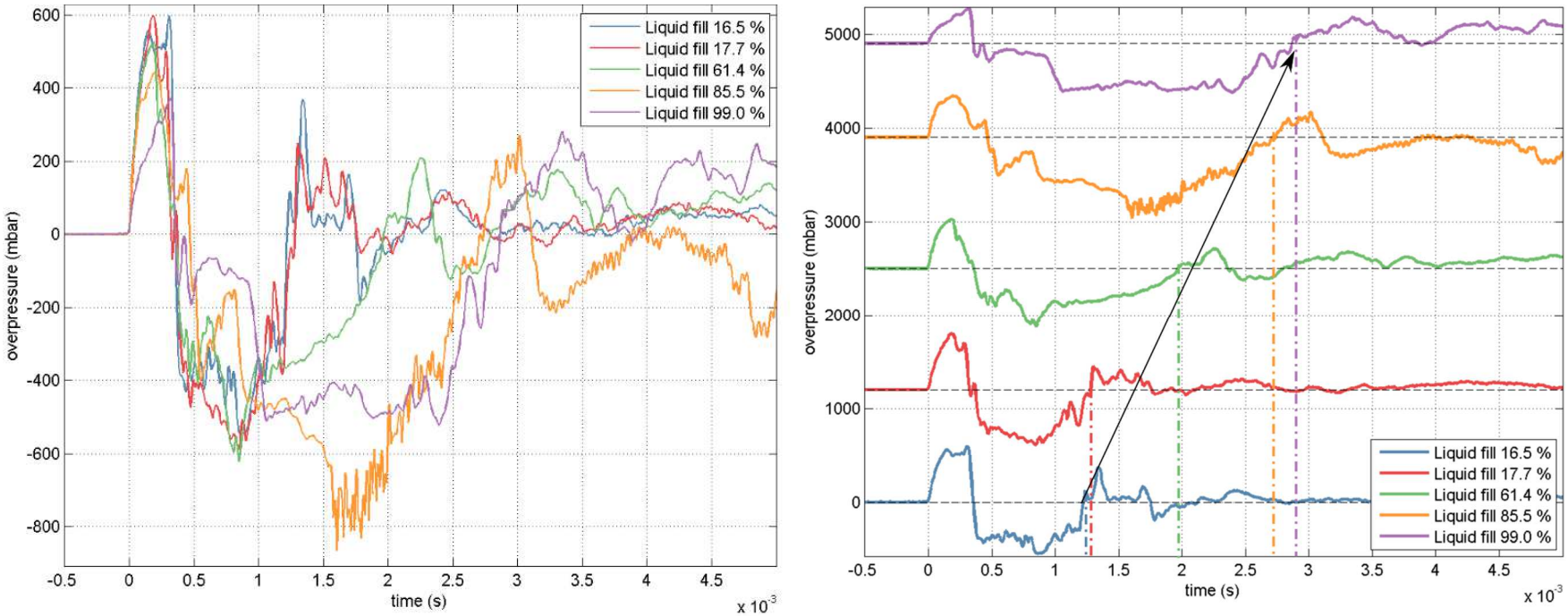

Figure 7-9 Overpressure measured above the vessel at dP1 (15cm), for various cases at $P_{fail} = 18.5 \pm 0.5bar, L_w = 150mm$ and varying liquid fill level

III - Conclusions

This chapter presented some interpretation of some secondary aspects of the flow beside lead shock overpressure.

- Some negative gage pressure similar to Mach shock formation and collapse from transient jet were observed with BLEVE. Literature showed that the second shock observed in the far-field of spherical explosion comes from the collapse of a similarly behavior Mach shock.
- A clear distinction was made between the Mach shock, visible only up to a certain distance in the near-field, and the second blast travelling outward in the far-field.
- A transparent dome at the exit of the vessel was observed on a few high speed imaging at early stage of BLEVE failure. This dome was related to the Mach shock phenomenon thanks to analogy with previous literature work.
- Influence of liquid content of the vessel on the duration of the Mach shock formation and collapse process was presented for cases of similar failure pressure. It was stated that liquid content tends to increase the duration before the collapse of the Mach shock, and thus the formation of the second blast propagating outward. However, this argument does not say anything on the intensity of the second blast wave.

These arguments were drawn mainly on qualitative observation of the flow field and pattern. Because the conditions necessary to generate such flow features were not the initial focus of the experiment, not enough data was available to conduct more quantitative study of the phenomenon. Suggestions for further investigations are numerical simulation with cylindrical vessel, similar to the small scale experimental setup, with varying opening size and energy in the vessel. This would allow to observe the influence of opening size on the generation of the initial transient jet of the BLEVE.

Other flow patterns were observed through the overpressure signal from different angles. However no interpretation was successfully drawn yet, due to lack of time on experimental analysis and analogy with numerical simulations.

Moreover, in order to deepen the understanding of the overpressure generation process and various flow patterns resulting from the BLEVE, one must investigate the boiling phase change behavior and consequences.

Chapter 8

Phase change observation and consequences

I - Introduction

Most findings and studies on BLEVE overpressure focused on characterizing and predicting the maximum overpressure generated by the explosion. As argued in the previous chapters, vapor expansion plays a major role in generating the lead shock overpressure. However this does not mean that liquid boiling is free of hazardous consequences. The liquid energy can produce projectiles, strong drag loading on nearby structures and a very large ground force. The next section includes discussion of how boiling can be characterized, how the timing of boiling supports the argument that vapor is the main source of initial peak overpressure, and introduces the potential hazards that may result due to the liquid boiling.

II - Objectives

This chapter describes the data collected to characterize the boiling process. In doing so:

- It presents the transient pressure signal and categorize it depending on the different profiles observed;
- It extracts quantitative characteristics from these graphs for the purpose of parametric analysis;
- It presents a chronological study to relate the different measurements to transient pressure;
- It uses simple physical models as the basis of understanding and estimation (expansion wave propagation, boiling wave propagation).

III - Detailed analysis

III-1. Transient pressure profiles

The transient pressure was measured at one end of the tube (Figure 8-1 left) using a high speed transient pressure transducer. The end cap of the tube was resting against a vertical hard plate to prevent it being propelled by the explosion. (Figure 8-1 right). When the vessel opened, pressure drop was observed. Moreover, other pressure patterns due to the physics of the expansion and the boiling in the

tube were measured. Various pressure profiles were measured through this sensor: some cases presented a continuous drop to atmospheric pressure (Figure 8-2 a) while other cases showed an increase in pressure during the expansion drop, either late in the drop (Figure 8-2 b) or earlier in the process (Figure 8-2 c).

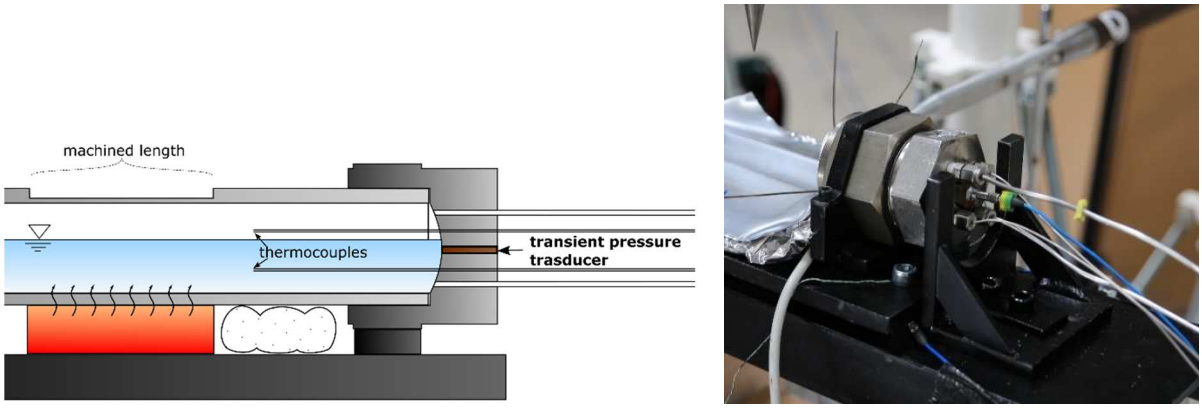

Figure 8-1 Transient pressure transducer location (left: scheme enlarged; right: photo of the transducer tube end with support plate)

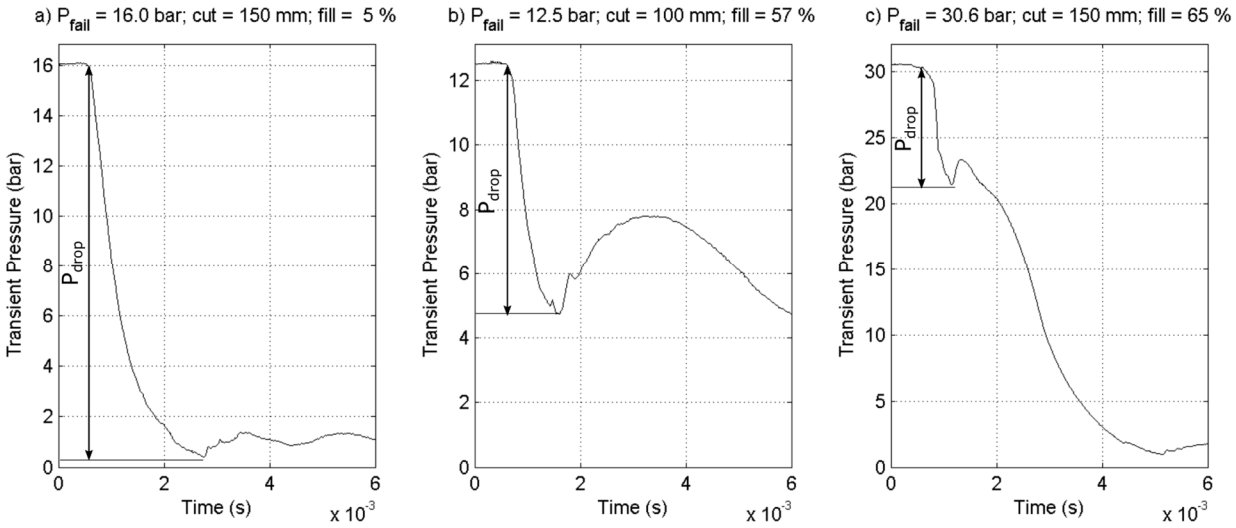

Figure 8-2 Pressure profiles with varying failure conditions (a) no repressurization; b) late repressurization ; c) early repressurization)

A classification of all the tests was made based on the pressure drop observed. From these different profiles, the pressure drop before stabilization, P_{drop}, was measured. This value allowed classification of all the tests according to their transient pressure profiles. The criterion chosen for classification was the following:

$$\begin{cases} a) & \dfrac{P_{drop}}{P_{fail}} > 0.9 \\ b) & 0.5 < \dfrac{P_{drop}}{P_{fail}} < 0.9 \\ c) & \dfrac{P_{drop}}{P_{fail}} < 0.5 \end{cases}$$

The classification of these cases was presented against the failure parameters (Figure 8-3). All cases in category (a) were low liquid fill cases, showing that pressure rise in the tube did not occur if the amount of liquid energy available in the tube was not sufficient. Late repressurization (category b) occured for most cases with low failure pressure but medium to high liquid fill, regardless of the cut length. In these cases, the pressure tended to increase smoothly in the tube over a long span of time (several milliseconds). Finally, early pressure rise (category c) was characteristic of high failure pressures. These cases led to a shorter, more violent pressure increase before dropping again.

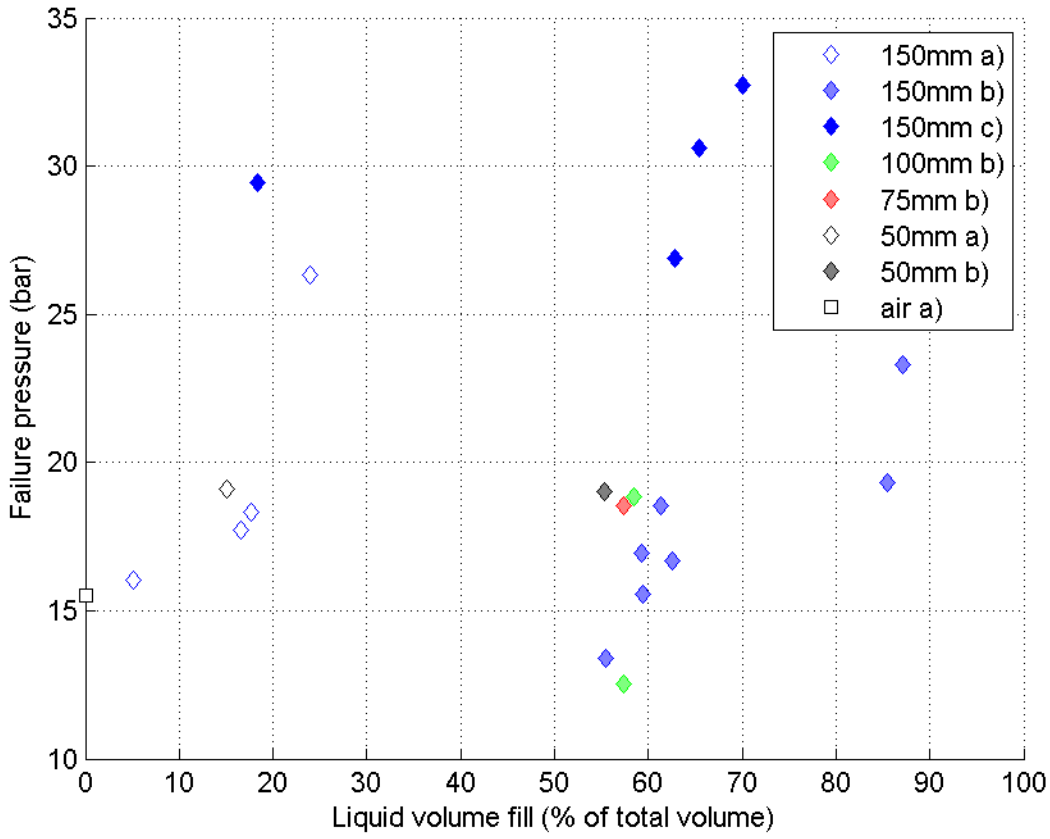

Figure 8-3 Transient pressure profile classification of all tests

As seen in the literature (Barbone, 1994; Chen et al., 2008), the pressure rise in the vessel is a consequence of superheat boiling. This was probably heterogeneous boiling at the liquid surface and along the walls of the tube rather than homogeneous boiling. In order to link the pressure drop to potential superheat degree of the liquid, the data points defining the previous classification were compared with thermodynamic stability line (Figure 8-4).

The failure conditions of all tests were close to saturation due to slow heating and a small volume to homogenize. The P-T diagram shows that the highest failure pressures were the ones presenting the smallest drop because the gap between saturation and spinodal line is smaller. As a reminder, the spinodal line defines a theoretical maximum superheat state at which the liquid reaches homogeneous nucleation and must starting boiling. The points presenting a pressure rise (category b and category c) followed this spinodal trend. It can be concluded that pressure increase in the tube was related to the boiling process in the tube. Moreover, the data presenting a pressure rise showed behavior similar to previous superheat boiling studies (Figure 2-15).

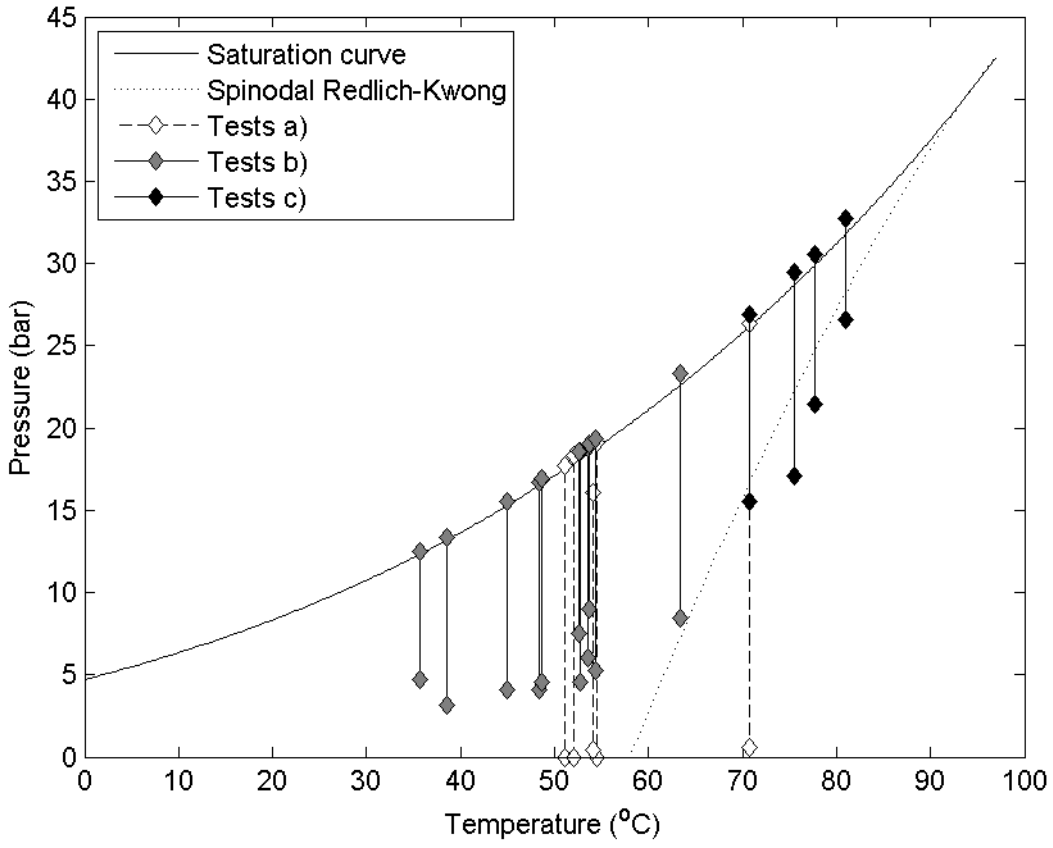

Figure 8-4 P-T diagram summary plot with failure condition and pressure drops before stabilization

On the other hand, no pressure rise on the transducer (category (a) corresponding to low fill) led to pressure drops to atmospheric pressure ignoring the spinodal line limit. No repressurization behavior was observed in these cases due to the low liquid level.

The diversity of pressure drops around the T_{SL} tended to show that there was no obvious behavior change before and after the T_{SL}. This was a criterion to differentiate hot and cold BLEVE in the literature. This set of experiments indicated once more that the difference of superheat between hot and cold BLEVE was not a sudden change in superheat and violence of boiling liquid. The T_{SL} defines the largest amount of potential superheat degree reachable by the liquid. This is defined as the isothermal pressure drop from the saturation line to the spinodal line with atmospheric ambient conditions. Thus the superheat energy available at boiling follows a continuous trend with a maximum around T_{SL} and decreases for higher pressures.

Finally, higher failure pressure cases dropped below the spinodal line. This disagreed with the statement that homogeneous nucleation is a theoretical limit never reached in practice. Howeverm we must be careful with this statement because no temperature measurements were valid after the burst. This behavior was explained as follow: small drops below spinodal for the high failure pressures of category (c) may be due to the wrong use of the assumption of isothermal pressure drop. As seen later in this chapter, when boiling was observed at the sensor at the end of the tube, it has already started some tenth or hundreds of microseconds before, in the center of the tube. Boiling, being an endothermic phase change, led to a temperature drop in the liquid before reaching the sides of the tube, thus invalidating the isothermal pressure drop assumption. However we do not know exactly when the liquid starts boiling, because we are able to look at the center of the tube. Thus this argument remains only a potential explanation, not a proof.

This introduction to the transient pressure profiles information showed a tendency for certain cases to recover internal pressure after the failure due to violent boiling. This pressure recovery was also dependent on all of the failure parameters (failure pressure, amount of liquid in the vessel, cut length –or how the vessel opened). A smaller cut, thus a more constricted area for fluid release, with a larger liquid volume and higher failure pressure are criteria leading to potential strong pressure recovery in the vessel.

The next section characterizes in more detail the pressure profile behavior.

III-2. **Quantification of transient pressure properties**

Several properties were found in most of the transient pressure measurements of the small scale BLEVE tests. The previous section dealt mainly with one of them: P_{drop}. In total, five principal parameters were extracted from the pressure signal (Figure 8-5):

- t_{drop}: time between the opening of the tube visible on high speed imaging ($t = 0$) and the start of the main pressure drop;
- $\left.\frac{\partial P}{\partial t}\right|_{max}$: maximum of the absolute value of the rate of pressure fall ;
- P_{drop}: amount of pressure drop before the beginning of the pressure recovery, or amount of pressure drop until atmospheric pressure if there is no recovery ;
- P_{rise}: when applicable (configuration (b) and (c), Figure 8-2), pressure increase from the recovery initiated by liquid boiling ;
- $t_{80\%}$: time at which 80% of the initial pressure has dropped.

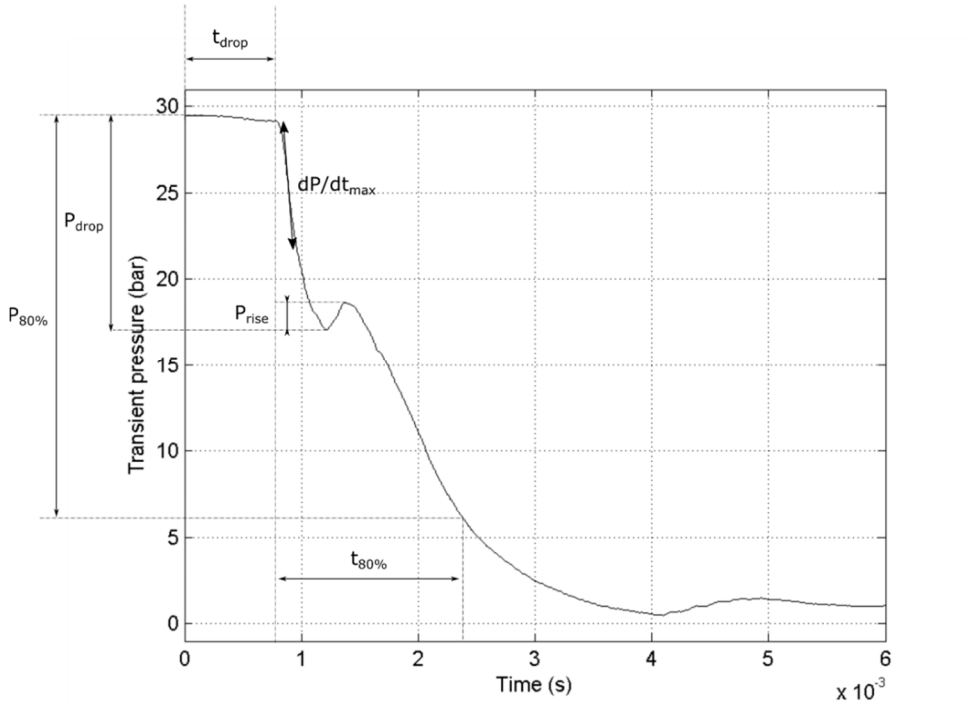

Figure 8-5 Description of the variables extracted from transient pressure signals ($P_{fail} = 29.5bar$, $\Phi_{liq} = 18\%, L_w = 150mm$)

These variables were measured for each case that allowed such a measurement. Similar to the lead shock variables, correlation analysis was undertaken on these parameters with respect to the failure parameters (Table 8-1).

Table 8-1 Correlation coefficient between transient pressure variables and failure parameters

	P_{fail}	Φ_{liq}	L_w
t_{drop}	-0.01	-0.65	-0.33
P_{drop}	-0.05	-0.58	0.08
P_{rise}	-0.07	0.64	-0.15
$t_{80\%}$	-0.53	0.53	-0.54
$\left\|\frac{\partial P}{\partial t}\right\|_{max}$	0.85	0.35	0.51

From these variables, some characterization and modeling studies were undertaken.

III-2.1. t_{drop}: time to pressure drop initiation

It was seen from the correlation study that time to initial drop had no relation to the failure pressure. However it was strongly negatively correlated to liquid fill level. Hence the more liquid, the quicker the drop happened. And it was mildly negatively correlated to the cut length: the larger the cut, the faster the drop happened.

A quick estimate was done through geometrical consideration of wave propagation. If one assumed that the pressure started dropping at the sensor when the expansion wave reached the sensor, one can quickly estimate this time by taking the shortest distance between the start of the opening (here assumed to be the center of the weakened length, also center of the tube length) and the location of the sensor (Figure 8-6). For the tests where imaging above the vessel was available, this assumption is valid within a 15% error range.

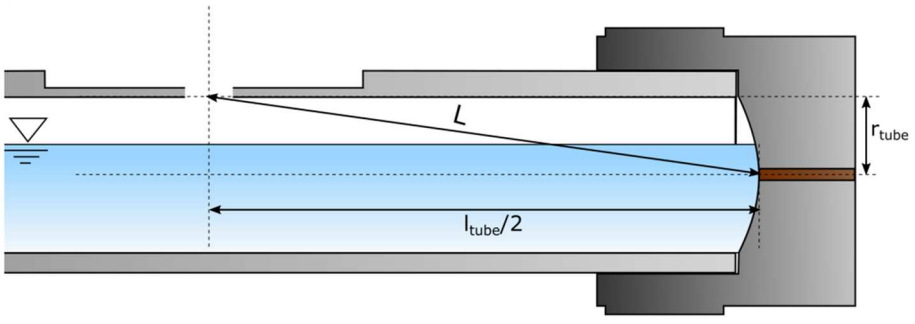

Figure 8-6 Path of the expansion wave from opening to pressure sensor

The head of the expansion traveled at the speed of sound of the medium considered. In this case, it was vapor propane and liquid propane at the failure pressure and temperature. The sensor was located at the center of the cylinder cross section. Thus, if the liquid level was below 50%, the wave traveled only through vapor propane. If the liquid level was above 50%, one must consider both media in order to estimate the travel time from opening to sensor:

$$t_{drop\ calculated} = \frac{L * (1 - x)}{a_{vap}} + \frac{L * x}{a_{liq}}$$

$$where \begin{cases} L = \sqrt{r_{tube}^2 + \left(\frac{l_{tube}}{2}\right)^2} \\ if\ \Phi_{liq} > 50\%: \quad x = \frac{\Phi_{liq}[\%] - 50}{50} \\ if\ \Phi_{liq} < 50\%: \quad x = 0 \end{cases} \tag{47}$$

where a_{vap} and a_{liq} are the sound speed in vapor and in liquid propane respectively at failure condition, r_{tube} is the radius of the tube (2.5cm) and l_{tube} is the full length of the tube (30cm).

Comparisons between experimental measurement and this estimation are presented Figure 8-7. Very good agreement was found between the experiments and the calculation. Most of the cases fell within a 20% error range. This validated the simple physical explanation of the expansion wave propagating from opening to the sensor. This also explained the 0.5 to 1ms delay between the information at the transducer and the behavior of the fluid at the center of the tube.

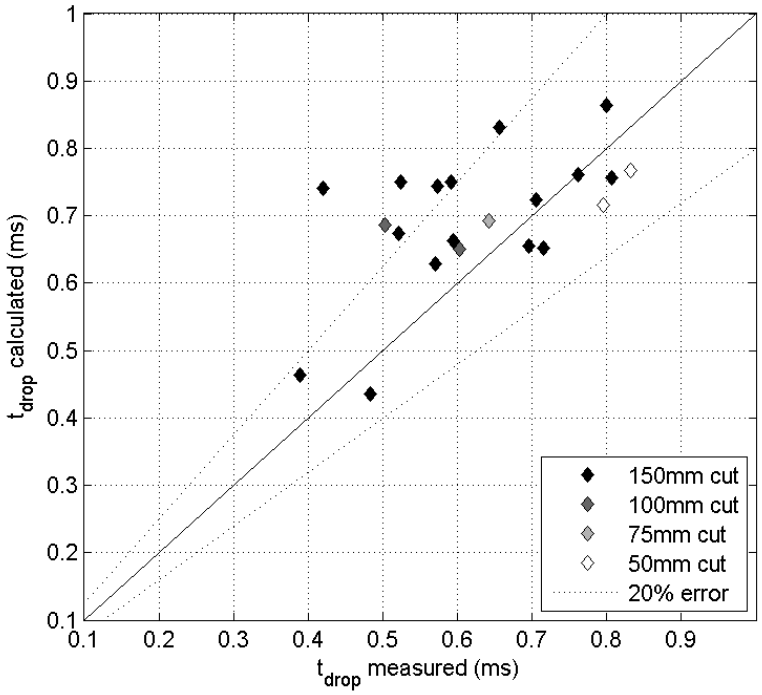

Figure 8-7 Parity plot between experimental measurement of t_{drop} and estimation of t_{drop} through wave propagation calculation

The distinction between the different cut lengths is shown in Figure 8-7. Table 8-1 showed a small negative correlation between t_{drop} and L_w. As it had not been implemented in the physical model from equation (47), the influence of this parameter was visible on the modeling parity plot. Indeed, smaller cut lengths, such as 50mm, resulted in a larger t_{drop} than larger cut lengths, such as 100mm. However no conclusions have been drawn on this point at this stage.

III-2.2. Other pressure parameters: physical interpretation

The correlation analysis guided the phenomenon interpretation in the next section. No modeling was performed on the following parameters.

III-2.2.1 Pressure drop P_{drop}

As seen previously, the drop in pressure before pressure recovery in the tube was mostly dependent on the liquid level; the more liquid, the smaller the drop before pressure starts rising again. The influence of the failure pressure did not show any correlation with the pressure drop.

III-2.2.2 Repressurization P_{rise}

P_{rise} corresponded to the increase in pressure when a pressure recovery happened. It depended mostly on liquid fill level. When there was more liquid, more mass of liquid boiled expanding from liquid to vapor through a limited space. A slight negative correlation with cut length indicated that a more restricted opened expansion area resulted in more pressure build up inside the vessel. This was in agreement with the critical flow theory (Chapter 3).

An interesting comparison made by authors studying experimental superheat boiling (Barbone, 1994) was the correlation of pressure drop and pressure rise. This work was done with depressurization of tubes (Figure 8-8 left). A similar plot was made for BLEVE experiments (Figure 8-8 right). The cases with no pressure rise (category a) were not plotted on the figure.

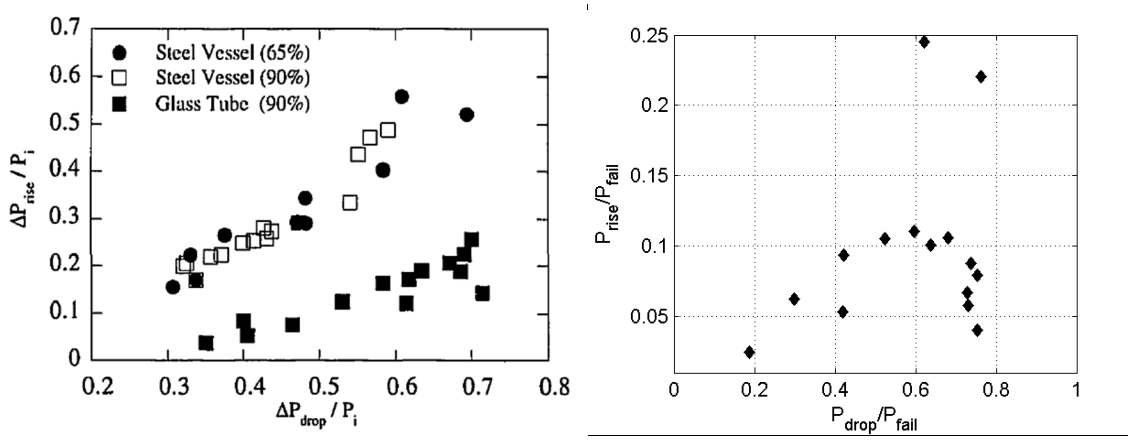

Figure 8-8 Pressure rise versus pressure drop (left: tube depressurization (Barbone, 1994)*; right: BLEVE experiments)*

The maximum pressure rise ratio for BLEVE experiments was only 0.25 versus 0.55 for tube experiments. Pressure rises were weaker in BLEVE experiments because the flow was less restricted with the pressure vessel failure geometry leading to choke for a shorter duration. This also explained why the relation between $\frac{P_{drop}}{P_{fail}}$ and $\frac{P_{rise}}{P_{fail}}$ was clearly increasing and proportional for tube experiments and not for BLEVE. The tube experiments had a more restricting cross section area, allowing the flow to be choked and repressurized long enough to reach a quasi-steady state. This was never the case for these BLEVE, thus the proportionality mentioned by the author of the tube experiment was not found with cylindrical BLEVE experiments.

The experiments presented in this work were all 1-step BLEVEs. No 2-step BLEVE were observed, as mentioned in the literature. It was assumed that such an event would lead to a high pressure rise in the tube when the crack stops opening and then limits the exiting flow. This pressure rise may trigger the

crack to start propagating again to full vessel opening, leading the nature of the accident to change from jet flow to BLEVE. The 2-step BLEVE was reported to be stronger than 1-step BLEVE. The delay of the catastrophic failure coupled with the pressure rise may lead to a stronger shock. However the experimental conditions leading to a 2-step BLEVE were not reproduced yet to verify that statement.

III-2.2.3 Depressurization time $t_{80\%}$

$t_{80\%}$ related to the time necessary to reach almost atmospheric pressure. The order of magnitude of $t_{80\%}$ ranged from 1ms for the fastest cases to 15ms for the slowest cases. Conclusions from correlation were fairly straightforward:

- $t_{80\%}$ increased with increasing liquid level: the more liquid, the more mass there was to empty from the vessel;
- $t_{80\%}$ decreased with increasing cut length: the longer the cut, the more surface area there was for the fluid to expand and escape, leading to a shorter emptying time;
- $t_{80\%}$ decreased with increasing failure pressure: the higher the failure pressure, the faster the tube opened fully, and the more violent the expansion and the boiling.

III-2.2.4 $\left|\frac{\partial P}{\partial t}\right|_{max}$

This parameter indicated the maximum rate of decrease of the pressure in the vessel. A faster rate led to a high degree of superheat before the boiling process started, and thus a more violent boiling. According to the correlation study:

- $\left|\frac{\partial P}{\partial t}\right|_{max}$ increased strongly with increasing failure pressure: the higher the failure pressure, the faster the opening of the vessel, but also the stronger the expansion of the vapor above, and thus a steeper drop in pressure.
- $\left|\frac{\partial P}{\partial t}\right|_{max}$ increased with increasing cut length: the longer the cut length, the larger surface area for the fluid to expand and the faster the tube opened.

III-3. **Chronology and evidence of delayed boiling**

This section compared transient pressure signal with overpressure signal and high speed imaging through the side window of the vessel. After a brief analysis of each of the parameters of the pressure

signal, all the data available was examined together in order to understand the timing of the different events happening during a BLEVE.

III-3.1. Comparing the timing of the events occurring outside and inside the vessel

A chronological study was performed in order to determine the contribution of the liquid and the vapor in the generation of the initial shock wave, and also to better understand the timing of the boiling process. This chronological study is presented Figure 8-9. Several key times were noted:

A. t = 0.14ms: slightly after the tube opened, a dome-shaped cloud became visible above the vessel. Nothing was noticeable on the blast gages above, in the vessel through the window or through the transient pressure transducer.

B. t = 0.4ms: the lead shock reached the first blast gage, 15cm above the vessel opening. The dome cloud grew considerably. The vapor phase appeared white in the vessel. The liquid phase seemed to whiten a bit too, but the diphasic flow did not reached the window yet. There was still no change on the internal pressure transducer.

C. t = 0.52ms: the lead shock reached the second blast gage, 20cm above. No other changes were observed.

D. t = 0.76ms: the internal pressure transducer showed that pressure started to drop at the transducer. Boiling may have started at the opening. However the diphasic flow did not reached the window yet. The transducer and the window were at similar distances from the center of the tube if we assume the opening to be symmetrical. This meant that the boiling was delayed relative to the pressure drop. This was an evidence of the superheat state of the liquid before boiling at the window. However this did not tell us what happened in the center of the tube.

E. t = 0.88ms: a small pressure recovery was observed on the transducer signal. The liquid phase through the window started to become white and opaque: the diphasic flow has reached the ends of the tube and started building up pressure due to the volume expansion from the violent boiling. Pressure has dropped significantly above the vessel.

F. t = 2ms: The pressure in the vessel dropped progressively. The diphasic phase has swollen in the vessel to occupy the full cross section area of the tube.

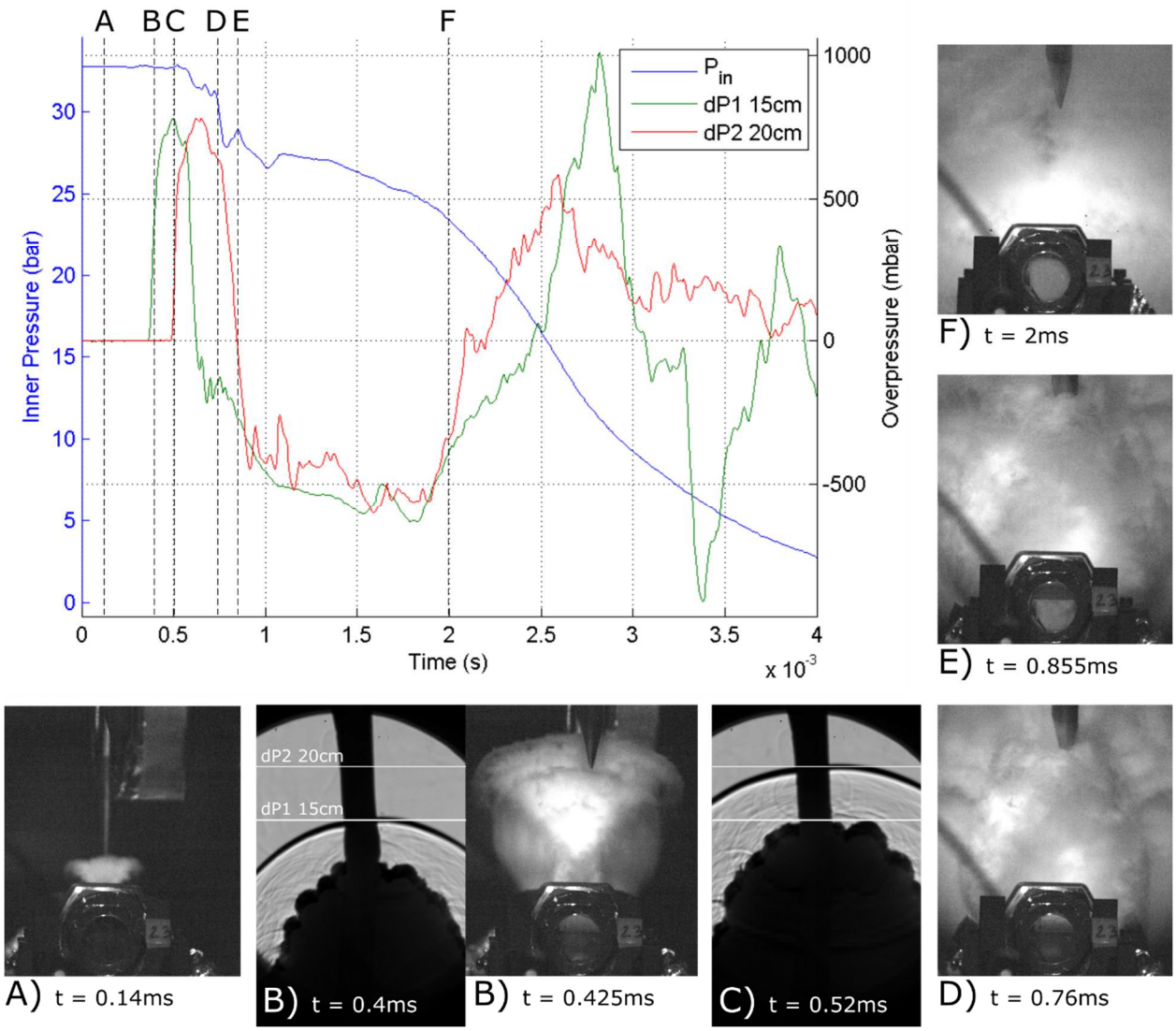

Figure 8-9 Chronology of events between sources of the BLEVE hazards inside the vessel (vapor expansion and liquid boiling) and consequences of the BLEVE (shock and cloud propagation) ($P_{fail} = 32.7bar$, $\Phi_{liq} = 70\%, L_w = 150mm$)

This chronological study illustrates a clear timeline of the different events occurring both inside and outside the vessel. These events are summarized Figure 8-10.

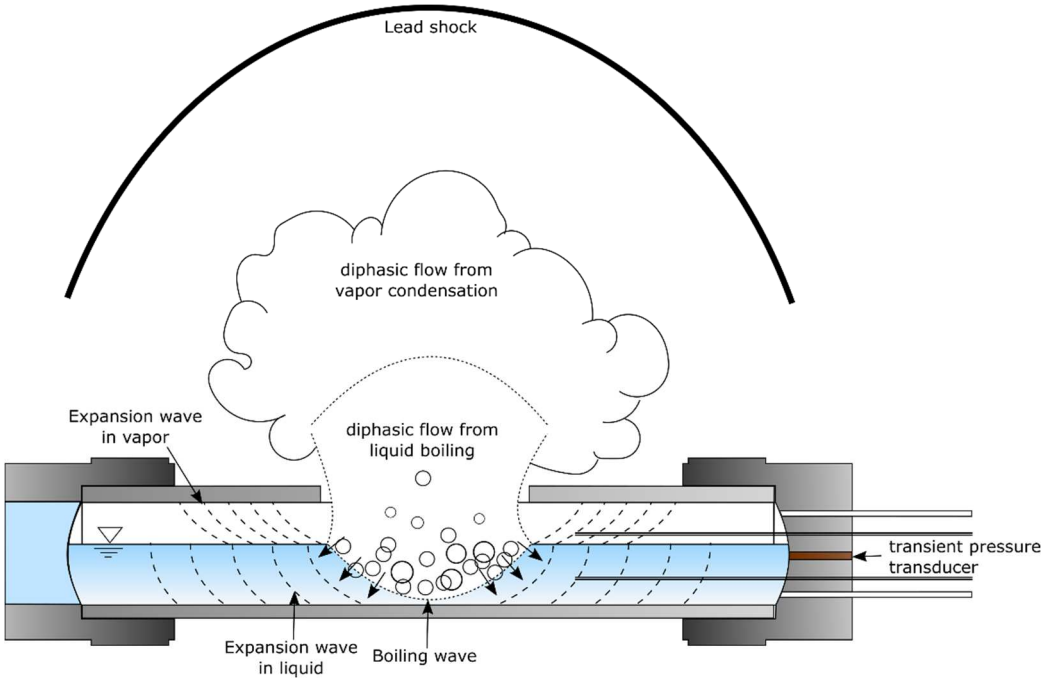

Figure 8-10 Events occurring when the vessel opened, both outside (blast and clouds propagation) and inside the tube (expansion and boiling wave propagation)

III-3.2. Delayed boiling with respect to tube opening and cloud projection

This section characterizes the boiling wave propagation from images. Figure 8-11 shows further evidence of the delayed critical boiling process. The different stages of the BLEVE expansion and boiling were:

- The vessel cracked open on the top. The crack propagated to the ends of the tube and expanded to the sides (t =0 →0.28ms)
- the vapor space expanded through the increasing opening of the tube (t=0.24 →0.28ms). Characteristic cat-ear pattern was visible in the flow, similar to under-expanded jets.
- the boiling cloud was then visible outside the vessel as being a much thicker cloud than the vapor cloud initially seen. (t=0.52 →0.84ms). However, the liquid-vapor surface at the window end was still level and undisturbed. The boiling wave did not reach the window (Figure 8-10).
- the boiling wave reached the end of the tube (t = 0.96ms).

- as the boiling wave progressed toward the bottom of the tube, the diphase flow swelled to fill the entire cross section area of the tube (t = 0.96→1.4 ms and after). During this process, a sustained thick cloud of diphasic flow escaped the tube.

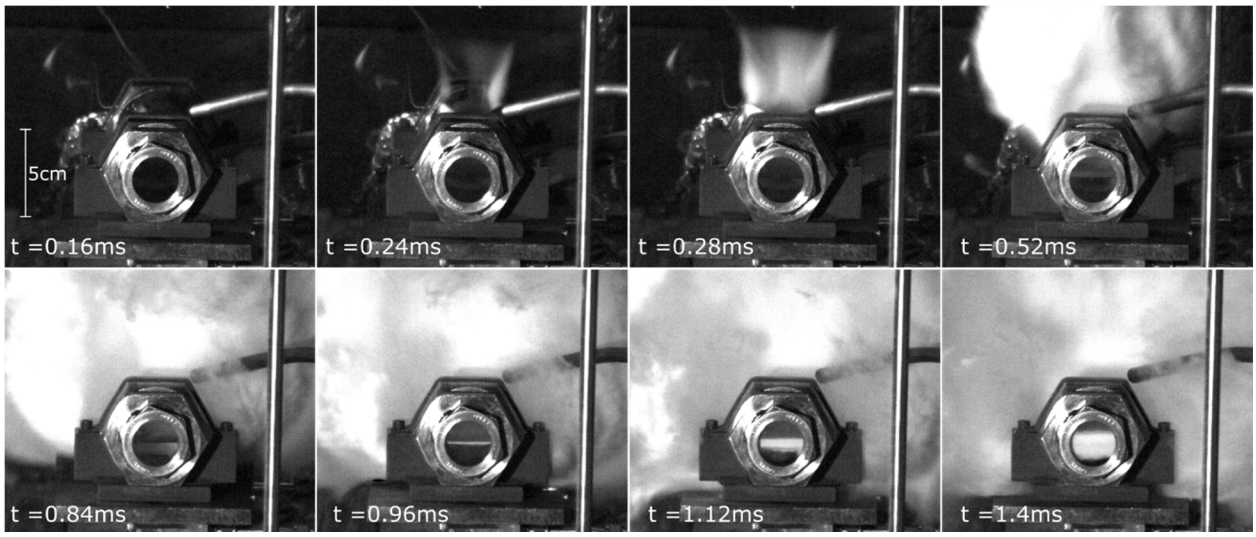

Figure 8-11 Side window view of small scale propane failure ($P_{fail} = 28\ bar; \Phi_{liq} = 56\% ; L_w = 75mm$)

Unfortunately, values for ground loading and internal transient pressure were not available for this test. However, the downward boiling wave velocity was experimentally defined based on the high speed imaging of the test shown in Figure 8-11, from the instant the boiling wave reached the window to the time it reached the bottom of the window (Figure 8-12).

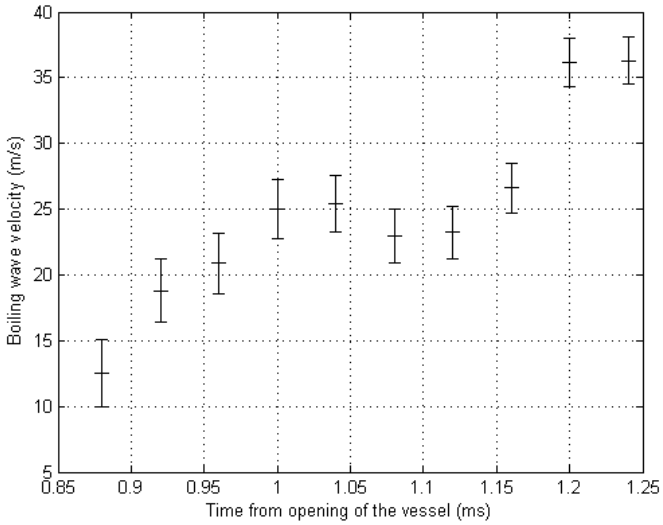

Figure 8-12 Boiling wave velocity through the window

As defined earlier in this chapter, a pressure rise in the vessel was characteristic of a choked flow somewhere near the vessel opening. The one dimensional modeling of critical flow through the boiling wave presented in the Chapter 3 was set to the initial conditions of this experimental case with an initial pressure of 28 bar in the vessel. The critical boiling wave velocity through a liquid phase was calculated to be 32 $m.s^{-1}$ Experiments gave an increasing velocity, with a plateau occurring at around $25m.s^{-1}$. These values were comparable. A justification for the larger theoretical value could be that the experimental measurement only considers the vertical component of the boiling wave propagating spherically from the center of the tube to the window. Also, model is a crude estimation of the boiling behavior in the vessel: the diphasic flow was assumed homogeneous and at equilibrium, which is certainly not the case in the experiments.

Data from literature presented some simulation of boiling wave velocity with equilibrium boiling consideration through spherical expansion (Yakush, 2016). The values obtained for similar failure pressure range between 41 and 51 $m.s^{-1}$. Equilibrium homogeneous flow was also assumed during these simulations. The spherical case may lead to a less restricted flow and faster boiling wave.

IV - **Conclusion**

In conclusion, it was understood that the shock was away from the vessel before the expansion wave reaches the sensor at the tube end.

The work described in this chapter led to the following conclusions:

- Depending on the liquid fill level and the failure pressure, the pressure in the vessel behaved as follow:
    - low liquid content led to a drop in vessel pressure to atmospheric pressure,
    - higher liquid content led to a smaller pressure drop in vessel relative to the failure pressure, describing the superheat state of the liquid before violent boiling and pressure rise in the vessel. This behavior followed fairly well the stability criterion of the spinodal line, with a practical heterogeneous behavior rather than a homogeneous theoretical behavior.
- The pressure did not rise as much during the BLEVEs as it did in the tube venting experiments reported in literature. The main explanation was that the size of the restriction area for escaping diphasic flow was much larger for vessel bursts than for tube venting.
- Chronology showed that the boiling at the end of the tube happened after the shock escaped through the sensors above the vessel.
- A simple boiling wave model was presented to describe the phenomenon with basic assumptions and conservation equations. When comparing the model to experimental boiling wave velocity, the results yielded a similar order of magnitude.

Chapter 9

Ground loading characterization

I - Introduction

Overpressure hazard studies showed that vapor is the main contributor to the maximum overpressure of the lead shock wave. Of course liquid boiling should not be neglected in the study of hazards induced by the BLEVE. It is the liquid energy that produces projectiles, local drag loading and ground force. The following section investigates the quantification of ground load resulting from a BLEVE where the liquid boiling appears to dominate.

II - Objectives and major findings

Measurements of the load generated by small scale BLEVEs are presented and analyzed. The purposes of this analysis are:

- to present experimental load data of small scale BLEVE experiments;
- to correlate the load generation to BLEVE opening mechanisms;
- to present a first estimation of the load in order to scale up to industrial-sized cylinder vessels.

III - Detailed analysis

III-1. Signal shape and timing analysis

Ground loading was measured on the base plate beneath the tube using 4 load cells (Figure 9-1)

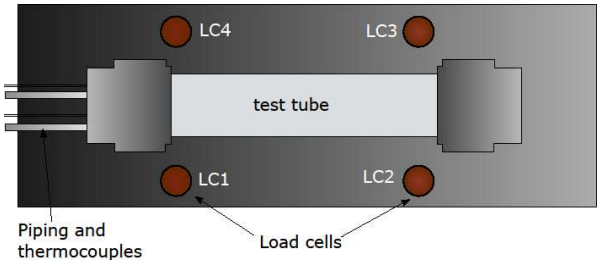

Figure 9-1 Load cell location around the test tube

The measured data gave three types of profiles depending on the tube failure mechanism (Figure 9-2). The data of interest was the sum of the signals measured by the 4 load cells. The main characteristic for all the measurement profiles was a bell shaped peak representing most of the ground loading from the BLEVE. The main peak lasted from 2 to 4ms and the order of magnitude of its maximum ranges from 10 to 55kN. A difference between the load profiles measured was the absence (Figure 9-2 a) or presence (Figure 9-2 c) of a small initial load increase before the main peak. When present, the initial load value was 10% or less of the maximum load.

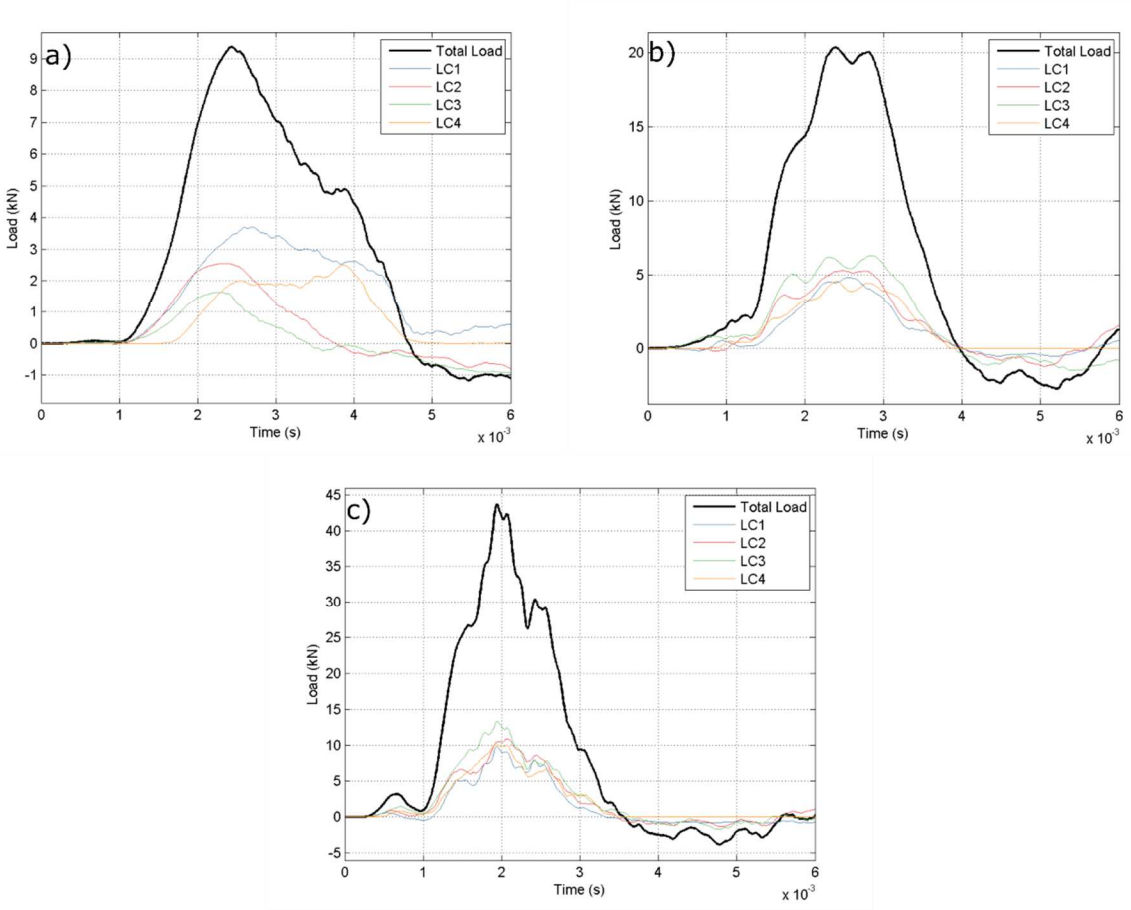

Figure 9-2 Ground loading measurement, gage by gage and total sum for 3 different profiles:

a) No initial load: $P_{fail} = 19bar,\ \Phi_{liq} = 56\%,\ L_w = 50mm;$

b) Progressive load build up: $P_{fail} = 18.6bar,\ \Phi_{liq} = 56\%,\ L_w = 75mm;$

c) Presence of initial load: $P_{fail} = 26.9bar,\ \Phi_{liq} = 61\%,\ L_w = 150mm$

The ground loading was generated because of momentum conservation: due to a pressure driven mass flow directed upward, a force was generated toward the ground to satisfy the momentum equation. There were two potential contributions to this upward mass flow:

- vapor expansion through the transient opening of the tube;
- two phase flow from the boiling liquid through the entire tube space.

The presence of the initial load was reported for all relevant tests (Figure 9-3). The initial load was generally present for high failure pressure and a large cut length (150mm cut only). These criteria were for fast opening vessels having the potential for stronger superheat.

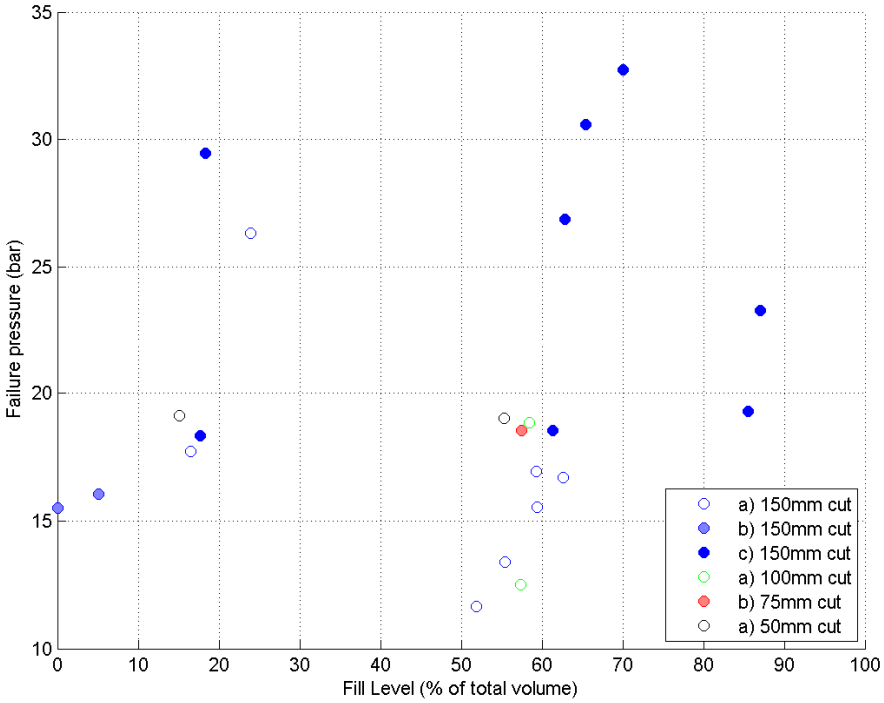

Figure 9-3 Test summary with specification of the presence or not of initial bump (a) No initial load; b) Initial load merged with main load; c) clear separated initial load)

Comparison of the evolution of ground loading in time with internal transient pressure strengthened the argument supporting the contributions of vapor and liquid. After the tube opened, the pressure inside the vessel dropped due to expansion of the pressurized fluid. However for strong superheated liquid states, a pressure increase was noticed during this drop. It was argued that this pressure increase was a result of superheated liquid suddenly boiling, thus repressurizing the vessel. The timing of the initial ground loading corresponded to the pressure drop from the expansion process before boiling. The timing of the stabilization of pressure and repressurization corresponded with the start of the major load peak (Figure 9-4).

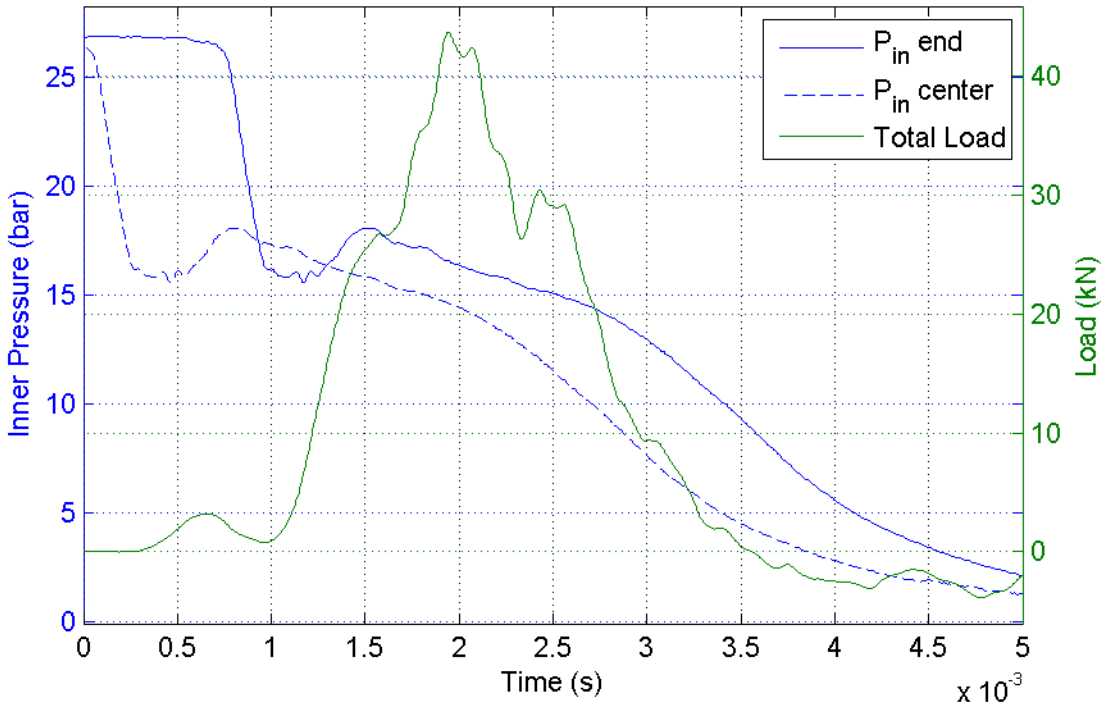

Figure 9-4 Timeline of ground loading and internal transient pressure for case c) presence of initial load $(P_{fail} = 26.9bar,\ \Phi_{liq} = 61\%,\ L_w = 150mm)$

Based on these observations, the argument was made that the major component of the load was due to liquid boiling. If the vessel opened fast enough, the liquid reached a strong superheat degree. Stronger superheat delayed the boiling of the liquid, thus indicating more clearly the contribution of the vapor phase and of the liquid phase (Figure 9-2 c). It also led to stronger ground loading overall. If the vessel did not open fast enough, the superheat degree was lower, leading to a more progressive boiling following the vapor expansion, thus merging both contributions in the main peak (Figure 9-2 a). Intermediate cases were noted showing the presence of the initial pressure merging with the liquid main ground force (Figure 9-2 b).

It was demonstrated through observation that a major contribution of the ground loading came from the boiling liquid phase. In the next section quantification of the data is undertaken in order to understand the influence of failure variables on the loading. Finally, this leads to a prediction model for this data.

III-2. **Maximum load, positive impulse, and correlation to failure parameters**

For all cases, the maximum load, the positive impulse and the duration of positive impulse were measured and then correlated with the failure parameters. The correlation results were presented Table 9-1.

Table 9-1 Correlation coefficients between load variable and failure variables

	P_{fail}	Φ_{fill}	L_w
F_{max}	0.77	0.55	0.33
I^+	0.53	0.78	0.32
t^+	-0.76	-0.28	-0.37

III-2.1. Load variables function of failure pressure

The comparison showed that an increase in failure pressure correlated with a strong increase in maximum ground loading, as well as its positive impulse. However the duration of the positive phase t^+ decreased significantly. Thus, at high failure pressure, the vessel opened more quickly and the fluid was expelled faster from the tube, making the duration of load smaller. The graphs in Figure 9-5 agreed with these statements, with a few exceptions.

When considering one cut length only (150mm being the largest sample for comparison), the trends of maximum load and duration of positive impulse agreed well with the correlation. It was not true for the load impulse, where weak failure pressure generated moderately strong impulse. Lower load with longer duration can potentially give large impulse.

Another exception to the correlation with failure pressure was observed in one test case with a 50mm cut length failing at 19bar. Its maximum load was smaller than that for other cases of similar failure pressure, as well as its positive impulse. However the duration of its impulse was larger. It behaved like a case with smaller failure pressure, making the size of the opening an important parameter in predicting the ground loading.

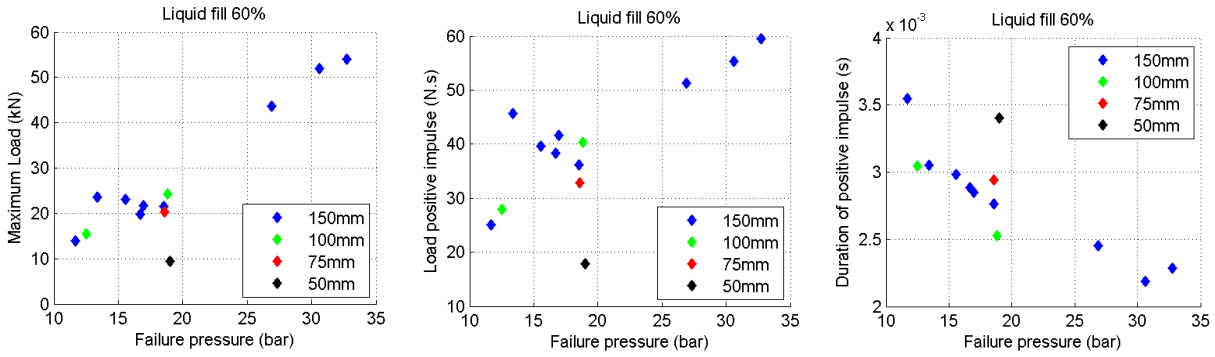

Figure 9-5 Correlation between failure pressure and (left to right) maximum load; positive impulse; duration of positive impulse

III-2.2. Load variables function of cut length

Fewer cases were available for a cut length variability study. Thus interpretation of correlation coefficient must be done with caution. The correlation coefficients indicated that increasing cut length led to an increase in maximum load and impulse and a decrease in the duration of impulse, which was similar to results found with the parameters studied previously. However Figure 9-6 showed that this was true only for cut lengths ranging from 50 to 100mm. The case presented for cuts lengths of 150mm showed an opposite trend. One explanation was that these results were taken at around 19 bar. From the graphs in Figure 9-5, it was seen that this was the failure pressure around which there was the most variability. It was difficult draw any further conclusions due to the lack of data.

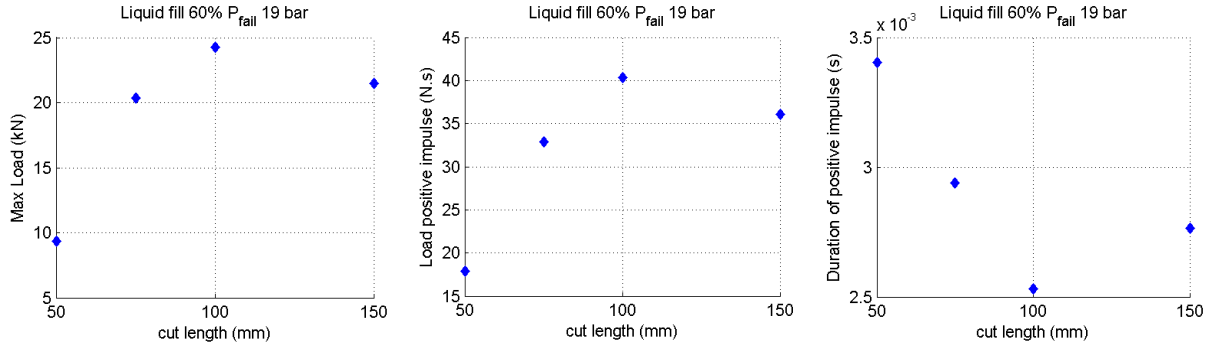

Figure 9-6 Correlation between cut length and (left to right) maximum load; positive impulse; duration of positive impulse

III-2.3. Load variables function of liquid fill level

Correlation coefficients showed that an acceptable positive correlation existed between liquid fill level and maximum load, a strong correlation for the impulse, and a slight influence impact on duration of impulse. Figure 9-7 illustrated validation of the first two statements, with the exception of the 50mm case already mentioned above. With regard to the duration of the impulse, Figure 9-7 (right) did not confirm the correlation. Cases of similar cut length all showed a similar duration of impulse.

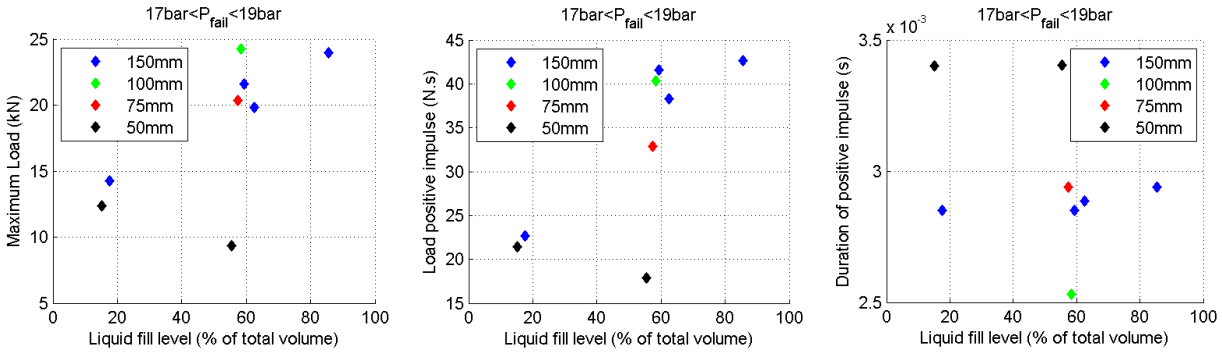

Figure 9-7 Correlation between liquid volume fill level and (left to right) maximum load; positive impulse; duration of positive impulse

III-2.4. Non-dimensionalization of the load variables

Based on the previous parametric study, the load parameters were non-dimensionalized. The maximum estimated load was evaluated to be the total failure pressure pushing on the fully flattened tube. Non-dimensionalization was done as follow:

$$\hat{F} = \frac{F_{max}}{P_{fail} * L_w * \pi * D_{tube}} \tag{48}$$

$$\hat{I} = \frac{I^+/t^+}{P_{fail} * L_w * \pi * D_{tube}} \tag{49}$$

Figure 9-8 left showed that for a liquid level similar to that in Figure 9-8 right, $\hat{F}$ varied little with P_{fail}. This showed that dimensioning F_{max} with P_{fail} was required in order to remove the failure pressure parameter for other comparisons.

The dimensioning parameters allowed the plotting of all cases on a single graph, rather than restricting the plotting to cases of similar failure conditions. Figure 9-8 right showed how $\hat{F}$ varies with liquid fill level. A clear separation was observed between the low liquid fraction cases (<25%) and the high liquid fraction cases (>50%). Values of $\hat{F}$ increase toward 1 with increasing liquid fill level, meaning that the force exerted by the failure pressure on the fully flattened plate was a good estimate of the maximum ground force that such a BLEVE can generate, and that the liquid phase was a large component in this.

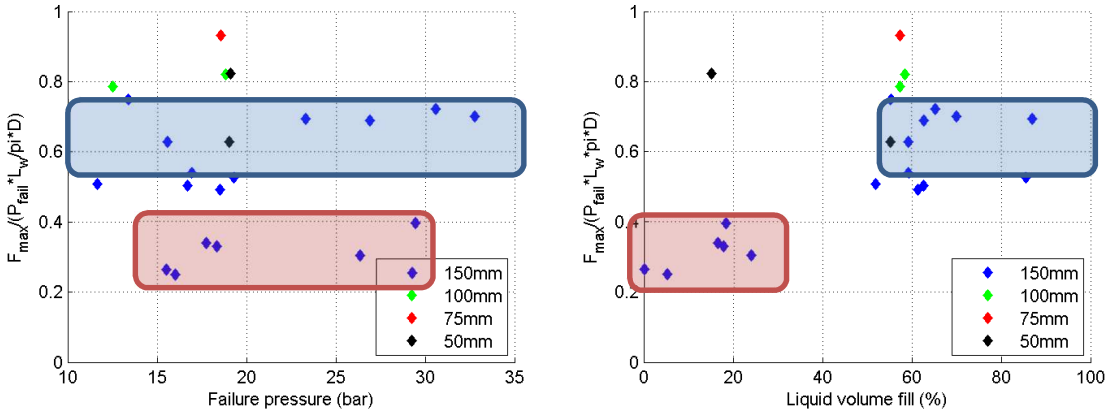

Figure 9-8 Non -dimensional maximum load as a function of failure pressure and liquid volume fill

Dimensioning the impulse with the duration of positive impulse showed a similar trend (Figure 9-9), as I^+/t^+ is equivalent to a force. Thus, with respect to fill level, a clear separation was seen between low and high liquid fill. This distinction was not present for failure pressure, as similar values of $\hat{I}$ spread over the full range of failure pressure.

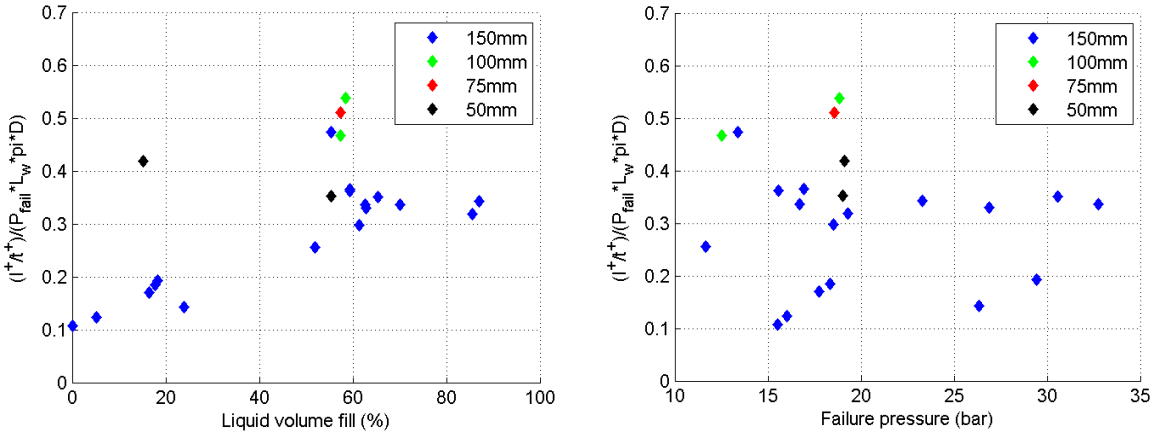

Figure 9-9 Non -dimensional impulse load as a function of liquid volume fill and failure pressure

IV - **Estimation model**

A rough prediction model was developed based on the behaviors observed previously for ground loading measured data. To estimate the maximum ground loading, it was assimilated to the force exerted on the piece of tube flattened in the explosion with the initial failure pressure pushing on it:

$$(A)\ F_{maxA} = P_{fail} * S_{tube} = P_{fail} * L_w * \pi * D_{tube} \quad (50)$$

where F_{maxA} is the ground load estimated using equation (50), S_{tube} is the estimated surface of the flattened tube, considering a rectangle of dimension weakened length L_w by $\pi * D_{tube}$, with D_{tube} the diameter of the tube known to be 50mm (Figure 9-10).

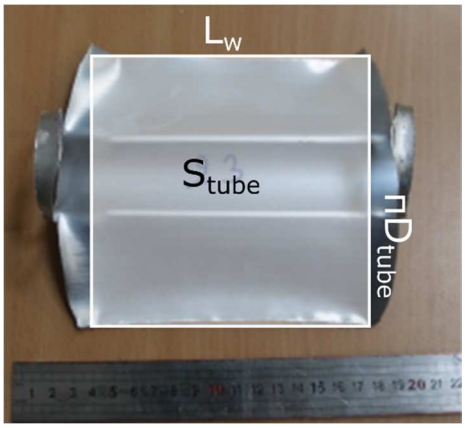

Figure 9-10 Description of the equivalent surface for ground loading estimation

As seen with the correlation study, the liquid fill level had a significant influence on the ground loading. The previous estimation was adapted to include the liquid fill parameter. Based on previous arguments when considering the timing of each event, the vapor space contributed to the initial load increase which usually does not go over 10% of the maximum. The liquid boiling cloud coincided with the maximum load peak in time. Thus a rough first approach was to consider that only the liquid volume contributed to the generation of the maximum ground force.

$$(B)\ F_{maxB} = P_{fail} * S_{tube} * \Phi_{liq} \tag{51}$$

where F_{maxB} is the ground load estimated through equation (51).

For convenience, the models based on equation (50) and equation (51) were referred to as model (A) and model (B) respectively. These two models were compared to experimental results in Figure 9-11.

Both models yielded results that were in reasonable agreement with experimental results. The models predicted the experimental results with errors often below 50%, which was acceptable considering the simplicity of the physics involved in the models. Model (A) tended to over-predict the results, while model (B) mostly under-predicted experimental results but was in much closer absolute agreement with the experimental data according to RMS calculation criterion: $R_A^2 = 0.59$; $R_B^2 = 0.82$. Model (B) was especially useful for predicting failures resulting in high loads, having errors ranging from 0 to 10%. However, from a safety perspective, overestimation was preferable in order to predict the worst case scenario.

Weak load cases were highly over-predicted by model (A). These cases mostly corresponded to cases with low liquid fill. This confirmed that vapor space has a limited impact on maximum load. But model (B) struggled to model weak load cases by under-predicting them too much. The consideration of the liquid phase contribution in Model B was not optimal for weak ground load cases. Liquid volume fraction was certainly not the sole contribution to the ground loading.

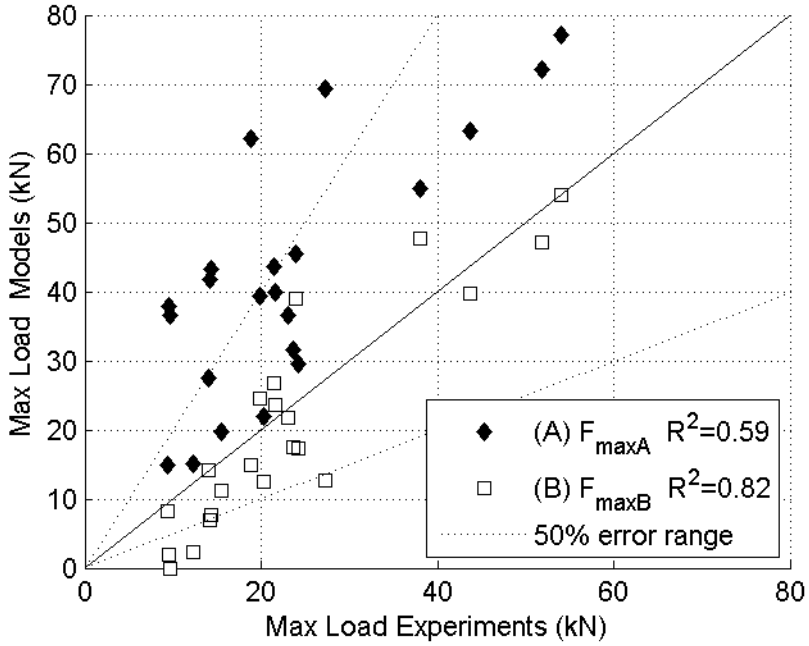

Figure 9-11 Parity plot comparing maximum load estimation models with experiments

V - Scaling to real size road tank truck

In order to determine if a road tanker BLEVE happening on a bridge leads to the collapse of the structure, the modeling of ground loading was implemented to larger scales available in experiments and to a real size road tanker scale. A wide variety of road tankers are available in the transportation field. The tank capacity most widely used for LPG is be 20m^3. The geometry of the road tanker was taken from the ASME 20CBM LPG road tanker which is commercially available. Initial conditions of rupture are:

- $P_{fail} = 20bar$
- $\Phi_{liq} = 0.5$

This configuration was chosen for the example of a propane storage failure with a high potential for superheat. The study can easily be extended to other cases depending on the interests of the reader. Model (B) was selected for this case as it best fitted these conditions for a small scale apparatus. As noted for the small scale experiment, the effective length used to calculate the estimated surface of the flattened vessel

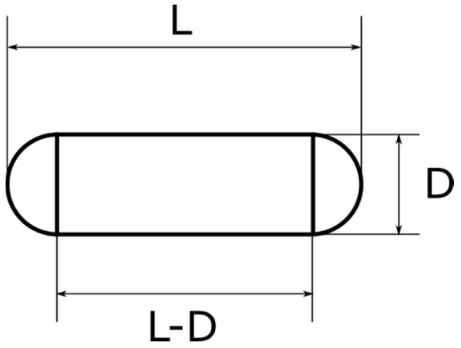

Figure 9-12 Effective length of cylinder vessel

was smaller than the full length of the tube or vessel. This length was known for the small scale experiment, but not for larger vessels. By assuming the ends of the vessels to be spherical caps, the linear length of the vessels on which the crack can propagate longitudinally was equal to $L - D$ (Figure 9-12).

Results of the modeling on various scales of vessel were summarized Table 9-2.

Table 9-2 Vessel geomteries of various scales, and ground loading estimation of a BLEVE

Reference	**Volume (m3)**	**Length (m)**	**Diameter (m)**	**Effective rupture length (m)**	**Estimated ground loading (kN)**
This work	0.00054	0.3	0.05	0.15	24
(Birk and Cunningham, 1994)	0.403	1.52	0.61	1.91	1700
(Birk et al., 2006b)	1.9	3.07	0.953	2.11	6300
(Johnson and Pritchard, 1991)	5.7	5	1.2	3.8	14400
Road tanker	20	6.1	2.1	4	27000

When scaling up this model to a real size vessel, a tank truck BLEVE could generate up to 27000 kN on the structure. This value should not be taken for design purposes, but it indicates the order of magnitude of such an event. For comparison, the Saturn V rocket that sent Apollo 11 to the moon had a thrust of 34000kN. However the duration of the BLEVE is a few milliseconds, while the Saturn V rocket thrust lasted over a minute to reach space. It is also equivalent to the force generated by the weight of more than a hundred 20 ton trucks on the structure where the explosion happens for the milliseconds of duration of the explosion. And this value was considering only the liquid phase. Using Model (A) would double this value.

From equations (50) and (51), the load scaled with $(L - D) * D$. By considering that vessels have ratios of L/D of similar order of magnitude ($2 < \frac{L-D}{D} < 3$), we can consider that load scaled with D^2.

One perspective of this study would concern the scaling of the impulse and duration of the BLEVE, in order to relate it to actual resistance criteria of specific structures. As initial thought, the duration of the event should scale with the length of the opening. As stated above, L/D was fairly steady depending on

the vessel considered. By assuming a constant crack propagation velocity for the opening process, the impulse should scale with D^3.

VI - Conclusions

This study on ground loading led to the following conclusions:

- liquid phase boiling dominated in the generation of the ground force;
- the contribution of the vapor space was minor and was observable on fast vessel opening configurations;
- the stronger the superheat, the stronger the ground force;
- an estimation model based on failure pressure applied to the fully flattened surface of the tube provided reasonable results for middle to high loads. The model was less accurate for weak loads;
- scaling up the model based on D^2 to a real size road tanker led to a maximum load of approximately 27000kN which is comparable to the thrust of Saturn V rocket for the short duration of the explosion.
- The model can be refined by using the generalized thrust equation used for rocket engine of change of momentum with time. However too many unknowns remain model the ground loading through these equations so far, particularly the mass flow exiting the vessel with time and the surface area of the dynamic opening.

Chapter 10

Conclusion

I - Contributions to BLEVE research and industrial safety

I-1. Experimental results

The small scale experimental setup reproduced realistic vessel failure and gave a wide range of data unavailable until now about BLEVE:

- Overpressure from many directions, particularly above the vessel and at 45° angle;
- High speed imaging from different angles;
- Transient pressure in the vessel;
- Ground loading under the vessel.

I-2. Lead shock and maximum overpressure characterization

- Anisotropy of the pressure field from top to sides was available for a decent range of failure pressure;
- The correlation between maximum overpressure and vapor phase volume fraction stated that vapor was the main contributor of the lead shock characteristics;
- Expansion energy models and fit with Sachs scaling give decent agreement with experimental results, within their hypothesis (side-on overpressure, conservative models, work better in the far-field). However their physics was based on wrong assumptions: liquid does not contribute to the lead shock overpressure.
- A model based on hemispherical vapor burst was developed to predict lead shock overpressure based on first principles compressible flow equations. A fitting factor, effective vapor fraction needs to be added to the model, to account for the non-ideal non-hemispherical aspect of the real explosion. This model scaled up with decent agreement with literature experimental data.

I-3. Secondary flow patterns

Link between imaging, overpressure data and simulation showed the presence of peculiar flow patterns in the vicinity of the vessel: a Mach shock collapsing back into the vessel, as a potential source of the second shock propagating outward in the far-field;

The Mach shock evidences explained the contribution from both the liquid and the vapor in the second shock formation;

I-4. Phase change

Classification of transient profiles leads to link pressure rise in the vessel to the process of boiling. This link led to timing evidence that boiling can hardly contribute to the lead shock overpressure.

I-5. Ground loading

Classification of transient profiles and correlation of load data with failure parameters led to assume there was a minor contribution on the ground from vapor expansion and a major contribution from liquid boiling;

Simple ground load prediction modeling was developed and was in decent agreement with small scale experimental data. Scaling up this model to real size road tanker vessel gave large numbers for maximum ground loading.

II - Answers to the main questions of BLEVE

- What is the contribution of the vapor phase and liquid in the BLEVE near-field hazards?
    - Vapor phase defines the maximum overpressure of the lead shock;
    - Vapor and liquid phase (the global energy available) defines potential second and third shocks after the lead shock;
    - Liquid boiling is the main contributor to ground loading.
- What are the consequences of a BLEVE on a bridge?

  From the ground loading modeling, large numbers for maximum load on the structure are given (estimation of 27MN of maximum force). However, conclusion on the damages induced to a structure such as a bridge will depend on other factors that require investigation: modeling the impulse of the ground load, and understanding the structural resistance of the bridge considered.

III - Opening and suggestions

Suggestions on the experimental setup are:

- To do more tests based cut length variation for more significant interpretations of this parameter;
- Put thermal insulation on the blast sensors, particularly close to the vessel;
- Stagnation pressure measurements: one of the consequences of the liquid flashing is the strong wind it generates in the near-field, thus the dynamic pressure in the vicinity of the vessel. No valid measurements of it have been done. Adding stagnation pressure probes close to the vessel will bring insight on this hazard.

The hemispherical F-W model may be improved with a more accurate prediction of the propane properties during the expansion (ratio of specific heat) would improve the accuracy of the model;

3D vessel meshing was started, but time did not allow to get significant validated results with CFD simulations:

- CFD work with vapor phase only would allow to confirm the tendencies observed with vapor content and maximum overpressure by increasing the vapor volume in the vessel;
- The CFD convenience would facilitate the visualization of secondary flow patterns such as vortices and Mach dome;
- Liquid boiling could be attempted through User Defined Function in Fluent, with the choked boiling model expressed in this work.

References

Abbasi, T., Abbasi, S.A., 2007. The boiling liquid expanding vapour explosion (BLEVE): Mechanism, consequence assessment, management. J. Hazard. Mater. 141, 489–519. doi:10.1016/j.jhazmat.2006.09.056

Abbett, M., 1971. Mach Disk in Underexpanded Exhaust Plumes 9, 512–514. doi:10.2514/3.6212

Asch, G., 2010. Les capteurs en instrumentation industrielle, in: Les Capteurs En Instrumentation Industrielle - 7ème Édition.

Baker, W.E., Cox, P.A., Westine, P.S., Kulesz, J.J., Strehlow, R.A., 1983. Explosion hazards and evaluation. Elsevier Scientific Pub. Co. doi:10.1016/0010-2180(85)90099-9

Balke, C., 1999. Study of the failure limits of a railway tank car filled with liquefied petroleum gas subjected to an open poolfire test . Final report. Berlin.

Barbone, R., 1994. Explosive Boiling of a Depressurized Volatile Liquid. McGill University, Montreal, Quebec, Canada.

Bauer, P., Chinnayya, A., Rességuier, T. de, 2015. Ondes de Choc et Détonations, Ellipses E. ed.

Birk, A.M., Cunningham, M.H., 1996. Liquid temperature stratification and its effect on BLEVEs and their hazards. J. Hazard. Mater. 48, 219–237. doi:10.1016/0304-3894(95)00157-3

Birk, A.M., Cunningham, M.H., 1994. The boiling liquid expanding vapour explosion. J. Loss Prev. Process Ind. 7, 474–480.

Birk, A.M., Davison, C., Cunningham, M., 2007. Blast overpressures from medium scale BLEVE tests. J. Loss Prev. Process Ind. 20, 194–206. doi:10.1016/j.jlp.2007.03.001

Birk, A.M., Dusserre, G., Heymes, F., 2013. Analysis of a Propane Sphere BLEVE. Chem. Eng. Trans. 31, 481–486. doi:10.3303/CET1331081

Birk, A.M., Poirier, D., Davison, C., 2006a. On the response of 500 gal propane tanks to a 25% engulfing fire. J. Loss Prev. Process Ind. 19, 527–541. doi:10.1016/j.jlp.2005.12.008

Birk, A.M., Poirier, D., Davison, C., 2006b. On the thermal rupture of 1.9 m3 propane pressure vessels with defects in their thermal protection system. J. Loss Prev. Process Ind. 19, 582–597. doi:10.1016/j.jlp.2006.02.006

Birk, A.M., Ye, Z., Maillette, J., Cunningham, M., 1993. Hot and cold BLEVEs observation and

discussion of two different kinds of BLEVEs.

Brode, H., 1959. Blast Wave from a Spherical Charge. Phys. Fluids 2, 217–229.

Casal, J., Salla, J.M., 2006. Using liquid superheating energy for a quick estimation of overpressure in BLEVEs and similar explosions. J. Hazard. Mater. 137, 1321–1327.

CCPS - American Institute of Chemical Engineers, 1994. Guidelines for Evaluating the Characteristics of Vapor Cloud Explosions, Flash Fires and BLEVEs. Wiley-AIChE.

Chang, J.C., Hanna, S.R., 2004. Air quality model performance evaluation. Meteorol. Atmos. Phys. 87, 167–196. doi:10.1007/s00703-003-0070-7

Chen, S., Sun, J., Wan, W., 2008. Boiling liquid expanding vapor explosion: Experimental research in the evolution of the two-phase flow and over-pressure. J. Hazard. Mater. 156, 530–537. doi:10.1016/j.jhazmat.2007.12.074

Ciccarelli, G., Melguizo-gavilanes, J., Shepherd, J.E., 2015. Pressure-field Produced by the Rapid Vaporization of a CO2 Liquid Column, in: 30th International Symposium on Shock Waves, Tel Aviv.

Edgerton, H.E., 1958. Shock wave photography of large subjects in daylight. Rev. Sci. Instrum. 29, 171–172. doi:10.1063/1.1716129

Frost, D.L., 1988. Dynamics of explosive boiling of a droplet. Phys. Fluids 31, 2554–2561. doi:10.1063/1.866608

Genova, B., Silvestrini, M., Leon-Trujillo, F.J., 2008. Evaluation of the blast-wave overpressure and fragments initial velocity for a {BLEVE} event via empirical correlations derived by a simplified model of released energy. J. Loss Prev. Process Ind. 21, 110–117.

Giesbrecht, H., Hess, K., Leuckel, W., Maurer, B., 1981. Analysis of Explosion Hazards on Spontaneous Release of Inflammable Gases into the Atmosphere Part 1. Ger. Chem. Eng. 4, 305–314. doi:0343-5539/81/0510-0305

Glass, I.I., 1974. Shock Waves and Man. University of Toronto Press, Toronto.

Hansen, O.R., Kjellander, M.T., 2016. CFD Modelling of Blast Waves from BLEVEs 48, 199–204. doi:10.3303/CET1648034

Hansen, P.M., 2018. Blast from pressurized carbon dioxide released into a vented atmospheric chamber. Shock Waves 28, 1053–1064.

Hargather, M.J.M.J., Settles, G.S.G.S., 2009. Retroreflective shadowgraph technique for large-scale flow visualization. Appl. Opt. 48, 4449–4457. doi:10.1364/AO.48.004449

Hemmatian, B., 2016. Contribution to the study of Boiling Liquid Expanding Vapor Explosions and their mechanical effects. Universitat Politecnica de Catalunya.

Hirsch, C., 2007. Numerical Computation of Internal and External Flows, 2nd editio. ed. John Wiley & Sons, Ltd.

Hopkinson, B., 1915. British ordnance board minutes 13565. Natl. Arch. Kew, UK.

INERIS, 2005. Arrêté du 29 septembre 2005 relatif à l ' évaluation et à la prise en compte de la probabilité d ' occurrence , de la cinétique , de l ' intensité des effets et de la gravité des conséquences des accidents potentiels dans les études de dangers des install.

INERIS, Heudier, L., 2013. Les éclatements de capacités, phénoménologie et modélisatin des effets - OMEGA 15.

Institution of Chemical Engineers, 1987. The Feyzin Disaster, Loss Prevention Bulletin. doi:0260-9576/08

Johnson, D.M., Pritchard, M.J., 1991. A large scale experimental study of BLEVEs. British Gas Report No I536, United Kingdom.

Kinney, G.F., Graham, K.J., 1985. Explosive shocks in air (Second edition), Berlin and New York. Springer.

Kornegay, W.M., 1965. Production and propagation of spherical shock waves at low ambient pressures, Distribution.

Laboureur, D., 2012. Experimental characterization and modeling of hazards : BLEVE and Boilover (PhD Dissertation). Von Karman Institute for Fluid Dynamics ; Universite Libre de Bruxelles.

Laboureur, D., Birk, A.M., Buchlin, J.M., Rambaud, P., Aprin, L., Heymes, F., Osmont, A., 2015. A closer look at BLEVE overpressure. Process Saf. Environ. Prot. 95, 159–171. doi:10.1016/j.psep.2015.03.004

Laboureur, D., Heymes, F., Lapebie, E., Buchlin, J.M., Rambaud, P., 2014. BLEVE overpressure: Multiscale comparison of blast wave modeling. Process Saf. Prog. 33, 274–284. doi:10.1002/prs.11626

Manda, L.D., 1975. Phase 11 Report on Full Scale Fire Tests.

Mengmeng, X., 2013. Thermodynamic and Gasdynamic Aspects of a Boiling Liquid Expanding Vapour Explosion.

Merzkirch, W., 1987. Flow Vizualization: 3 - Optical Flow Visualization, in: Merzkirch, W. (Ed.), Flow Vizualization. Academic Press, pp. 115–231.

Pinhasi, G.A., Ullmann, A., Dayan, A., 2007. 1D plane numerical model for boiling liquid expanding vapor explosion (BLEVE). Int. J. Heat Mass Transf. 50, 4780–4795.

Planas-Cuchi, E., Salla, J.M., Casal, J., 2004. Calculating overpressure from BLEVE explosions. J. Loss Prev. Process Ind. 17, 431–436. doi:10.1016/j.jlp.2004.08.002

Prugh, R.W., 1991. Quantitative Evaluation of Bleve Hazards. J. Fire Prot. Eng. 3, 9–24. doi:10.1177/104239159100300102

Radulescu, M.I., Law, C.K., 2007. The transient start of supersonic jets. J. Fluid Mech. 578, 331–369. doi:10.1017/S0022112007004715

Reid, R.C., 1983. Rapid Phase Transitions from Liquid to Vapor, in: Advances in Chemical Engineering. Academic Press, pp. 105–208. doi:10.1016/S0065-2377(08)60252-5

Reid, R.C., 1979. Possible Mechanism for Pressurized-Liquid Tank Explosions or BLEVE's. Science 203, 1263–1265. doi:10.1126/science.203.4386.1263

Rothkopf, E.M., Low, W., 1976. Shock formation distance in a pressure driven shock tube. Phys. Fluids 19, 1885. doi:10.1063/1.861423

Sachs, R.G., 1944. The dependence of blast on ambient pressure and temperature, No. BRL-466.

Salla, J.M., Demichela, M., Casal, J., 2006. BLEVE: A new approach to the superheat limit temperature. J. Loss Prev. Process Ind. 19, 690–700. doi:10.1016/j.jlp.2006.04.004

Settles, G.S., 2001. Schlieren and shadowgraph techniques: Visualizing phenomena in transparent media. Springer-Verlag, Berlin.

Shepherd, J.E., Sturtevant, B., Sherperd, 1982. Rapid evaporation at the superheat limit. J. Fluid Mech. 121, 379–402. doi:10.1016/0017-9310(88)90281-5

Slangen, P., Lauret, P., Heymes, F., Aprin, L., Lecysyn, N., 2016. High-speed imaging optical techniques for shockwave and droplets atomization analysis. Opt. Eng. 55, 121706. doi:10.1117/1.OE.55.12.121706

Slangen, P., Long, N., Long, N., 2016. Imagerie numérique ultrarapide Imagerie 33.

Strehlow, R.A., Baker, W.E., 1976. The characterization and evaluation of accidental explosions. Prog. Energy Combust. Sci. 2, 27–60. doi:10.1016/0360-1285(76)90007-1

TNO, 1997. CPR 14E (Yellow Book) Methods for the calculation of Physical Effects - Due to releases of hazardous materials (liquids and gases).

van den Berg, A.C., van der Voort, M.M., Weerheijm, J., Versloot, N.H.A., 2004. Expansion-controlled evaporation: a safe approach to BLEVE blast. J. Loss Prev. Process Ind. 17, 397–405.

Van den Berg, A.C.C., 2008. Blast Charts for Explosive Evaporation of Superheated Liquids. Am. Inst. Chem. Eng. Process Saf. Prog. 27, 219–224. doi:10.1002/prs

White, F.M., 2008. Fluid Mechanics. McGraw-Hill.

Yakush, S.E., 2016. Model for blast waves of Boiling Liquid Expanding Vapor Explosions. Int. J. Heat Mass Transf. 103, 173–185. doi:10.1016/j.ijheatmasstransfer.2016.07.048

Chapter 11

Appendices

Appendix A: **Overpressure prediction models: expansion energy calculation**

Brode (1959): rupture of vapor high pressure capacity

Brode evaluated the energy liberated from a bursting pressurized gas space, from the first principle of thermodynamics.

$$E_{Brode} = \frac{(P_{fail} - P_{atm}).V_v}{\gamma_1 - 1} \quad (1)$$

With E_{brode} the expansion energy in kJ, P_{fail} and P_{atm} respectively the failure pressure and atmospheric pressure in kPa, V_v the volume of vapor in m^3 and γ_1 the specific heat ratio of the compressed gas. The Brode energy shows the increase in internal energy from atmospheric state to compressed state, before failure (INERIS and Heudier, 2013).

The scaled distance is calculated from the expansion energy with the TNT-equivalent:

$$\overline{R_{Brode}} = \frac{r}{(E_{Brode}/W_{TNT})^{1/3}} \quad (2)$$

Prugh (1991): isentropic ideal gas expansion

Prugh (Prugh, 1991) considers a full isentropic expansion of the vapor phase from compressed to expanded state of the PLG. Combining the isentropic hypothesis (equation (3)) with the perfect gas hypothesis (equation (4)), he calculates an expansion energy depending on the failure pressure, atmospheric pressure and an equivalent vapor volume (equation (5)). The liquid phase contribution is considered by adding a flash fraction to the volume of expanding gas (equation (6)). This flash fraction is calculated based on mass and energy balance on the liquid, with adiabatic vaporization (equation (7)), taking into account that C_p and H_v vary with temperature (equation (8)). This is a conservative case overestimating most cases of BLEVE.

$$E = \Delta U = \int PdV \quad (3)$$

$$PV^{\gamma} = constant \quad (4)$$

$$E_{Prugh} = \left(\frac{P_{fail}.V^*}{\gamma - 1}\right)\left(1 - \frac{P_{atm}}{P_{fail}}\right)^{\frac{\gamma-1}{\gamma}} \quad (5)$$

$$V^* = V_v + V_l.f\left(\frac{\rho_l}{\rho_v}\right) \quad (6)$$

$$f = 1 - exp\left(-2.63\left(\frac{C_p(T_b)}{H_v}\right)(T_{crit} - T_b)\left(1 - \left(\frac{T_{crit} - T_{fail}}{T_{crit} - T_b}\right)^{0.38}\right)\right) \quad (7)$$

$$H_v = h_{e,v}(T_b) - h_{e,l}(T_b) \quad (8)$$

When expansion energy is well defined, the conversion to TNT mass equivalent and scaled distance follows equation (9):

$$\overline{R_{Prugh}} = \frac{r}{(E_{Prugh}/W_{TNT})^{1/3}} \quad (9)$$

Planas-Cuchi (2004): adiabatic irreversible real gas expansion

Planas-Cuchi (Planas-Cuchi et al., 2004) considers a more realistic approach, evaluating an adiabatic but irreversible expansion, with real gas behavior. To do so, only the work done by the volume variation is considered for the internal energy calculation:

$$\Delta U = -P_0 \Delta V \quad (10)$$

The resolution of the problem is then either a graphical resolution (intersect of the curves of ΔU and $-P_0\Delta V$ depending on the vapor fraction) (Figure 11-1), or analytically through an iterative process (equations (11) to (13))

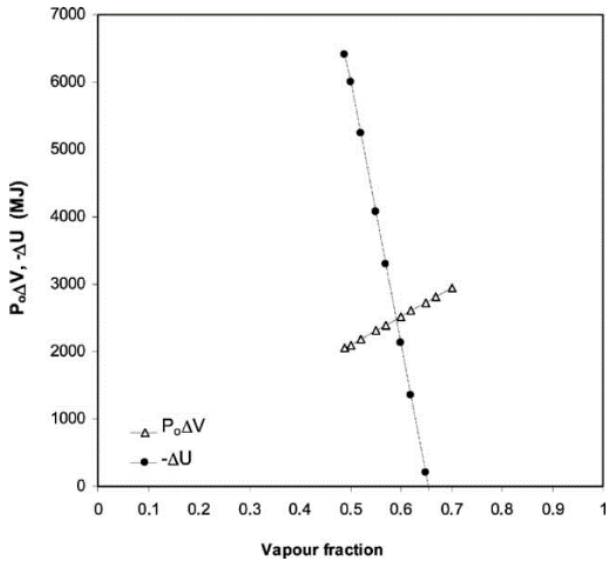

Figure 11-1 Variation of U and $P_0\Delta V$ as a function of the vapor fraction of the theoretical final condition (Planas-Cuchi et al., 2004)

$$\Delta U = (u_l - u_v)m_T.x - m_T.u_l + U_i \quad (11)$$

$$P_0.\Delta V = P_0[(v_v - v_l).m_T.x + m_T.v_l - V_i \tag{12}$$

$$x = \frac{m_T.P_0.v_l - V_i.P_0 + m_T.u_l - U_i}{[(u_l - u_v) - (v_v - v_l).P_0].m_T} \tag{13}$$

Author does mention the energy transferred into the mechanical deformation of the vessel at opening, by adding an empirical factor when converting the internal energy to scaled distance ($\beta = 0.4$)

$$\overline{R_{Planas}} = \frac{r}{(\beta * \Delta U/W_{TNT})^{1/3}} \tag{14}$$

Casal (2006): Liquid Superheat Energy

Casal (Casal and Salla, 2006) defines the expansion energy based on the calculation of the Superheat Energy (SE). This method is based on the energetic approach of superheat limit temperature calculation mentioned earlier (Planas-Cuchi et al., 2004). According to the author, by assuming an adiabatic process, the excess heat stored in the liquid when reaching superheat will directly contribute to the expansion and blast generation. The superheat energy is considered as the heat available in the liquid that will not boil. This liquid will go from superheat temperature at atmospheric pressure to ambient pressure T_0.

$$SE = h_l(T_{fail}) - h_l(T_0) \tag{15}$$

From this, expansion energy and TNT-equivalent mass is calculated

$$m_{TNT-Casal} = \beta.m_l.\frac{SE}{W_{TNT}}$$
$$\text{with } \beta = \begin{cases} 0.14\ for\ isentropic\ expansion \\ 0.07\ for\ irreversible\ expansion \end{cases} \tag{16}$$

β represents the fraction of superheat energy involved in the expansion work. It is calculated as follow (calculation of expansion work are taken from (Planas-Cuchi et al., 2004; Prugh, 1991)

$$\beta = 0.5 * \frac{W}{SE}$$
$$\text{with } W = \begin{cases} \Delta U\ for\ isentropic\ expansion \\ P_0\Delta V\ for\ irreversible\ expansion \end{cases} \tag{17}$$

The factor 0.5 introduced in the calculation of β take into account the ductile mechanical rupture. It is calculated for various known substances (water, propane…) and a maximum of 0.14 is found for isentropic expansion, and 0.07 for adiabatic irreversible process.

$$\overline{R_{Casal}} = \frac{r}{(m_{TNT-Casal})^{1/3}} \quad (18)$$

Genova (2008): Excess Heat for isentropic expansion

Similarly to Casal superheat energy, Genova (Genova et al., 2008) considers the so called excess heat available in the liquid after pressure drop, through an adiabatic process. Equation (19) is obtained.

$$E_{Genova} = \chi . m_l . C_p\left(T_{fail} - T_{boil}\right) \quad (19)$$

$$C_p = \frac{C_p\left(T_{fail}\right) + C_p(T_{boil})}{2} \quad (20)$$

The factor $\chi = 0.07$ is determined by fitting with experimental data available on BLEVE overpressure (Birk et al., 2006a; Birk and Cunningham, 1996; Salla et al., 2006) and some data from a BLEVE accident in Italy in 2005.

The scaled distance is calculated with Sachs scaling

$$\overline{R_{Genova}} = r * \left(\frac{P_{atm}}{2 * E_{Genova}}\right)^{\frac{1}{3}} \quad (21)$$

The models of Casal and Genova are very similar in the concept, calculating excess heat available in the superheated liquid to evaluate a fraction of this heat contributing to expansion work and overpressure generation. The main differences between the models are:

- The excess here is calculated in the fraction of superheated liquid that does not boil for Casal, while Genova considers the excess heat of the whole liquid.
- The fraction of excess heat converted into expansion work is calculated through a comparison with literature expansion work calculation on known substance at superheat limit temperature for Casal, while Genova simply compares it to experimental results available in literature.

TNO Yellow Book: Variation of internal energy of each phase through isentropic expansion

The TNO method models the contribution of each phase through the calculation of variation of internal energy, assuming isentropic expansion (equation (22)). The scaled distance is calculated with Sachs scaling (equation (23)).

$$E_{TNO} = m_l \left(u_{l\,fail} - u_{l\,atm}\right) + m_v(u_{v\,fail} - u_{v\,atm}) \quad (22)$$

$$\overline{R_{TNO}} = r * \left(\frac{P_{atm}}{2E_{TNO}}\right)^{1/3} \tag{23}$$

The conversion to overpressure considers a different method if $\overline{R_{TNO}} > 2$ (far field) or $\overline{R_{TNO}} < 2$ (near-field).

- $\overline{R_{TNO}} > 2$: the far-field calculation is based on graphical resolution on the curve from Baker (Figure 2-26 Right).
- $\overline{R_{TNO}} < 2$: the near-field calculation is based on estimation of an initial overpressure and initial distance of shock generation. The initial distance is evaluated as the radius of a hemispherical tank with the volume equivalent to the actual volume (equation (24)). The assumption is made that the blast will be completely symmetrical. The initial overpressure is calculated with the implicit equation (25), an equivalent to the shock tube equation where the high pressure chamber is considered to be the vessel before failure, and the low pressure chamber is the ambient air.

$$R_{init} = 0.782\, V_v^{1/3} \tag{24}$$

$$\frac{P_{fail}}{P_{atm}} = (P_{init} + 1)\left[1 - \frac{(\gamma - 1)(a_a/a_p)P_{init}}{\sqrt{2\gamma_a(2\gamma_a + (\gamma_a + 1))P_{init}}}\right]^{-2\gamma/(\gamma-1)} \tag{25}$$

Then, the curve closest to (R_{init}, P_{init}) is chosen from Figure 11-2, to convert graphical the TNO scaled distance into overpressure.

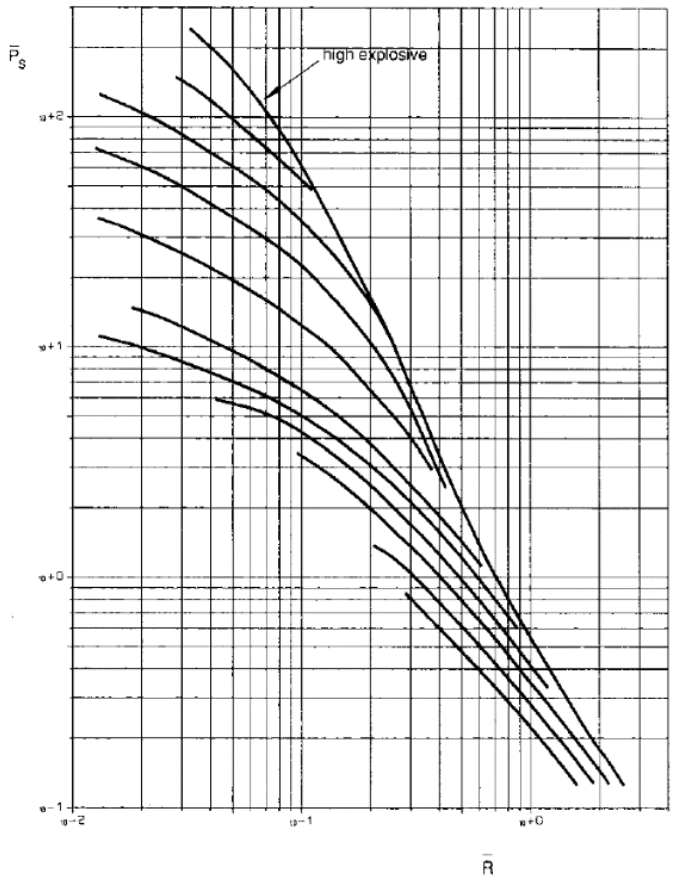

Figure 11-2 Overpressure versus Sachs scaled distance, for TNO near-field estimation (TNO, 1997)

Birk (2007): Variation of internal energy of the vapor phase through isentropic expansion

Birk (Birk et al., 2007) proposes a quick estimation of the overpressure, based on some of the basic assumptions mentioned already, such as isentropic expansion and perfect gas. The calculation of the expansion energy is then made with the difference of internal energy, similar to TNO (TNO, 1997). Moreover, it is assumed that only vapor contributes to the first shock generation, so only the internal energy of the vapor space is used for the calculation (equation (26)). It is then converted to TNT-scaled distance (equation (27))

$$E_{birk} = m_v(u_{v\,fail} - u_{v\,atm}) \tag{26}$$

$$\bar{R}_{Birk} = \frac{r}{(E_{Birk}/W_{TNT})^{1/3}} \tag{27}$$

Appendix B: Apparatus initial designs and evolutions

I - Initial test campaign: summer 2014

The small scale BLEVE experiment started in the summer of 2014 in Kingston, Ontario, Canada. The purpose of this testing was to verify the capability of the lab to generate a small scale BLEVE safely and with control over the failure. Initially, water was chosen as the liquid in the tube in order to avoid dealing with the flammable hazard. The tube was pressurized using a small burner set beneath it, and heating the liquid phase without weakening the wall structure. The failure was triggered by heating the top of the tube with a large burner to increase drastically the temperature of the aluminum wall until it ruptured. Two different tube wall thicknesses were used depending on the tests: 1.65mm or 0.9mm. The purpose of the different wall thicknesses was to obtain a wider range of failure pressures.

High speed imaging was set up (SA5 7000 fps) to capture details of the vessel opening process, an event lasting no more than 10ms. Figure 11-3 presents an overall view of the experimental setup during this initial testing. No high speed camera was available at that time to view through end window. Blast gages, transient pressure transducers and strain gage load cells were used to measure respectively the blast outside the tube, the pressure drop and potential build-up in the tube and the ground force generated by the explosion.

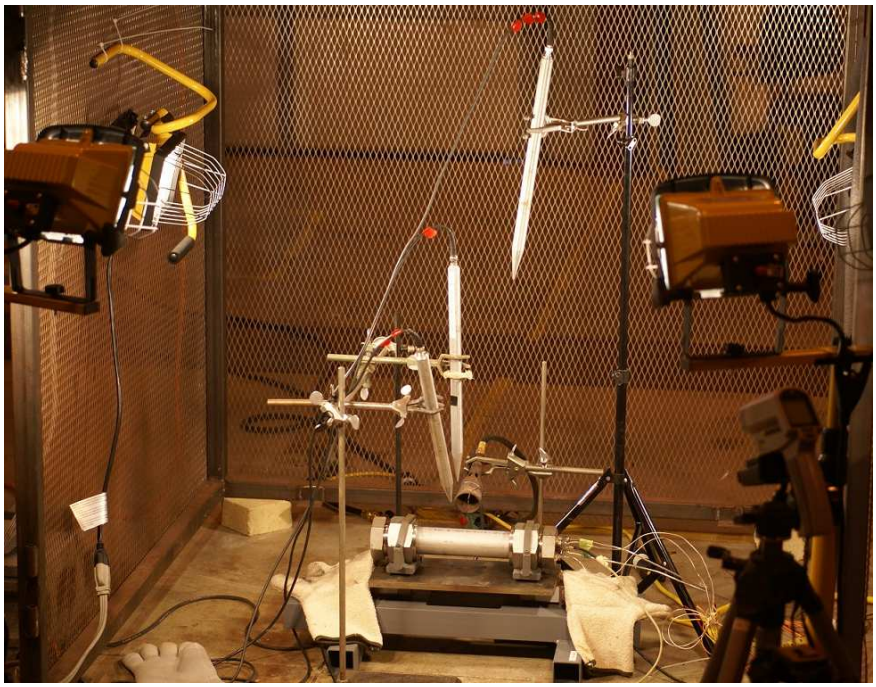

Figure 11-3 General view of the small scale BLEVE apparatus (1st test campaign: summer 2014)

The outcome of these tests was 8 partial vessel openings and 9 water BLEVEs. Successful measurements of blast overpressure were made as well as some interesting high speed imaging.

However the control over the failure pressure was limited for 2 reasons:

- The failure pressure depended on the following two variables:
    - pressure of the water in the vessel
    - ultimate strength of the weakened tube wall

  When the top burner was on, both variables were changing as the tube was being severely heated.
- Control over the weakened length of the tube was another parameter of interest. However the only control over this variable was in varying the inclination and distance of the top burner, thus having also an influence on the failure pressure of the vessel.

Other difficulties, such as defective strain gage sensors, poor transient pressure measurement because the ends of the tube were propelled axially, and lighting issues for high speed imaging left room for improvement. From this limited test series the following was determined:

- The apparatus concept was sound;
- We needed at least two high speed cameras, more if we want shadowgraph;
- Loads cells were destroyed by down force. Strain gage lead cells not appropriate.
- We need more blast gages;
- We need a better heating method or failure method.

At that time a second version of the apparatus was manufactured and shipped to France.

II - Second test campaign: spring 2015

The second series of tests with the small scale BLEVE apparatus occurred over the spring of 2015 in Ales France. The purpose of this set of tests was to improve the measurement setup (blast gages, optical setup) to better map the shock propagation, and to obtain better control over the failure pressure.

The same tube size was tested, with the end caps and Swagelok ferrules. Water was used for the first tests in this series. In subsequent tests the tubes were filled with commercial LPG (approximately 80% propane 20% butane). The tubes were pressurized from a bottom burner until rupture occurred. Control over the failure pressure was attempted by:

- Machining of the top of the tube: in order to weaken the tube to reasonable failure pressures with some range of predictability. A notch was machined on most of the tubes used in these tests (*Figure 11-4*). The depth of the notch defined the maximum internal pressure the tube could withstand, and the length of the notch provided control over the weakened length, giving more independent control over each of these failure variables. For this purpose, the tubes with a wall thickness of 1.65mm were used, the thinner walls being too malleable for machining.
- Heat treatment (annealing) of the aluminum tube was used to reduce the material yield strength by about 50% in order to allow a reasonable range of notch depth for the machining process. Details of the heat treatment are given in the next paragraph which describes the final setup of the apparatus.

Figure 11-4 Machined slot on top of the tube for controlled failure

Blast gages were setup around the tube for a 3D mapping of the shock propagation in the vicinity of the vessel (from 20 to 90cm from the tube wall) (*Figure* 11-5 left). A similar setup was used for pressure and temperature control in the vessel, as well as the ground loading and the high speed transient pressure in the vessel. The high speed optical imaging setup was improved, with a radial high speed imaging of the tube through retroreflective shadowgraph (detailed after) and a direct high speed imaging of the window situated at one end of the tube.

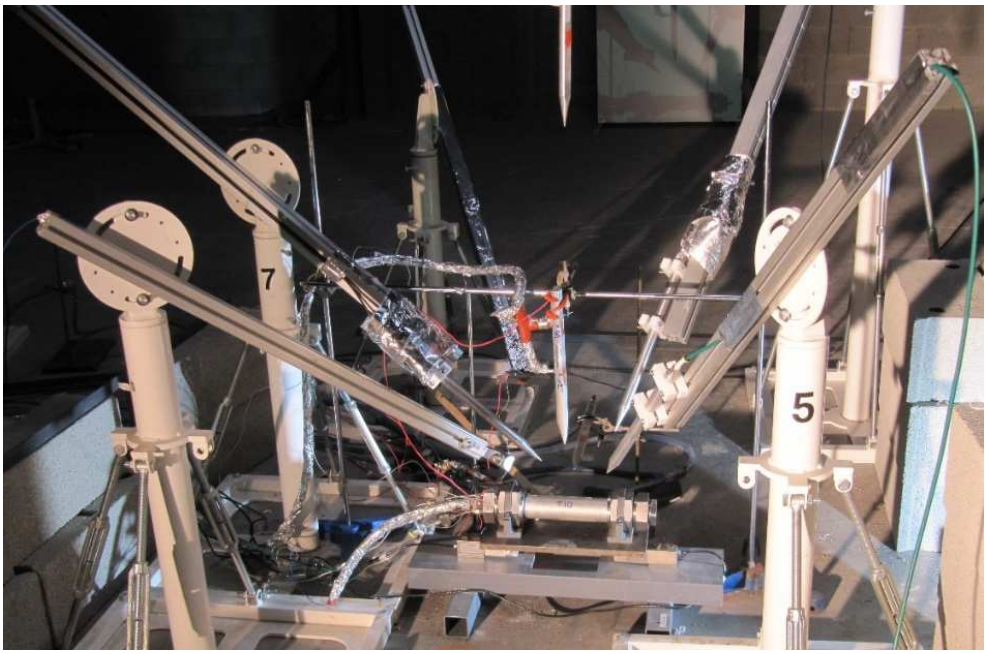

Figure 11-5 General view of the small scale BLEVE apparatus (2nd test campaign: spring 2015)

The outcome of this test campaign was 5 water BLEVE and 11 LPG BLEVE. The mapping of the 3D propagation of the shock wave was improved, as well as its decay up to 90cm above the vessel. The high speed imaging showed interesting results in terms of shock visualization and clean visualization of the boiling wave through the window.

Areas for improvement in the testing were the following:

- Acquisition of down force load data was unsuccessful. Once again load cells were destroyed. The strain gage technology needed to be changed;
- Problems of defective high speed pressure transducers were still present and needed to be addressed;
- Pressurizing the tube with a flame led to convective volutes visible with the shadowgraph imaging, impairing the shock visualization in the vicinity of the shock and this needed to be addressed;
- The machining process led to numerous problems because of the malleability of the aluminum. Most of the test campaign was spent trying to master this process for achieving better control over the failure pressure, but issues of machining defect as well as tube irregularities were not fully resolved;
- The design of a blast probe is required to measure the decay close to the vessel.

II-1. **Optical setup**

One specificity of this test campaign was the optical technic used. Direct Retroreflective shadowgraph (also recently called Pure In Line Shadowgraph, or PILS (P. Slangen et al., 2016)) is simple in principle, and similar to the examples of shadowgraph encountered in daily life, as the one described above. It was first used by Edgerton (Edgerton, 1958), hence the term "Edgerton shadowgraph" sometimes used in literature. It originally used sun light from the back of the screen as light source. It was then redefined as retroreflective shadowgraph when a retroreflective screen was implemented (Hargather and Settles, 2009).

It requires a light source, a camera and a retroreflective screen on which to project the shadow. By placing the camera and the light source very adjacent to the optical path, the object of study and its shadow will be superposed. The particularity of this technique lies in the screen, which has retroreflective properties (cat's eye-like micro balls or prisms) meaning that it redirects light rays back in the same direction from which they came, thus maximizing the amount of light received by the camera placed near the light source.

The maximum sensitivity of this setup is for $0.3h < g < 0.7h$, optimum at $g = 0.5h$. The advantage of this setup is its ability to observe a large field phenomenon. The drawback is a loss of sensitivity in capturing smaller scales of the phenomenon.

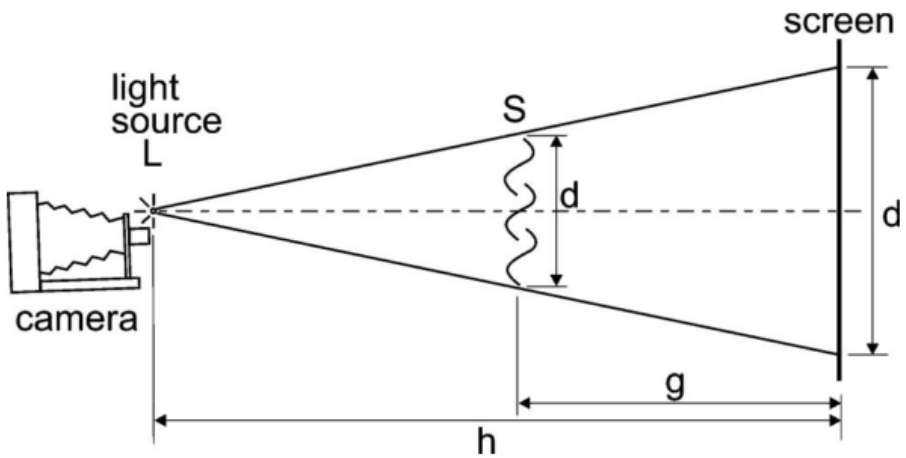

Figure 11-6 Retroreflective shadowgraph setup schematic (Hargather and Settles, 2009)

II-2. **Optical results**

As mentioned above, the advantage of this method was a larger field of view that was not dependent on the size of the parabolic mirrors, but at the cost of a loss in resolution over the phenomenon in the vicinity of the tube. Thus, the shock formation was visible (Figure 11-7 a) to c)) but not as clearly as it was with the Z-type shadowgraph setup (Figure 5-20 and Figure 5-23). Another visible aberration was the thermal volutes above the tube which were induced by the heating from the burner below the tube. These also made the detection of the shock at its early stage more difficult. This led to the decision to use an electric heater for the 2017 test series.

Figure 11-7 f) showed the aluminum tube getting flattened on the base plate. Because there was no heater under the tube in this configuration, there was a strong impact between the tube and the base plate. This impact generated a side shock wave, visible on Figure 11-7 g to i).

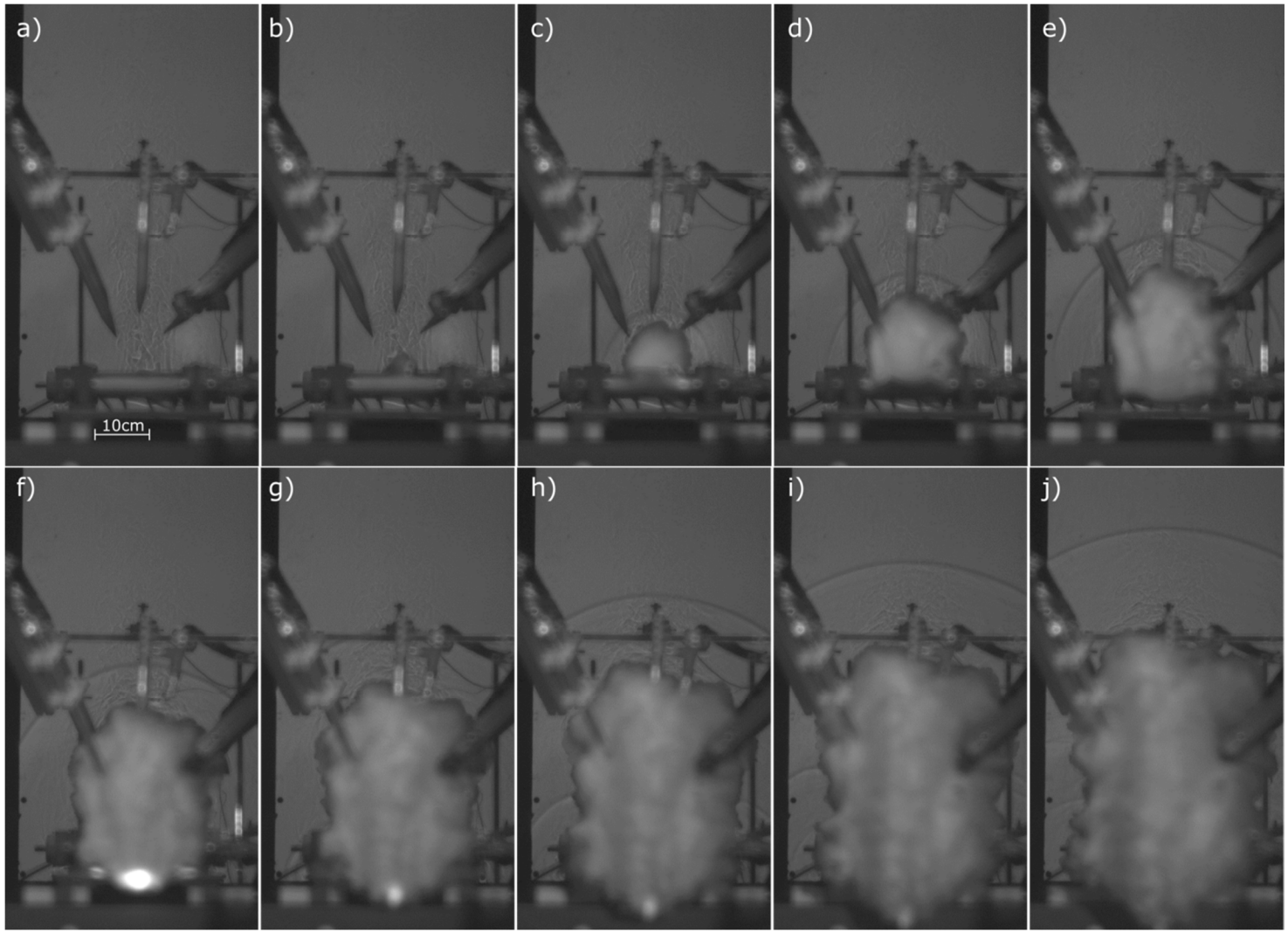

Figure 11-7 Radial view with high speed retroreflective shadowgraph (Camera V711, $\Delta t = 115\mu s$, $P_{fail} = 37\ bar, \Phi_{liq} = 61\%, L_w = 100mm$)

III - Final apparatus design: spring 2017

This test series incorporated several improvements including:

- Pure propane was used instead of water or commercial LPG, not available before;
- An electric heater was used to heat liquid to burst pressure, removing a source of ignition and improving the shadowgraph;
- The annealing and machining process of tubes was improved for controlled failure pressure;
- The technology for load cells was changed;
- The optical methods were improved: more sensitivity of the shadowgraph on the near-field and more high speed cameras available
- More blast gages were used to map the near-field and far-field of the explosion;
- A high speed transducer was used inside the vessel for transient pressure measurements.

The apparatus was set up in two separate rooms at the Spark test facility of Institut des Sciences du Risque: one room housed the apparatus itself along with the instrumentation, and a second room served as the control room from which the experiments were monitored.

The final design is introduced paragraph II. The instrumentation on the last experiments is presented next.

Appendix C: Test tubes after rupture

The following appendix presents the tubes after burst for each tests in 2015 and 2017.

I - BLEVE experiments 2015

The bursts from 2015 experiments include five water tests (test 1 to test 5) and twelve commercial propane tests (test 6 to test 17)

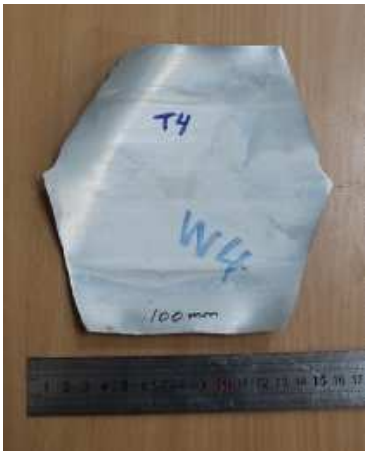

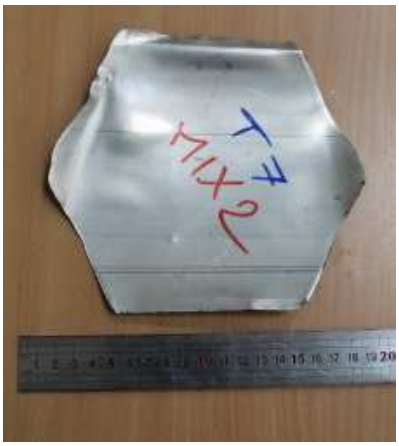
T7
Mix2

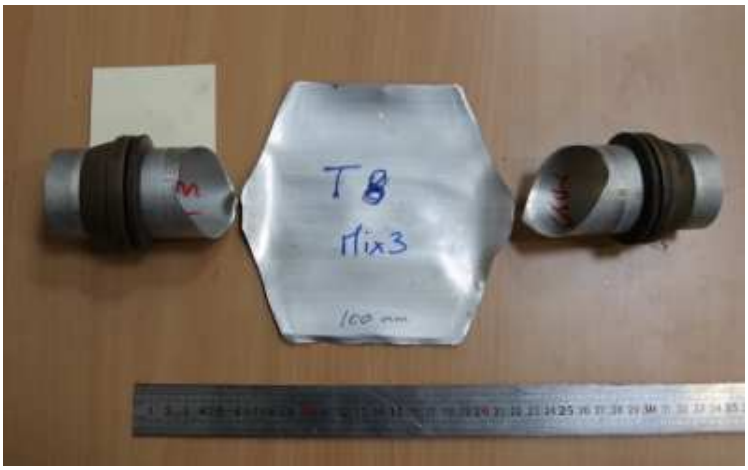
T8
Mix3
100 mm

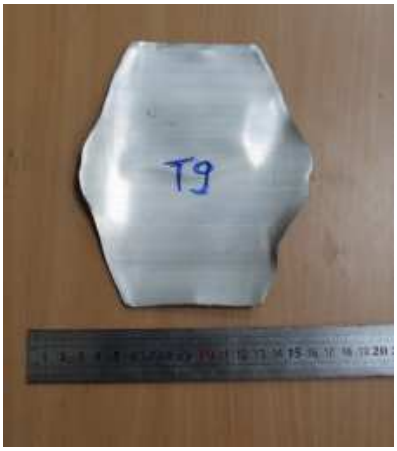
T9

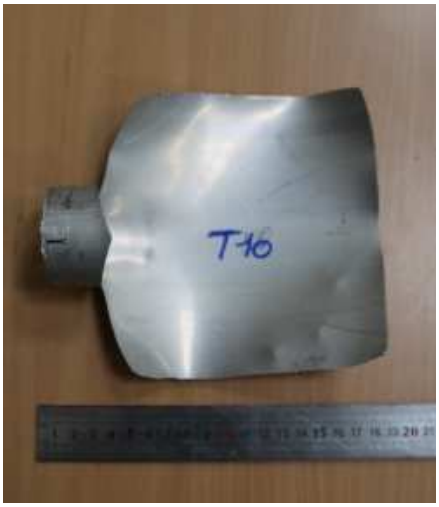
T10


T11


T12


T13


T15


T16


T17

II - **BLEVE experiments 2017**

The bursts from 2017 experiments include twenty-four propane tests and one air test (test 15).


16,7 bar


13


14


15


16


18


20


21


22


23


24


25


26

Appendix D: Validation of the 4-sensor probe

For 2 tests, the measurement from the 4th sensor of the 4-sensor gage was backed up by using a blast gage placed at a similar position in order to validate the signal obtained at the end of the 4-sensor gage (Figure 11-8). A comparison of these led to the following statements:

- The error made between the 2 sensors on the maximum overpressure measured was 6%;
- The maximum slope of pressure increase was very similar (error < 1%)
- The general shape of the first positive impulse was validated. The 4-sensor gage measurement showed a small plateau when reaching the maximum overpressure that the sensor alone did not show. The error on the positive impulse calculation was 9%.
- The negative pressure phase was more important on the lone sensor than on the 4-sensor probe. No conclusions were drawn on the data of this fourth gage in the present work. It can however be a track for improvement for further study.
- A small pressure oscillation occurs before the main pressure increase on the 4-sensor probe. For 15 tests this signal shape was observed only on the fourth sensor of the probe, but not the first three. This oscillation was not seen on the PCB sensor.

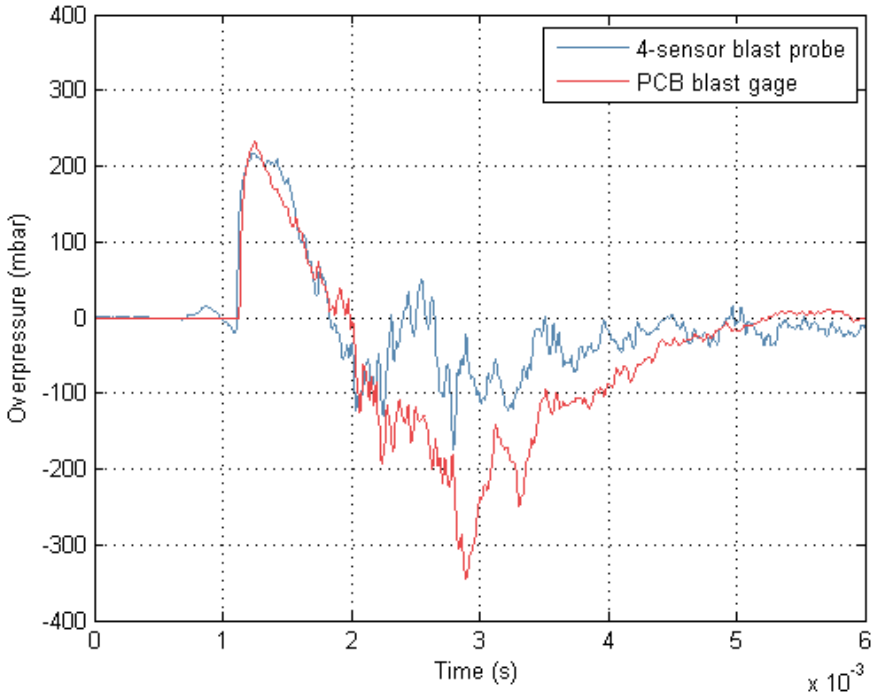

Figure 11-8 Overpressure signal at 40cm above the vessel with 2 different sensors ($P_{fail} = 16bar - \Phi_{liq} = 5\% - L_w = 150mm$)

Various phenomena can initiate these differences:

- A phenomenon intrinsic to the 4-sensor probe (example: boundary layer forming along the probe), justifying the need of calibration of such device.
- Slight difference in orientation. Although both probes were positioned as accurately as possible, a small distance separated them. Thus a spherical flow may impact each probe at a slightly different angle. This may explain some differences such as the negative pressure phase.

As most of the study focused on the maximum overpressure generated by the BLEVE, it was safe to consider the error of 6% as a maximum error for the homemade probe in comparison with other classic probes.

Appendix E: Data and plots from BLEVE 2017

The following appendix presents the data of all the BLEVE tests performed during the spring of 2017. First is presented a reminder of the position of the different blast transducers Figure 11-9.

Then a summary of the failure conditions of all the tests is given through a map of the failure parameters (Figure 11-10) that were:

- Failure pressure;
- Liquid volume fill;
- Weakened length;

A P-T diagram reminding the saturation condition of the tests is presented Figure 11-11 together with Table 11-1 giving the failure data for each test.

Finally, 6 plots are presented for each test:

- A P-T diagram of the pressurizing process;
- The internal transient pressure signal P_{in} coupled with the ground loading signal;
- The signal of the overpressures measured above the vessel in the near-field, dP_1 to dP_4;
- The signal of the overpressures measured at 45° angle from the vessel in the near-field, dP_5 to dP_8;
- The signal of the overpressures measured at the horizontal of vessel in the near-field, dP_9 to dP_{11};
- The signal of the overpressures measured in the far-field, horizontal and vertical around the vessel, dP_{12} to dP_{21};

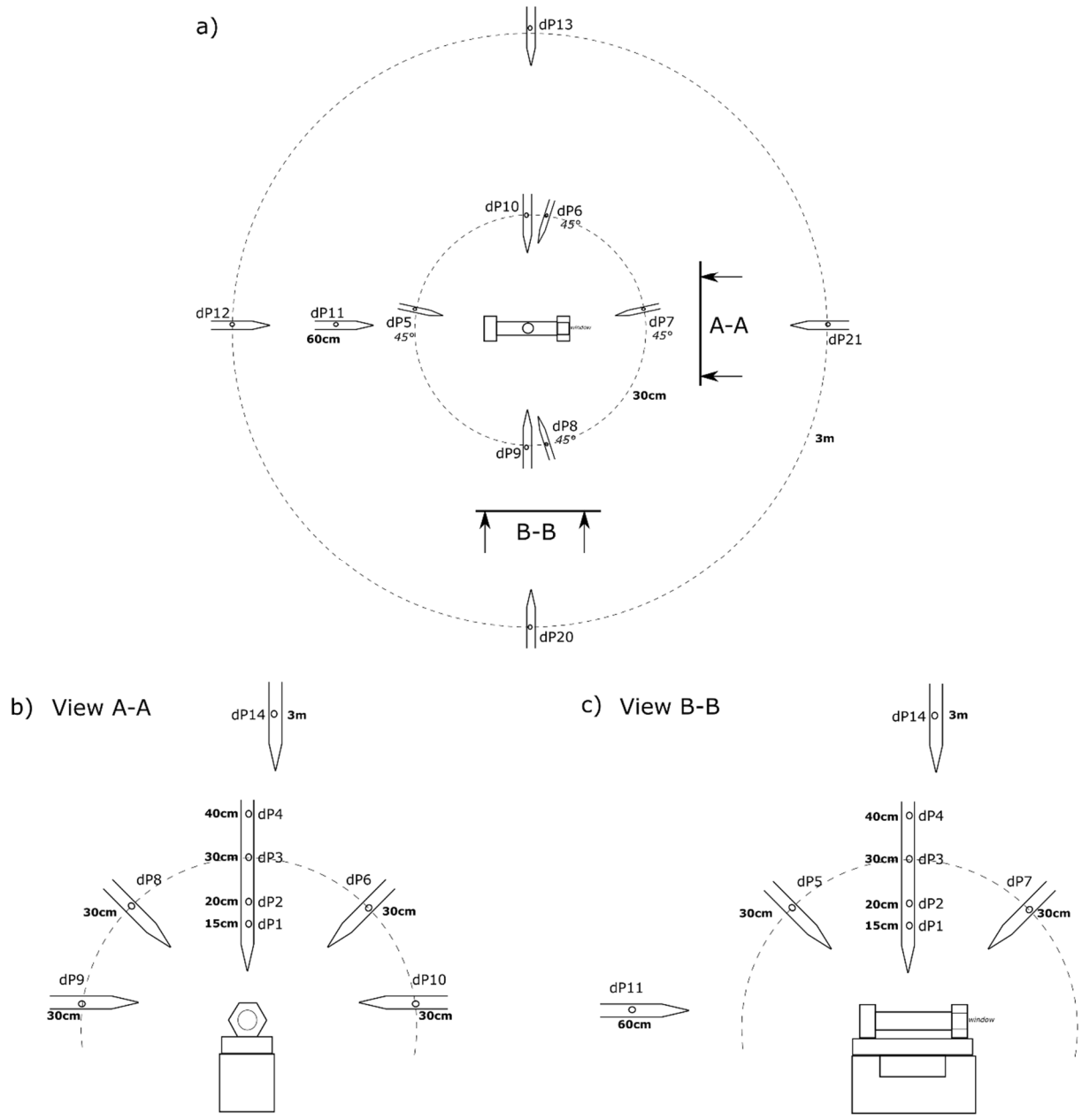

Figure 11-9 Blast transducers positions

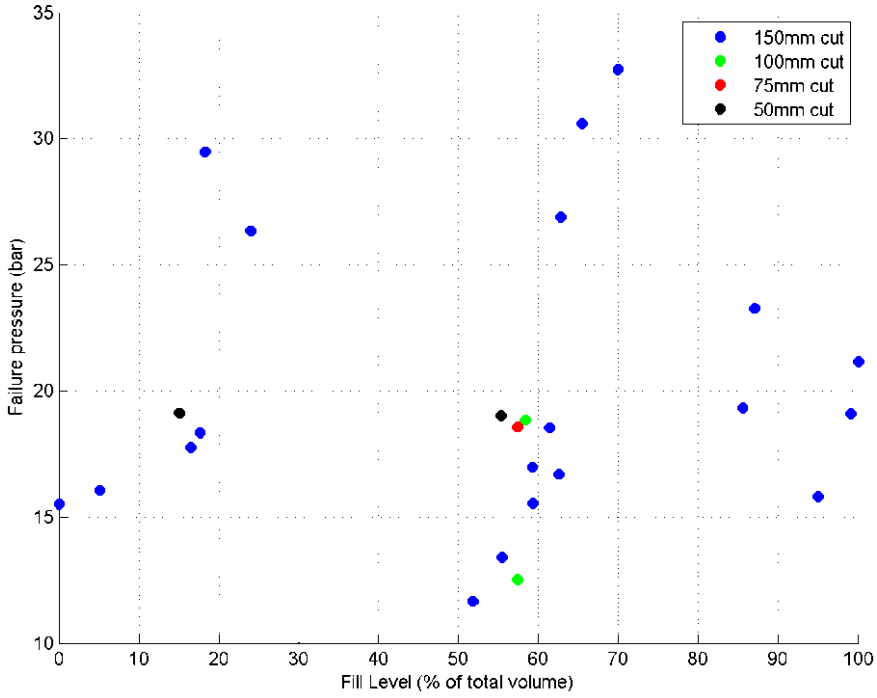

Figure 11-10 Failure control parameters of all tests on a Liquid Fill - Failure Pressure scatter plot

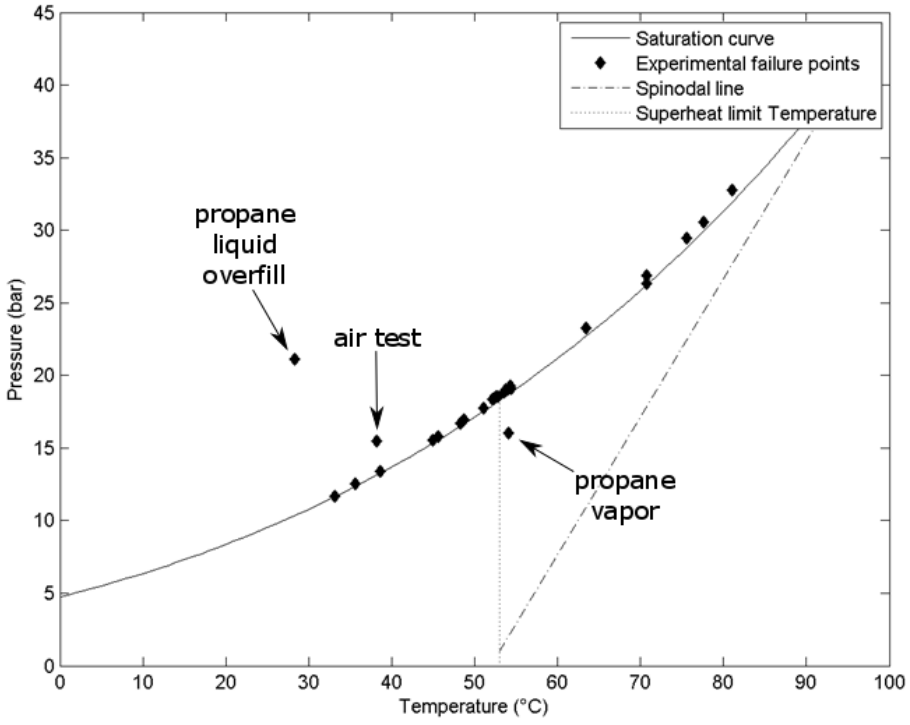

Figure 11-11 P-T diagram with failure condition of all plots with propane saturation curve

Table 11-1 Summary the failure conditions of each BLEVE 2017

Test #	*Mass propane (g)*	P_{fail} *(abs) (bar)*	T_{fail} *(oC)*	Φ_{liq} *(%)*	L_w *(mm)*
2	146	11,66	33,09	52,80%	150
3	153	13,38	38,60	56,49%	150
4	160	15,55	44,94	60,52%	150
5	166	16,69	48,30	63,80%	150
6	158	16,95	48,68	60,45%	150
7	154	18,84	53,56	59,58%	100
8	159	12,51	35,65	58,48%	100
9	147	19,01	53,75	56,47%	50
10	58	19,12	54,45	15,59%	50
11	60	17,74	51,10	16,97%	150
12	243,5	19,06	53,94	100,89%	150
13	243,5	15,80	45,62	96,72%	150
14	63	18,34	52,11	18,13%	150
15	Air	15,50	38,2	0	150
16	31	16,04	54,03	4,88%	150
17	228	21,15	28,32	100,00%	150
18	155,5	18,54	52,78	60,13%	150
19	149	30,59	77,63	63,87%	150
20	149	26,87	70,76	61,41%	150
21	206	19,31	54,35	83,86%	150
22	200,5	23,28	63,42	85,32%	150
23	155,5	32,74	81,03	70,00%	150
24	79	26,33	70,77	23,23%	150
25	72	29,45	75,54	17,56%	150
26	147	18,56	52,61	56,28%	75

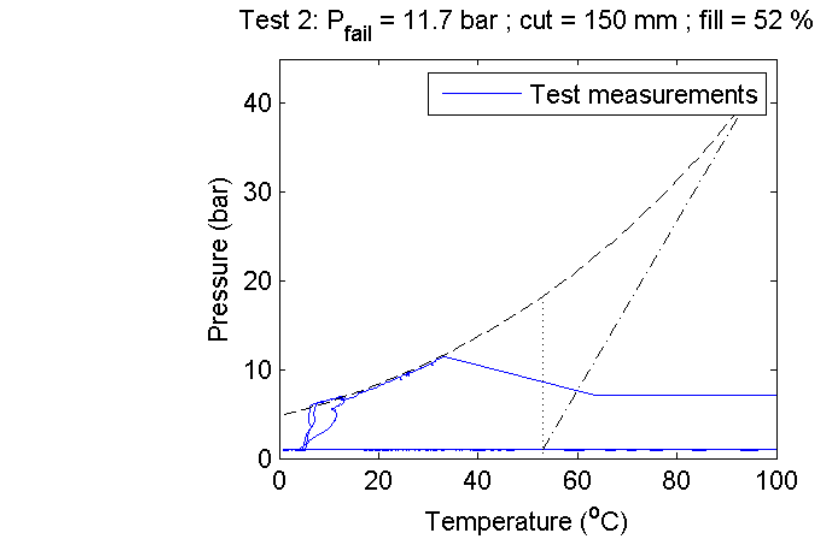
Test 2: P_fail = 11.7 bar ; cut = 150 mm ; fill = 52 %
Test measurements
Pressure (bar)
Temperature (°C)

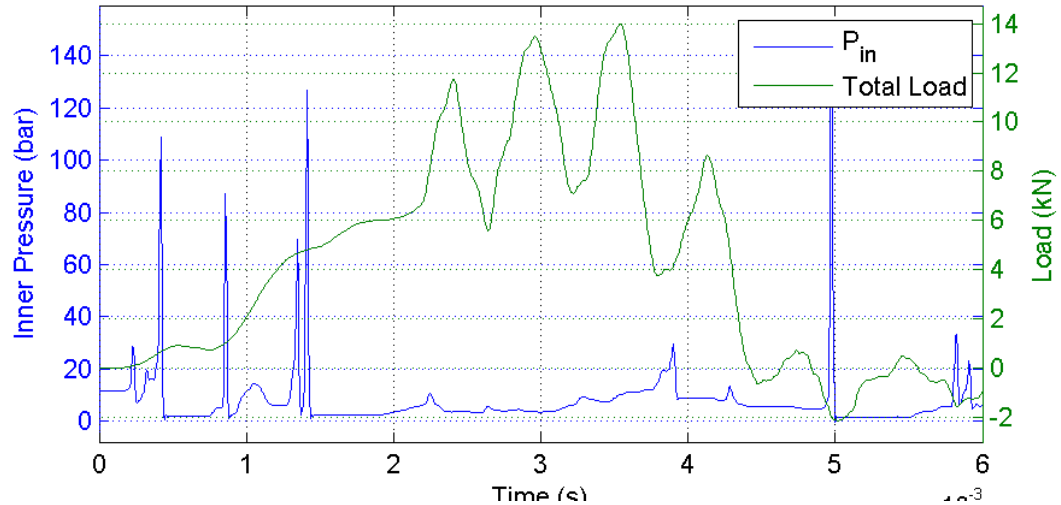
P_in
Total Load
Inner Pressure (bar)
Load (kN)
Time (s)

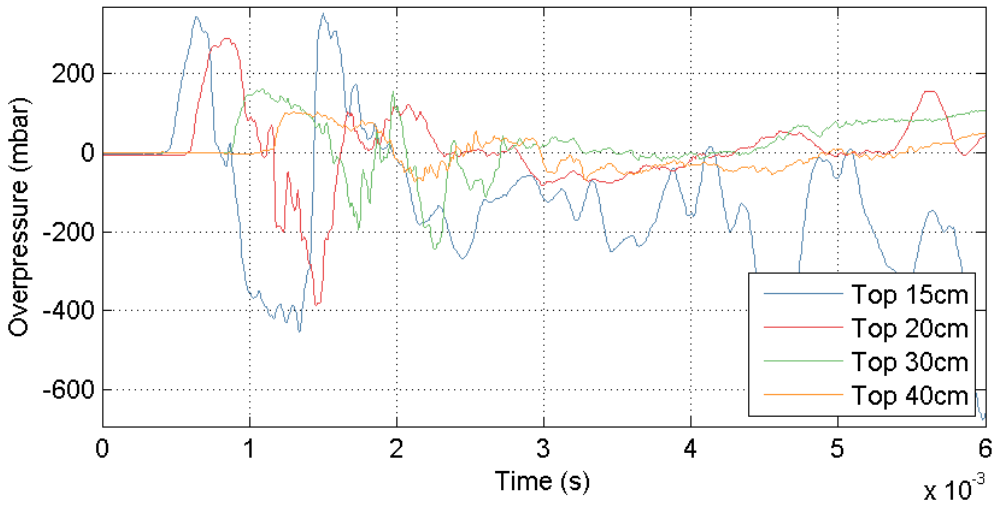
Top 15cm
Top 20cm
Top 30cm
Top 40cm
Overpressure (mbar)
Time (s)
x 10^-3

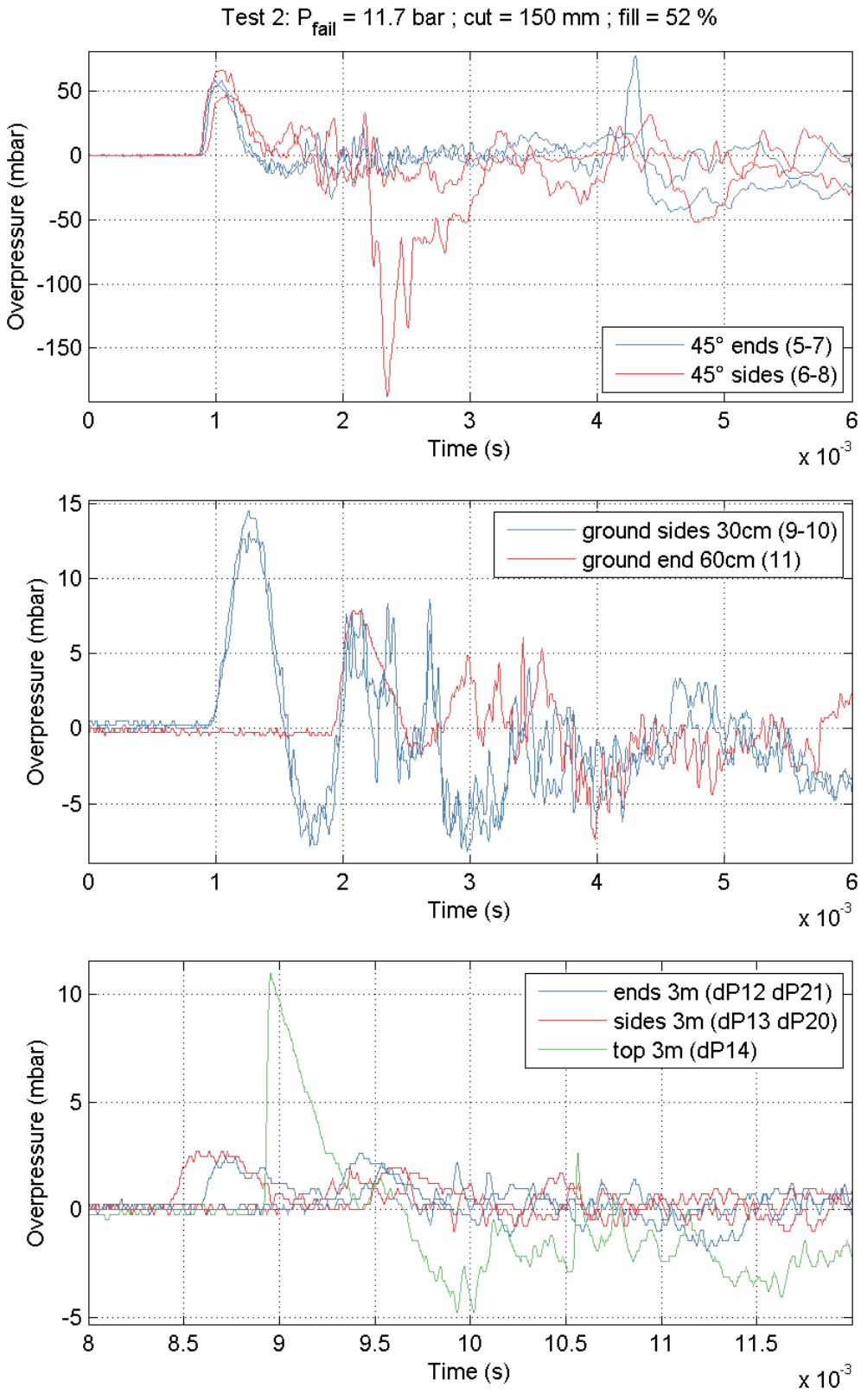
Test 2: P_fail = 11.7 bar ; cut = 150 mm ; fill = 52 %
Overpressure (mbar)
50
0
-50
-100
-150
0
1
2
3
4
5
6
Time (s)
x 10^-3
45° ends (5-7)
45° sides (6-8)
Overpressure (mbar)
15
10
5
0
-5
0
1
2
3
4
5
6
Time (s)
x 10^-3
ground sides 30cm (9-10)
ground end 60cm (11)
Overpressure (mbar)
10
5
0
-5
8
8.5
9
9.5
10
10.5
11
11.5
Time (s)
x 10^-3
ends 3m (dP12 dP21)
sides 3m (dP13 dP20)
top 3m (dP14)

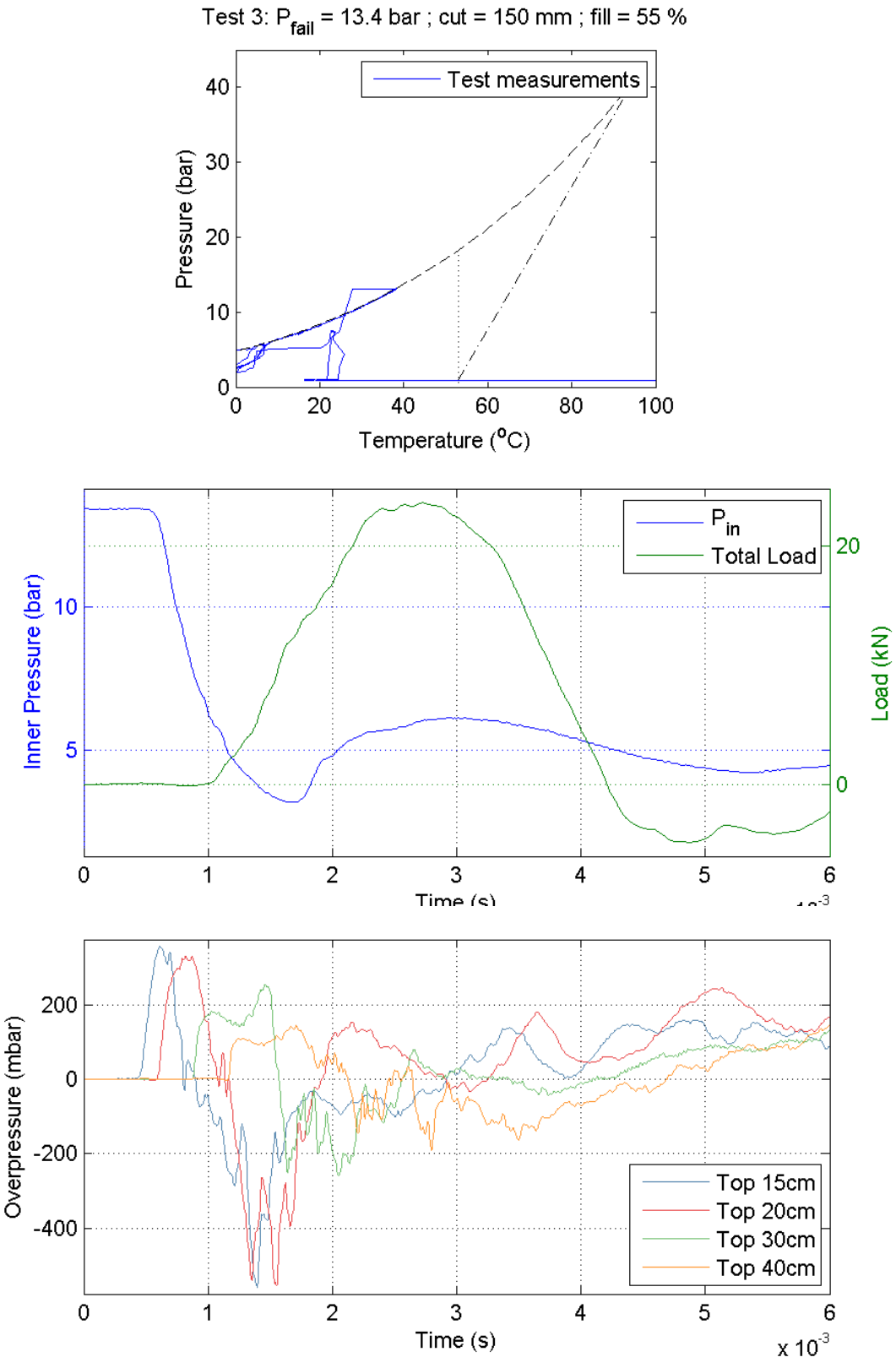
Test 3: P_fail = 13.4 bar ; cut = 150 mm ; fill = 55 %
Test measurements
Pressure (bar)
Temperature (°C)
P_in
Total Load
Inner Pressure (bar)
Load (kN)
Time (s)
Overpressure (mbar)
Top 15cm
Top 20cm
Top 30cm
Top 40cm
x 10^-3

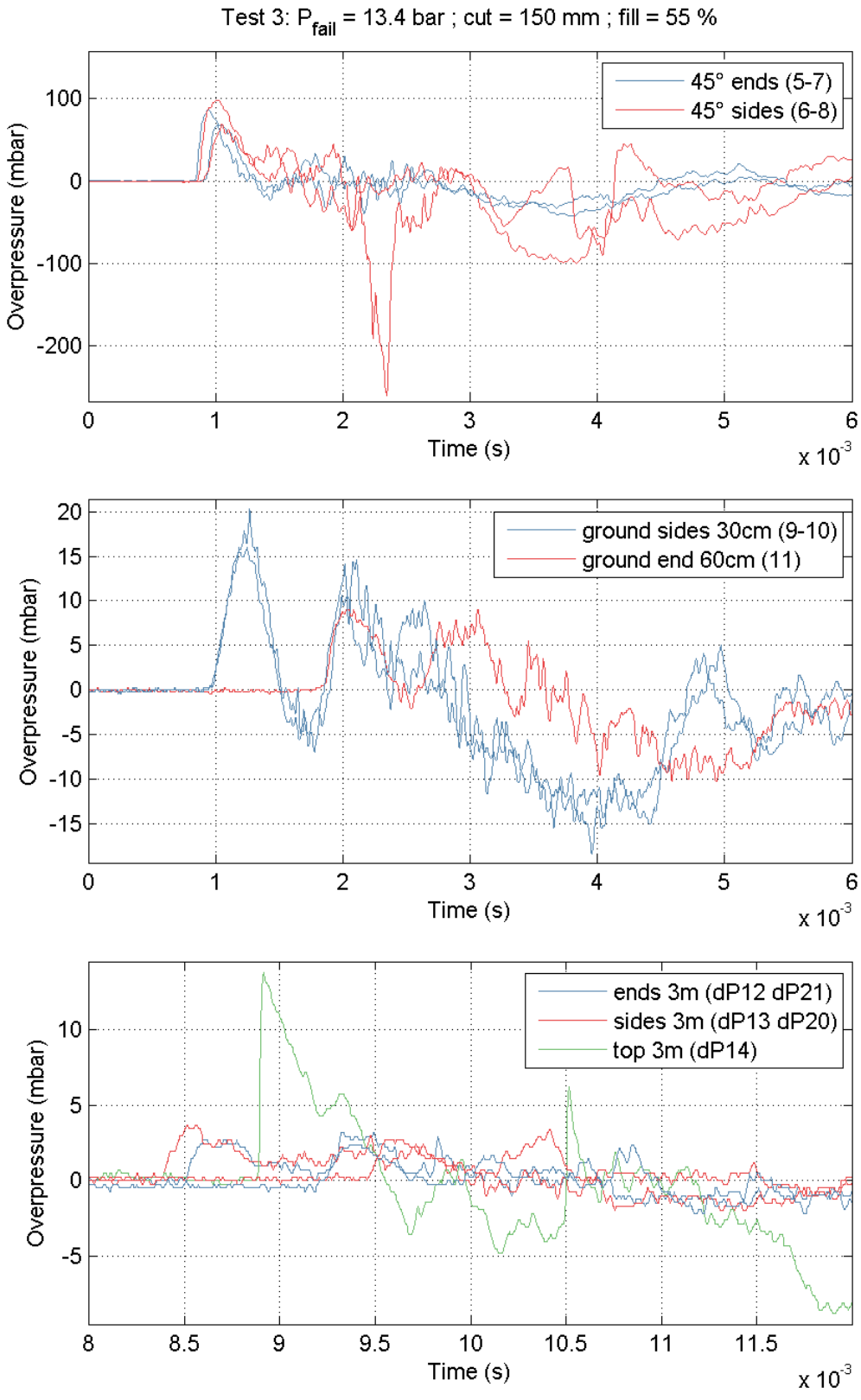
Test 3: P_fail = 13.4 bar ; cut = 150 mm ; fill = 55 %
45° ends (5-7)
45° sides (6-8)
Overpressure (mbar)
Time (s)
x 10^-3
ground sides 30cm (9-10)
ground end 60cm (11)
Overpressure (mbar)
Time (s)
x 10^-3
ends 3m (dP12 dP21)
sides 3m (dP13 dP20)
top 3m (dP14)
Overpressure (mbar)
Time (s)
x 10^-3

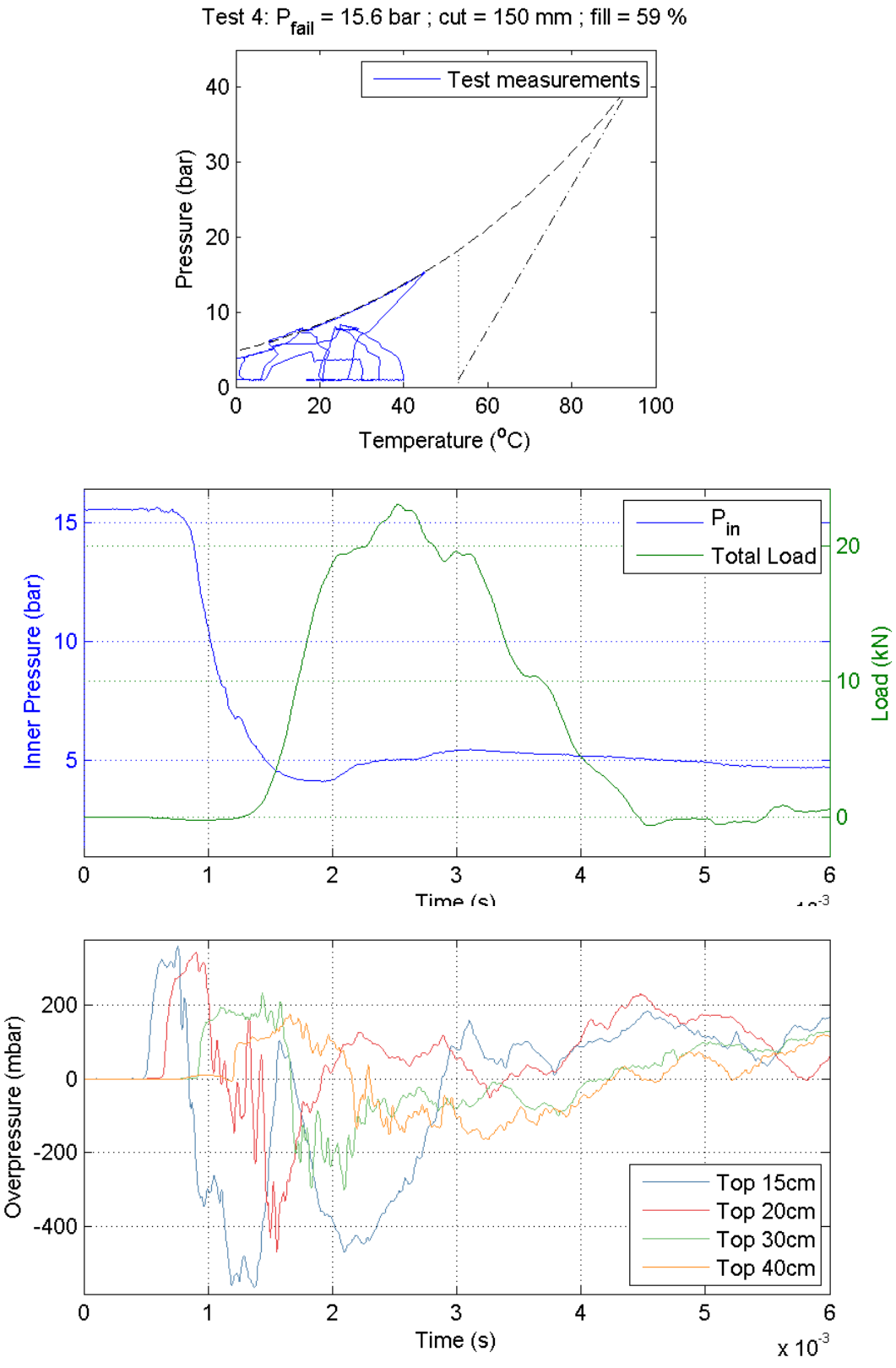
Test 4: P_fail = 15.6 bar ; cut = 150 mm ; fill = 59 %
Test measurements
Pressure (bar)
Temperature (°C)
P_in
Total Load
Inner Pressure (bar)
Load (kN)
Time (s)
x 10^-3
Overpressure (mbar)
Top 15cm
Top 20cm
Top 30cm
Top 40cm
Time (s)
x 10^-3

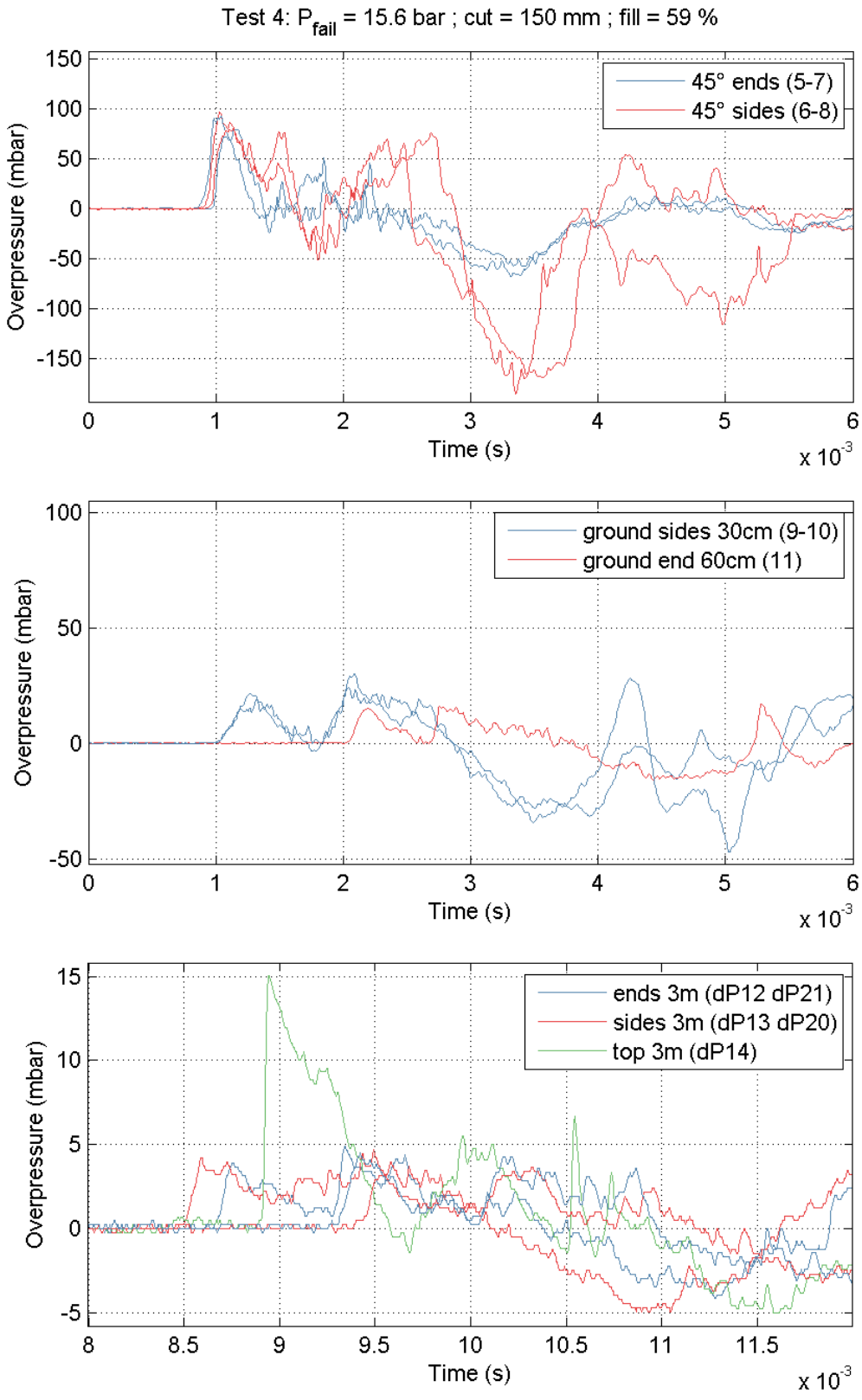
Test 4: P_fail = 15.6 bar ; cut = 150 mm ; fill = 59 %
45° ends (5-7)
45° sides (6-8)
Overpressure (mbar)
Time (s)
x 10^-3
ground sides 30cm (9-10)
ground end 60cm (11)
Overpressure (mbar)
Time (s)
x 10^-3
ends 3m (dP12 dP21)
sides 3m (dP13 dP20)
top 3m (dP14)
Overpressure (mbar)
Time (s)
x 10^-3

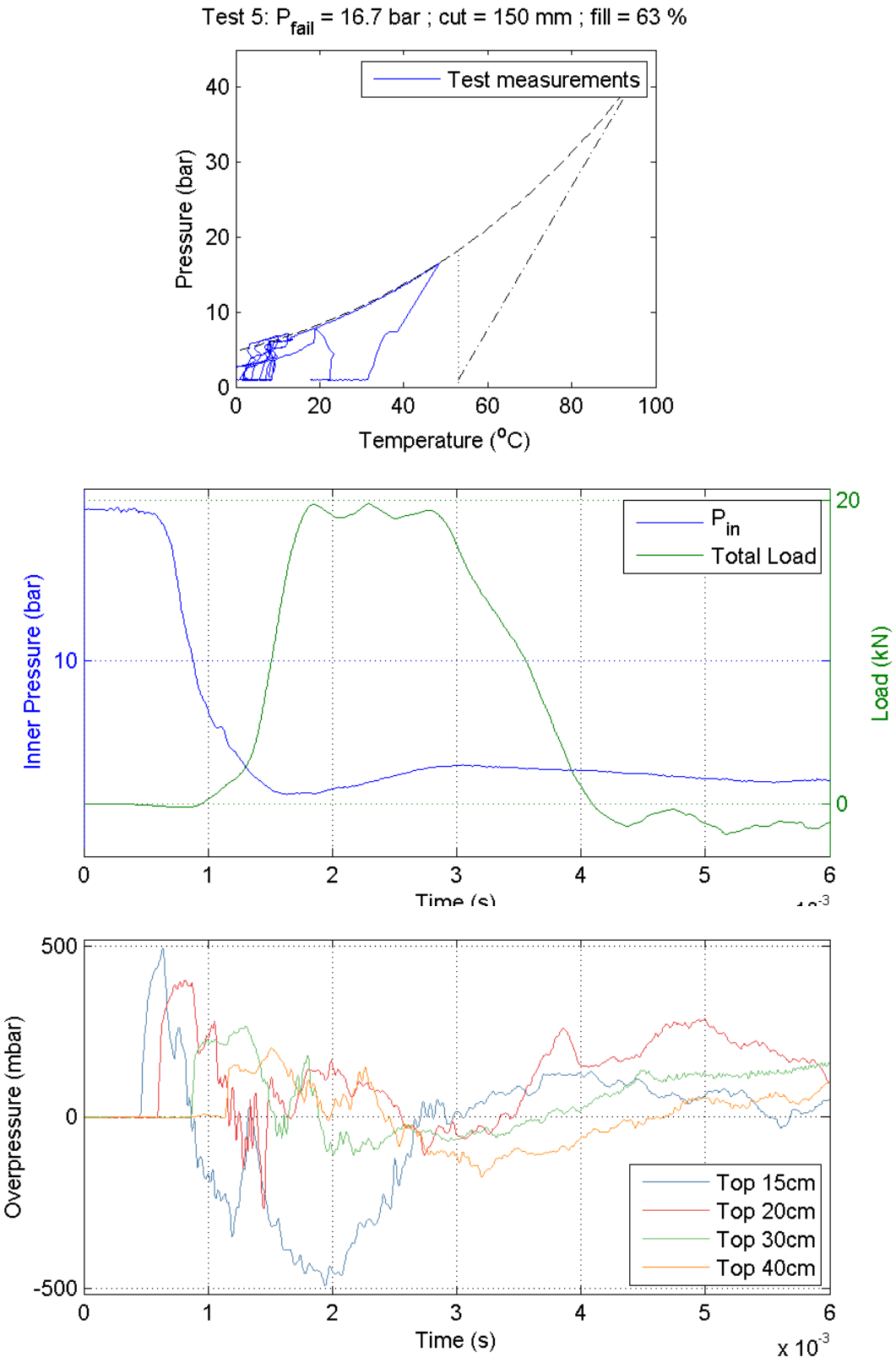
Test 5: P_fail = 16.7 bar ; cut = 150 mm ; fill = 63 %
Test measurements
Pressure (bar)
Temperature (°C)
P_in
Total Load
Inner Pressure (bar)
Load (kN)
Time (s)
x 10^-3
Overpressure (mbar)
Top 15cm
Top 20cm
Top 30cm
Top 40cm
Time (s)
x 10^-3

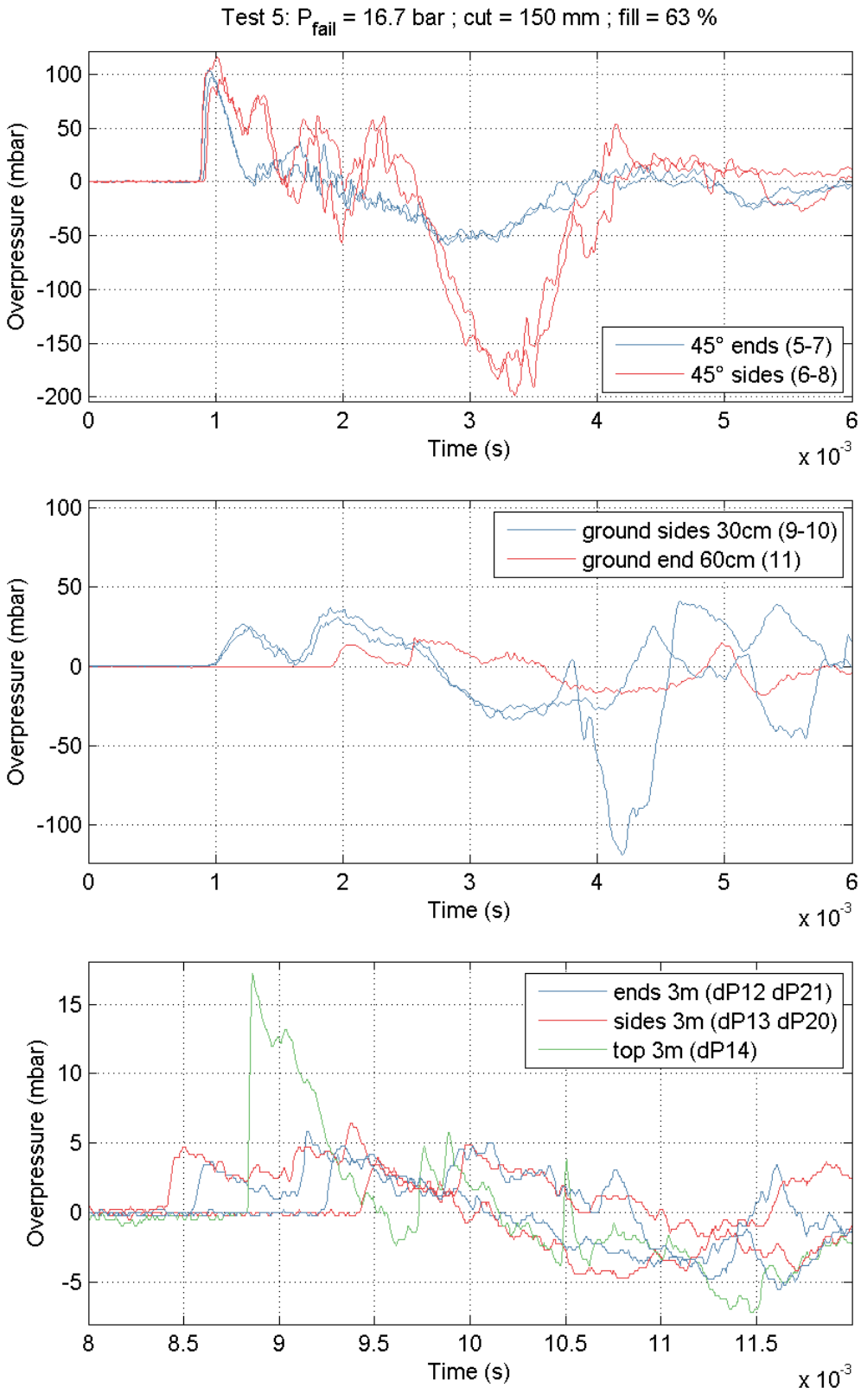
Test 5: P fail = 16.7 bar ; cut = 150 mm ; fill = 63 %
Overpressure (mbar)
Time (s)
x 10-3
45° ends (5-7)
45° sides (6-8)
ground sides 30cm (9-10)
ground end 60cm (11)
ends 3m (dP12 dP21)
sides 3m (dP13 dP20)
top 3m (dP14)

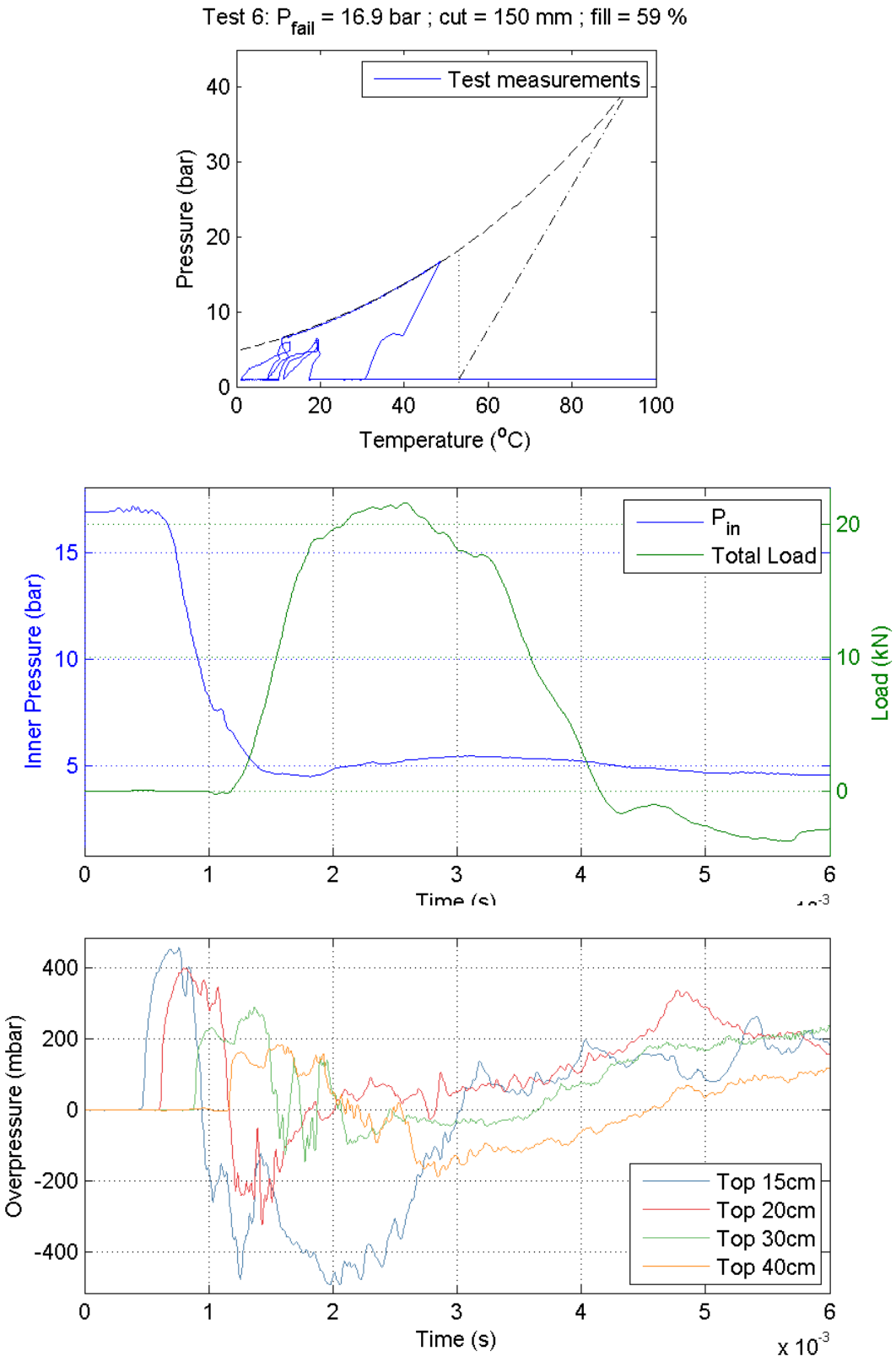
Test 6: P_fail = 16.9 bar ; cut = 150 mm ; fill = 59 %
Test measurements
Pressure (bar)
Temperature (°C)
P_in
Total Load
Inner Pressure (bar)
Load (kN)
Time (s)
x 10^-3
Overpressure (mbar)
Top 15cm
Top 20cm
Top 30cm
Top 40cm
Time (s)
x 10^-3

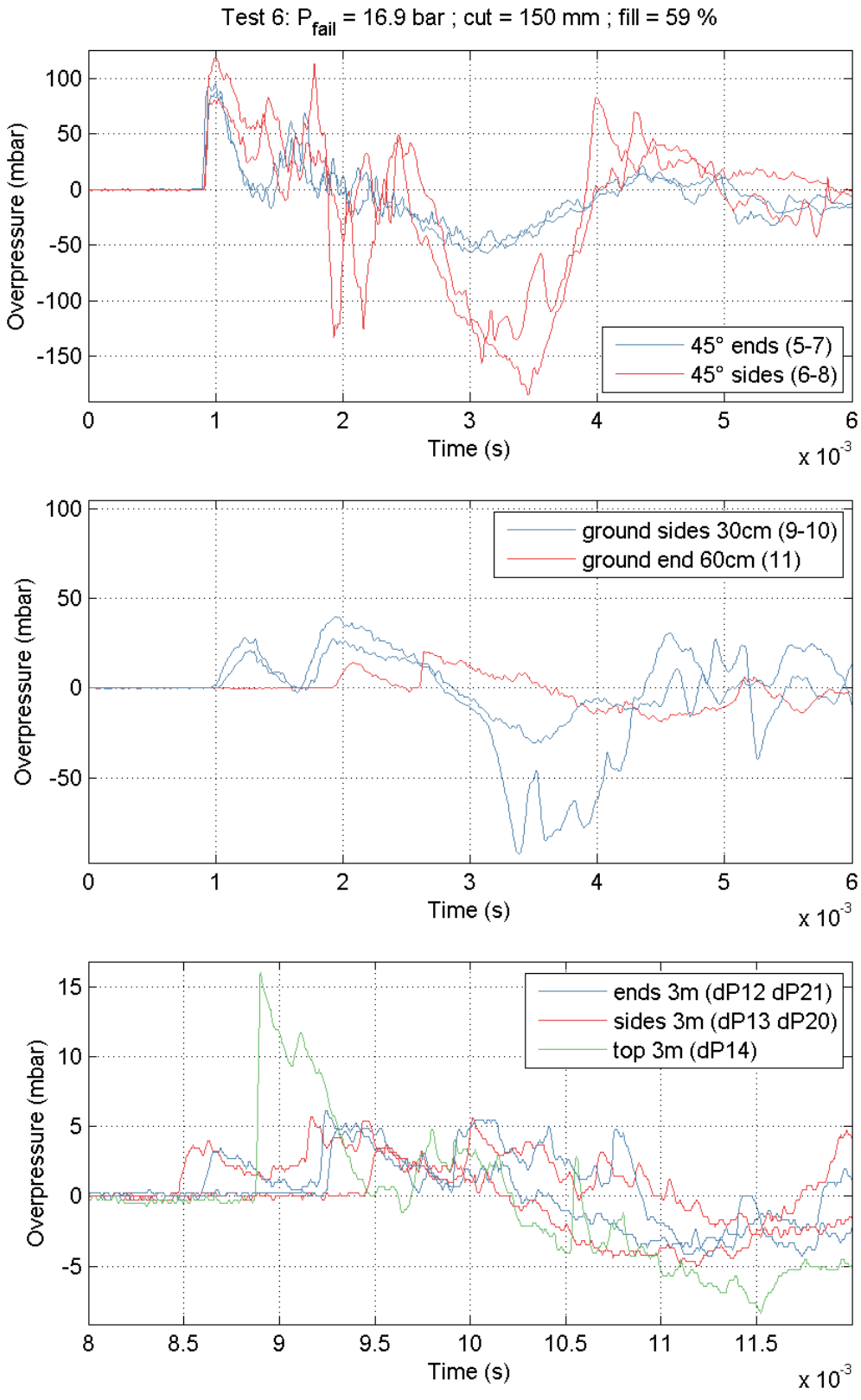
Test 6: P_fail = 16.9 bar ; cut = 150 mm ; fill = 59 %
Overpressure (mbar)
Time (s)
x 10^-3
45° ends (5-7)
45° sides (6-8)
ground sides 30cm (9-10)
ground end 60cm (11)
ends 3m (dP12 dP21)
sides 3m (dP13 dP20)
top 3m (dP14)

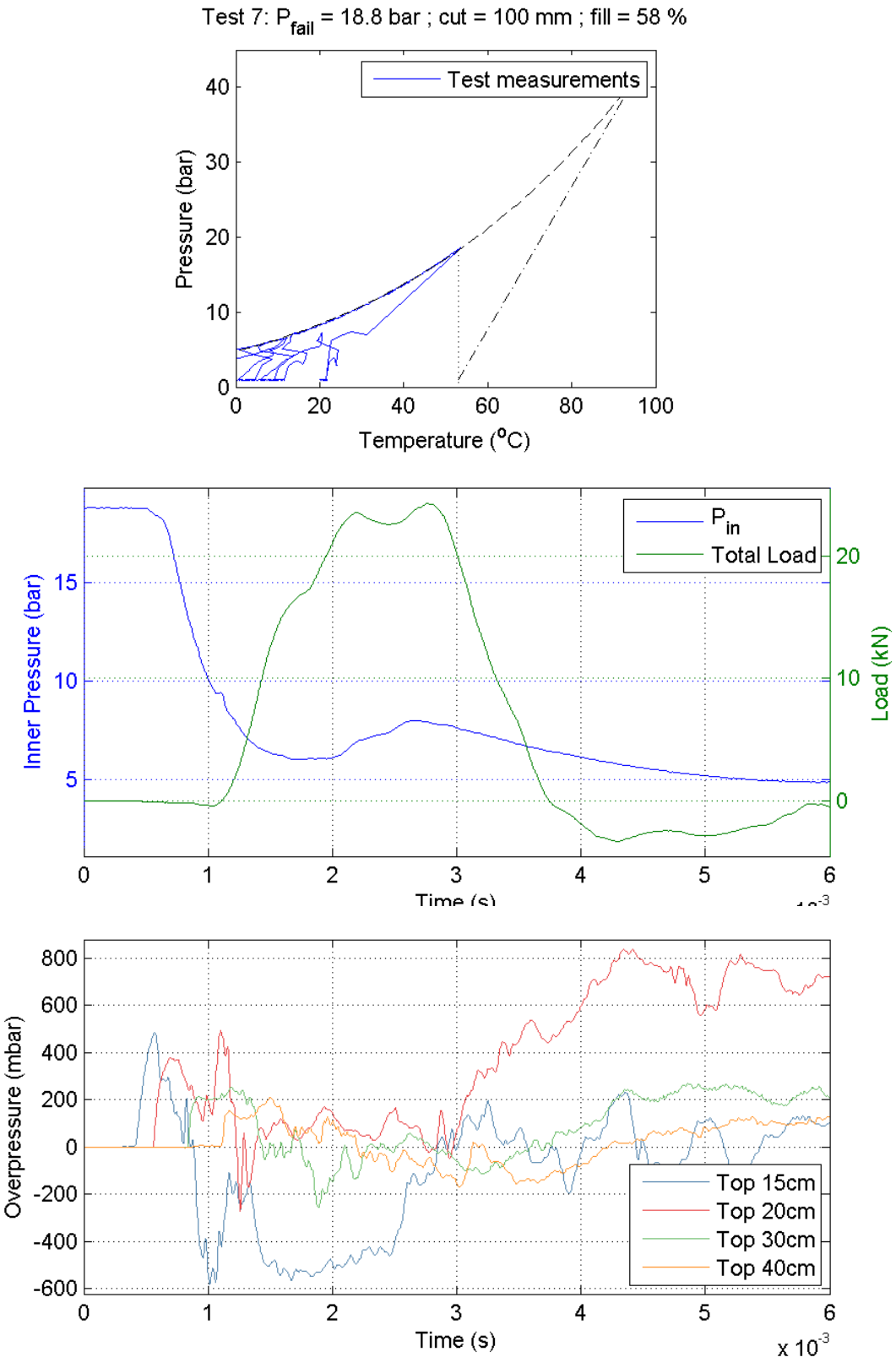
Test 7: P_fail = 18.8 bar ; cut = 100 mm ; fill = 58 %
Test measurements
Pressure (bar)
Temperature (°C)
P_in
Total Load
Inner Pressure (bar)
Load (kN)
Time (s)
x 10^-3
Overpressure (mbar)
Top 15cm
Top 20cm
Top 30cm
Top 40cm
Time (s)
x 10^-3

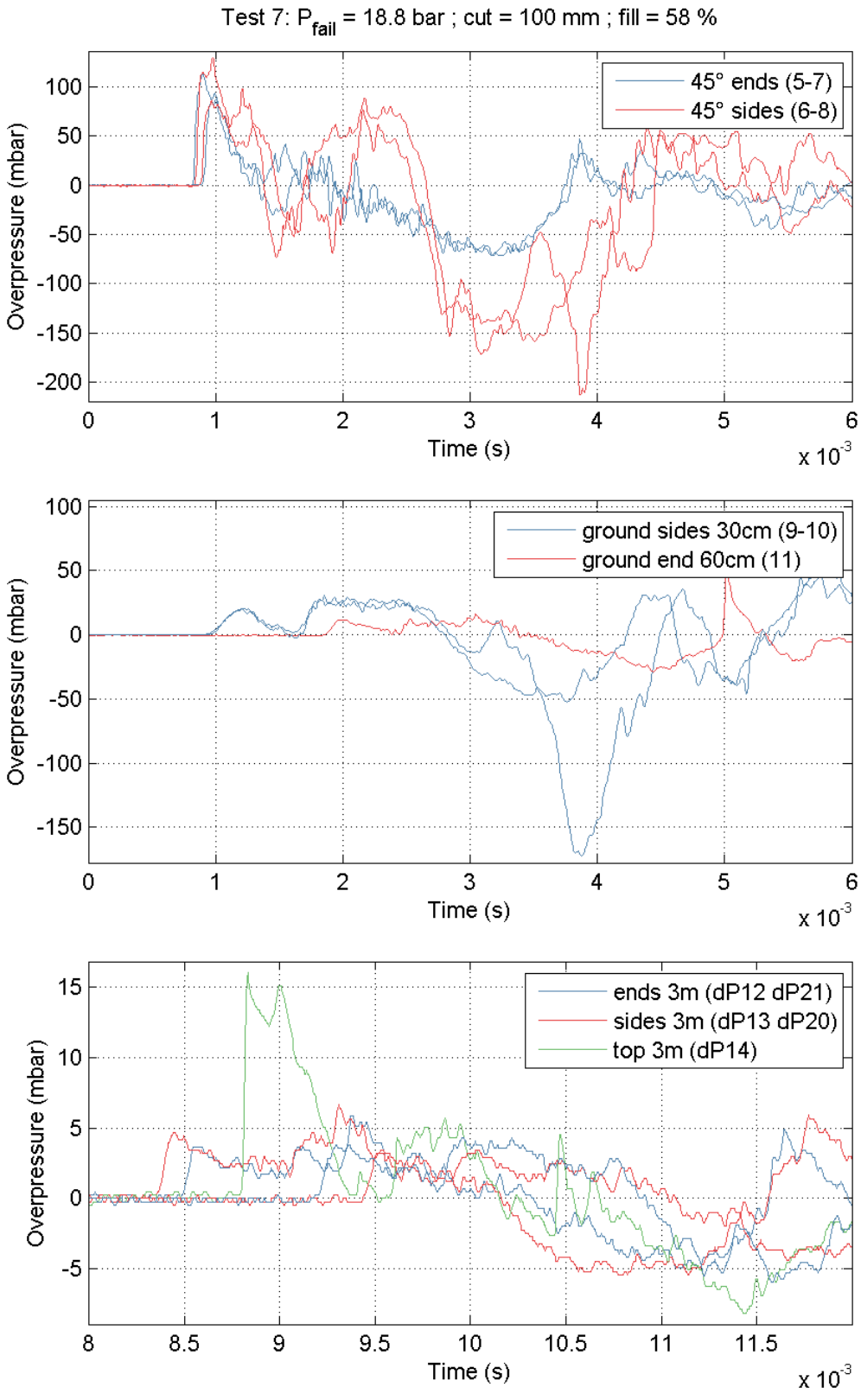
Test 7: P_fail = 18.8 bar ; cut = 100 mm ; fill = 58 %
45° ends (5-7)
45° sides (6-8)
Overpressure (mbar)
Time (s)
x 10^-3
ground sides 30cm (9-10)
ground end 60cm (11)
Overpressure (mbar)
Time (s)
x 10^-3
ends 3m (dP12 dP21)
sides 3m (dP13 dP20)
top 3m (dP14)
Overpressure (mbar)
Time (s)
x 10^-3

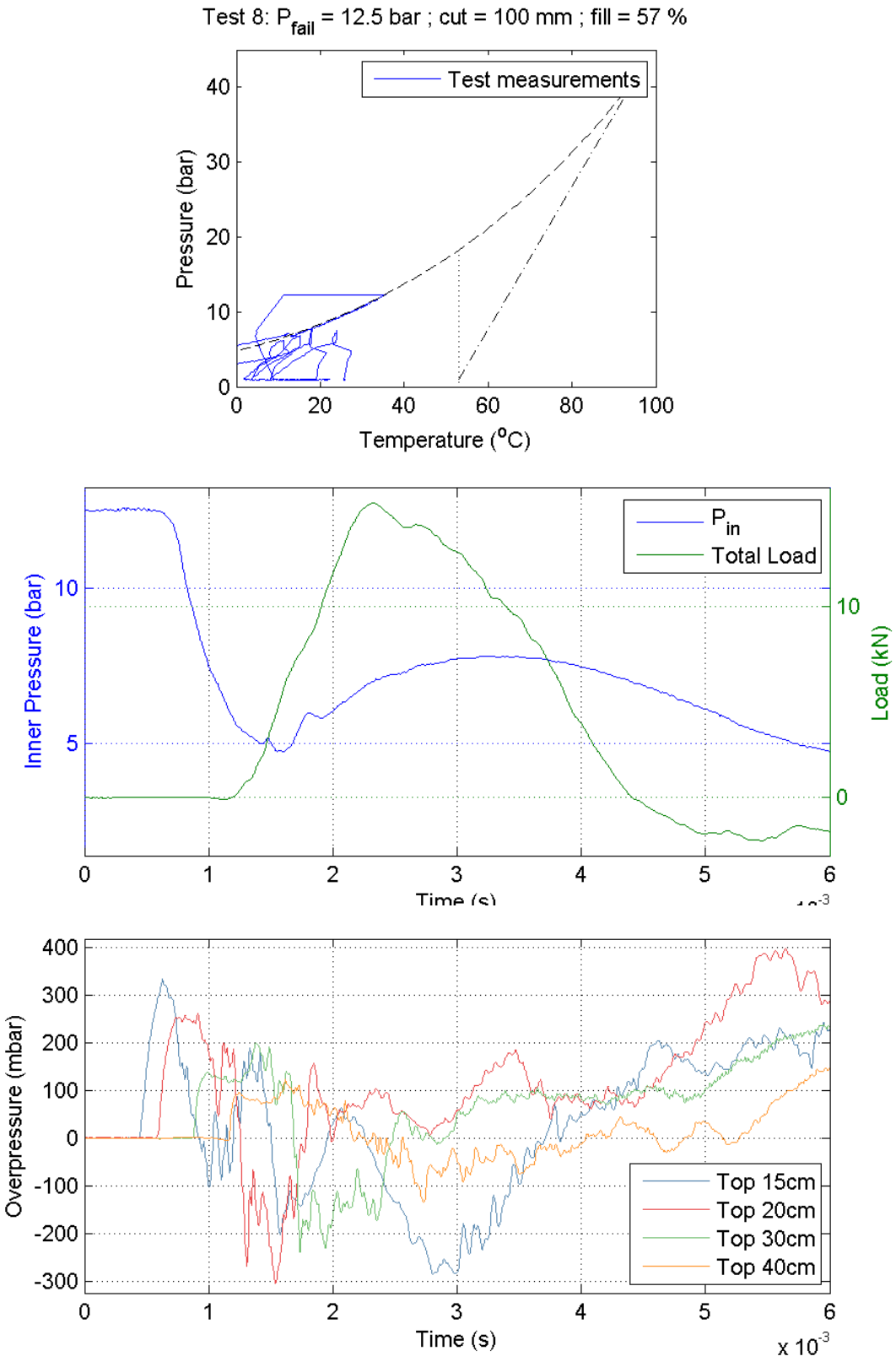
Test 8: P_fail = 12.5 bar ; cut = 100 mm ; fill = 57 %
Test measurements
Pressure (bar)
Temperature (°C)
P_in
Total Load
Inner Pressure (bar)
Load (kN)
Time (s)
x 10^-3
Overpressure (mbar)
Top 15cm
Top 20cm
Top 30cm
Top 40cm
Time (s)
x 10^-3

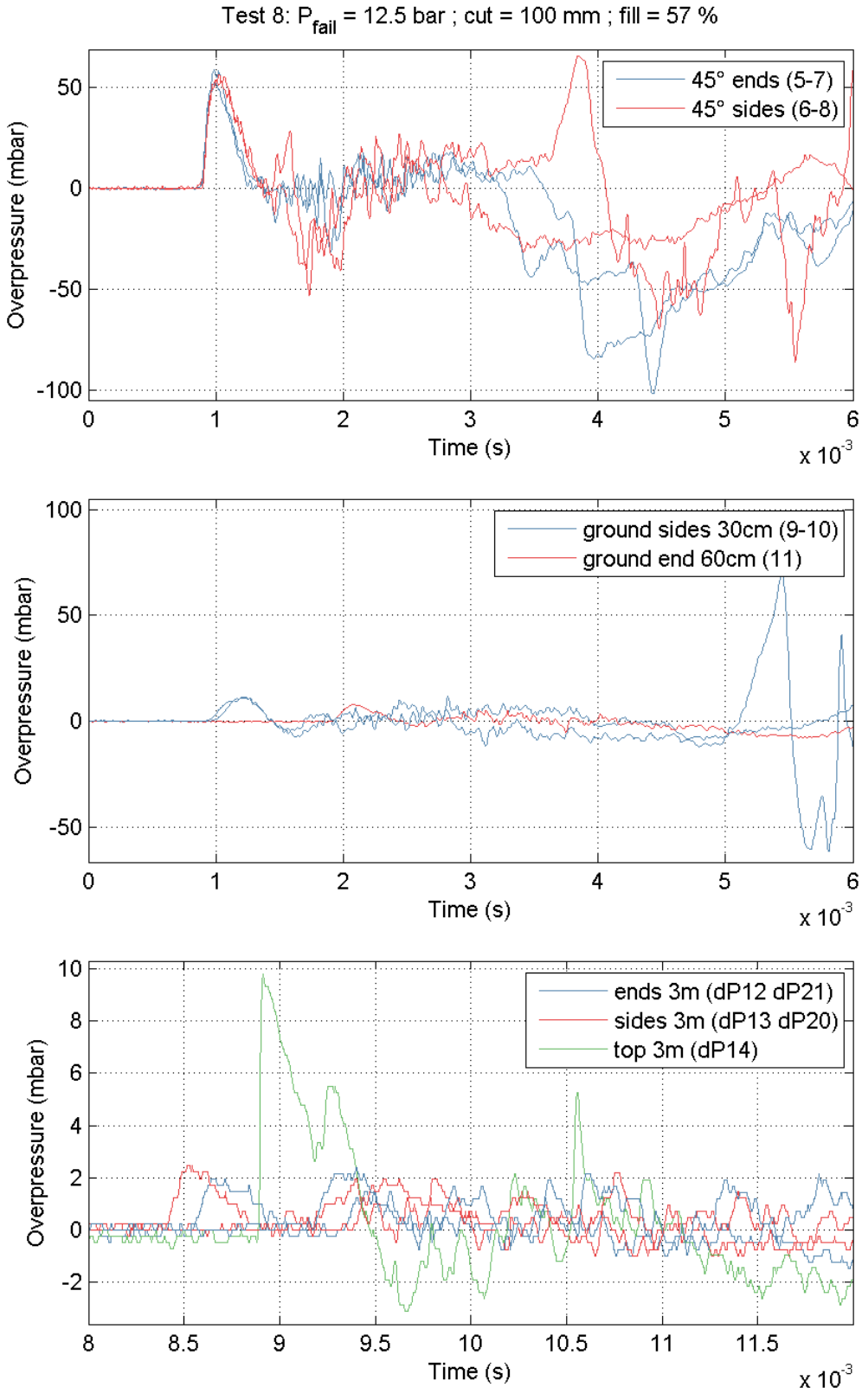
Test 8: P_fail = 12.5 bar ; cut = 100 mm ; fill = 57 %
45° ends (5-7)
45° sides (6-8)
Overpressure (mbar)
Time (s)
x 10^-3
ground sides 30cm (9-10)
ground end 60cm (11)
Overpressure (mbar)
Time (s)
x 10^-3
ends 3m (dP12 dP21)
sides 3m (dP13 dP20)
top 3m (dP14)
Overpressure (mbar)
Time (s)
x 10^-3

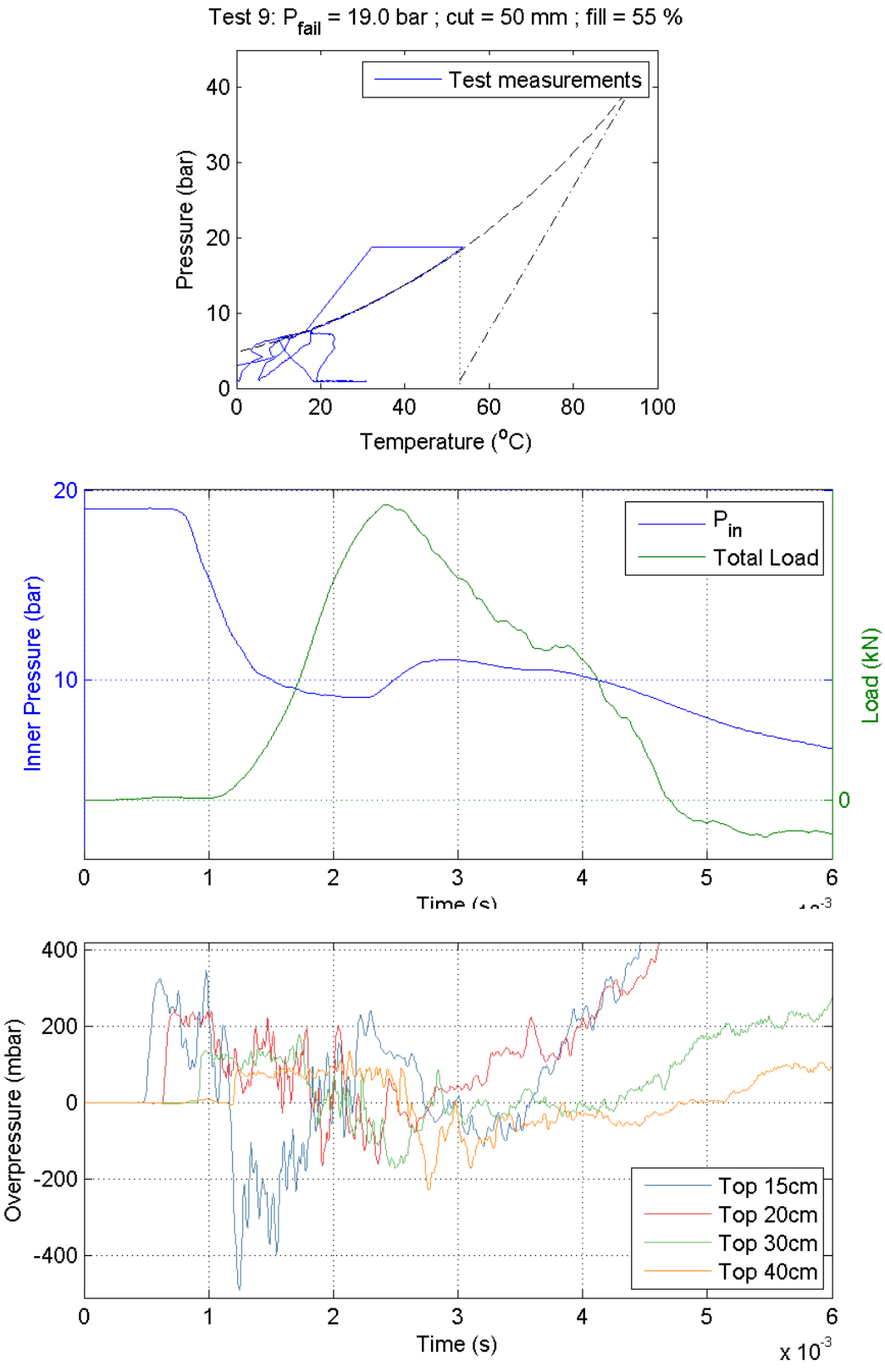
Test 9: P_fail = 19.0 bar ; cut = 50 mm ; fill = 55 %
Test measurements
Pressure (bar)
Temperature (°C)
P_in
Total Load
Inner Pressure (bar)
Load (kN)
Time (s)
x 10^-3
Overpressure (mbar)
Top 15cm
Top 20cm
Top 30cm
Top 40cm
Time (s)
x 10^-3

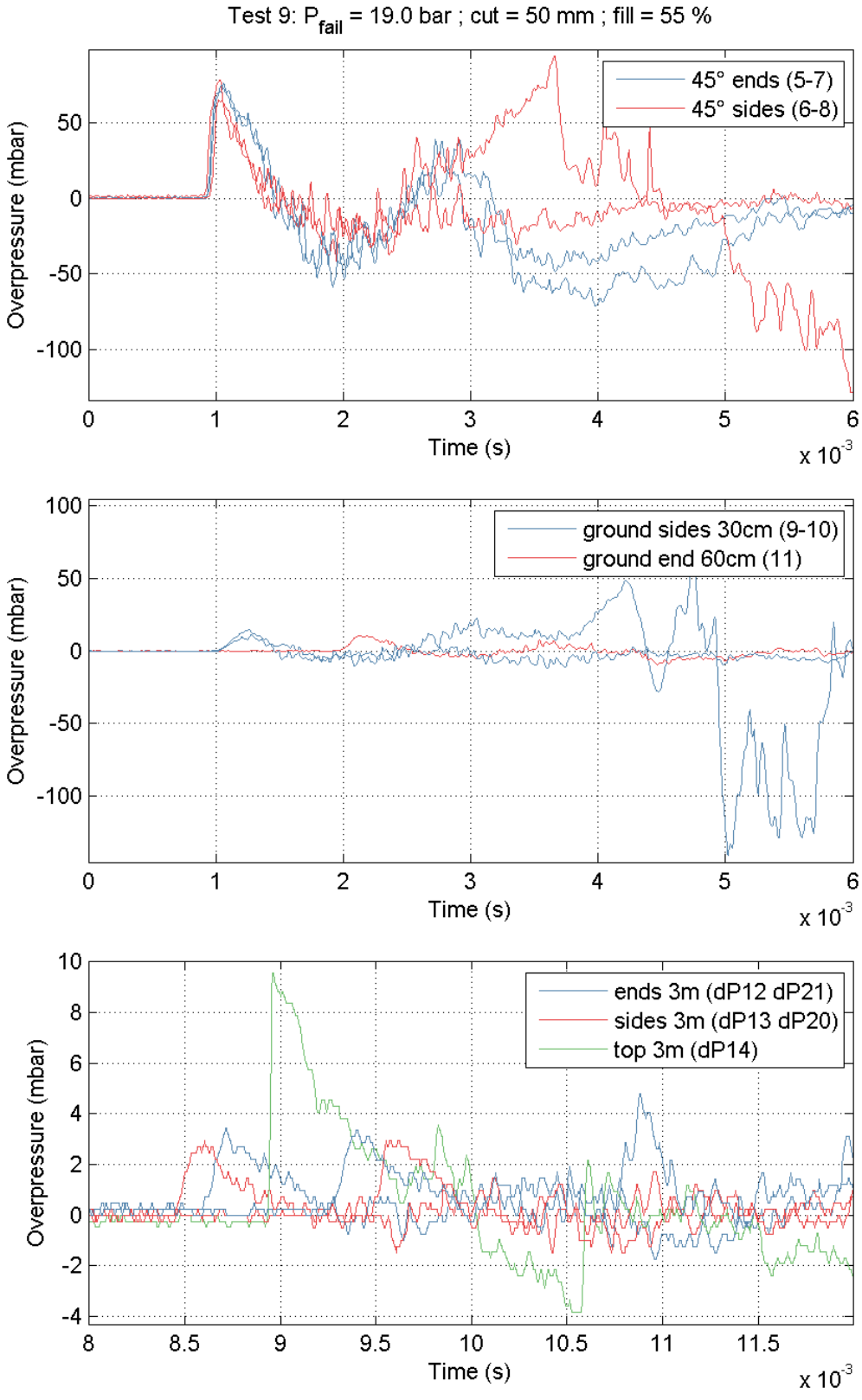
Test 9: P fail = 19.0 bar ; cut = 50 mm ; fill = 55 %
45° ends (5-7)
45° sides (6-8)
Overpressure (mbar)
Time (s)
x 10-3
ground sides 30cm (9-10)
ground end 60cm (11)
Overpressure (mbar)
Time (s)
x 10-3
ends 3m (dP12 dP21)
sides 3m (dP13 dP20)
top 3m (dP14)
Overpressure (mbar)
Time (s)
x 10-3

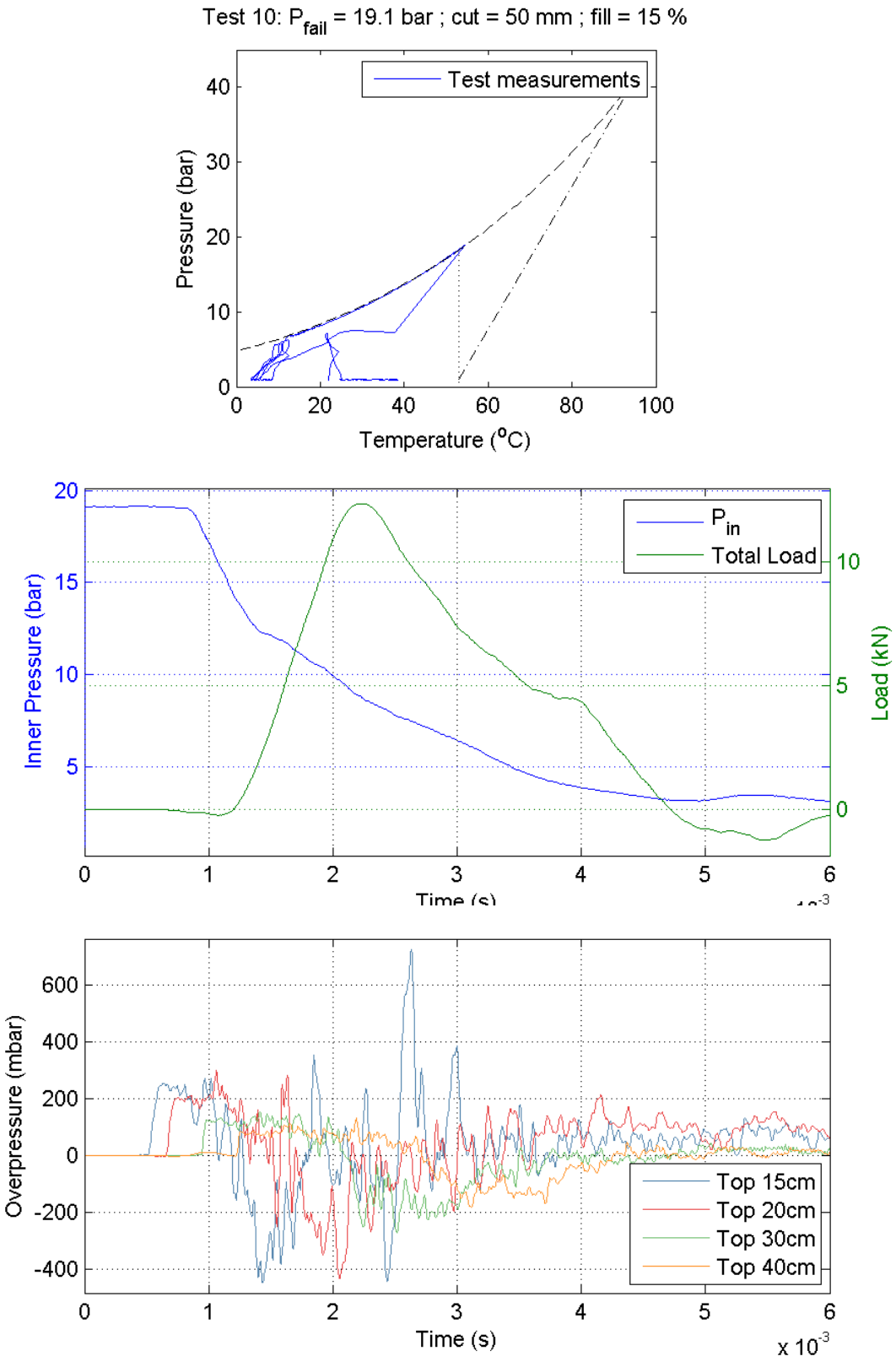
Test 10: P_fail = 19.1 bar ; cut = 50 mm ; fill = 15 %
Test measurements
Pressure (bar)
Temperature (°C)
P_in
Total Load
Inner Pressure (bar)
Load (kN)
Time (s)
x 10^-3
Overpressure (mbar)
Top 15cm
Top 20cm
Top 30cm
Top 40cm
Time (s)
x 10^-3

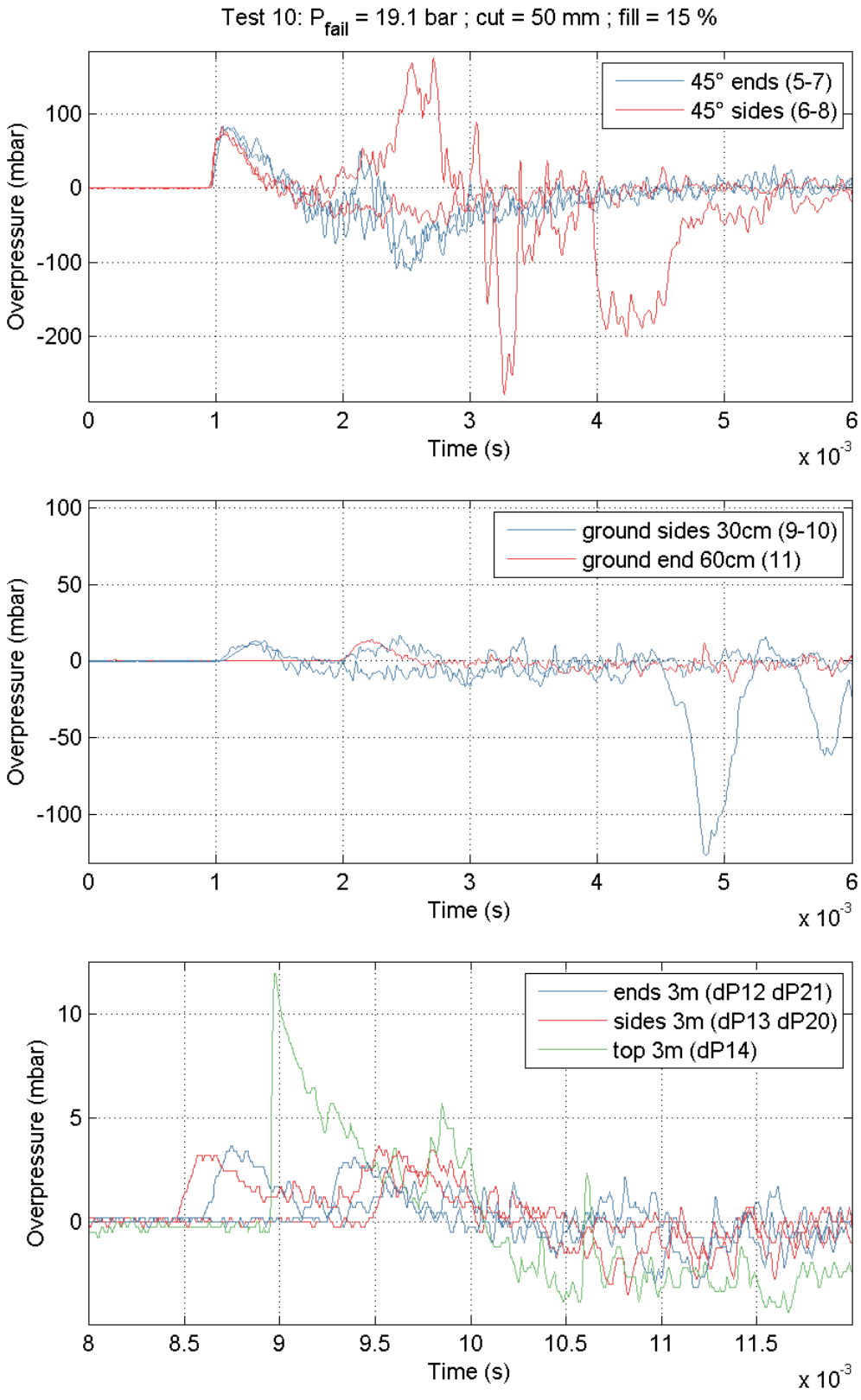
Test 10: P fail = 19.1 bar ; cut = 50 mm ; fill = 15 %
45° ends (5-7)
45° sides (6-8)
Overpressure (mbar)
Time (s)
x 10-3
ground sides 30cm (9-10)
ground end 60cm (11)
Overpressure (mbar)
Time (s)
x 10-3
ends 3m (dP12 dP21)
sides 3m (dP13 dP20)
top 3m (dP14)
Overpressure (mbar)
Time (s)
x 10-3

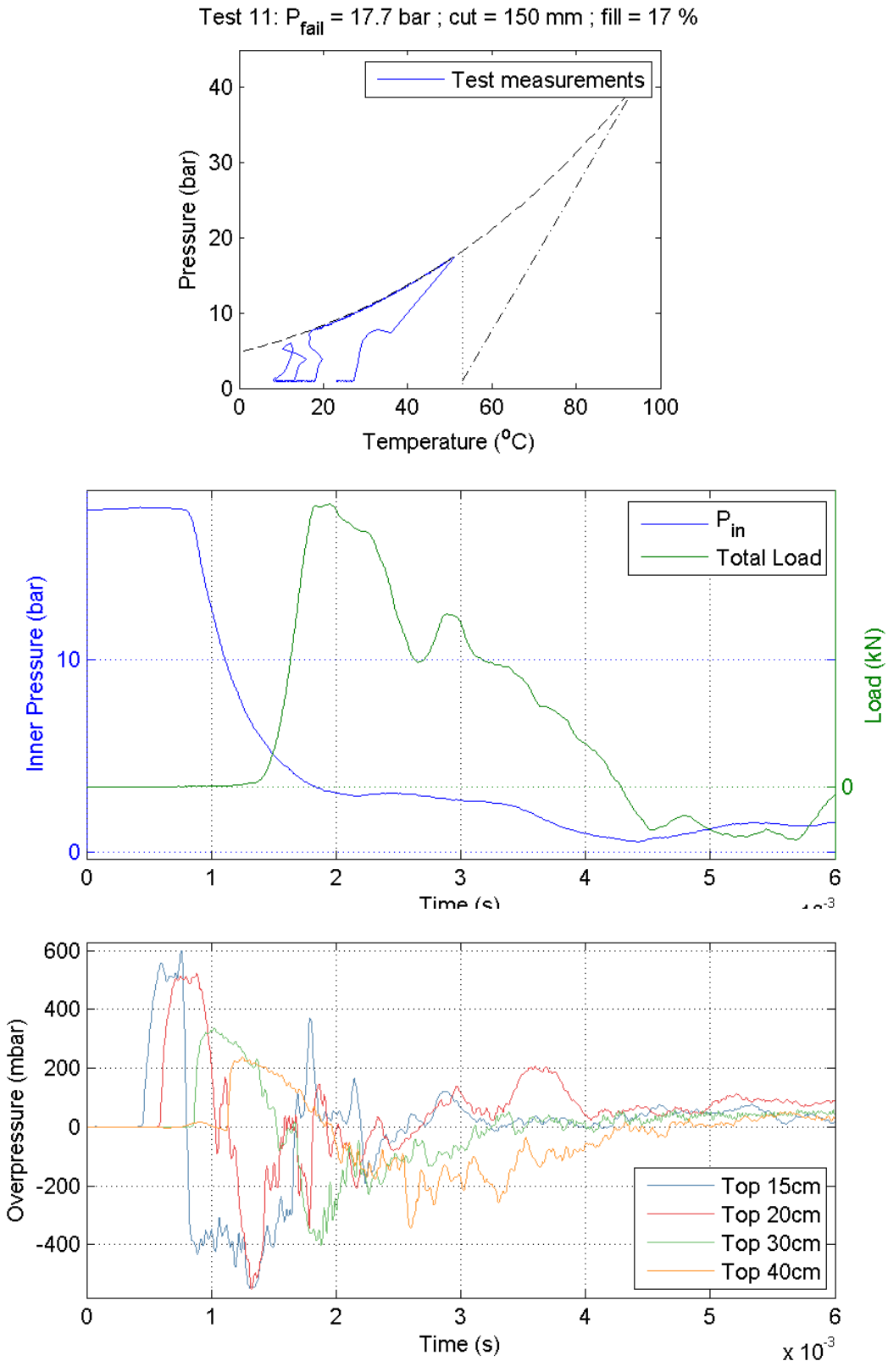
Test 11: P_fail = 17.7 bar ; cut = 150 mm ; fill = 17 %
Test measurements
Pressure (bar)
Temperature (°C)
P_in
Total Load
Inner Pressure (bar)
Load (kN)
Time (s)
x 10^-3
Overpressure (mbar)
Top 15cm
Top 20cm
Top 30cm
Top 40cm
Time (s)
x 10^-3

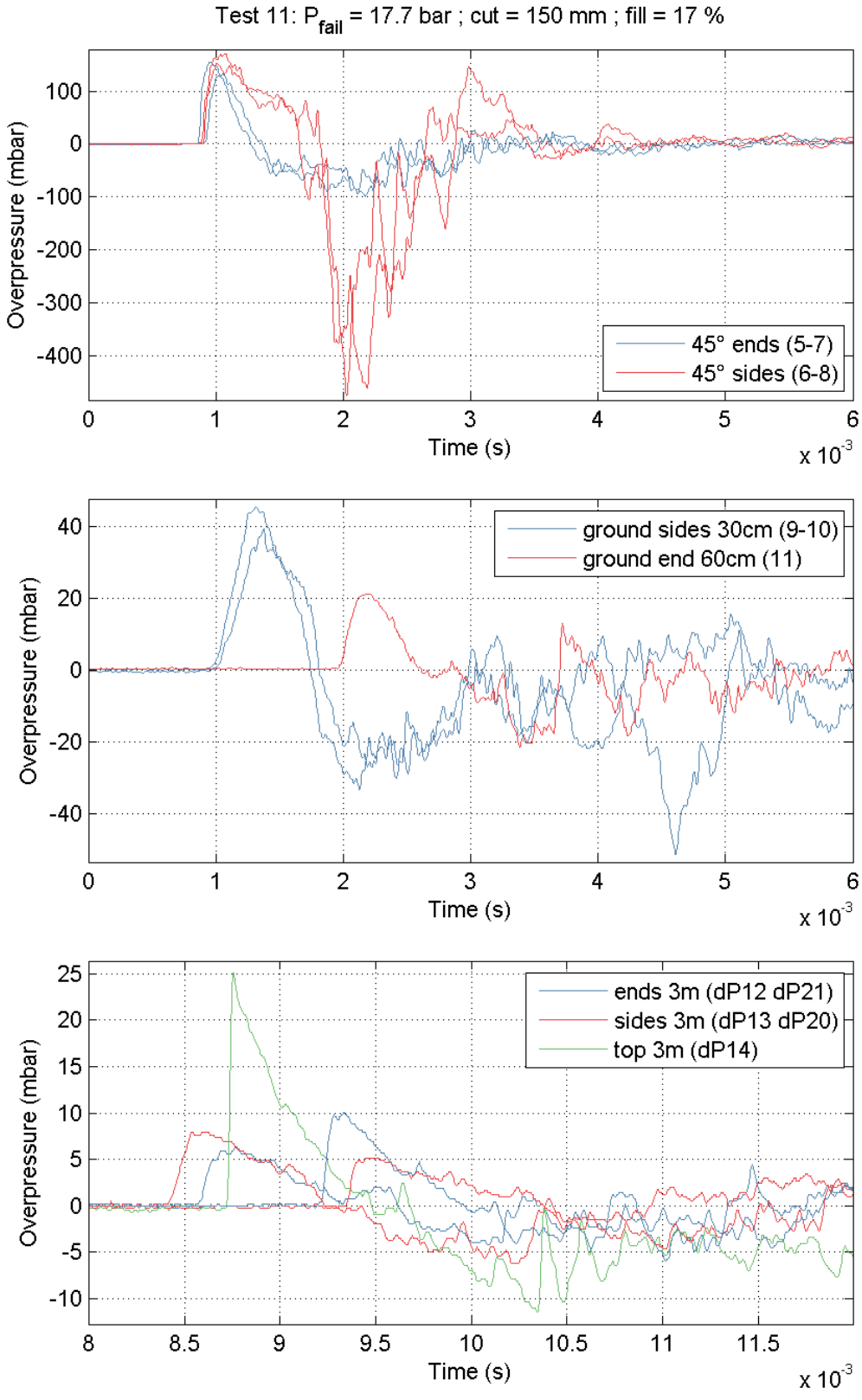
Test 11: P fail = 17.7 bar ; cut = 150 mm ; fill = 17 %
Overpressure (mbar)
Time (s)
x 10-3
45° ends (5-7)
45° sides (6-8)
ground sides 30cm (9-10)
ground end 60cm (11)
ends 3m (dP12 dP21)
sides 3m (dP13 dP20)
top 3m (dP14)

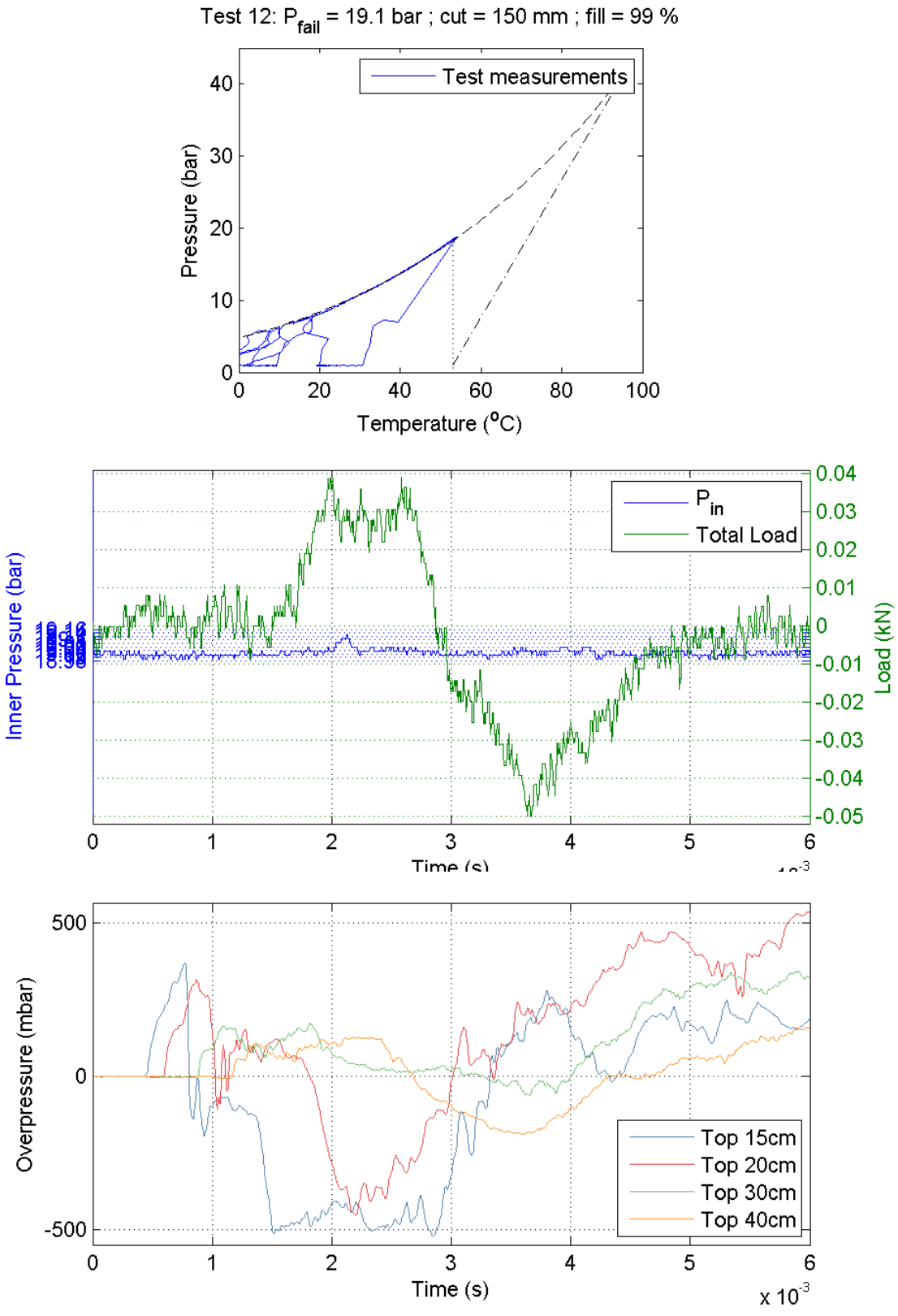
Test 12: P_fail = 19.1 bar ; cut = 150 mm ; fill = 99 %
Test measurements
Pressure (bar)
Temperature (°C)
P_in
Total Load
Inner Pressure (bar)
Load (kN)
Time (s)
x 10^-3
Overpressure (mbar)
Top 15cm
Top 20cm
Top 30cm
Top 40cm
Time (s)
x 10^-3

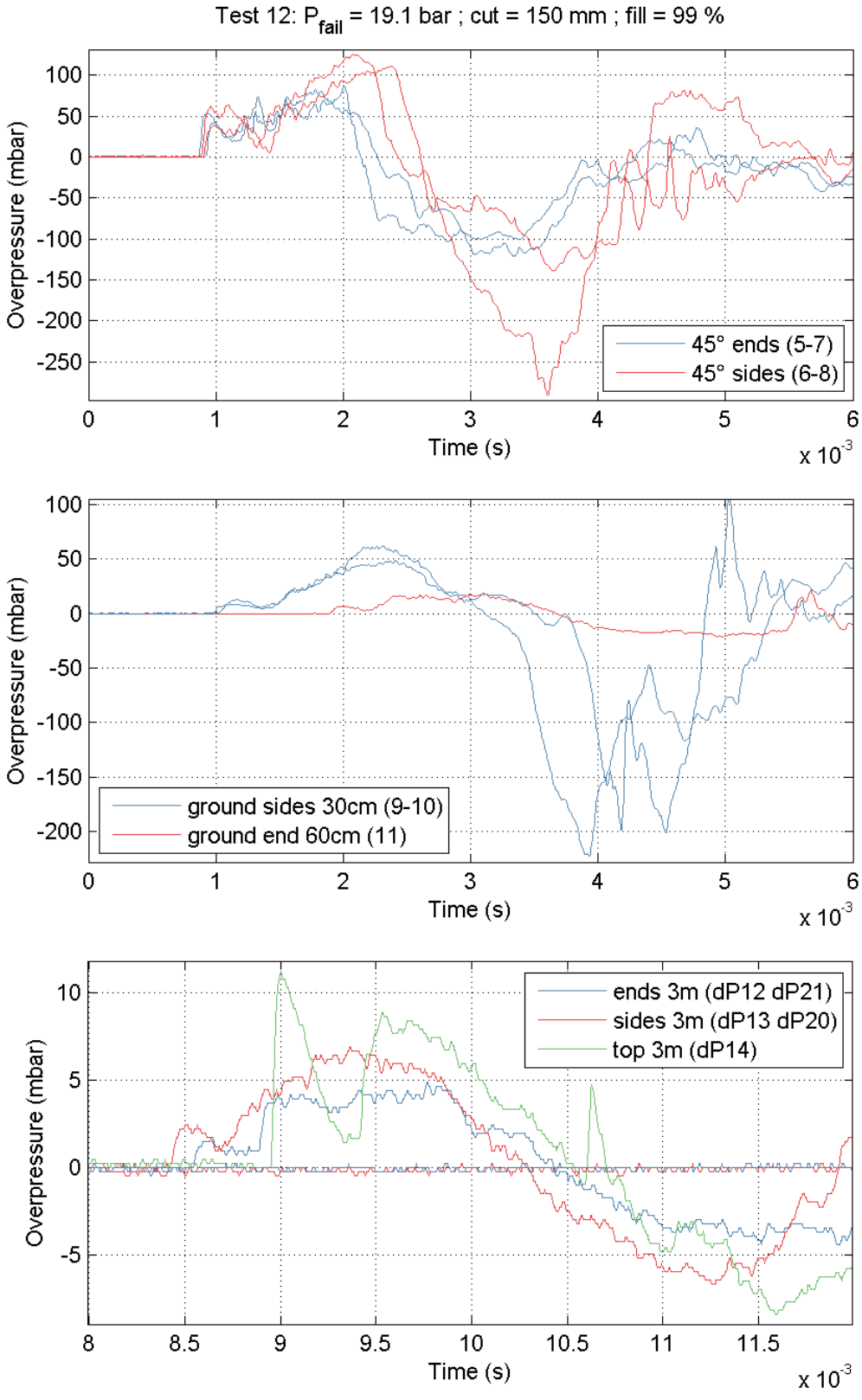
Test 12: P fail = 19.1 bar ; cut = 150 mm ; fill = 99 %
Overpressure (mbar)
Time (s)
x 10-3
45° ends (5-7)
45° sides (6-8)
ground sides 30cm (9-10)
ground end 60cm (11)
ends 3m (dP12 dP21)
sides 3m (dP13 dP20)
top 3m (dP14)

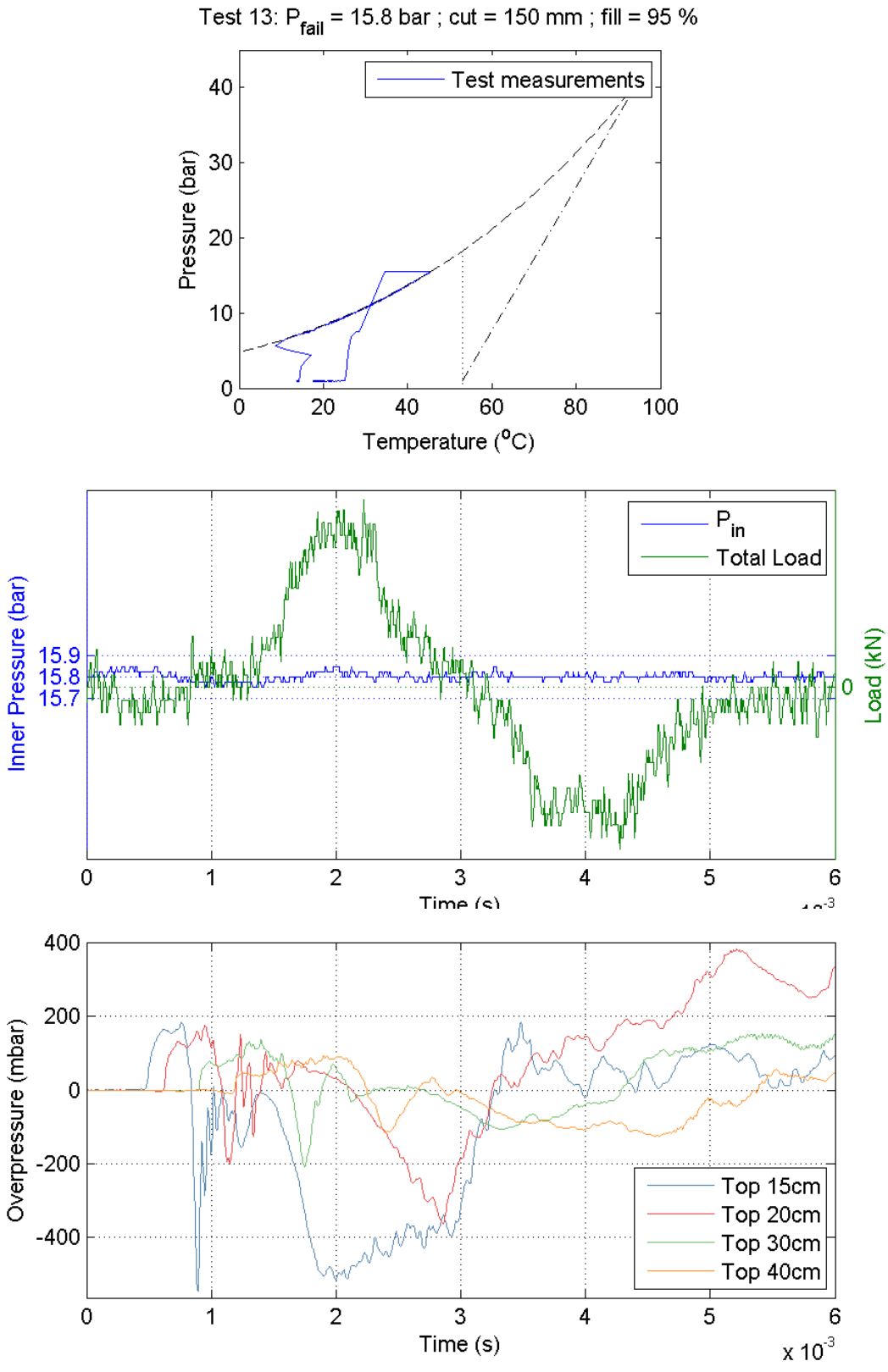
Test 13: P_fail = 15.8 bar ; cut = 150 mm ; fill = 95 %
Test measurements
Pressure (bar)
Temperature (°C)
P_in
Total Load
Inner Pressure (bar)
Load (kN)
15.9
15.8
15.7
Time (s)
Overpressure (mbar)
Top 15cm
Top 20cm
Top 30cm
Top 40cm
x 10^-3

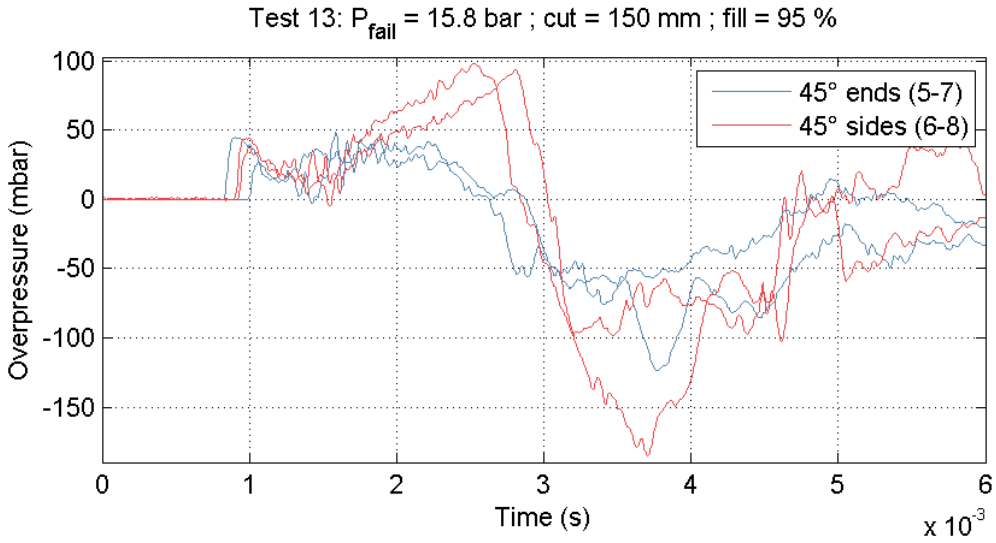
Test 13: P fail = 15.8 bar ; cut = 150 mm ; fill = 95 %
45° ends (5-7)
45° sides (6-8)
Overpressure (mbar)
Time (s)
x 10-3

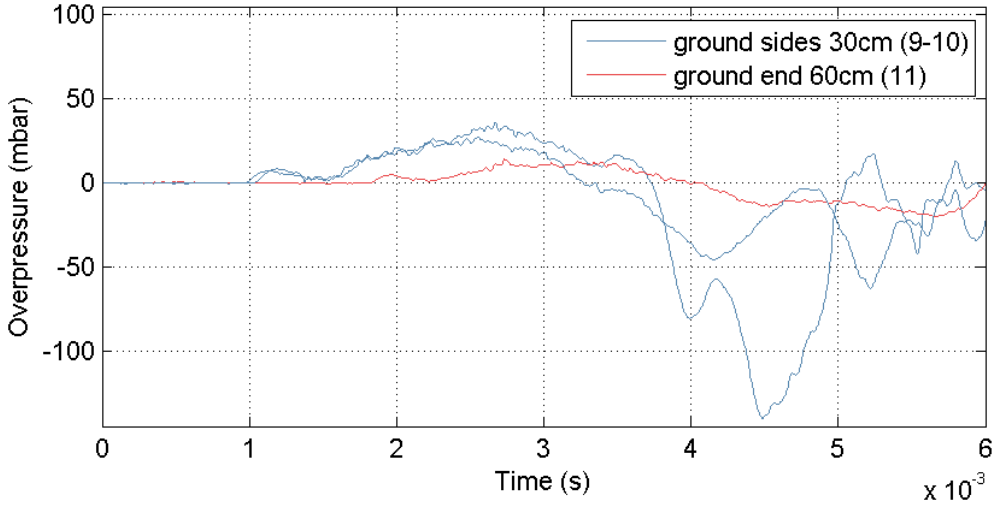
ground sides 30cm (9-10)
ground end 60cm (11)
Overpressure (mbar)
Time (s)
x 10-3

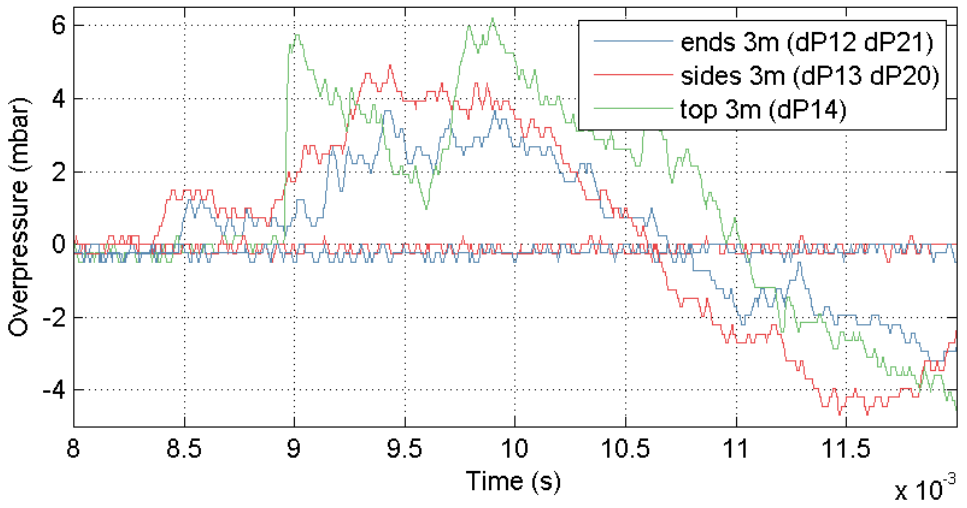
ends 3m (dP12 dP21)
sides 3m (dP13 dP20)
top 3m (dP14)
Overpressure (mbar)
Time (s)
x 10-3

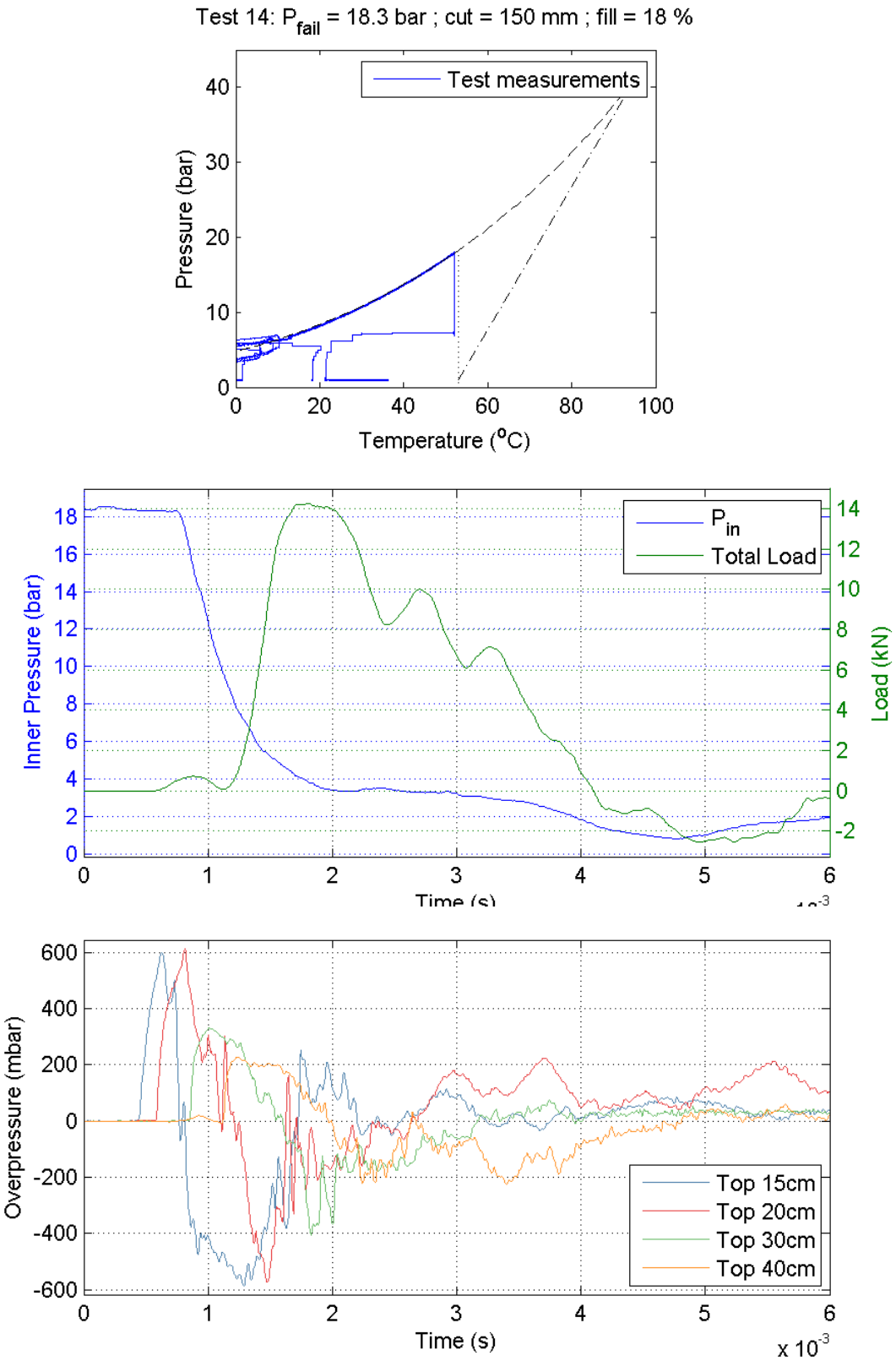
Test 14: P_fail = 18.3 bar ; cut = 150 mm ; fill = 18 %
Test measurements
Pressure (bar)
Temperature (°C)
P_in
Total Load
Inner Pressure (bar)
Load (kN)
Time (s)
Overpressure (mbar)
Top 15cm
Top 20cm
Top 30cm
Top 40cm
Time (s)
x 10^-3

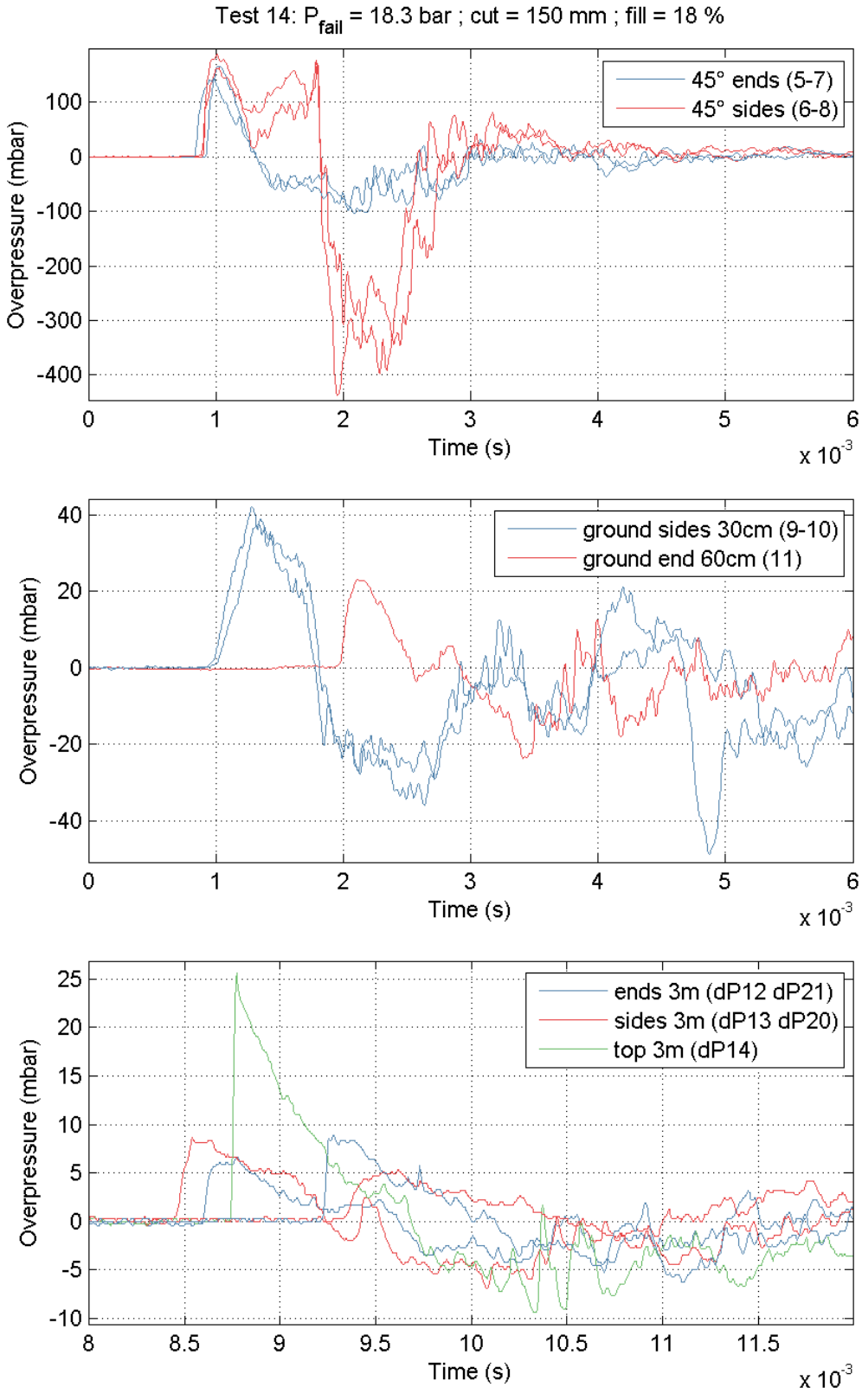
Test 14: P fail = 18.3 bar ; cut = 150 mm ; fill = 18 %
45° ends (5-7)
45° sides (6-8)
Overpressure (mbar)
Time (s)
x 10-3
ground sides 30cm (9-10)
ground end 60cm (11)
Overpressure (mbar)
Time (s)
x 10-3
ends 3m (dP12 dP21)
sides 3m (dP13 dP20)
top 3m (dP14)
Overpressure (mbar)
Time (s)
x 10-3

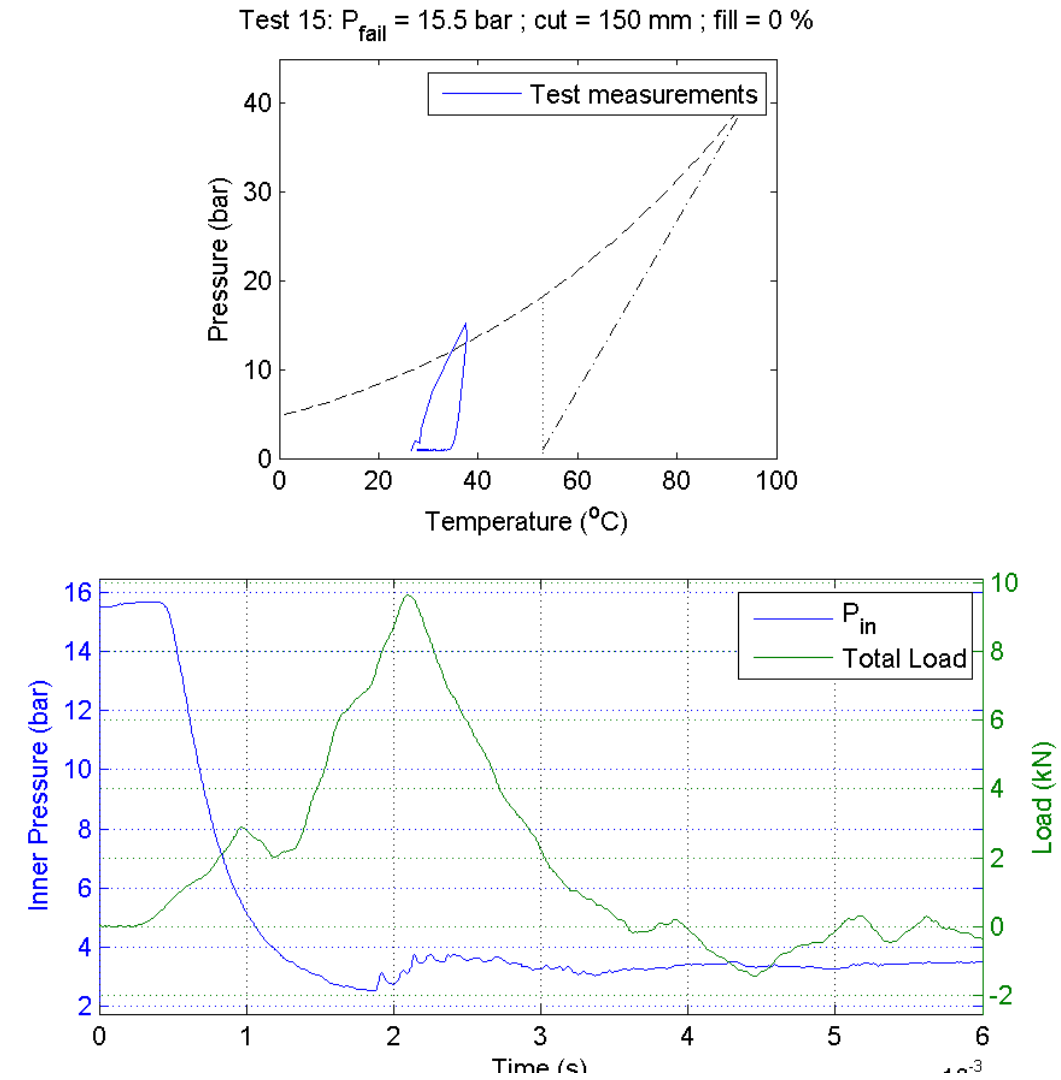
Test 15: P_fail = 15.5 bar ; cut = 150 mm ; fill = 0 %
Test measurements
Pressure (bar)
Temperature (°C)
P_in
Total Load
Inner Pressure (bar)
Load (kN)
Time (s)
Top 15cm
Top 20cm
Top 30cm
Top 40cm
Overpressure (mbar)
Time (s)
x 10^-3

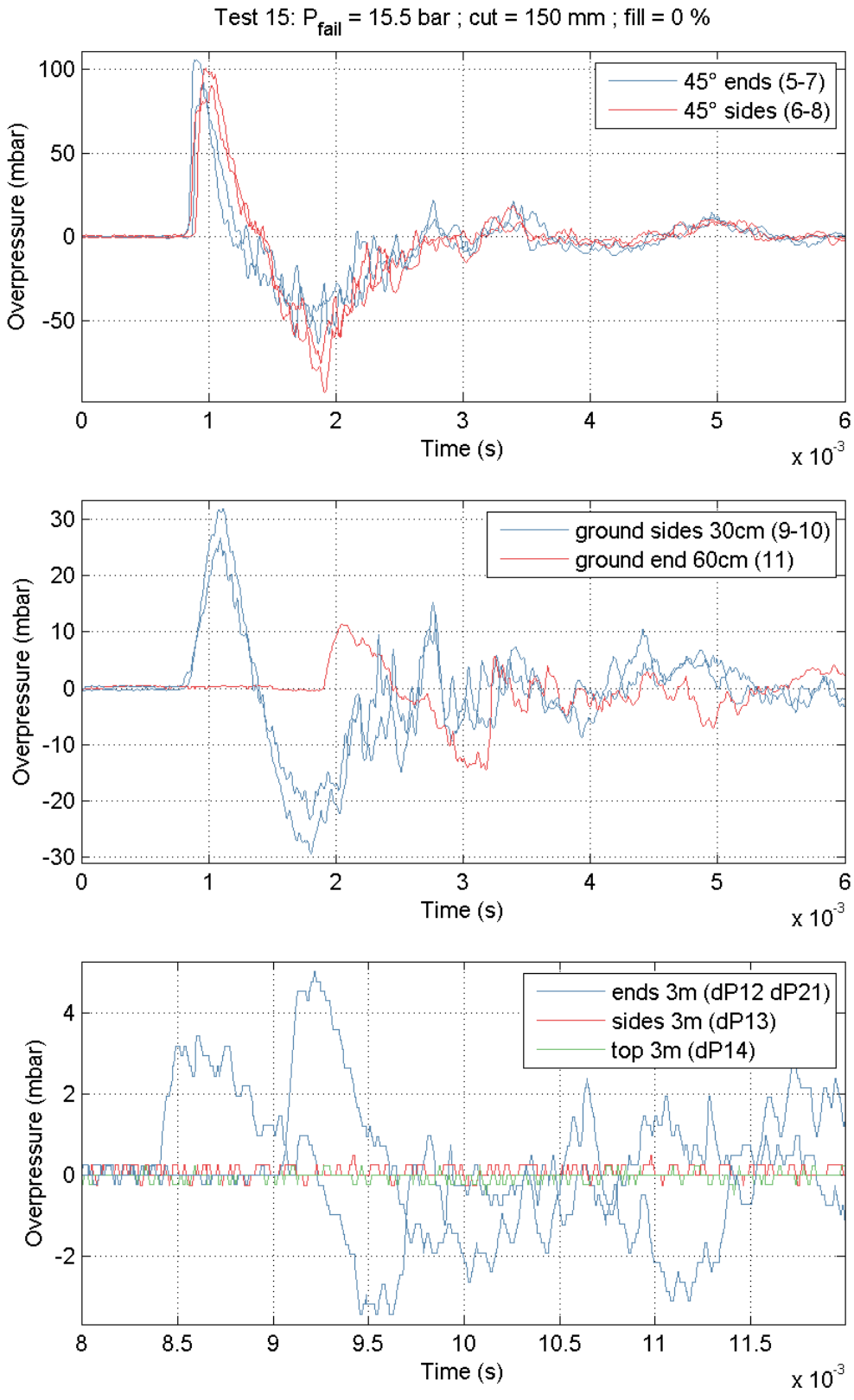
Test 15: P_fail = 15.5 bar ; cut = 150 mm ; fill = 0 %
45° ends (5-7)
45° sides (6-8)
Overpressure (mbar)
Time (s)
x 10^-3
ground sides 30cm (9-10)
ground end 60cm (11)
Overpressure (mbar)
Time (s)
x 10^-3
ends 3m (dP12 dP21)
sides 3m (dP13)
top 3m (dP14)
Overpressure (mbar)
Time (s)
x 10^-3

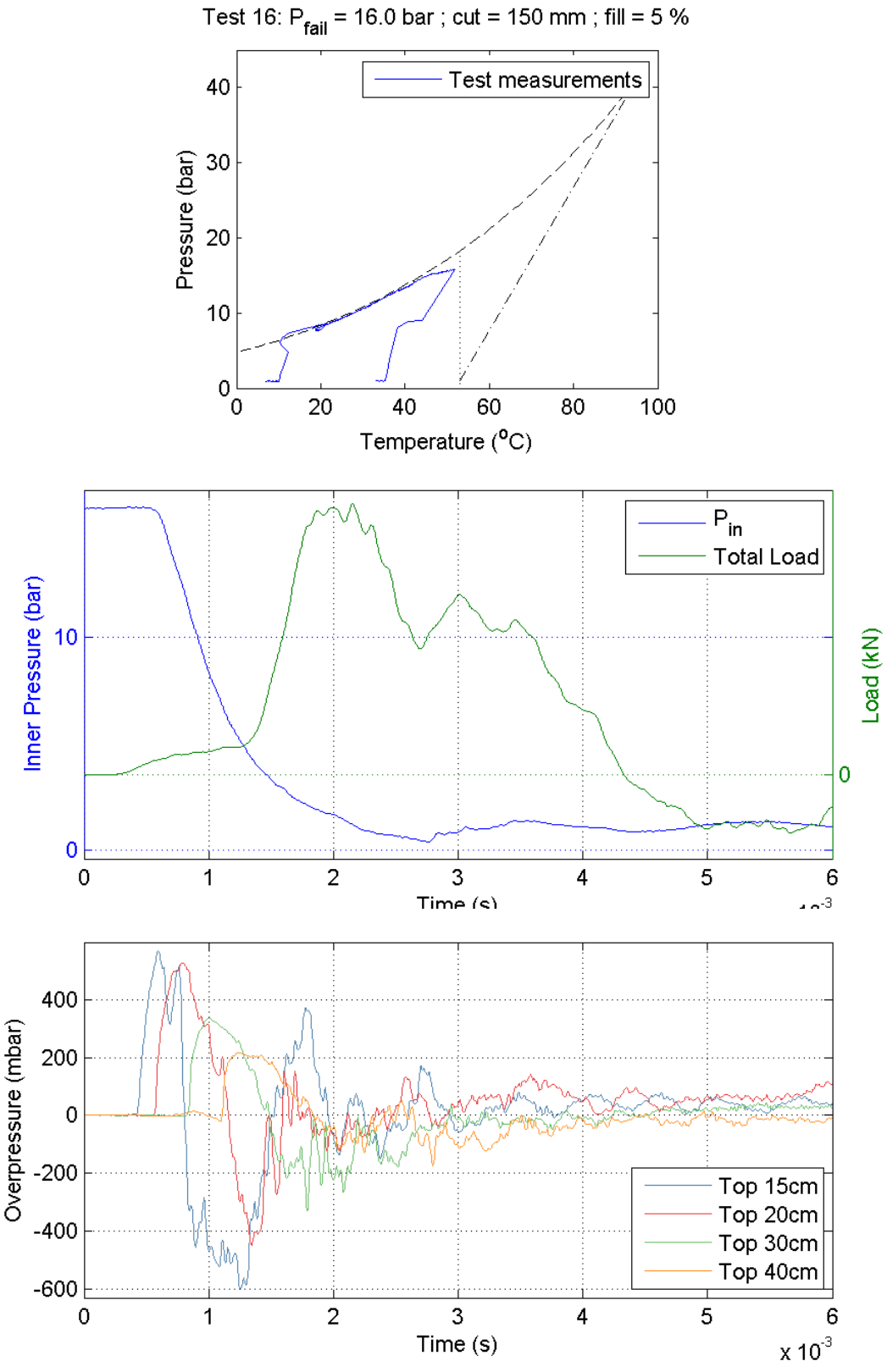
Test 16: P_fail = 16.0 bar ; cut = 150 mm ; fill = 5 %
Test measurements
Pressure (bar)
Temperature (°C)
P_in
Total Load
Inner Pressure (bar)
Load (kN)
Time (s)
x 10^-3
Overpressure (mbar)
Top 15cm
Top 20cm
Top 30cm
Top 40cm
Time (s)
x 10^-3

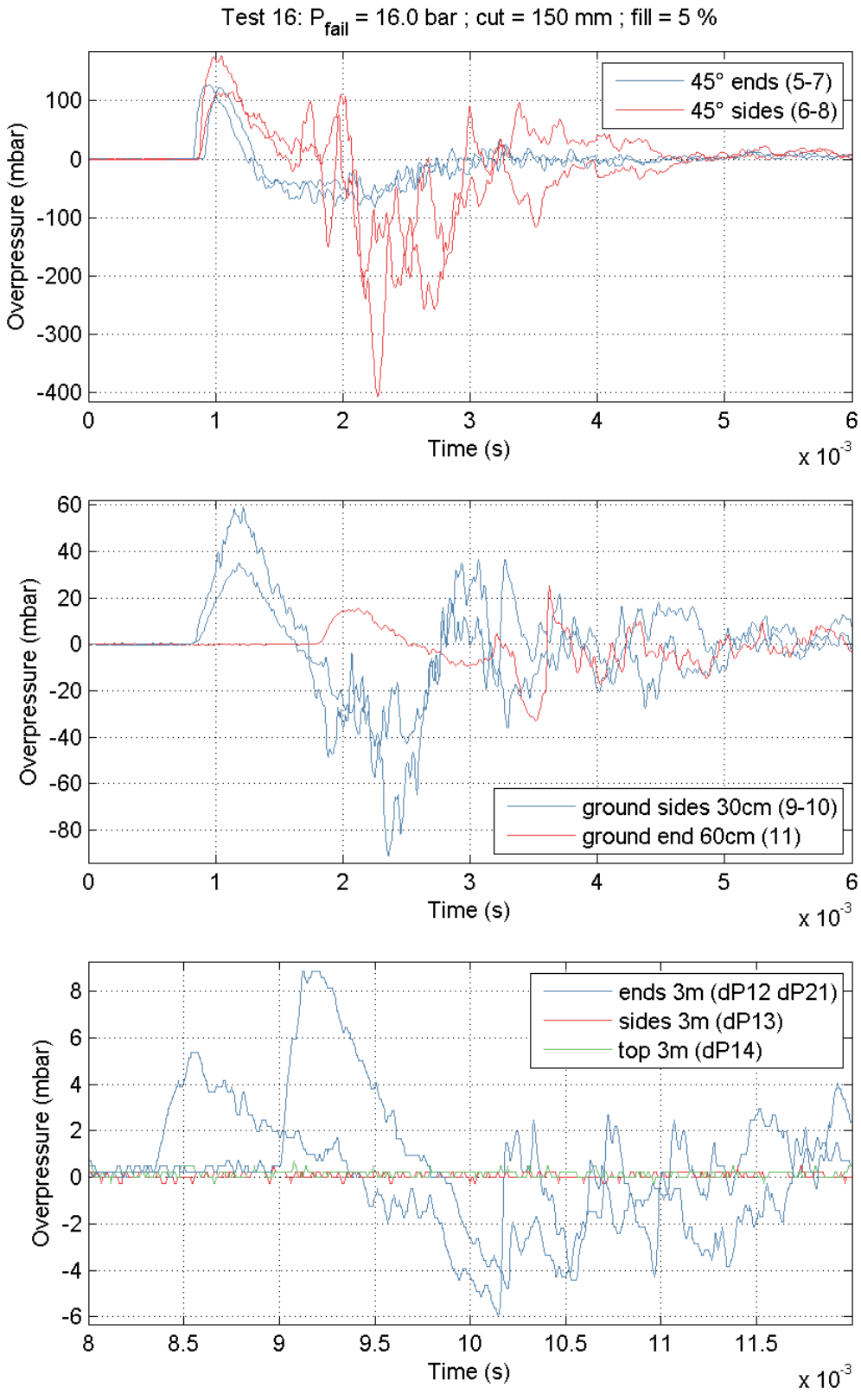
Test 16: P fail = 16.0 bar ; cut = 150 mm ; fill = 5 %
45° ends (5-7)
45° sides (6-8)
Overpressure (mbar)
Time (s)
x 10-3
ground sides 30cm (9-10)
ground end 60cm (11)
Overpressure (mbar)
Time (s)
x 10-3
ends 3m (dP12 dP21)
sides 3m (dP13)
top 3m (dP14)
Overpressure (mbar)
Time (s)
x 10-3

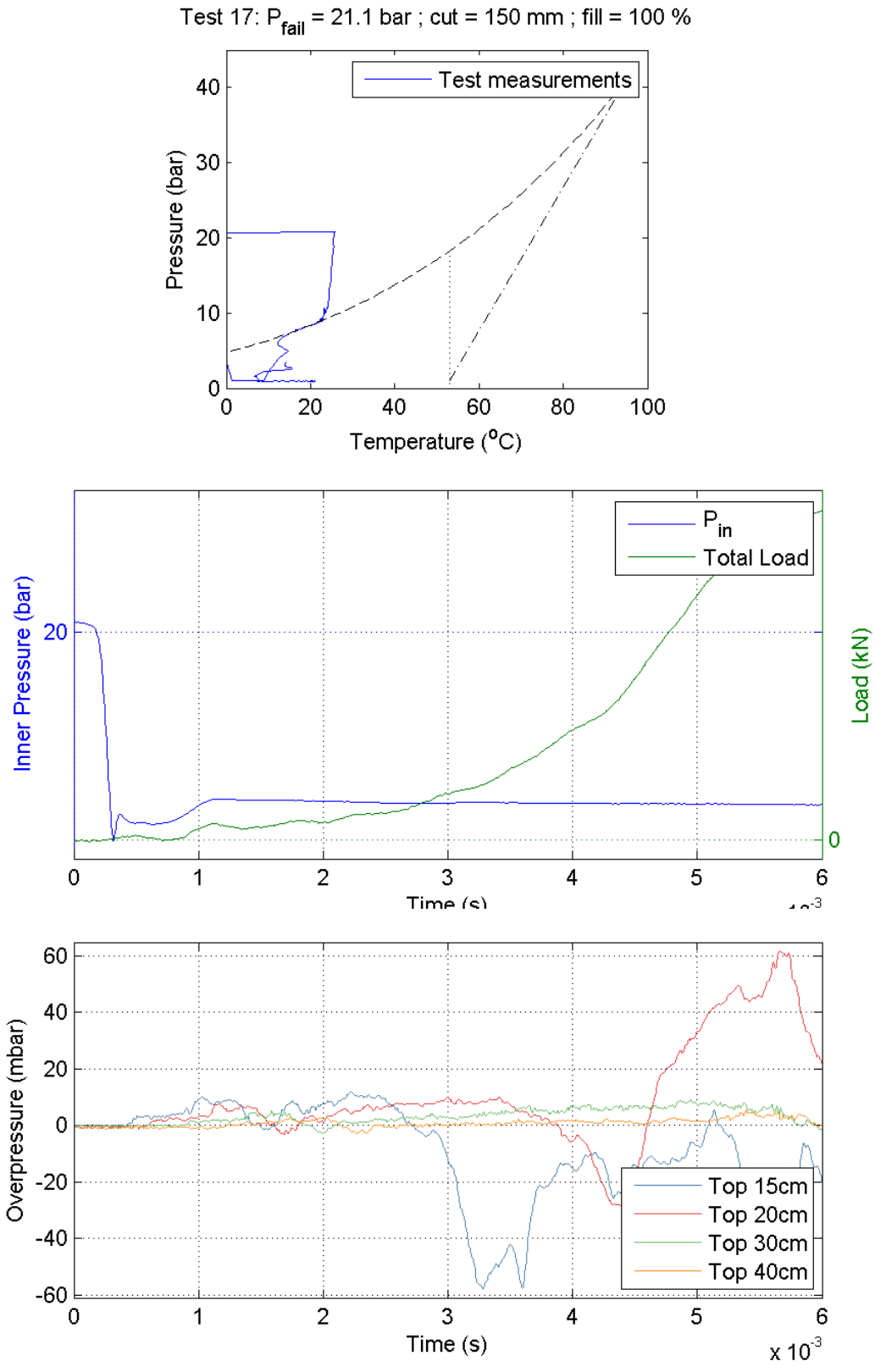
Test 17: P_fail = 21.1 bar ; cut = 150 mm ; fill = 100 %
Test measurements
Pressure (bar)
Temperature (°C)
P_in
Total Load
Inner Pressure (bar)
Load (kN)
Time (s)
x 10^-3
Top 15cm
Top 20cm
Top 30cm
Top 40cm
Overpressure (mbar)

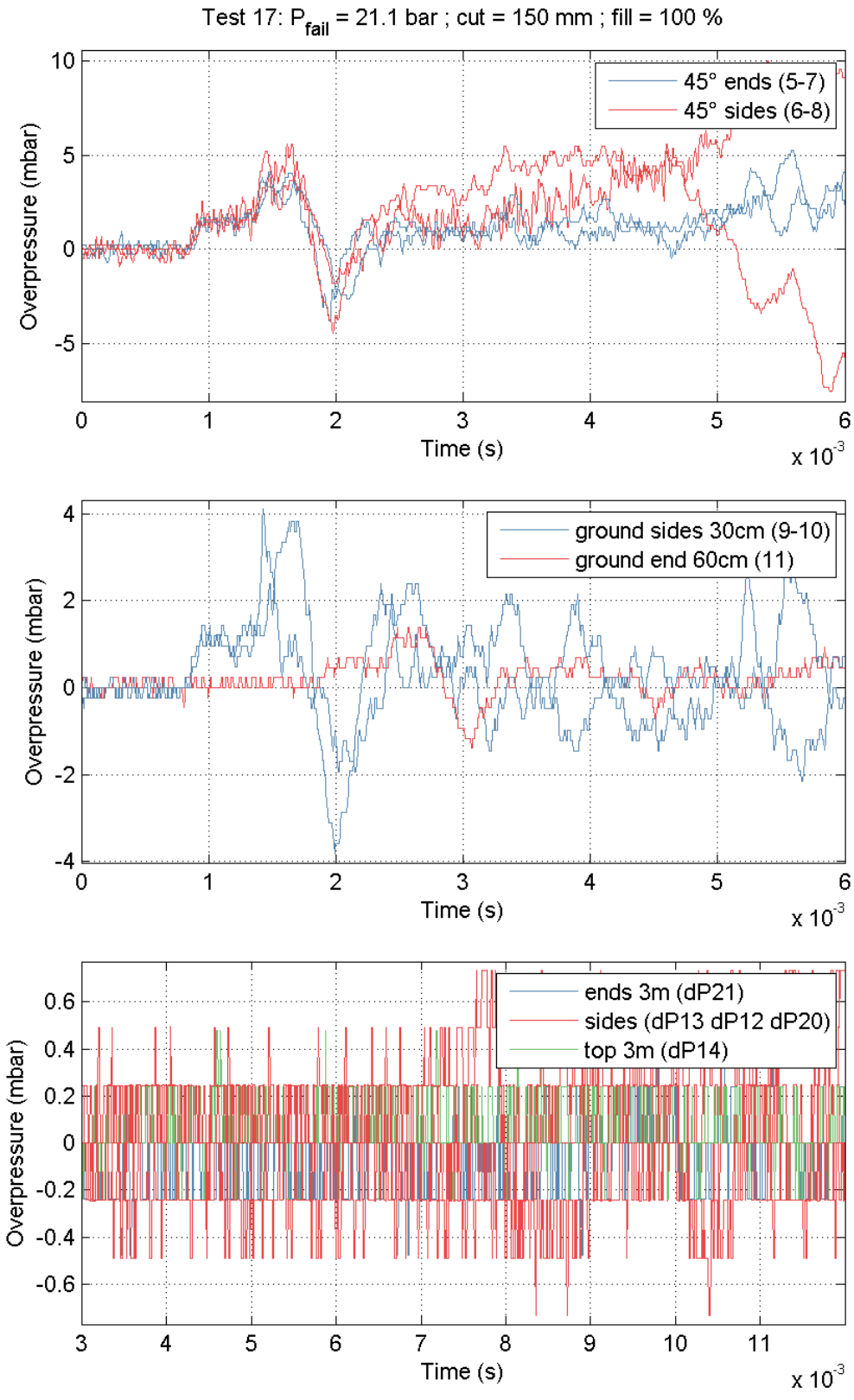
Test 17: P_fail = 21.1 bar ; cut = 150 mm ; fill = 100 %
45° ends (5-7)
45° sides (6-8)
Overpressure (mbar)
Time (s)
x 10^-3
ground sides 30cm (9-10)
ground end 60cm (11)
Overpressure (mbar)
Time (s)
x 10^-3
ends 3m (dP21)
sides (dP13 dP12 dP20)
top 3m (dP14)
Overpressure (mbar)
Time (s)
x 10^-3

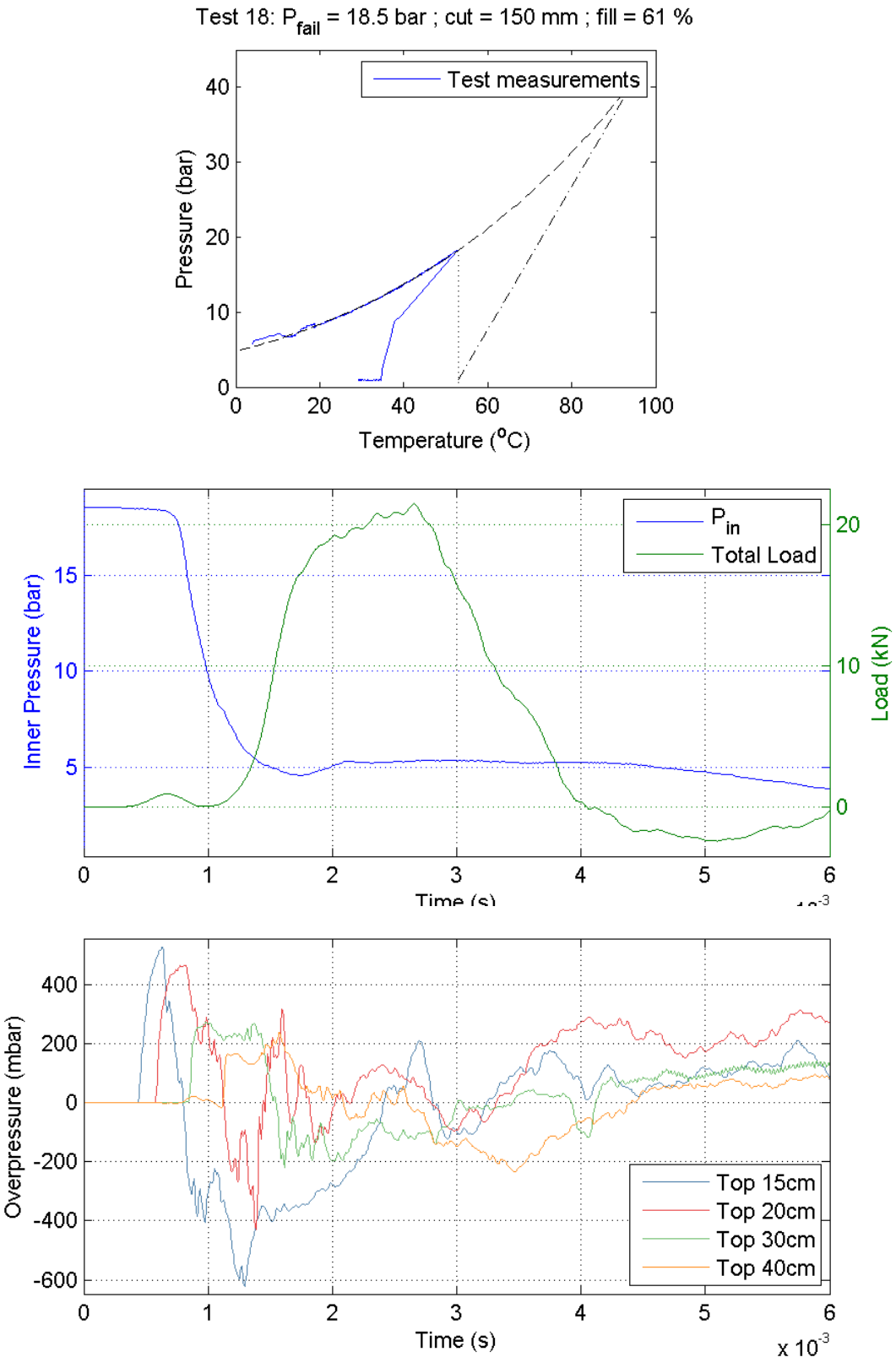
Test 18: P_fail = 18.5 bar ; cut = 150 mm ; fill = 61 %
Test measurements
Pressure (bar)
Temperature (°C)
P_in
Total Load
Inner Pressure (bar)
Load (kN)
Time (s)
Overpressure (mbar)
Top 15cm
Top 20cm
Top 30cm
Top 40cm
Time (s)
x 10^-3

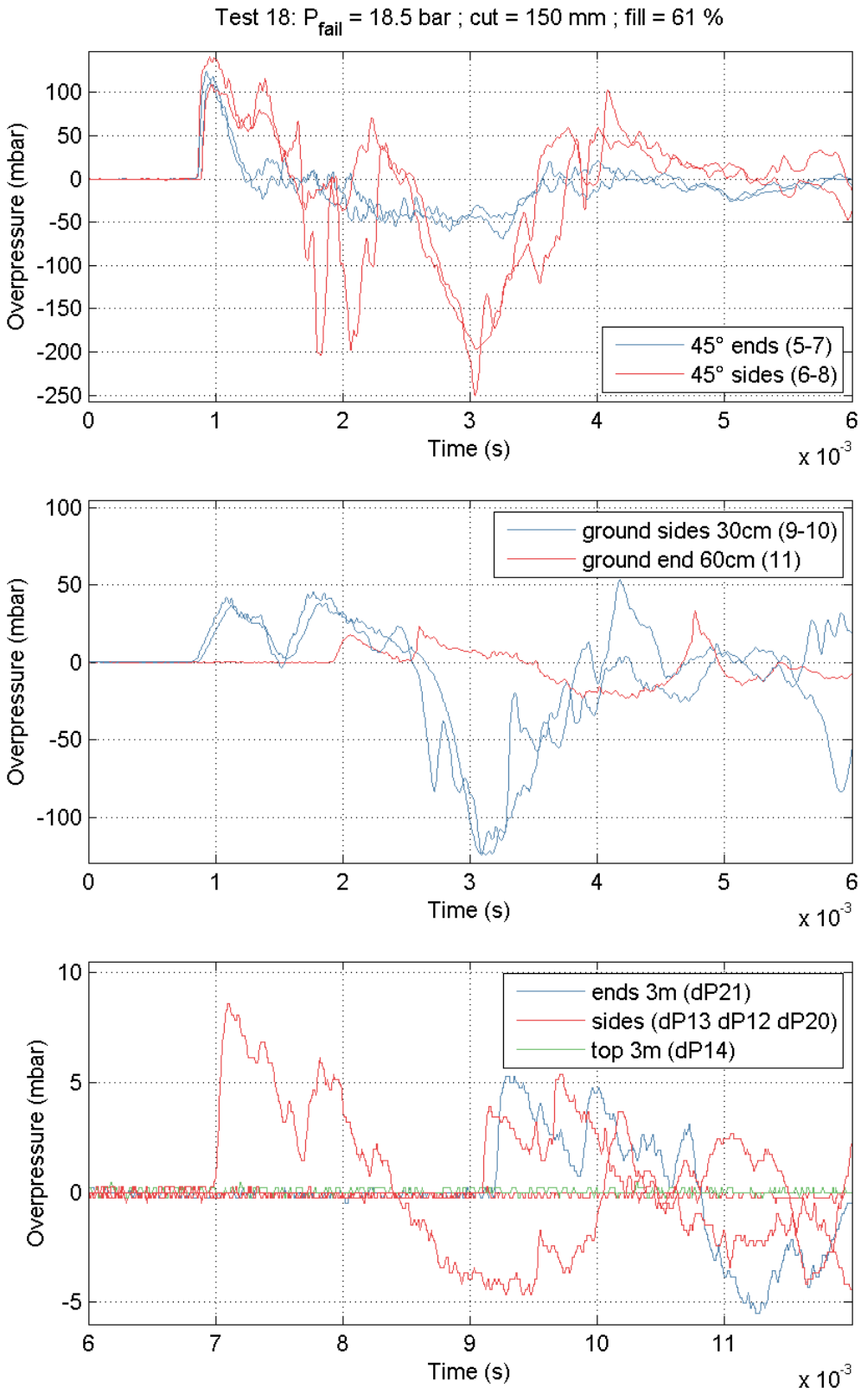
Test 18: P fail = 18.5 bar ; cut = 150 mm ; fill = 61 %
Overpressure (mbar)
Time (s)
x 10-3
45° ends (5-7)
45° sides (6-8)
ground sides 30cm (9-10)
ground end 60cm (11)
ends 3m (dP21)
sides (dP13 dP12 dP20)
top 3m (dP14)

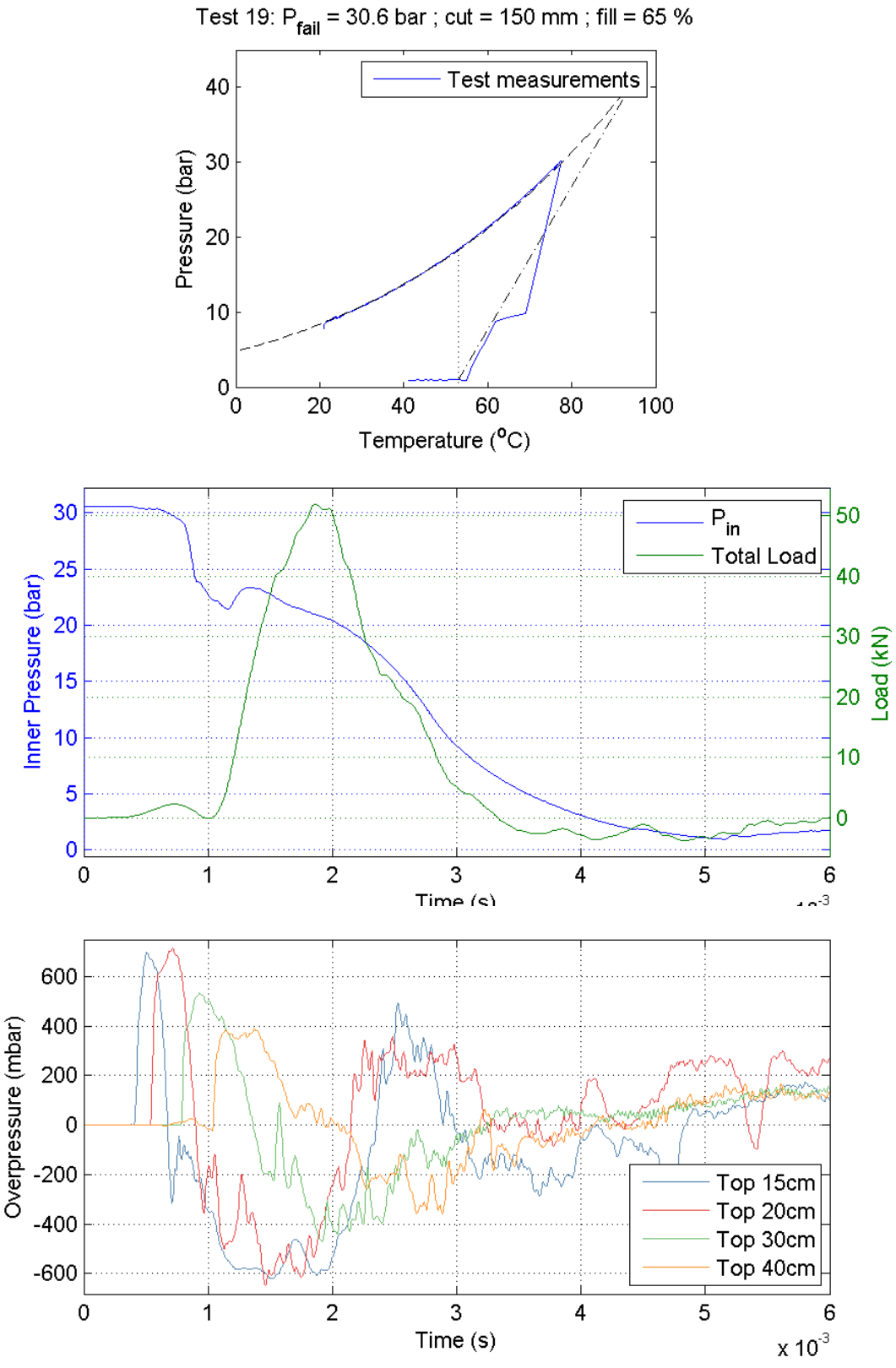
Test 19: P_fail = 30.6 bar ; cut = 150 mm ; fill = 65 %
Test measurements
Pressure (bar)
Temperature (°C)
P_in
Total Load
Inner Pressure (bar)
Load (kN)
Time (s)
Top 15cm
Top 20cm
Top 30cm
Top 40cm
Overpressure (mbar)
Time (s)
x 10^-3

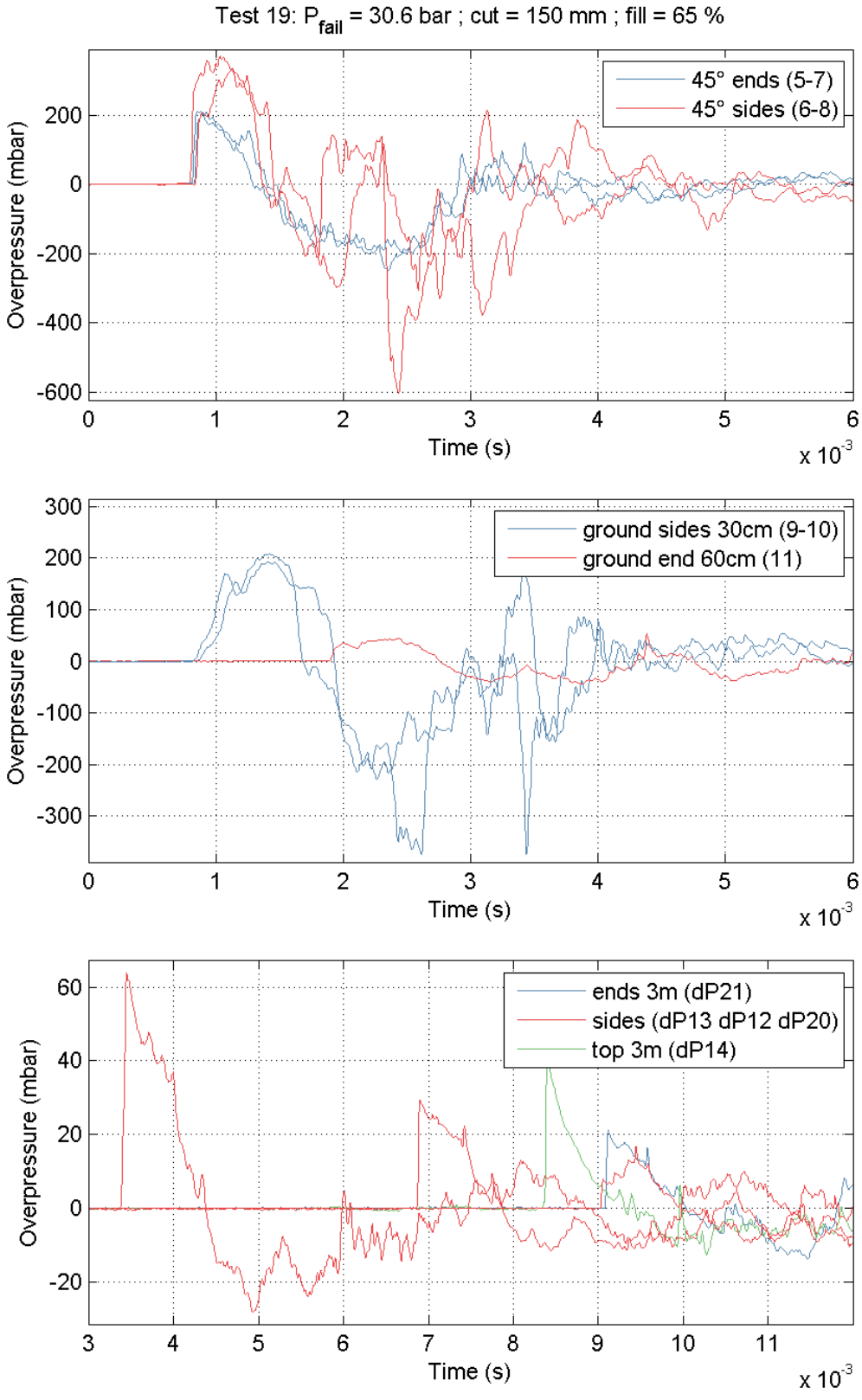
Test 19: P fail = 30.6 bar ; cut = 150 mm ; fill = 65 %
45° ends (5-7)
45° sides (6-8)
Overpressure (mbar)
Time (s)
x 10-3
ground sides 30cm (9-10)
ground end 60cm (11)
Overpressure (mbar)
Time (s)
x 10-3
ends 3m (dP21)
sides (dP13 dP12 dP20)
top 3m (dP14)
Overpressure (mbar)
Time (s)
x 10-3

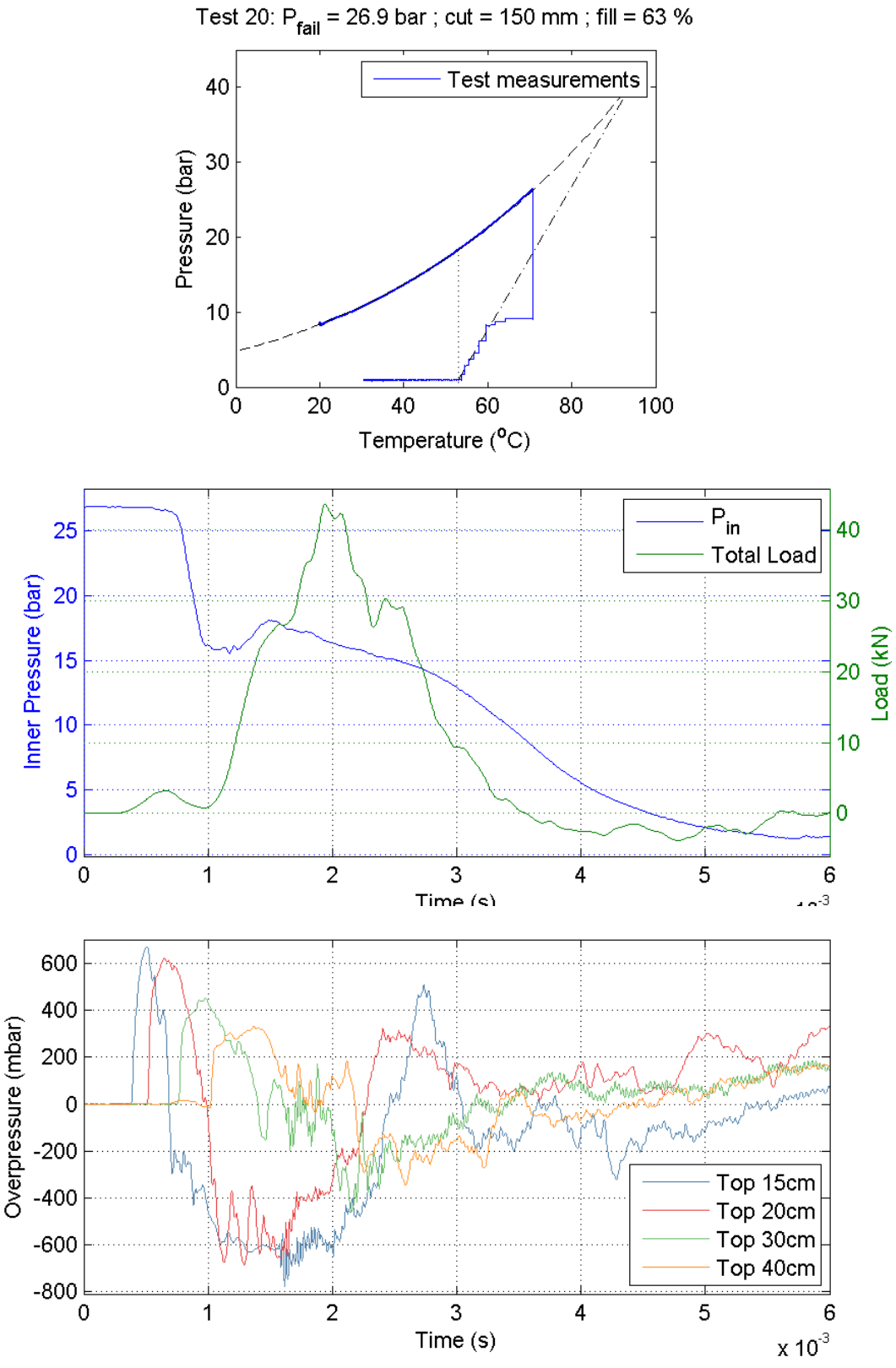
Test 20: P_fail = 26.9 bar ; cut = 150 mm ; fill = 63 %
Test measurements
Pressure (bar)
Temperature (°C)
P_in
Total Load
Inner Pressure (bar)
Load (kN)
Time (s)
Overpressure (mbar)
Top 15cm
Top 20cm
Top 30cm
Top 40cm
Time (s)
x 10^-3

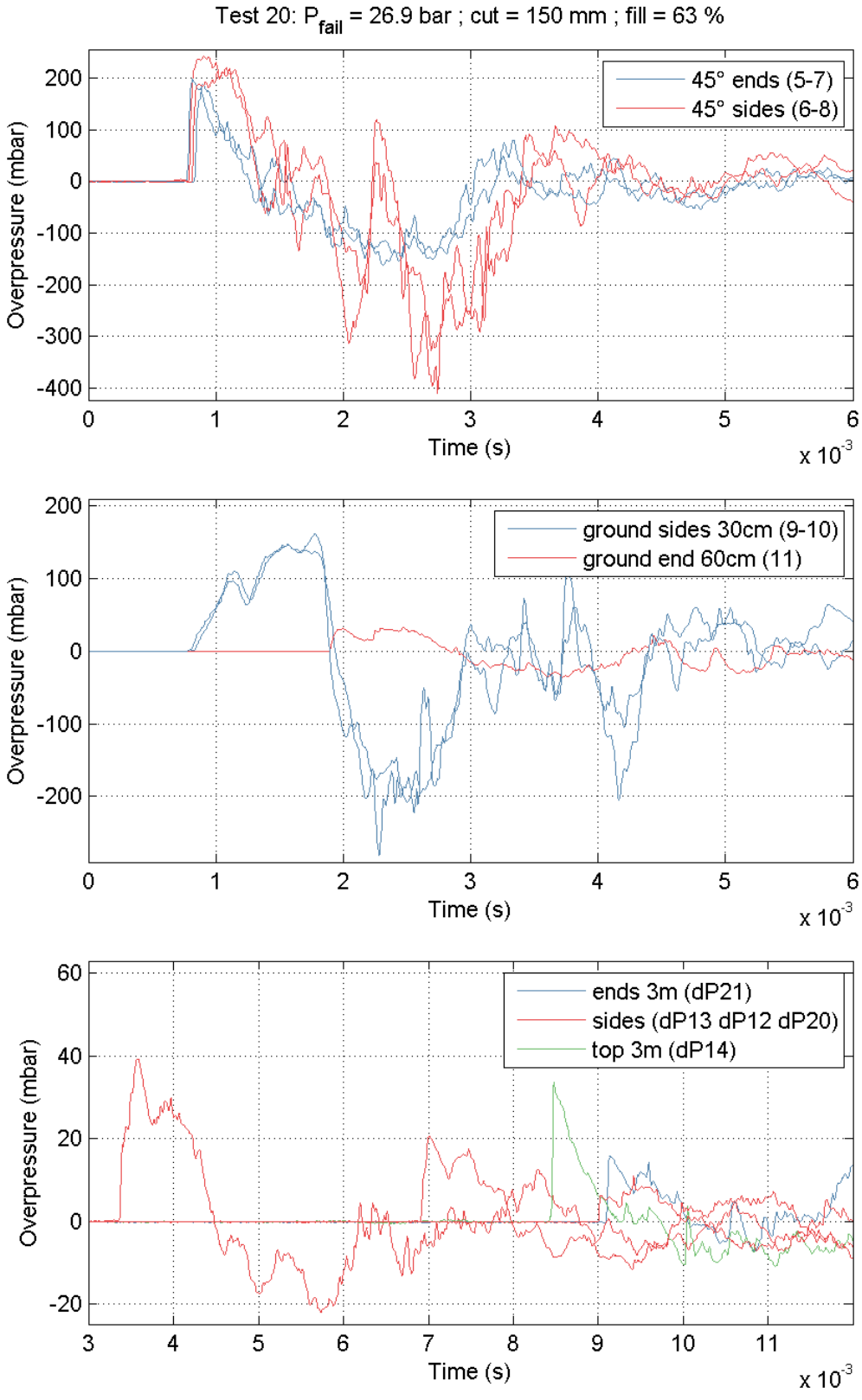
Test 20: P fail = 26.9 bar ; cut = 150 mm ; fill = 63 %
45° ends (5-7)
45° sides (6-8)
Overpressure (mbar)
Time (s)
x 10-3
ground sides 30cm (9-10)
ground end 60cm (11)
Overpressure (mbar)
Time (s)
x 10-3
ends 3m (dP21)
sides (dP13 dP12 dP20)
top 3m (dP14)
Overpressure (mbar)
Time (s)
x 10-3

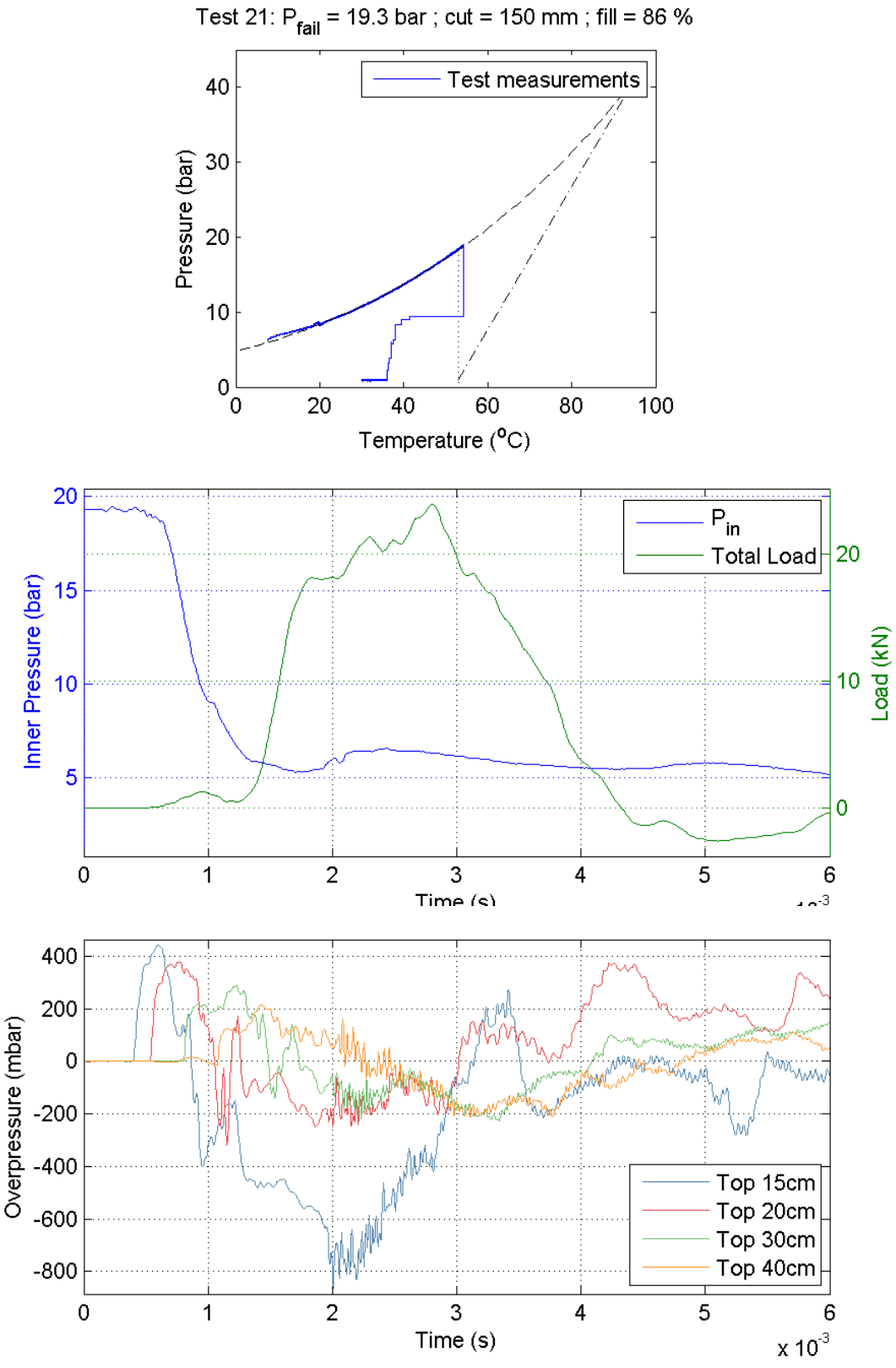
Test 21: P_fail = 19.3 bar ; cut = 150 mm ; fill = 86 %
Test measurements
Pressure (bar)
Temperature (°C)
P_in
Total Load
Inner Pressure (bar)
Load (kN)
Time (s)
Overpressure (mbar)
Top 15cm
Top 20cm
Top 30cm
Top 40cm
Time (s)
x 10^-3

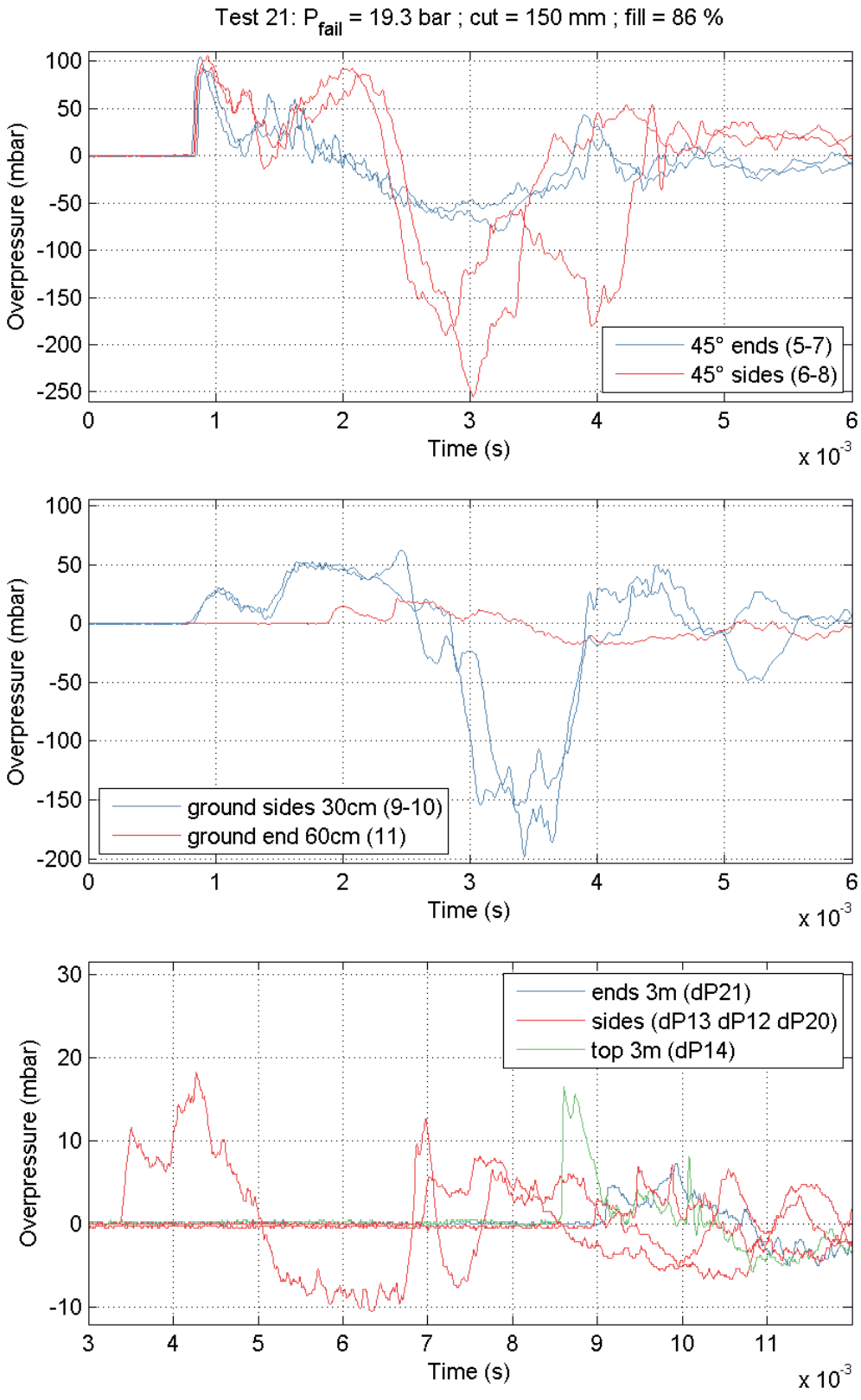
Test 21: P fail = 19.3 bar ; cut = 150 mm ; fill = 86 %
Overpressure (mbar)
Time (s)
x 10-3
45° ends (5-7)
45° sides (6-8)
ground sides 30cm (9-10)
ground end 60cm (11)
ends 3m (dP21)
sides (dP13 dP12 dP20)
top 3m (dP14)

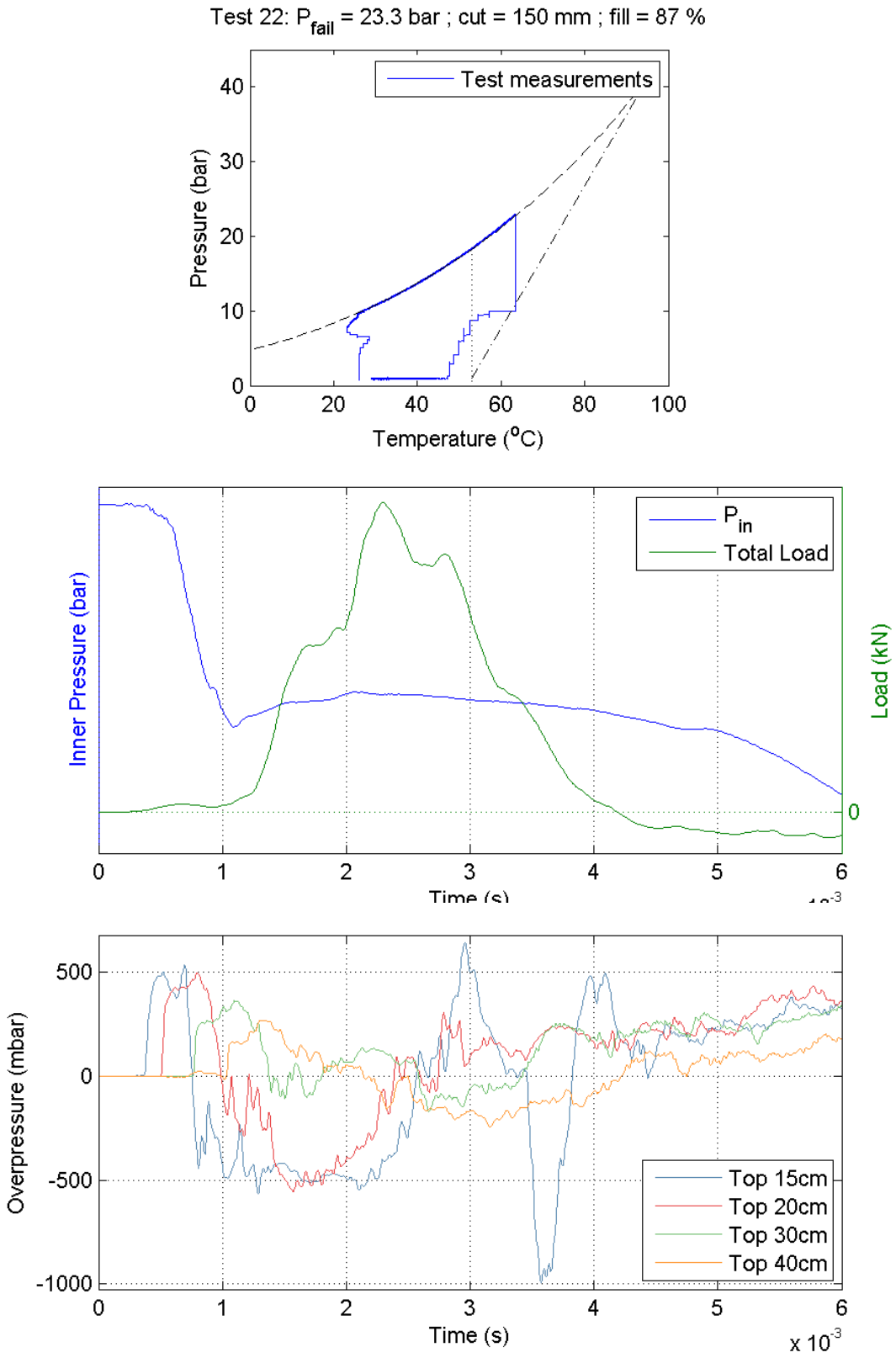
Test 22: P_fail = 23.3 bar ; cut = 150 mm ; fill = 87 %
Test measurements
Pressure (bar)
Temperature (°C)
P_in
Total Load
Inner Pressure (bar)
Load (kN)
Time (s)
Top 15cm
Top 20cm
Top 30cm
Top 40cm
Overpressure (mbar)
Time (s)
x 10^-3

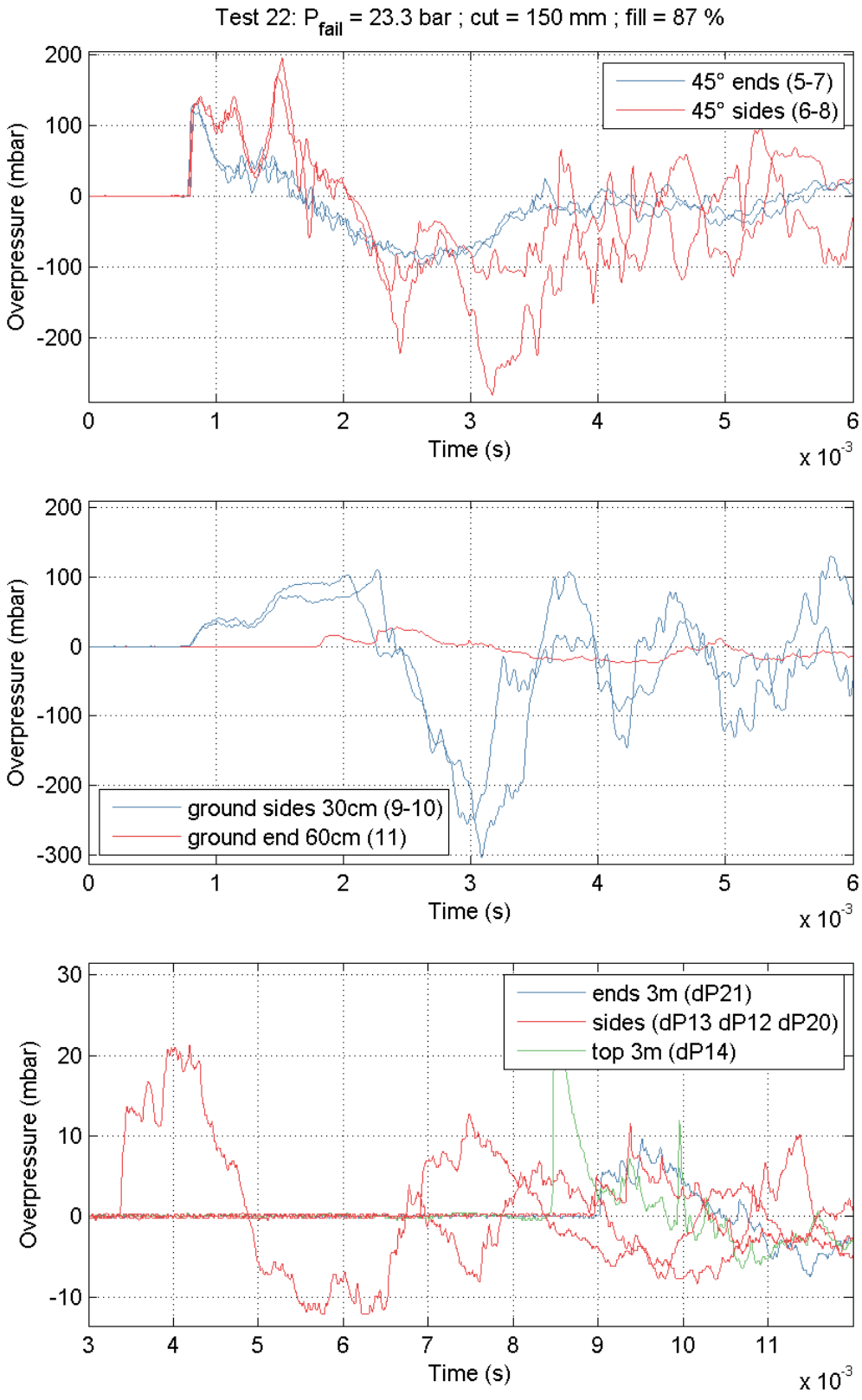
Test 22: P fail = 23.3 bar ; cut = 150 mm ; fill = 87 %
45° ends (5-7)
45° sides (6-8)
Overpressure (mbar)
Time (s)
x 10-3
ground sides 30cm (9-10)
ground end 60cm (11)
ends 3m (dP21)
sides (dP13 dP12 dP20)
top 3m (dP14)

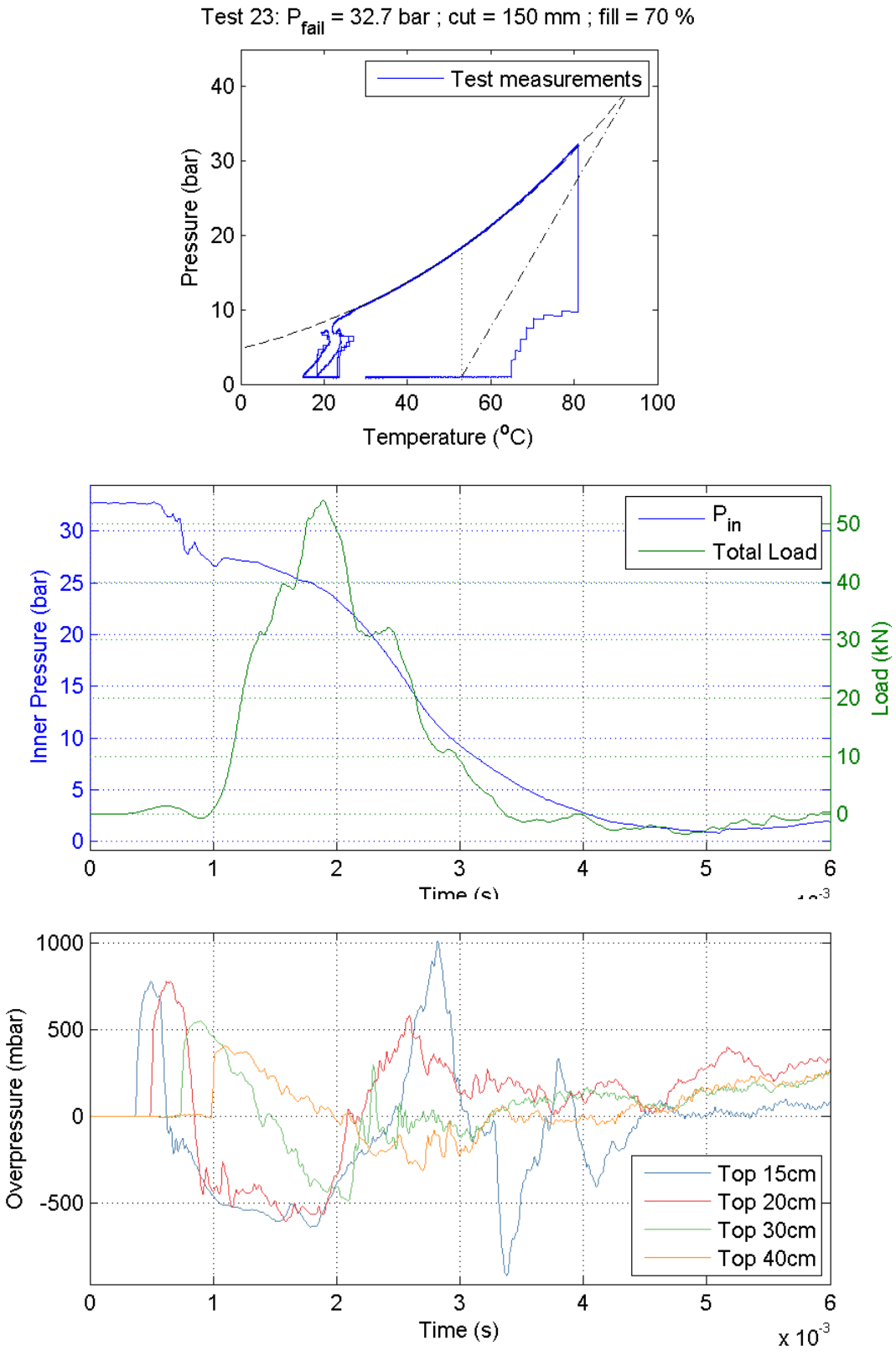
Test 23: P_fail = 32.7 bar ; cut = 150 mm ; fill = 70 %
Test measurements
Pressure (bar)
Temperature (°C)
P_in
Total Load
Inner Pressure (bar)
Load (kN)
Time (s)
x 10^-3
Overpressure (mbar)
Top 15cm
Top 20cm
Top 30cm
Top 40cm
Time (s)
x 10^-3

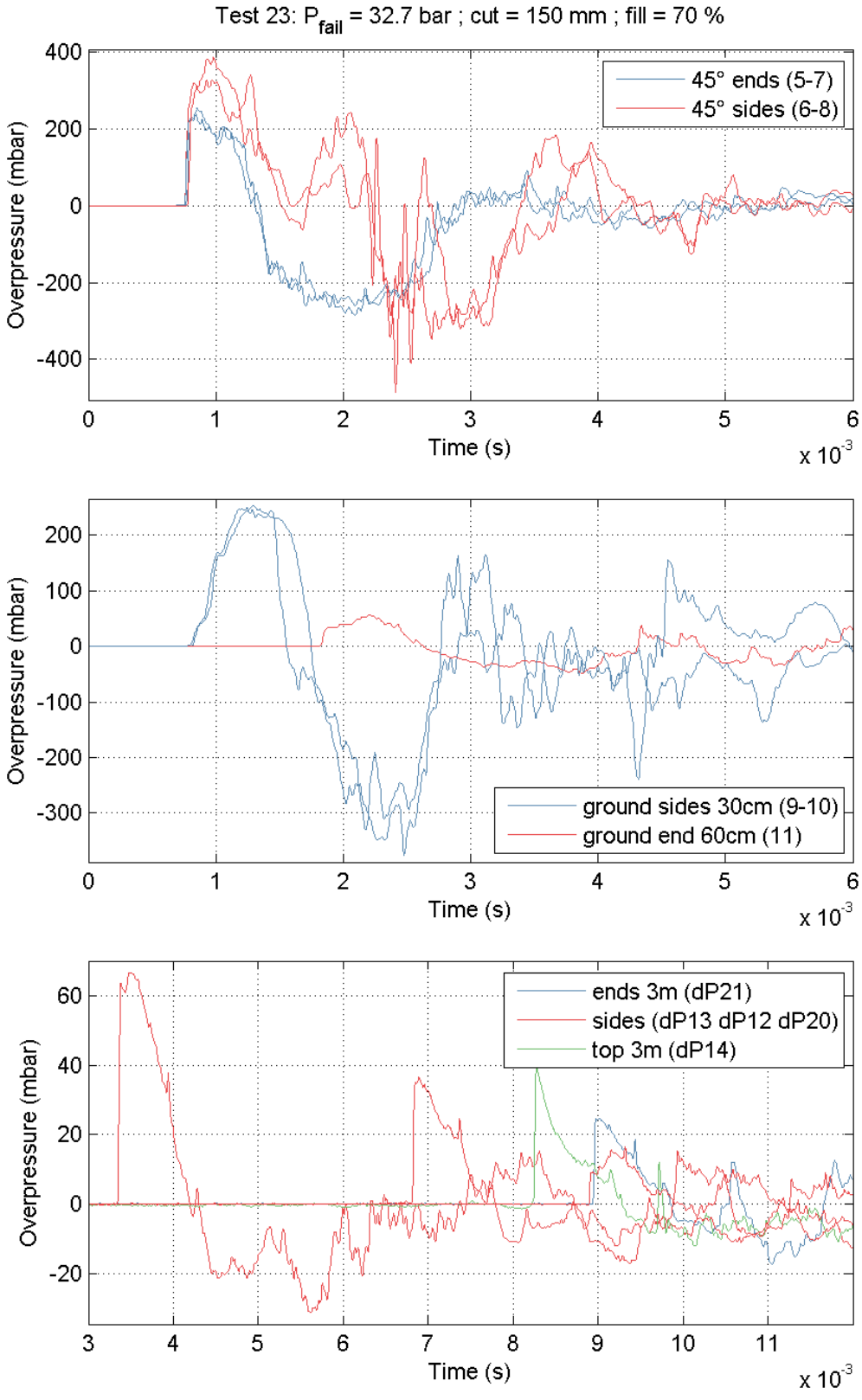
Test 23: P fail = 32.7 bar ; cut = 150 mm ; fill = 70 %
45° ends (5-7)
45° sides (6-8)
Overpressure (mbar)
Time (s)
x 10-3
ground sides 30cm (9-10)
ground end 60cm (11)
ends 3m (dP21)
sides (dP13 dP12 dP20)
top 3m (dP14)

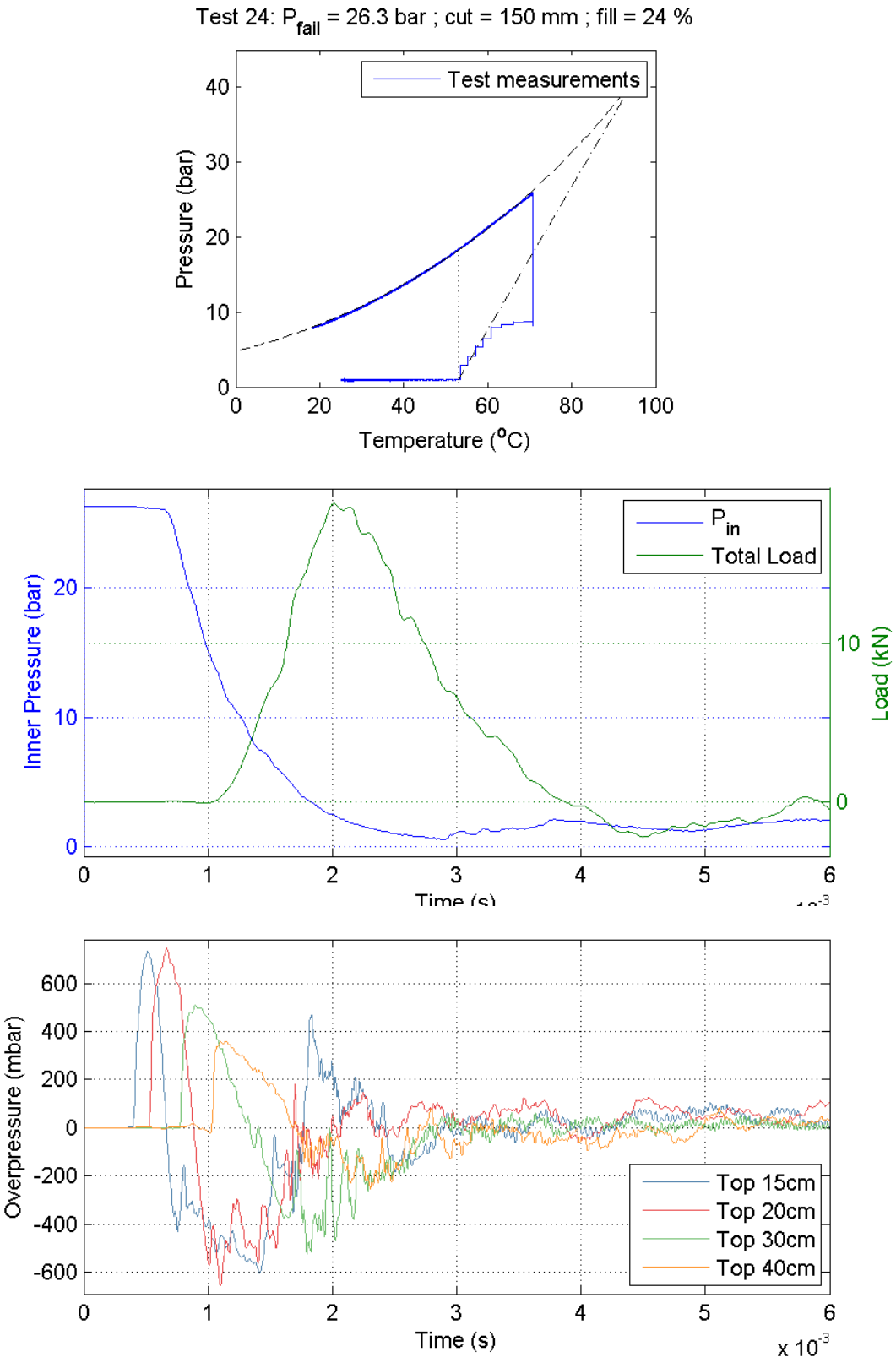
Test 24: P_fail = 26.3 bar ; cut = 150 mm ; fill = 24 %
Test measurements
Pressure (bar)
Temperature (°C)
P_in
Total Load
Inner Pressure (bar)
Load (kN)
Time (s)
Overpressure (mbar)
Top 15cm
Top 20cm
Top 30cm
Top 40cm
Time (s)
x 10^-3

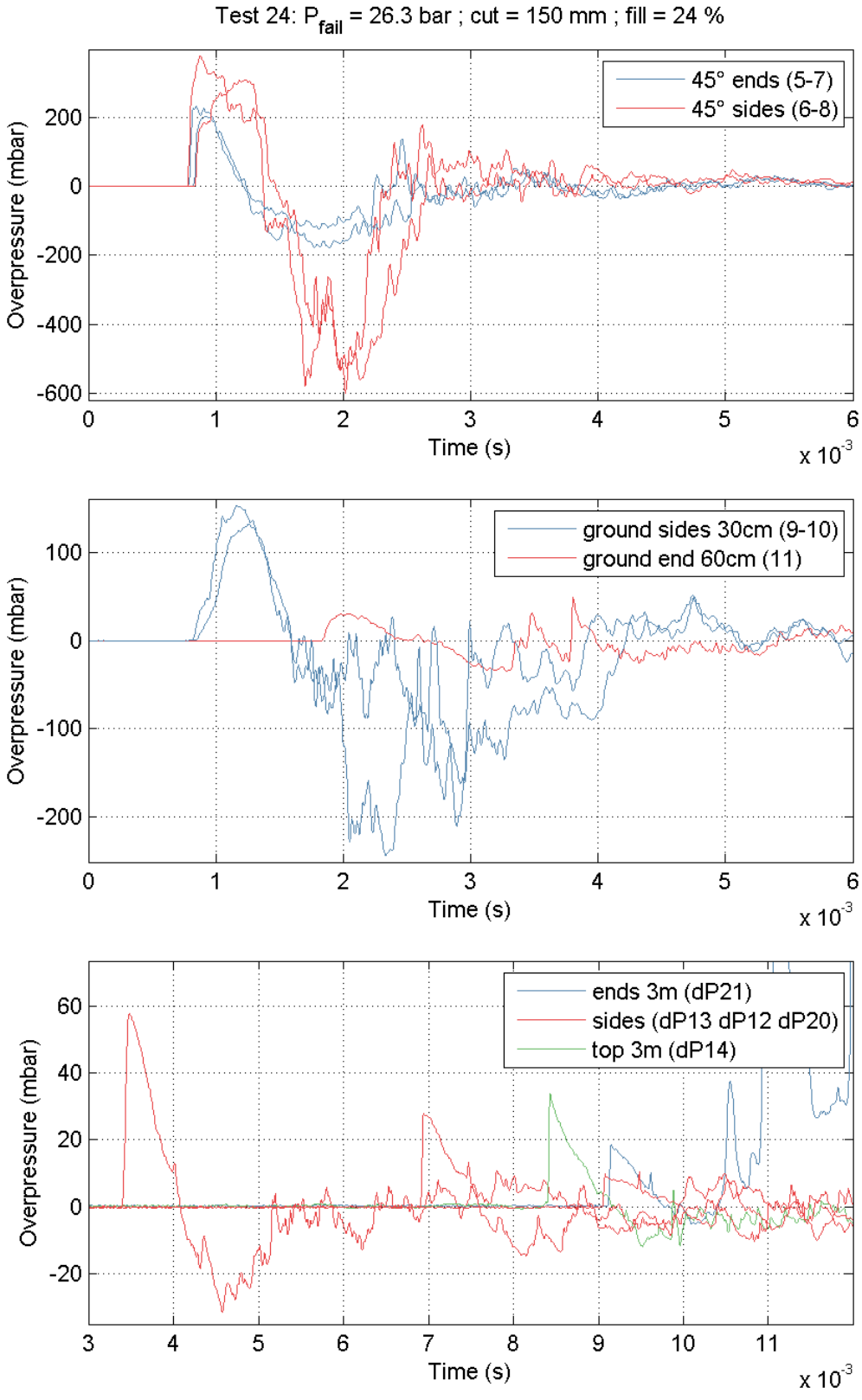
Test 24: P fail = 26.3 bar ; cut = 150 mm ; fill = 24 %
45° ends (5-7)
45° sides (6-8)
Overpressure (mbar)
Time (s)
x 10-3
ground sides 30cm (9-10)
ground end 60cm (11)
Overpressure (mbar)
Time (s)
x 10-3
ends 3m (dP21)
sides (dP13 dP12 dP20)
top 3m (dP14)
Overpressure (mbar)
Time (s)
x 10-3

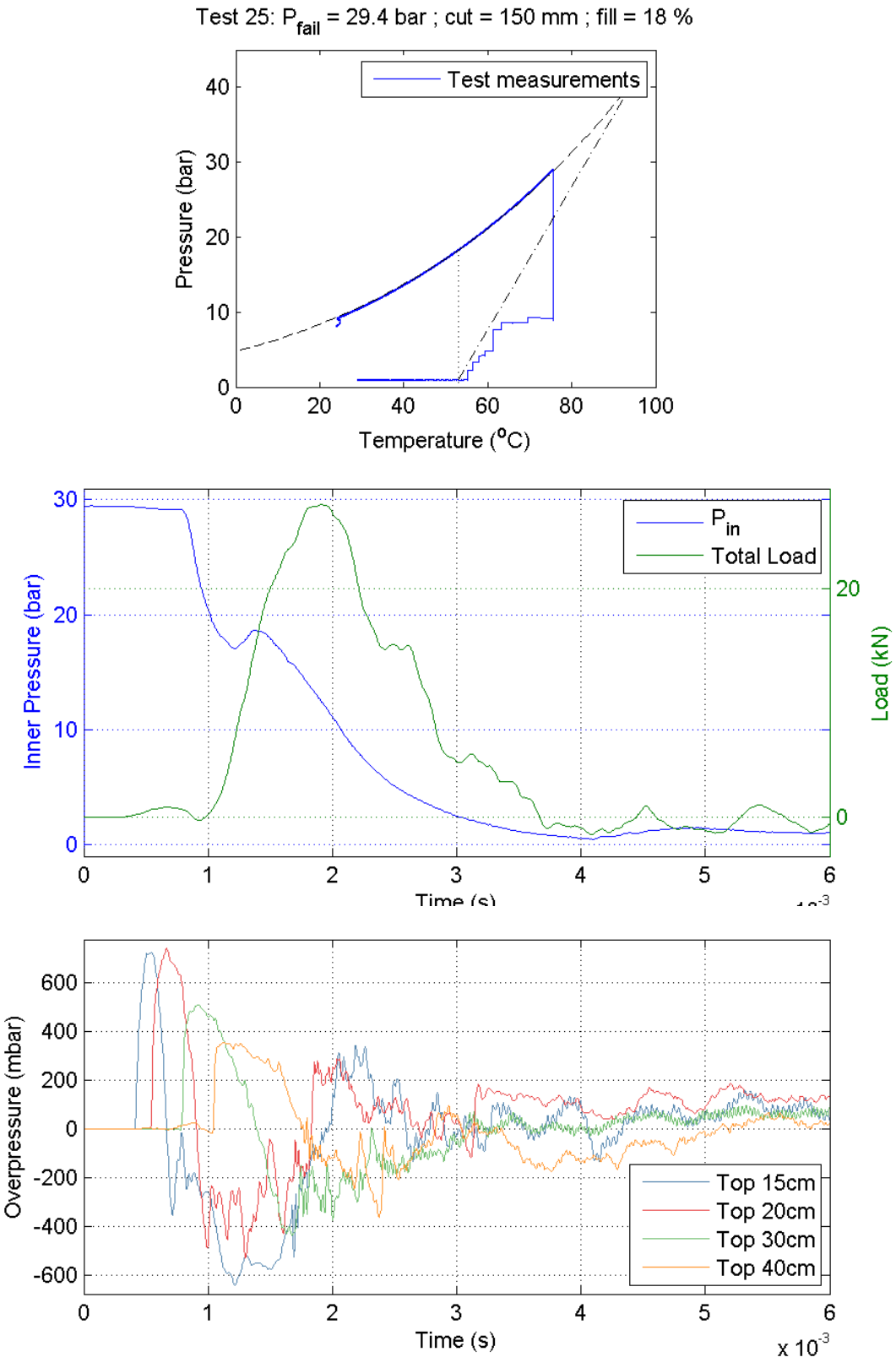
Test 25: P_fail = 29.4 bar ; cut = 150 mm ; fill = 18 %
Test measurements
Pressure (bar)
Temperature (°C)
P_in
Total Load
Inner Pressure (bar)
Load (kN)
Time (s)
Overpressure (mbar)
Top 15cm
Top 20cm
Top 30cm
Top 40cm
x 10^-3

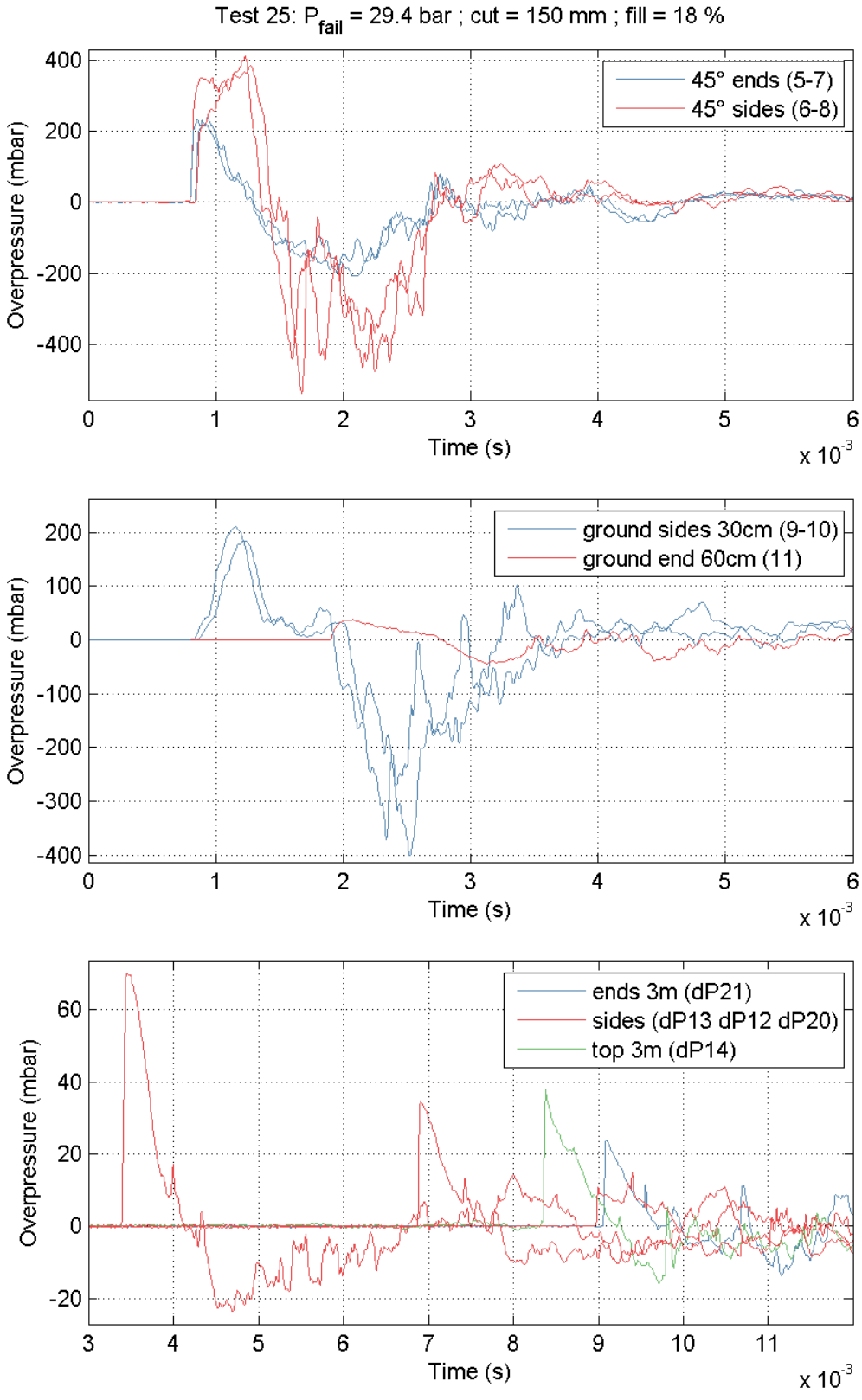
Test 25: P fail = 29.4 bar ; cut = 150 mm ; fill = 18 %
45° ends (5-7)
45° sides (6-8)
Overpressure (mbar)
Time (s)
x 10-3
ground sides 30cm (9-10)
ground end 60cm (11)
Overpressure (mbar)
Time (s)
x 10-3
ends 3m (dP21)
sides (dP13 dP12 dP20)
top 3m (dP14)
Overpressure (mbar)
Time (s)
x 10-3

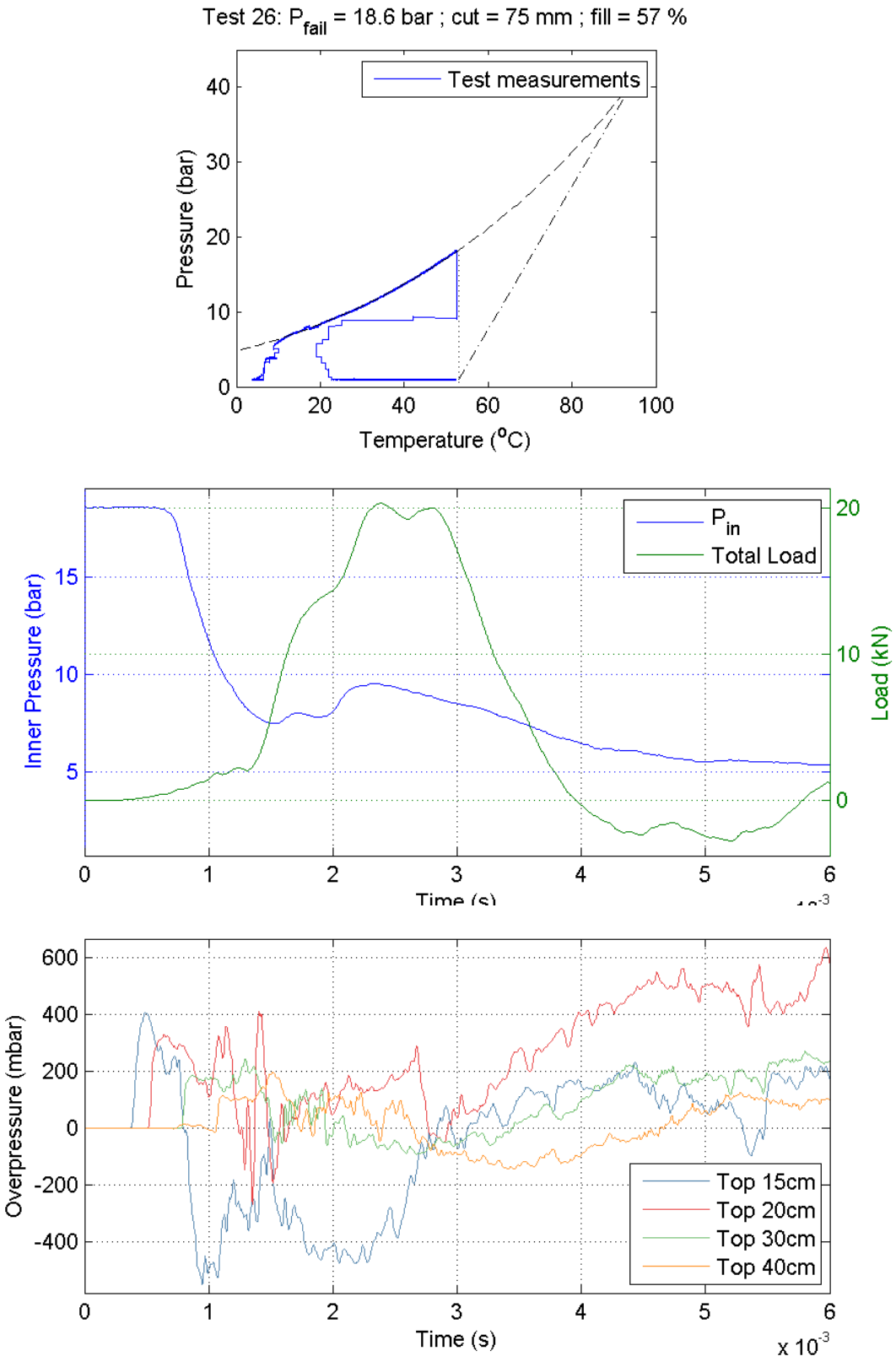
Test 26: P_fail = 18.6 bar ; cut = 75 mm ; fill = 57 %
Test measurements
Pressure (bar)
Temperature (°C)
P_in
Total Load
Inner Pressure (bar)
Load (kN)
Time (s)
x 10^-3
Overpressure (mbar)
Top 15cm
Top 20cm
Top 30cm
Top 40cm
Time (s)
x 10^-3

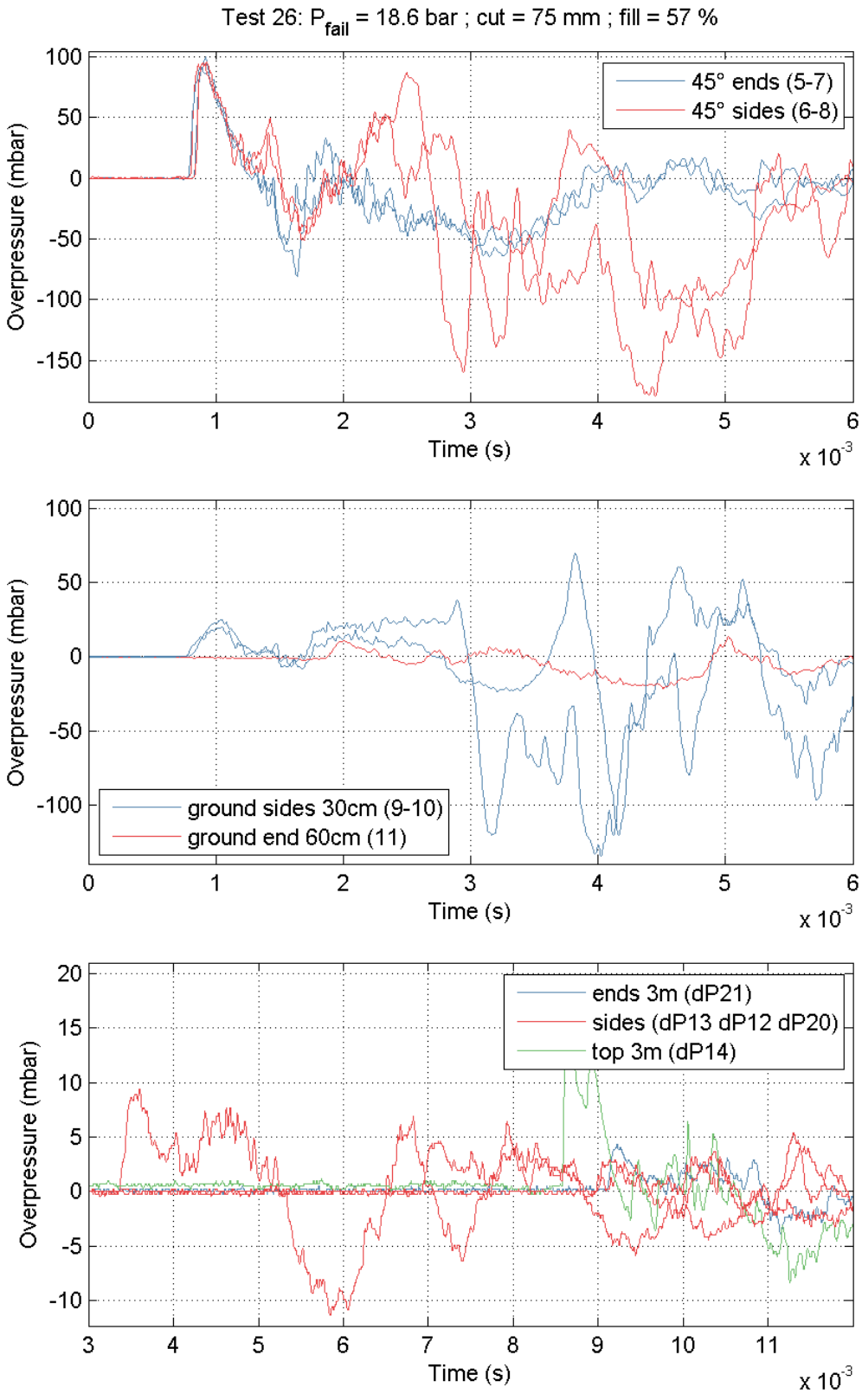
Test 26: P fail = 18.6 bar ; cut = 75 mm ; fill = 57 %
45° ends (5-7)
45° sides (6-8)
Overpressure (mbar)
Time (s)
x 10-3
ground sides 30cm (9-10)
ground end 60cm (11)
ends 3m (dP21)
sides (dP13 dP12 dP20)
top 3m (dP14)

Appendix F: Graphic User Interface for timeline analysis

In order to synchronize the data collected and have a larger picture of the BLEVE, a Graphic User Interface (GUI) was developed through Matlab (Figure 11-12). The purpose of the GUI was to have most of the data from a single test on the screen, and be able to navigate through it with a common time reference.

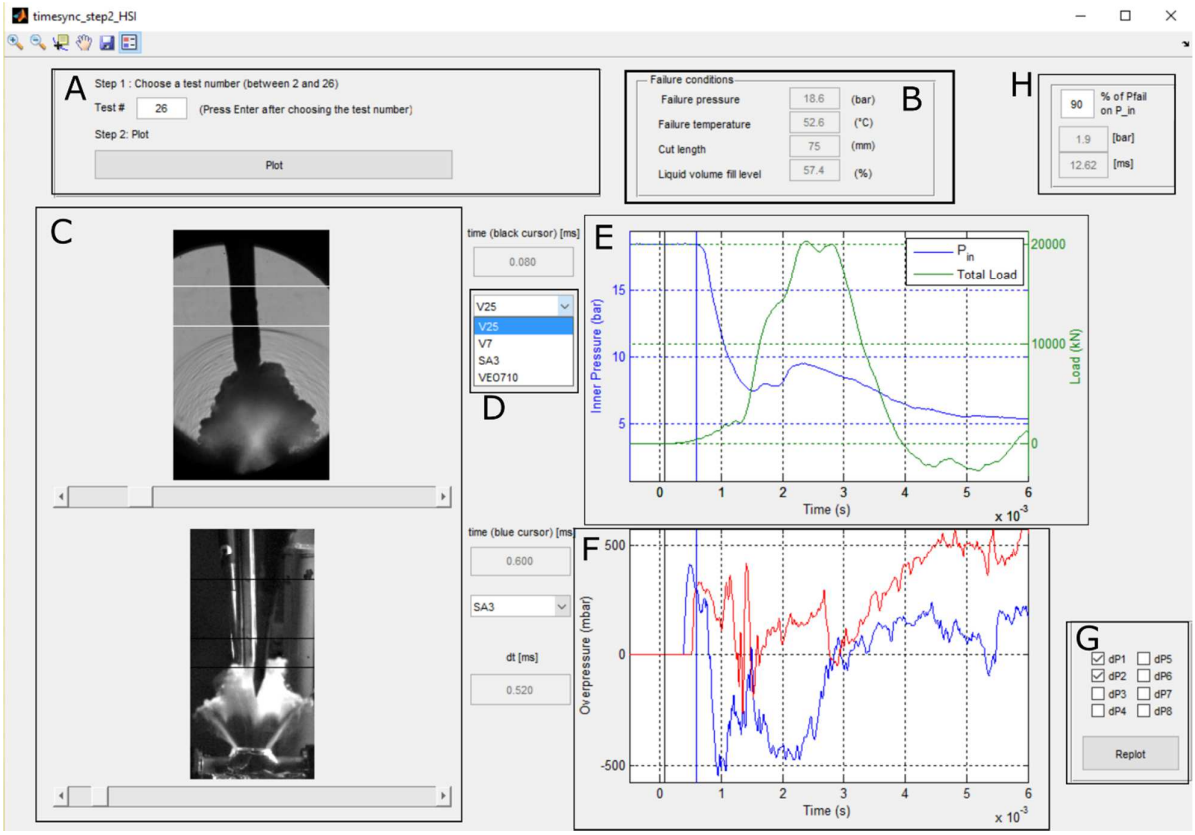

Figure 11-12 Description of the different sections of the Graphic User Interface

To use this interface, the first step is to choose the test case which needs to be plotted (Figure 11-12 A). When the case is chosen and plotted, its failure conditions are presented (Figure 11-12 B).

The left side of the screen was dedicated to high speed imaging (Figure 11-12 C). The scroll bar bellow each image allows to navigate through the imaging sequence frame by frame. A popup menu to the right of each image allows to switch between the different camera views available (Figure 11-12 D).

The right side of the screen showed the plots of internal transient pressure, ground loading (Figure 11-12 E), and blast overpressure in the near-field (Figure 11-12 F). It is possible to choose which overpressure one wants to plot thanks to the checkbox menu (Figure 11-12 G). Finally, it is also

possible to check the time it takes for the pressure to drop down a certain percentage of the failure pressure (Figure 11-12 H).

The navigation through time was made possible with the scrollbars on the imaging, and was followed by two cursors on the signal plots (Figure 11-13). The origin was defined as stated above: t = 0 corresponded to the beginning of the crack opening, defined through the shadowgraph views. Each imaging scrollbar had a cursor associated on the signal plots. Their time to origin was written in the textboxes to the right of each image, and the difference between the two cursors was calculated in the last bottom textbox.

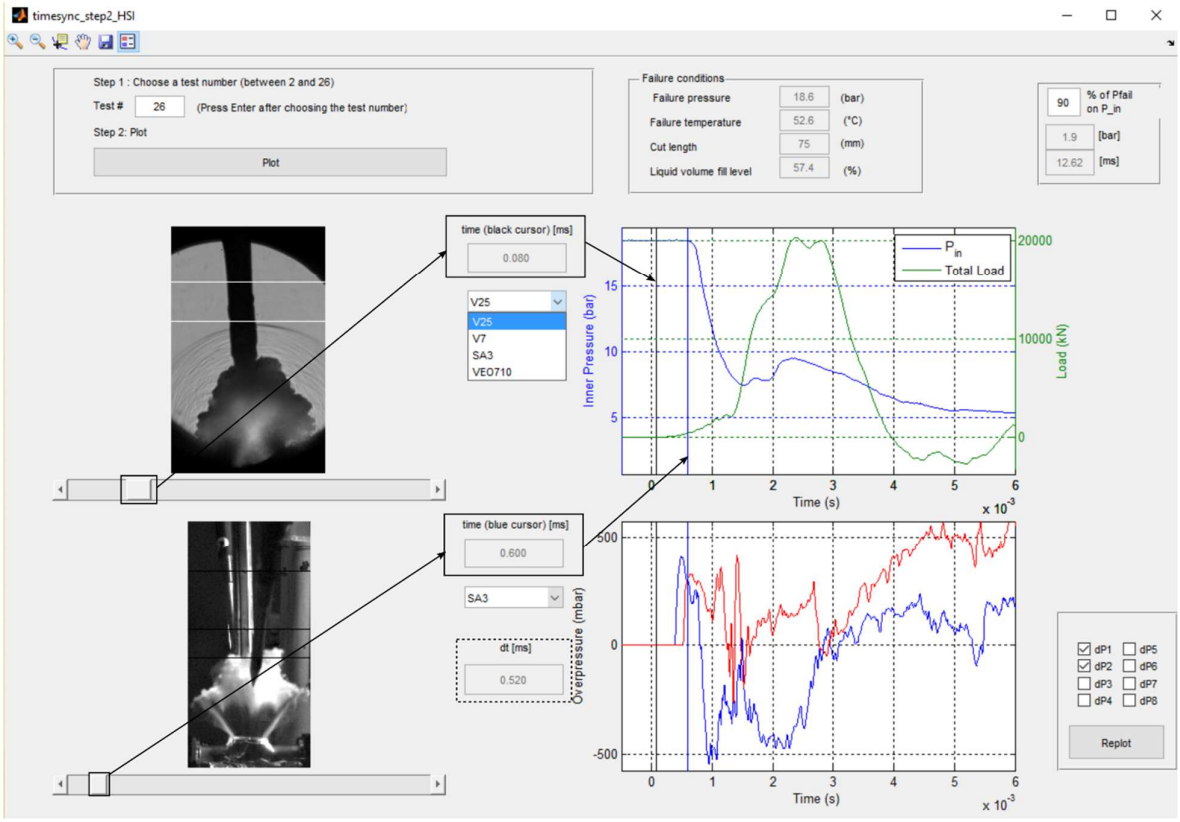

Figure 11-13 Use of the timeline on the Graphic User Interface

Appendix G: 2D CFD of the Open-ended shock tube

CFD simulation was initially setup for various purpose in this work: predicting safety distance for experimental setup based on overpressure criteria, modeling the boiling liquid impact on the pressure field, and understanding the flow patterns and phenomena involved in the expansion through the dynamic opening. Ultimately, CFD was used for the last objective mentioned above only. This appendix introduces quickly the concept of CFD, its main characteristics related to the problem solved. Then it presents the simulation case studied and presents a brief independence study.

I - Introduction to CFD theory

CFD, or Computational Fluid Dynamics, is the resolution of the Navier-Stokes equations through numerical simulation. The main challenge of CFD is to translate non-linear differential fluid flow equations on a continuous domain into linear algebraic equations solved iteratively on a discretized domain.

This process involves the following steps:

I-1. Definition of the geometry and discretization

The first step of CFD is to define the domain of study, with the level of detail necessary for the study. Then the geometry defined is discretized in small cells through what is called the mesh, on which the algebraic equations of fluid will be solved. The level of detail in the geometry description is directly correlated to the number of cells of the mesh, and thus the computational power needed to solve the problem. Some simplifications and symmetries may be used to reduce the number of cells needed to describe the geometry accurately, based on the needs of the problem.

The mesh can be 2D or 3D. This depends on the problem studied and the simplifications that can be applied to it. An airfoil flow can be treated as 2D if sufficiently far from the tip and the plane structure. A flow study around a full plane cannot be simplified in 2D, and thus requires a 3D geometry and mesh.

The mesh can be or structured or unstructured. Building a structured mesh means that the overall structure of the mesh follows a coherent indexing thanks to regular meshing patterns. Typical cell shape for structured mesh are quadrilateral in 2D and hexahedrons in 3D. They are cheaper in number of cells and computational memory, but they are more complex to build, and are not always easy to optimize if the geometry is intricate. An unstructured mesh implies that the cells are not organized and indexed regularly through the domain, but only based on their neighboring cells. Typical cell shape for unstructured mesh are triangles in 2D and tetrahedral in 3D. Unstructured meshes usually have a larger amount of cells, but are faster to generate from a user perspective.

I-2. Transformation of the differential equations to algebraic equations: model and solver choices

The transformation of the continuous differential Navier-Stokes equations into algebraic equations solvable numerically is made through a certain range of models and solvers available in the CFD code chosen, in our case ANSYS FLUENT.

I-2.1. Models

The choice of the model is based on the physics needed to describe properly the problem. Is temperature necessary in solving the problem? How do we want to deal with viscosity? Do we need to consider only one type of fluid or several species? One fluid phase or more? These are all questions that makes the user choose through the library of model available in FLUENT: energy, turbulence, species, multiphase flow models and more.

I-2.2. Solvers

When models are chosen and the physics of the problem is defined, the solver must be chosen to solve this physics properly. These solvers linearize the fluid flow equations to calculate a solution to the problem through an iterative process until convergence is met. Several characteristics are defined to choose the proper solver.

FLUENT solvers are classified into two categories: pressure-based solvers and density-based solver. Historically, pressure-based solvers were developed for low-speed incompressible flow, while density-based solvers were involved in high-speed compressible flow. The difference lies in how they solved all the equations defined by the models, either sequentially (pressure-based), or simultaneously (density-based).

The solvers can then be explicit or implicit. Explicit solvers will calculate the solution of the new iteration based only on the solution of the previous iteration, while implicit solvers consider the variables of the current iteration in the solution. The first lead to cheaper iteration cost, but are less stable and may take a larger number of iteration converge, while the latter are more robust, but each iteration is more expansive in term of memory.

The order of discretization of the solver is a choice on how many neighboring cells are taken into in the solution of the calculation of the solution on the next cell. A solver can be first order or second order, central or upwind, etc. Again, this choice depends on the physics of the problem to solve.

I-3. Transient flow stability criterion

Steady or transient problem bring the question of how to solve time in the equations. Time is discretized with solvers similar to spatial discretization, with a certain order of discretization (first or second order). The calculation then solves time steps one by one, involving a certain amount of iteration per time step. When the convergence criterion is met for one time step, the calculation goes to the next.

A stability criterion is defined through a variable specific to transient CFD problem: the Courant-Friedrichs-Lewy number (or CFL number). This number defines the number of cells of size Δx crossed by the fastest flow feature of velocity u over one time step Δt. Over the whole mesh, CFL must be smaller than for a stable transient resolution of the flow.

$$CFL_{max} = u * \frac{\Delta t}{\Delta x} > 1 \tag{52}$$

II - Meshing and problem setup

The problem was based on the geometry of an experimental prototype of pressurized cylinder with diaphragm disk at one end of its end. This prototype was meant to visualize the boiling process inside the cylinder while measuring the blast generated through its exit. No experiment was run with it so far. However preliminary simulations were engaged to understand the physics involved. Simulations were started on this geometry because of its simplicity and low computational cost. Some of the phenomena observed helped understand the physics involved in the small scale experimental BLEVE.

The geometry of the tube was 70.4cm long for 17.2cm diameter.

The simulation geometry was chosen to be 2D axisymmetric along the axis of the tube, to save computational power. Due to software requirement, the axis of symmetry must be the x-axis, thus the tube was oriented horizontally for the simulation. This did not impact the physics of the flow.

The domain was extended 3m along the axis above the tube opening and 1.5m from the axis on the radial direction. Domain size was chosen so that the phenomena of interest (the Mach shock formation and collapse) was over when the lead shock reached the boundaries to reflect back. Thus it was assumed that the domain size did not influence the flow until reflection of the lead blast wave.

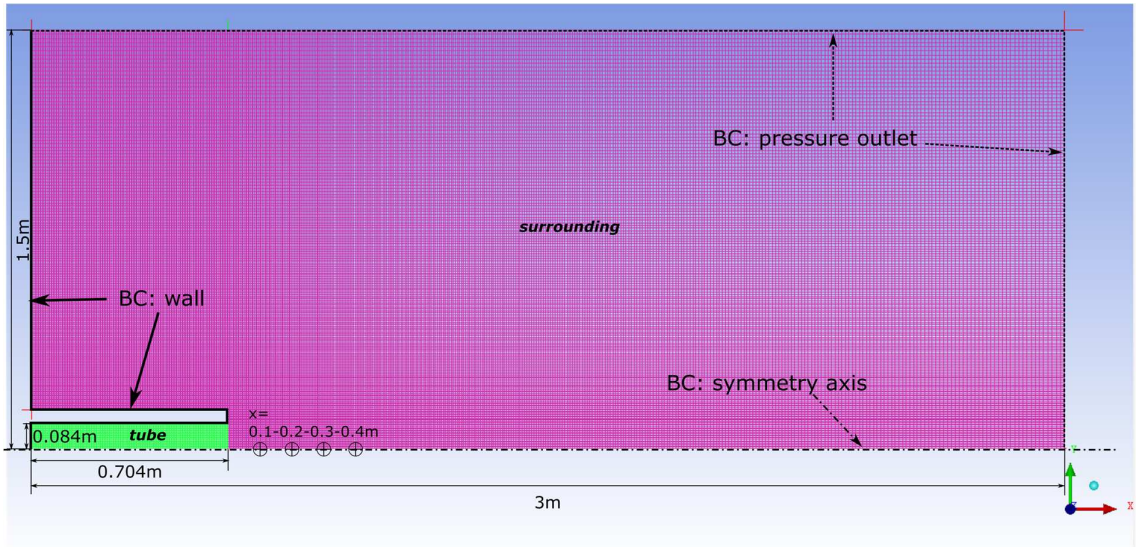

Figure 11-14 Geometry and mesh description of the high pressure tube for transient jet simulation

The cases ran for the purpose of this analysis were air burst. The following models and solvers were chosen:

- Energy model for temperature, inviscid model for Euler equation flow, commonly used for physical explosion simulations;
- Ideal gas for air properties;
- Density-based, AUSM, second order spatial discretization, first order time discretization;

The initial condition of the reference test is the following:

- Ambient conditions: $P_{atm} = 1.01\ bar; T_{atm} = 25^o C$
- Pressurized tube: $P_{fail} = 20\ bar; T_{fail} = 59^o C$

The boundary conditions chosen for this configuration were:

- Axisymmetry along the x-axis;
- Wall on the tube sides;
- Wall on the left side of the surrounding, to simulate the ground;
- Pressure outlet on the top and right side of the surrounding.

The convergence criterion was 10^{-6} for each time step on each equations. The final time of the simulation was chosen at $t_{final} = 8ms$ based on the flow behavior. The number of time step was based on the time step size chosen and this final time.

The mesh size and time step size were based on the following independence studies.

III - Grid independence study

The mesh was a regular square mesh in the tube. It remained small at the exit of the tube, as it was the critical region of interest, and coarsened with distance further in the domain. The final size of a cell at the far end of the domain was 30mm square.

For the purpose of this simulation, the grid independence study was ran on the following 3 meshes, based on the mesh size of cells in the tube: $\Delta x = 8.70$mm, 4.35mm; 2.18mm. For these comparison, time steps were adapted for each mesh size to satisfy the CFL stability criterion, and keep a constant CFL number: $\Delta t =$ 5e-6s, 2.5e-6s, 1.25e-6s. Considering the fastest flow feature observed was the lead shock wave at 400m/s, this led to a CFL = 0.23.

Several criteria were observed to validate the mesh independence: pressure monitor profiles, lead shock overpressure and Mach shock characteristics on the concerned pressure monitors. Based on the results used Chapter 7 , the monitors of interests were the location x=0.1 – 0.2 – 0.3 – 0.4m from the tube exit along the axis of the tube. The pressure profiles on these monitors were plotted against time for each mesh size (Figure 11-15).

From these plots, the following statements were noticed:

- The lead shock was accurate in time, but varied in amplitude due to the cell size (Figure 11-16). The lead shock overpressure was larger with smaller mesh size, as the flow discontinuity was better described;
- The description in time and overpressure of the passage of the Mach shock on sensors x = 0.2 and x = 0.3m were not dependent on the mesh size based on the model chosen;
- The flow after the Mach shock collapse (t > 6ms) varied a lot depending on the mesh. As the contour plot Figure 7-2 shows, many vortices follow the Mach shock collapse. Because inviscid flow was chosen for the simulation, there was no viscous dissipation of these phenomena. The size of the vortices the simulation can describe was directly correlated to the mesh size. These vortices were instabilities in the flow following the Mach shock, leading to large difference in the flow field depending on the mesh size.

The focus of this simulation was on the Mach shock itself. From the comments above and the graphs, it was observed that the Mach shock sufficiently well described with the mesh size $\Delta x =$ 4.35mm.

The mesh size and model choice need to be improved for the convergence of the other criteria such as lead shock overpressure and flow features after the Mach dome collapse.

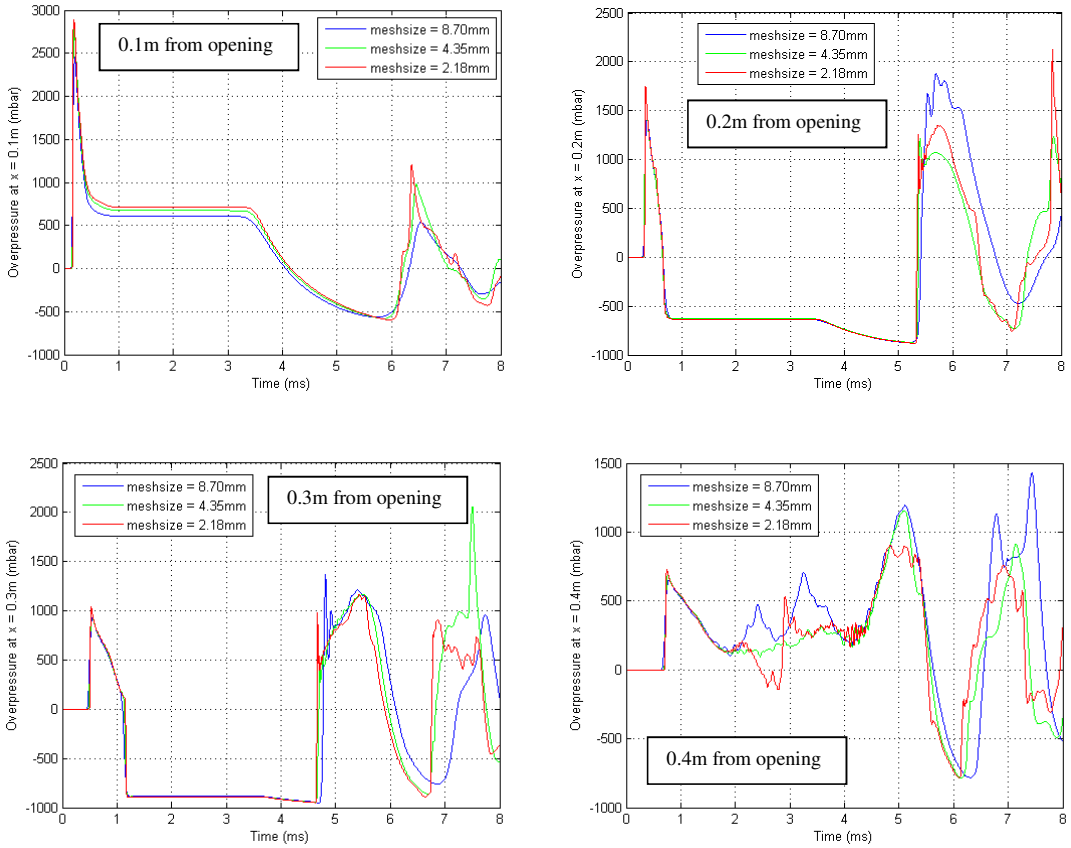

Figure 11-15 Pressure profile versus time for monitors along the tube axis with different mesh sizes

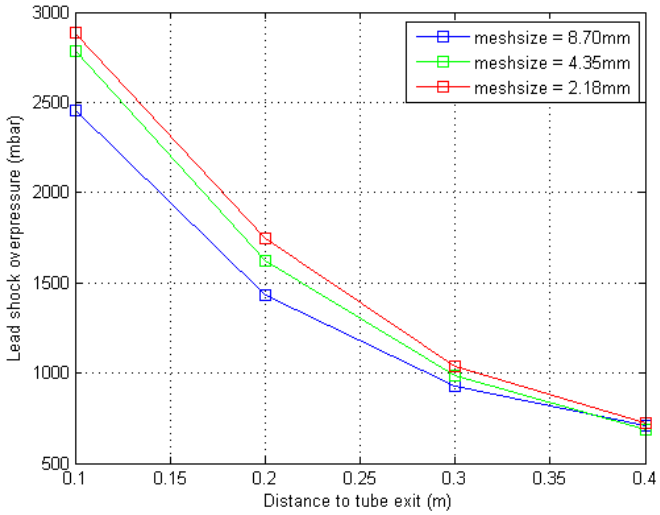

Figure 11-16 Lead shock overpressure versus distance for different mesh sizes

IV - Time step size and CFL independence study

Because of the transient aspect of the simulation, the influence of the time step (or CFL) at constant mesh size was also investigated. For the chosen mesh size above ($\Delta x = 4.35$mm), time steps $\Delta t =$ 5e-6s, 2.5e-6s, 1.25e-6s were used for computation, leading to CFL = 0.46, 0.23, 0.115 respectively. It was noticed during the simulation that smaller time steps led to a smaller number of iteration per step to reach convergence, but obviously a larger number of time steps to simulate the final time of simulation ($t_{final} = 8ms$ here). The comparison of the pressure profiles for each monitor along the axis are presented Figure 11-17.

Similar comments were made on these graphs than on Figure 11-15:

- Lead shock overpressure was also dependent on the time step size, increasing with smaller time step (Figure 11-18).
- The Mach shock passage was well described, with very little variation in the time at which it passes through x = 0.2 and x = 0.3m, as well as the negative pressure plateau reached;
- The flow features after the collapse of the Mach shock differed depending on the time step size. However the differences were smaller than the one observed for mesh size dependence study. The smaller time step size resulted in large oscillations after the collapse of the Mach shock. Changing the order of the discretization scheme (spatial and time discretization) may improve this problem.

The conclusion of this dependence study was that the phenomenon studied was well described for all time steps. The smallest time step presented some unwanted oscillations after the Mach shock collapse. The time step $\Delta t =$2.5e-6s was chosen as a good compromise between oscillating behavior and efficiency of the number of iteration per time step.

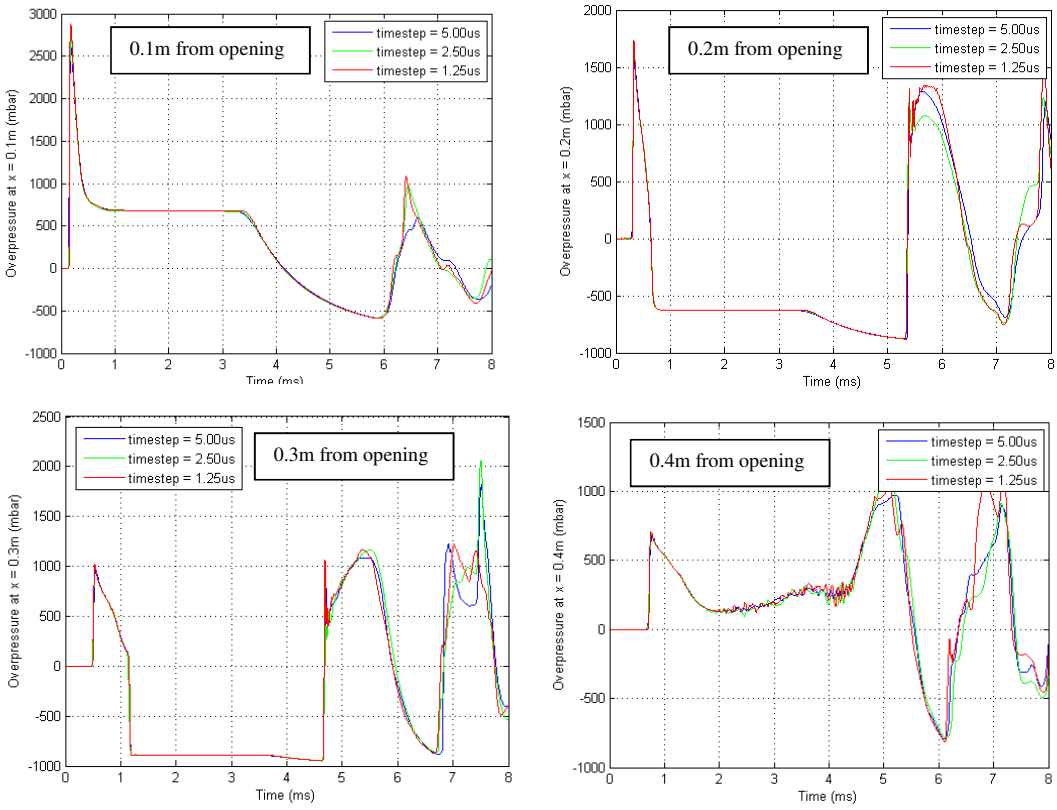

Figure 11-17 Pressure profile versus time for monitors along the tube axis with different time steps

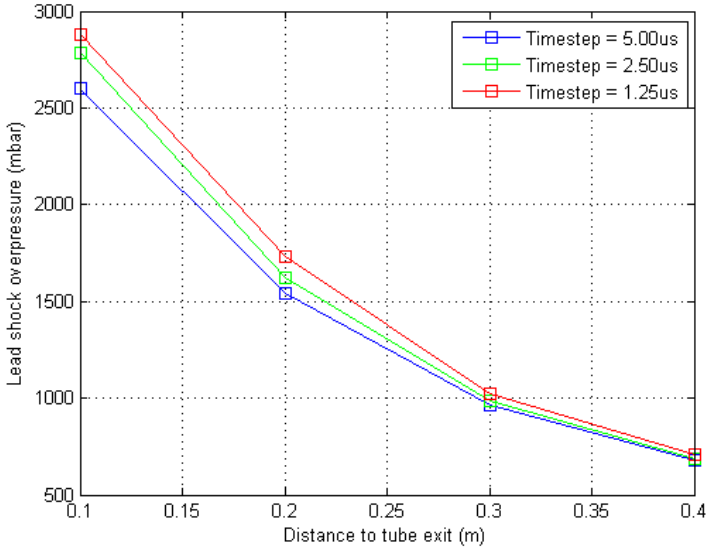

Figure 11-18 Lead shock overpressure versus distance for different time steps

École Nationale Supérieure des Mines

de Saint-Étienne

NNT : 2018LYSEM020

Roland EYSSETTE

CHARACTERIZATION AND MODELING OF BLEVE NEAR-FIELD OVERPRESSURE HAZARD AND GROUND LOADING

Speciality: Environmental Engineering

Keywords: BLEVE, explosion, experiment, modeling, fluid mechanics, thermodynamics, superheat, phase change, shock wave

Abstract:

Boiling Liquid Exploding Vapor Explosion (BLEVE) is one of the most feared accident in the industry. Even though it has been studied for over 6 decades, many safety questions remain poorly answered: what happens if a BLEVE occurs in a congested urban or industrial area? What if a road tanker BLEVE happens on a bridge? These questions require to look closer to the vessel. This work focuses on understanding the physics involved in overpressure generation in the near field surrounding of the vessel, to understand the contribution of the fluid phases (liquid and vapor) in the near-field hazards of a BLEVE. For this purpose, a small scale experimental prototype was designed to reproduce realistic BLEVE failure. Twenty-four propane BLEVEs were performed. A wide range of data was recorded from these tests: blast overpressure all around the vessel, transient pressure inside the vessel, ground loading under the vessel, and high speed imaging through various angles. Results give more insight on the anisotropy of the pressure field around the cylindrical vessel. It also shows a strong dependency between vapor content and maximum overpressure from the lead shock. Moreover, the chronology of the phase change observed through transient pressure measurements show that the main contributor of the maximum overpressure is the vapor phase. The phase change is studied through pressure transient in the vessel and high speed imaging, giving a better understanding of the time scales involved with this phenomenon. Finally, ground loading measurements are analyzed to give insight on the order of magnitude involved in this hazard.

École Nationale Supérieure des Mines
de Saint-Étienne

NNT : 2018LYSEM020

Roland EYSSETTE

CARACTERISATION ET MODELISATION DU CHAMP DE SURPRESSION PROCHE ET DU CHARGEMENT AU SOL D'UN BLEVE

Spécialité: Génie de l'environnement

Mots clefs : BLEVE, explosion, modélisation, mécanique des fluides, thermodynamique, surchauffe, changement de phase, onde de choc

Résumé :

Le BLEVE (Boiling Liquid Exploding Vapor Explosion) est l'un des accidents les plus craints dans l'industrie. Bien qu'il soit étudié depuis plus de soixante ans, certains dangers et situations restent mal anticipés, tels que : quelles seraient les conséquences de la surpression d'un BLEVE dans un milieu urbain confiné ? Qu'adviendrait-il si un camion de transport de GPL venait exploser sur un pont ? Ces questions nécessitent d'étudier la physique du BLEVE au plus proche du conteneur. Ce travail explore les phénomènes physiques générant la surpression aérienne en champ proche de l'explosion, en essayant de comprendre la contribution des phases du contenu (liquide et vapeur) dans les dangers en champ proche du BLEVE. Un prototype expérimental petite échelle a été conçu dans le but de reproduire les BLEVE de cuves cylindriques de manière réaliste. Vingt-quatre BLEVEs de propane ont été effectués. Un large spectre de données a été collecté lors de ces tests : surpression aérienne dans de multiples directions autour du conteneur, variations de pression dans le conteneur avant et après rupture, chargement au sol dû à l'explosion, visualisations en imagerie rapide selon un certain nombre d'angles. Les résultats montrent une dépendance forte entre les caractéristiques de la phase vapeur et la suppression maximale générée par l'explosion. La reconstruction chronologique du phénomène confirme ce résultat. Cependant, la phase liquide joue un rôle capital dans la génération du chargement au sol, qui est un danger considérable, mais peu considéré jusque-là.